The robustness of timber structures

A comparative study on methods to design for robustness.

Scott van den Kieboom

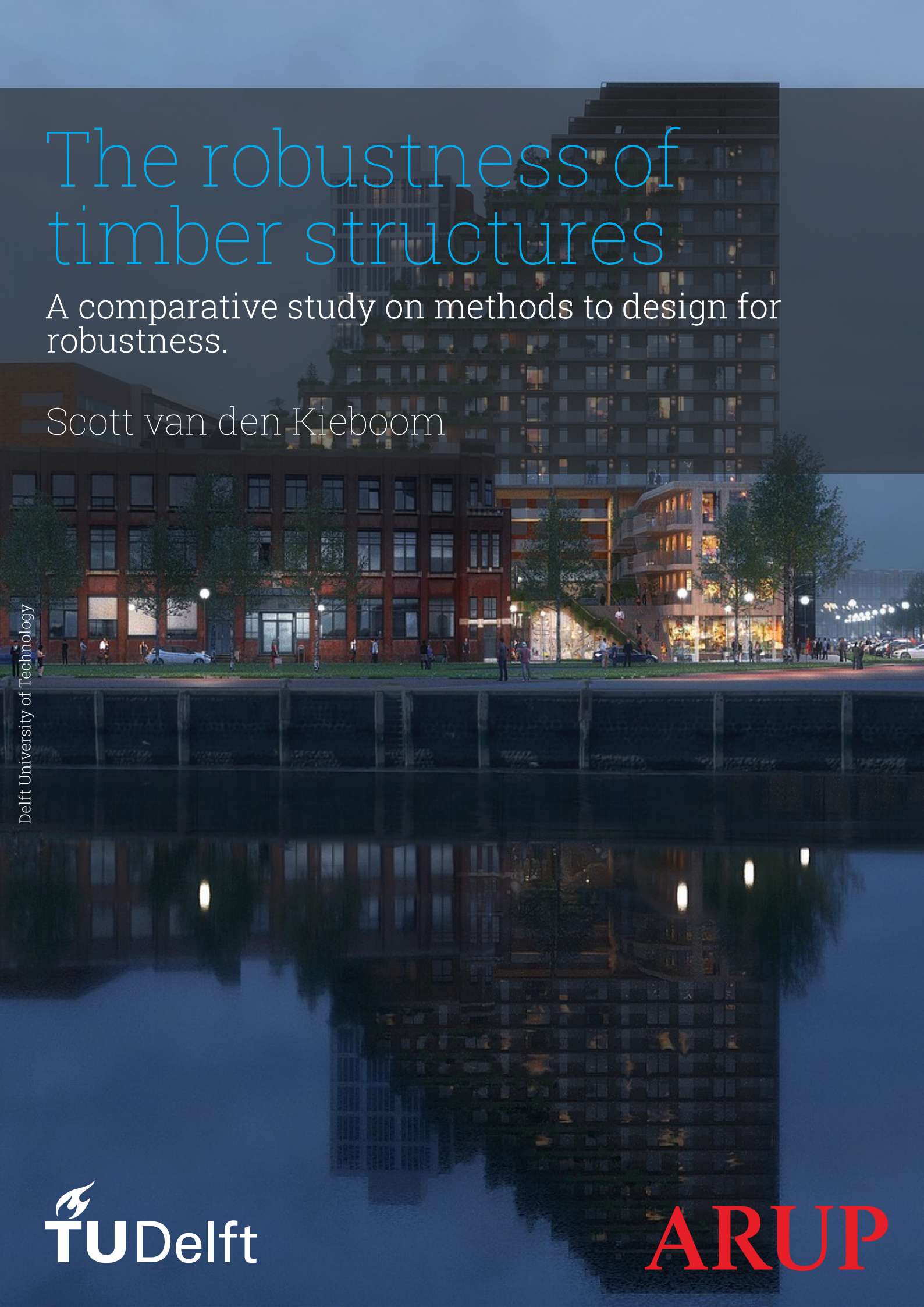

Delft University of Technology

TU Delft

ARUP

The robustness of timber structures

A comparative study on methods to design for robustness.

by

Scott van den Kieboom

Student name	Student number
Scott van den Kieboom	4903536

Thesis committee:	ir. L. van der Linden	Arup
	ir. M.P. Felicita	EMPA Zurich
	dr. ir. G.J.P. Ravenshorst	Tu Delft
	dr. ir. P.C.J. Hoogenboom	Tu Delft (chair)
Faculty:	Civil engineering	Delft

Cover: SAWA building Rotterdam

TU Delft ARUP

Preface

Scott van den Kieboom
Delft, January 2026

My interest in this topic developed from three main directions. The first is my long-standing interest in numerical modeling. Throughout my studies I have spent a significant amount of time building and using models, and I have consistently been fascinated by what can be captured with them, where their limitations lie, and how they can be used to support engineering decisions. Modeling, to me, is not only a tool for producing results, but also a way to explore structural behavior and to better understand the mechanics behind it.

The second source of interest is nonlinear structural response. Several courses introduced nonlinear systems as both challenging and surprisingly elegant: problems that initially appear complex can sometimes be described with clear physical reasoning and relatively compact formulations. These courses also reinforced the role of modeling, as nonlinear behavior is often difficult to treat analytically and is therefore a natural area where numerical methods become essential. The combination of mechanics, approximation, and computation is something I found particularly engaging.

The third component is timber. This interest emerged later. While timber was introduced through coursework, what truly sparked my curiosity was seeing tall timber buildings in practice. Observing these large-scale structures in real life their scale, detailing, and construction logic raised questions for me about load transfer, connection behavior, and, more broadly, structural safety under extreme scenarios. Timber structures, especially when designed for taller applications, combine a compelling architectural and sustainability narrative with demanding engineering challenges.

My motivation for choosing this thesis topic ultimately stems from the intersection of these three interests: the material behavior of timber, the nonlinear and dynamic response that can govern robustness problems, and the modeling strategies required to describe these phenomena with sufficient realism. I found it especially rewarding to translate structural mechanisms into computational models and to see how different modeling assumptions influence predicted behavior. At the same time, this work offered an opportunity to learn more about timber material modeling, connection representation, and robustness strategies, and to reflect on what constitutes reliable and practical engineering assessment.

With these motivations in mind, I undertook this thesis with the hope that it contributes, even in a modest way, to the ongoing development of robust design approaches for tall timber buildings. I also hope it supports further exploration of modeling strategies that can realistically capture nonlinear behavior while remaining applicable in engineering practice.

Acknowledgments

I would like to thank everyone who contributed to this thesis and supported me throughout the process:

Pierre Hoogenboom: Thank you for your guidance and advice throughout this thesis, and for helping me keep the work feasible and aligned with the expected scope. Your support was invaluable. You also sparked my interest not only in nonlinear mechanics, but also in the modeling of these phenomena. Thank you as well for your feedback and expertise during the project.

Geert Ravenhorst: Thank you for providing valuable insight into timber materials and connections. Your feedback helped me strengthen the thesis, and your questions during our meetings challenged me to think critically and often guided me toward the right direction in completing this work.

Lennert van der Linden: Thank you for arranging the opportunity to conduct this thesis at Arup and for giving me the freedom to shape the topic into my own project. I greatly appreciated our discussions and the detailed feedback you provided. Thank you also for continuously encouraging me to explore topics further, which increased my interest and engagement as the work progressed. In addition, I am grateful for the relevant papers you shared, and for the design-oriented questions you raised, which helped me view the work not only from a research perspective but also from that of a practicing engineer.

Maria Felicita: Thank you for your insightful suggestions on which methods to pursue and, equally importantly, what to focus on within those methods. Your feedback and questions made the thesis clearer and more detailed. I also appreciate your availability throughout the process and your encouragement whenever I needed it.

Guido Slobbe: Thank you for always thinking along with me on modeling-related questions and for helping me resolve the issues I encountered. I really enjoyed our discussions, and you showed me both the breadth and the potential of this kind of modeling.

Family: Thank you all for believing in me and encouraging me throughout this research. I am especially grateful to those who helped reread parts of the thesis to improve clarity, and to everyone who listened patiently when I talked about my work time and again.

Friends: Thank you for your understanding and for always being there during this period. I look forward to seeing you more often again.

Summary

The construction of tall timber buildings is becoming increasingly common, driven both by timber's favorable sustainability profile and its excellent strength-to-weight ratio. However, this trend raises concerns regarding structural safety, as timber is a brittle material prone to local failures. Such failures can easily escalate into progressive collapse, making robustness a critical design requirement. Interest in robustness is further amplified by the fact that current design codes for timber are often considered unreliable or insufficiently prescriptive in this regard.

This research aims to bridge the gap between two methods for designing robust timber structures, evaluating whether they are accurate, flexible, and usable in practice. The robustness strategy adopted is the notional element removal scenario, in which a structural element is removed to assess whether the system can develop alternative load paths to redistribute forces despite the missing component.

Two modeling approaches are introduced: the analytical method and the finite element (FE) method. For the analytical method, a pseudo-static energy approach is used to approximate dynamic forces and displacements. For the FE model, both the pseudo-static energy method and a dynamic drop-down model are implemented, allowing comparison between static approximation and explicit dynamic simulation.

These modeling approaches are validated against three physical experiments: a connection moment test, a quasi-static push-down test, and a dynamic drop-down test. All tests are conducted on quarter-scale portal frames featuring identical connection configurations, representing scaled versions of full-size building applications.

Before presenting the models and results, the materials, connections, and validation tests are described in detail. The analytical method requires only basic mechanical properties as input, while the FE model demands comprehensive material models. In particular, laminated veneer lumber (LVL) is modeled with care to replicate its behavior accurately, and sufficient detail is provided for the metallic elements. For the connections, the analytical model employs simplified spring representations, with rotational and translational capacities and stiffness's calculated explicitly. The FE model, by contrast, uses general connection elements, with the full connection setup detailed in the modeling chapter.

The validation tests are documented thoroughly, based on representative papers, to ensure a clear understanding of their procedures and the mechanical behavior observed. Each model is then presented per test, beginning with the setup and followed by results compared against experimental data. Differences are highlighted and discussed.

The results are analyzed to explain observed discrepancies, and recommendations are made to improve the alignment between models and tests. The overall conclusions demonstrate that both methods have strong potential for robustness modeling, but each has limitations: the FE model suffers from uncertainties, while the analytical model tends to be overly conservative. It is shown that the pseudo-static approach in the FE model performs significantly better than the drop-down model, and that amplification factors derived from these models are not reliable indicators of robustness. Furthermore, the analytical method assumes an initial stiffness that is too low at the start and too high before plasticity. Configurations without a gap perform best, though this outcome is influenced by the omission of self-weight, which would alter the results.

In summary, the thesis shows that both analytical and FE approaches can be valuable tools for robustness design in timber structures. However, careful calibration, recognition of limitations, and further refinement are necessary to ensure reliable application in practice.

Contents

Preface i

Acknowledgments ii

Summary iii

1 Introduction 1
- 1.1 The interest in robustness of timber buildings . . . 1
- 1.2 Relevance of the work . . . 2
  - 1.2.1 Scientific relevance . . . 2
  - 1.2.2 Design relevance . . . 2
- 1.3 Research objective . . . 2
- 1.4 Methodology . . . 3
  - 1.4.1 Part 1: theory . . . 3
  - 1.4.2 Part 2: modeling . . . 3
  - 1.4.3 part 3: conclusions and recommendations . . . 3
- 1.5 Scope limitations . . . 4

I Theory 5

2 Robustness in structures 6
- 2.1 What is robustness? . . . 6
- 2.2 When to enhance robustness . . . 6
- 2.3 Design methods for robustness . . . 6
  - 2.3.1 Prevent local failure . . . 7
  - 2.3.2 Assume local failure . . . 7
- 2.4 Alternative load path mechanisms . . . 8
- 2.5 Chosen analysis methods and expected output . . . 10

3 Introduction case study 12
- 3.1 Column removal scenario . . . 12
- 3.2 Column removal test . . . 13
- 3.3 Chosen connection . . . 13
- 3.4 Simplifications for the models . . . 14
  - 3.4.1 Simplification for the analytical model . . . 14
  - 3.4.2 Simplification for the FE model . . . 15

4 Design methods 17
- 4.1 Analytical push down method . . . 17
  - 4.1.1 Analytical Push down Analysis . . . 18
  - 4.1.2 Dynamic response . . . 23
- 4.2 Finite element static push down method . . . 24
- 4.3 Finite element drop down method . . . 26

5 Structural materials 28
- 5.1 Timber . . . 28
  - 5.1.1 Introduction to timber . . . 28
  - 5.1.2 Laminated vaneer lumber (LVL) . . . 29
  - 5.1.3 Material modeling of timber for finite element analysis . . . 29
  - 5.1.4 Validation of timber material model . . . 32
- 5.2 Metals . . . 35
  - 5.2.1 Introduction to aluminum . . . 35
  - 5.2.2 Material model for FE analysis . . . 35
  - 5.2.3 Bolts and dowels of steel . . . 36

6 Connections **38**
6.1 General background on timber connections . . . 38
6.2 Modeling connections for the analytical method . . . 38
6.2.1 Rotational capacity . . . 40
6.2.2 Rotational stiffness . . . 48
6.2.3 Horizontal translation capacity . . . 52
6.2.4 Horizontal translational stiffness . . . 54
6.3 Modeling connections for the dynamic method . . . 55
6.3.1 Discrete beam elements . . . 55
6.3.2 Contact elements . . . 56
6.3.3 Nodal rigid bodies . . . 57

II Tests and models **59**

7 Validation Tests **60**
7.1 Overview of the tests . . . 60
7.2 Connection moment test . . . 60
7.3 Push down test . . . 62
7.4 Sudden column removal test . . . 65
7.5 Conclusions from test data . . . 68

8 Validation models **69**
8.1 General modeling requirements . . . 69
8.2 Moment connection test models . . . 74
8.2.1 Analytical method connection model . . . 74
8.2.2 FE connection model . . . 75
8.3 Push down test models . . . 77
8.3.1 Analytical push down model . . . 77
8.3.2 Push down FE model . . . 80
8.4 Sudden column loss models . . . 82
8.4.1 Pseudo static energy model . . . 83
8.4.2 FE sudden column loss model . . . 84

III Conclusions and recommendations **92**

9 Model differences, possible improvements and recommendations **93**
9.1 Analytical method . . . 93
9.1.1 Moment model . . . 93
9.1.2 Push down model and pseudo static model . . . 94
9.1.3 Conclusion and recommendations . . . 95
9.2 Finite element model . . . 95
9.2.1 Connection model . . . 95
9.2.2 Push down model . . . 96
9.2.3 Column loss scenario models . . . 97
9.3 Model comparison . . . 99
9.4 Improved model . . . 102

10 Conclusions and recommendations **105**
10.1 Primary objective conclusion . . . 105
10.2 Overarching conclusions and recommendations . . . 105
10.3 Recommendations for further research . . . 106

IV Appendix **109**

A Softening curve material model **110**

B Analytical connection calculation **112**
B.1 Rotational capacity . . . 112

B.2 Rotational stiffness 116
B.3 Translational capacity 119
B.4 Translational stiffness 120

C Code for the analytical method **121**

1 Introduction

1.1. The interest in robustness of timber buildings

The increasing attention to robustness in timber design can be attributed to three main factors:

- The growing use of timber in tall buildings;
- The inherently brittle failure behavior of timber;
- The inadequacy of existing design codes for timber, which are often viewed as insufficiently detailed and unreliable regarding robustness.

To explain the growing use of timber in tall buildings, two advantages are set out: its high strength to weight ratio and its favorable sustainability profile. When responsibly sourced, timber offers significant environmental benefits. For instance, studies indicate that cross laminated timber structures can reduce CO_2 emissions by up to 42.9% compared to conventional alternatives (Liu et al., 2016). However, this ecological advantage is counterbalanced by the engineering challenge of ensuring robustness. As timber is increasingly used in high-rise applications, these structures become more susceptible to progressive collapse, necessitating reliable methods to demonstrate their ability to withstand such scenarios.

Secondly, the inherently brittle behavior of timber presents two key challenges for robustness design. First, local failures may occur at comparatively low load levels relative to other structural materials, or may be triggered by environmental actions. Due to the brittle nature of timber, such localized damage can readily propagate, potentially leading to progressive collapse. Second, because structural connections are formed within a brittle base material, their ductility is inherently constrained. As a result, timber connections typically exhibit limited rotational capacity, which reduces their ability to redistribute loads following local damage. This restricted load redistribution capability consequently undermines the overall robustness of timber structures.

Finally, the confidence in current design codes regarding robustness of timber structures remains low. As highlighted by (Mpidi Bita et al., 2019), timber ranks among the materials with the least satisfactory standards for preventing disproportionate collapse. Although Eurocodes provide general guidance on robustness, these provisions are largely informative rather than prescriptive (*NEN-EN 1990*, 2021). Municipal authorities, such as those in Rotterdam, often require buildings to withstand scenarios involving removal of structural elements, leading to inconsistent robustness demands across projects. Current practice frequently relies on simplified approaches, such as applying a fixed Dynamic Amplification Factor (DAF) of 2 *NEN-EN 1995-1-1*, 2024. Yet experimental results show that actual amplification factors can vary considerably: values up to 3.5 have been observed in flexible connections (A. S. Cao et al., 2025), while in plastic regimes the factor may be closer to 1.5 (Cheng et al., 2021). This demonstrates that a fixed value of 2 can either underestimate or overestimate structural demands. so this won't give a reliable strategy for robustness design or analysis.

Furthermore, while Finite Element (FE) modeling is recommended in current design codes, no standardized modeling framework is prescribed. Depending on the required level of detail, FE models may range from sophisticated three dimensional simulations to simplified beam representations with rotational springs. In robustness assessment, column removal scenarios can be analyzed either through explicit dynamic simulation—modeling the sudden loss of a column—or through a pseudo static approach. Each method offers distinct advantages and disadvantages, yet existing codes provide no guidance on their application. Moreover, the literature does not establish the necessary level of detail for such models, nor does it provide consensus on which approach yields more reliable results. This

uncertainty underscores the need for systematic evaluation of analytical and FE methods in the context of timber robustness design.

In light of these challenges, this research thesis aims to explore and enhance the understanding of using alternative load paths to ensure robustness in timber structures. The study evaluates different design methods by applying them to a representative test case, thereby assessing whether the chosen approaches are reliable, usable, and flexible to support practical design for robustness.

1.2. Relevance of the work

The relevance of this research can be considered in two main areas: its scientific relevance and its design relevance.

1.2.1. Scientific relevance

Structural robustness has received increasing attention as its relevance to overall structural safety has become more widely recognized. However, for timber buildings, robustness has not yet been investigated in a systematic and comprehensive manner. Although a limited number of experimental studies have been conducted and several analytical approaches have been proposed, the existing methods are often developed for specific structural configurations or failure scenarios and therefore lack broader applicability. In addition, many of these approaches are not formulated in sufficient detail to enable reliable implementation in practical assessments. Moreover, these approaches are rarely validated against experimental results.

This thesis seeks to address these shortcomings by investigating multiple modeling approaches for assessing the robustness of timber structures and evaluating their respective applicability and performance. The proposed methods are compared against experimental data to identify areas of good predictive accuracy as well as aspects where discrepancies remain. In doing so, the study also aims to improve the understanding of mechanical behaviors which may have a significant influence on the structural resistance of timber structures.

1.2.2. Design relevance

With the increasing use of timber in tall buildings, reliable design methods are essential to ensure that these structures are sufficiently robust and safe. Such methods must be both usable and flexible so that engineers can apply them in practice without excessive complexity. This thesis offers recommendations for best practices in applying analytical and FE based approaches, ensuring that they are accurate enough to inform design decisions while remaining practical for engineering use. Since current design codes provide only limited and largely conservative guidance on robustness, this work proposes alternative approaches that are less conservative yet more accurate. In doing so, it aims to bridge the gap between code provisions and practical design needs, supporting the safe and efficient use of timber in modern tall structures.

1.3. Research objective

The primary objective of this thesis is to determine whether analytical and FE models can accurately represent column removal scenarios, thereby validating their use in robustness design. The models should meet three criteria to ensure they can be used and will be used to design for robustness:

- **Usability**: straightforward enough for engineers to apply without excessive complexity.
- **Accuracy**: results should align with experimental data within acceptable margins.
- **Flexibility**: adaptable to different structural configurations and connection properties.

A method that satisfies these criteria can be considered suitable for designing timber structures with robustness in mind.

This can then be translated into an main research question which is: **Can analytical and finite element models accurately simulate column removal scenarios and be applied in robustness design for timber structures?**
The main research question is addressed through the following sub-research questions:

1. Which robustness design strategies are applicable to timber structures given their brittle material behavior and connection ductility limitations, and why does the notional element removal method provide a representative and conservative basis for assessing robustness in this context?
2. How can a notional column removal scenario be translated into a physically realizable experimental test that captures the critical load redistribution mechanisms relevant to timber frame robustness?
3. How can analytical and finite element models be formulated to represent the structural response of a timber frame following sudden column removal, including alternative load path development and dynamic effects?
4. How can timber and metals be modeled in analytical and finite element frameworks such that their stiffness, strength, and post elastic behavior are sufficiently represented for robustness assessment?
5. How can the selected beam to column connection be represented in analytical and finite element models in a manner that captures its rotational and translational stiffness, capacity, and deformation limits under column removal loading?
6. What are the key experimental response characteristics—such as load displacement behavior, connection rotations, and failure modes—observed during connection, push down and column removal tests on the timber frame system?
7. How do the analytical and finite element models perform in terms of accuracy, usability, and flexibility when compared to experimental results, and which modeling assumptions most strongly influence these performance metrics?
8. How do the analytical and finite element modeling approaches compare in their prediction of structural response, dynamic amplification, and failure mechanisms for timber frames subjected to column removal?

1.4. Methodology

The methodology is divided into three parts which should offer the answers to the research questions.

1.4.1. Part 1: theory

- Literature study on robustness concepts and terminology;
- Review of material properties, followed by development of material models for FE analysis;
- Literature study on connection modeling, with detailed analytical treatment and general FE considerations;
- Review of design methods, and a detailed explanation of the analytical method and some general considerations for the FE model.

1.4.2. Part 2: modeling

This part of the study focuses on the numerical modeling and validation of the experimental tests. The experimental setups are first introduced, and their results are presented and discussed to ensure a clear understanding of the observed structural behavior. Subsequently, each test is modeled using the proposed modeling strategies, including one analytical model and one finite element (FE) model per test.

For the column removal scenario, two distinct FE modeling approaches are employed to assess their relative performance. These include a pseudo static approach, which is also adopted in the analytical model, and an element removal approach, in which the structural response is simulated by explicitly deleting elements to induce a dynamic response. For each modeling approach, the model setup is described in detail, followed by a presentation and discussion of the corresponding results.

1.4.3. part 3: conclusions and recommendations

This part will start with a discussion about the models and comparisons with the tests then The chapter will also discuss possible improvements to the models, as well as the inherent drawbacks that arise from the chosen modeling approaches. Based on these analyses, conclusions will be drawn regarding

the effectiveness of the methods and their ability to realistically represent structural behavior for design purposes. Finally, recommendations will be provided to indicate how the models can be refined to deliver more reliable results and to capture structural behavior in a more realistic manner.

1.5. Scope limitations

The following limitations are adopted to ensure that the scope of the research remains focused on addressing the main research question. These limitations define the boundaries of the study and are summarized as follows:

- Only a single experimental test is considered for the column removal scenario. This choice is primarily motivated by the limited availability of comparable experimental data. Existing tests often differ significantly in terms of structural configuration, connection detailing, and boundary conditions, which can lead to substantially different structural responses and complicate direct comparison and modeling.
- The study focuses on a single robustness strategy. Given that robustness encompasses a wide range of possible design approaches, the investigation is restricted to the notional element removal method. This approach is selected as it represents a conservative worst case scenario and does not rely on the assumption of preventive or protective measures.
- The numerical models replicate the experimental setups without modification. This ensures that the numerical results can be directly validated against test data; extending the models beyond the tested configurations would preclude reliable validation and limit the reliability of the conclusions.
- Simplifications are introduced in the modeling of materials and connections. Due to modeling constraints and the objectives of the study, different material representations are employed in the analytical and finite element models, without fully capturing all aspects of material behavior. Similarly, connection models are simplified in both approaches, primarily as a result of modeling limitations.
- The experimental and numerical investigations are limited to a quarter scale representation of a full structural system, consistent with the available test data. While scale effects may influence the structural response at full scale, these effects are not examined in this thesis.
- Only two modeling approaches are considered. These approaches are selected and implemented in a targeted manner to maintain feasibility within the available time frame of the study. Consequently, alternative modeling strategies and parameter variations are not explored in detail.

Part I: Theory

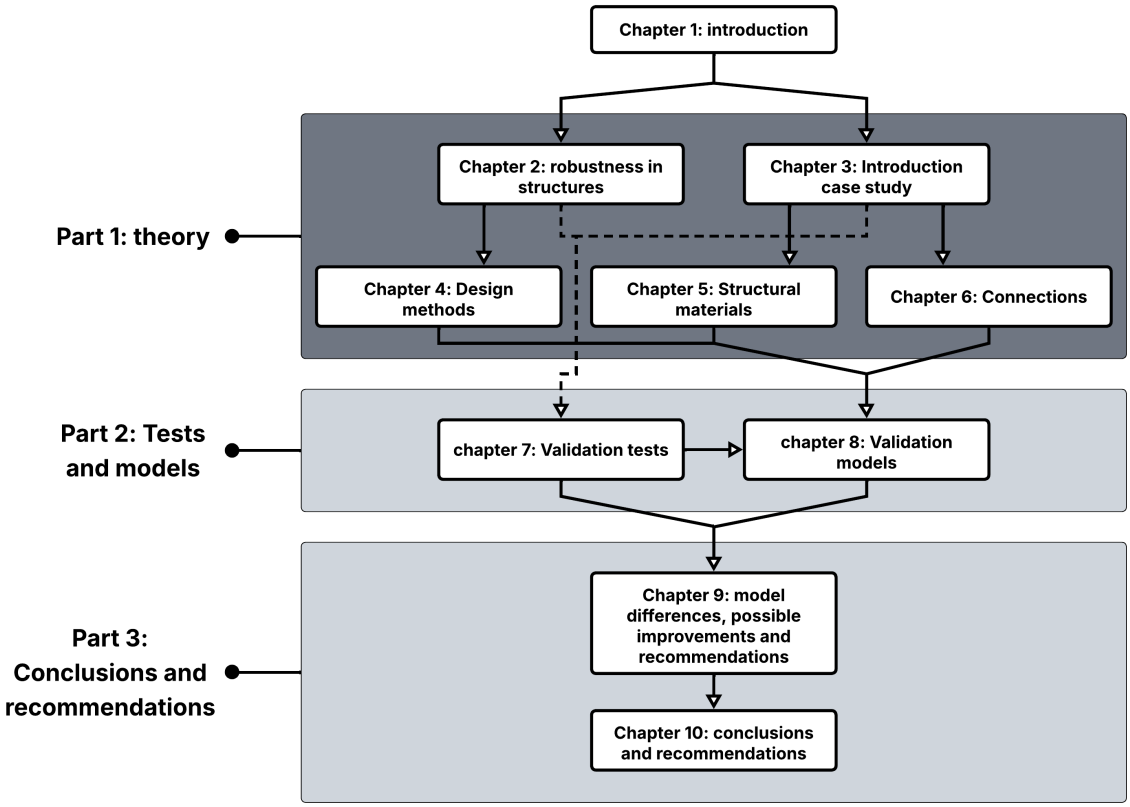

2
Robustness in structures

This chapter introduces the concept of structural robustness, clarifies closely related terminology, outlines when and how robustness should be enhanced, and summarizes the design approaches used later in the thesis. We begin with definitions drawn from standards and recent state of practice literature, then present a framework of design strategies, and finally describe the specific analysis methods adopted in this work.

2.1. What is robustness?

In *EN 1990:2021*, robustness is framed as a global design objective: a structure during its design working life should *not be damaged by unforeseen adverse events, such as the failure of a member or part of the structure to an extent disproportionate to the original cause*. Progressive (or disproportionate) collapse is highlighted as a characteristic form of such damage (*NEN-EN 1990*, 2021).

A recent state of the art report refinements this notion: *robustness is the ability of a building to accommodate an initial local damage without propagation leading to disproportionate consequences* (Palma & Fink, 2022). In complementary terminology, Starossek (2018) distinguishes between (i) disproportionate collapse as a design concept tied to chosen objectives and acceptance criteria, and (ii) progressive collapse as the physical mechanism by which local damage spreads through a system.

Two points are central to the terminology used in this thesis:

- Hazardous initiating events are often unforeseen or even unforeseeable; explicit design against a complete set of such hazards is therefore impractical (Palma & Fink, 2022).
- Insufficient robustness can result in progressive collapse following local failure, yielding consequences that are disproportionate to the hazard (Starossek, 2018).

Accordingly, the term robustness here refers to the capacity of the structure to prevent the spread of local damage into a system wide failure under low likelihood, high consequence unforeseen scenarios.

2.2. When to enhance robustness

EN 1990:2021 states that measures to enhance robustness should be applied when required by the authority having jurisdiction or, if not specified, agreed among relevant parties for the specific project (*NEN-EN 1990*, 2021). It also observes that most conventionally designed structures already achieve an adequate level of robustness without additional measures. Identified accidental actions are treated via *EN 1991* provisions; however, relying solely on specified accidental actions is not sufficient for general robustness because many hazardous events are unforeseen in nature (Palma & Fink, 2022).

In practice, some authorities formulate that removal of structural element needs to be able to resisted. This is in most cases a column or wall segment. In this the worst scenario needs to be assumed to take out the right column. so when this building can't carry the instantaneous load due to this column removal this building needs robustness enhancements.

2.3. Design methods for robustness

Design methods for robustness are divided into two main strategies these are:

- **Preventing local failure**: often impractical in timber due to its brittle nature and the large cross-sections required in tall buildings.
- **Assume local failure**: a more feasible approach, allowing the structure to redistribute loads after

local damage.

A conceptual framework for robustness design, illustrating the different strategies available, is presented in Figure 2.1. This framework serves as a general guideline for determining appropriate measures to enhance robustness in structural systems. 2.1.

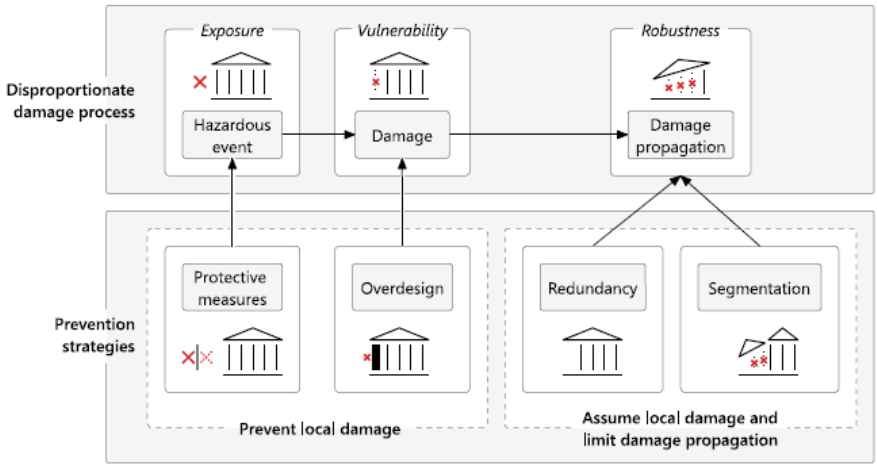

Figure 2.1: Robustness framework (Palma & Fink, 2022).

2.3.1. Prevent local failure

Strategies to prevent local failure can be grouped in:

1. **Protection measures** that reduce the likelihood or severity of the hazardous event (outside the engineering scope of this study);
2. **Over design measures**, notably key element design, wherein potentially critical members are proportioned to directly resist the postulated hazard (Palma & Fink, 2022).

While key element design is sometimes necessary, prior reviews caution against relying on it as a primary approach because it is scenario specific, costly, and may still leave the system vulnerable to alternative triggers (Arup, 2011; Huber et al., 2018). In this thesis, we therefore focus on systemic strategies that assume local failure and prevent its propagation.

2.3.2. Assume local failure

Assuming a local failure has occurred, the goal shifts to avoiding progressive collapse by ensuring that alternative load paths can form. Two broad families are common:

Redundancy based approaches.

One method is the tie force method (e.g., horizontal ties) as found in *EN 1991-1-7*, which prescribes minimum tie capacities to develop catenary action when an element is lost (*NEN-EN 1991-1-7*, 2021). In practice, an assumed vertical deflection is often used to keep required tie forces within a realistic range; for example, an idealized mid span deflection on the order of 0.16 times the sum of adjacent spans is sometimes adopted in guidance documents also shown in figure 2.2.

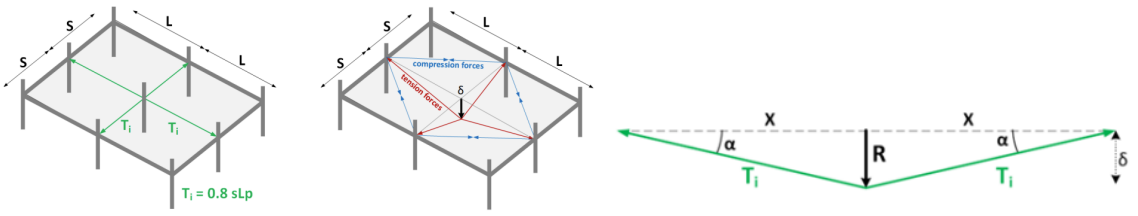

(a) 3d tie method.

(b) 2d tie method.

Figure 2.2: Tie force method (J et al., 2024).

In this the internal tie forces T_i are providing vertical equilibrium against the resultant R. which can be put into equation form like this:

$$\sum_i T_i \sin \alpha \; = \; R, \tag{2.1}$$

Where α is the tie inclination after deformation.This approach is intentionally simplified and typically neglects ductility and rotation limits; in particular, the assumed rotation can be unrealistically large if not checked against detailing and connection capacities (J et al., 2024).

A more direct approach is the notional element removal method: remove a column or a wall segment in analysis and verify that the damaged structure exhibits sufficient residual strength and bridging capacity. Falling debris effects should also be considered where relevant (Arup, 2011; J et al., 2024). For static analyses, a dynamic amplification factor (DAF) of about 2 is commonly used to approximate impulsive effects; alternatively, explicit dynamic analysis can be performed (Arup, 2011; Ellingwood et al., 2007; *NEN-EN 1995-1-1*, 2024). So this will result in four different calculation methods:

- Linear static with DAF;
- Nonlinear static with DAF;
- Linear dynamic;
- Nonlinear dynamic.

These methods are also shown in figure 2.3 with their positives and negatives next to them.

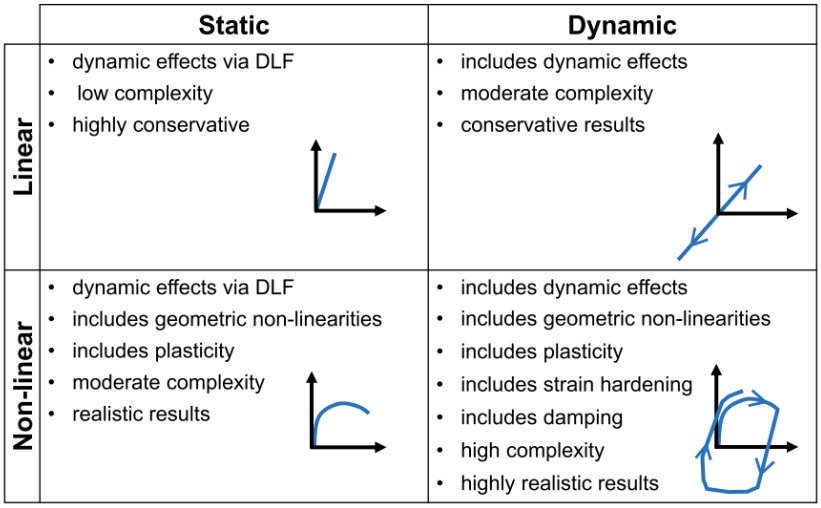

Figure 2.3: Analysis procedures (Huber et al., 2018)

Segmentation.
Instead of relying on redundancy, the structure can be segmented to limit the horizontal spread of damage, e.g., via deliberate structural fuses in large low-rise systems (J et al., 2024). Or by *the division of a structure into dependent structural components which are in themselves robust* (Ellingwood et al., 2007).

2.4. Alternative load path mechanisms

Since this thesis focuses on redundancy based robustness approaches, the structural system is assumed to redistribute loads following the removal of one or more load bearing elements. This redistribution includes not only the applied loads but also the internal forces that were previously carried by the removed elements. To enable this force redistribution, the structure must be capable of activating alternative load path mechanisms. Several such mechanisms may develop in frame structures, depending on the structural configuration, boundary conditions, and connection behavior. The most relevant mechanisms are outlined and discussed below.

- Catenary action;
- Compressive arching;
- Shear transfer of deep beams;
- Tensile membrane action;
- Vierendeel action.

Each mechanism has distinct deformation demands and detailing requirements (Arup, 2011). These mechanism are also shown in figure 2.4.

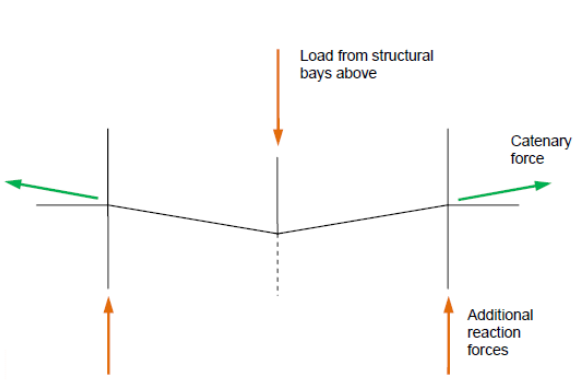

(a) Catenary action (Arup, 2011).

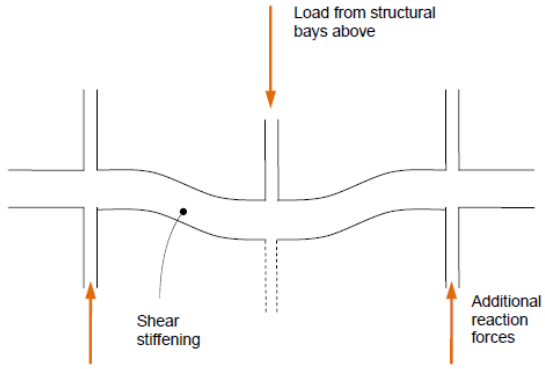

(b) Shear transfer deep beams (Arup, 2011).

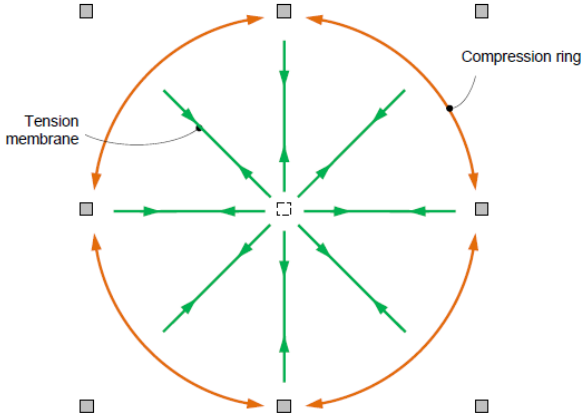

(c) Tensile membrane (Arup, 2011).

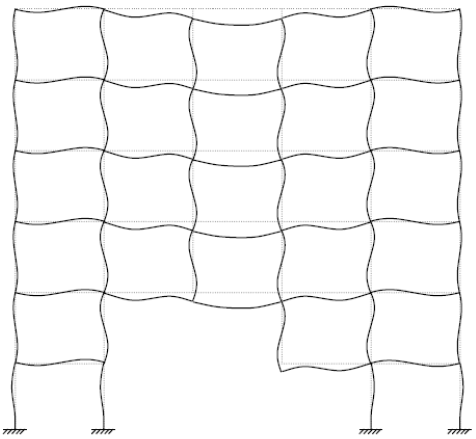

(d) vierendeel action (Arup, 2011).

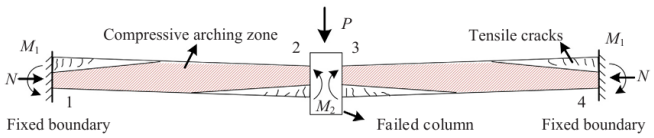

(e) Compressive arching (Lu et al., 2018).

Figure 2.4: Alternative load path structural mechanism.

When a structural column is removed, a catenary action mechanism may develop as a result of mid span deflection in the beams. In this state, the vertical load is primarily resisted through axial tension in the beams. However, this mechanism necessitates substantial beam elongation and significant rotational capacity at the connections to prevent excessive internal forces. This approach is commonly considered when assessing the residual load carrying capacity of beams and connections under an assumed deformation scenario.

For the shear transfer mechanism, the system relies on a deep beam to redistribute the load. In this case, the removed column's load is transferred to adjacent supports predominantly through shear rather

than flexure action. Although catenary and shear mechanisms can coexist in practice, simultaneous design for both is highly complex due to differing deformation and detailing requirements.

The membrane action mechanism operates similarly to catenary action but occurs in two way spanning slabs. Here, the slab develops in plane tensile forces, enabling load redistribution in multiple directions. This mechanism is particularly relevant in structures with continuous slabs and beams, where it can act in conjunction with catenary and shear mechanisms.

For vierendeel action, the loads resulting from the loss of one or more columns are redistributed through bending moments and shear forces in the remaining frame members. This mechanism requires a high degree of joint rigidity, as the connections must sustain significantly greater moments and shear forces than those considered in conventional static design.

For compressive arching to develop, both the column and the beam must possess high compressive strength and be capable of forming the compression zones illustrated in Figure 2.4. In this mechanism, compressive forces arise at the top of the beam near the central column and at the bottom of the beam near the adjacent supports. These opposing forces generate a resisting moment, which counteracts the downward displacement of the middle column.

2.5. Chosen analysis methods and expected output

As discussed previously, this thesis adopts a redundancy based approach to robustness, requiring an assessment method that can explicitly capture load redistribution following local failure while representing a conservative, worst case scenario. For this reason, the notional element removal method is selected. This method is particularly appropriate because it explicitly accounts for unforeseen initiating events, is frequently required by regulatory authorities, and provides a realistic representation of severe local damage. Consequently, the notional element removal method is widely recognized in both engineering practice and the literature as a benchmark approach for evaluating structural robustness under local failure conditions.

To implement this method, two complementary modeling approaches are employed:

- An **analytical beam model**, using non-linear springs to simulate static structural behavior (hereafter referred to as the analytical method).
- A **finite element (FE) model**, capable of capturing dynamic effects and material failure mechanisms.

Both modeling approaches are applied to a representative substructure and follow a structured and consistent workflow, which is summarized below:

- **Selection of the element to remove.** The removed element should represent a plausible or worst case scenario for the considered part of the building and must not be a designated key element. In practice, representative cases include internal, facade, and corner columns on a typical floor (J et al., 2024).
- **Structural modeling.** For static analyses, the structural response can be represented using a simplified beam model with springs and supports, as demonstrated by B. Izzuddin et al., 2008. For dynamic analyses, a detailed finite element (FE) model is constructed and analyzed in the time domain to capture the transient response following element removal. In both approaches, the analyzed substructure is isolated from the global system, with the influence of the surrounding structure represented through boundary springs.
- **Application of loads.** The applied loading must represent both the removal of a structural element and the forces that were previously carried by that element. When a column is removed, the resulting force redistribution is therefore evaluated by applying the load at the location previously occupied by the column. Depending on the objective of the analysis, this loading may be considered in combination with the self-weight and live loads acting on the remaining structure.
- **Element removal.** In the analytical approach, the removed element is assumed to be absent from the start of the analysis, while dynamic effects are approximated using a pseudo static energy

based approach. In the FE approach, element removal is simulated either through a static push down analysis combined with the energy method or through a dynamic drop down simulation, in which the stiffness of the removed element is reduced to a negligible value over a short time interval (e.g., $0.001\,\mathrm{s}$) (Mpidi Bita, 2019).

- **Assessment of collapse resistance.** For the analytical model, robustness is evaluated by verifying that connection rotations remain within acceptable limits. In the FE model, collapse resistance is assessed by identifying material and connection failure mechanisms directly from the numerical simulation.

This workflow provides a structured basis for comparing the analytical and FE approaches. Following this, the thesis explains in detail how each method is implemented and how materials are modeled.

An important consideration in both modeling approaches is the type of output that can be obtained and how these outputs can be used to assess structural robustness. Table 2.1 summarizes the key outputs for the finite element (FE) model and the analytical model.

FE model	Analytical model
Load and displacement response	
• Maximum dynamic load capacity from peak dynamic responses or highest release load without failure; • Maximum dynamic displacement obtained from the dynamic response with the pseudo static approach and drop down analyses.	• Maximum dynamic load capacity and displacement obtained from the dynamic response with the pseudo static approach.
Dynamic amplification factor (DAF)	
The dynamic amplification factor is evaluated by matching dynamic and static responses, and may be defined in terms of either force or displacement.	
• DAF from push down and dynamic response curves, including drop down analyses.	• DAF from push down and dynamic response curves from the pseudo static approach.
Internal forces and rotations	
• Connection rotations, bending moments, and axial forces from static and dynamic analyses.	• Connection rotations, bending moments, and axial forces calculated from the analytical response.
Failure mechanisms and robustness	
• Failure mechanisms and progressive collapse behavior captured inherently through material and connection modeling.	• Failure mechanisms are not explicitly modeled and must be verified through separate robustness checks.

Table 2.1: Comparison of key outputs available from the FE and analytical models

3
Introduction case study

This chapter introduces the case study adopted in this thesis. First, the implementation of the notional element removal scenario within the case study is described. Subsequently, the column removal test is discussed at a general level, with further details provided in Chapter 7. The selected connection configuration is then presented and briefly explained. Finally, the simplifications required to translate the experimental setup into both the analytical and finite element models are outlined.

3.1. Column removal scenario

In this section, the translation of the notional element removal scenario into a practical test setup is explained. To accurately simulate the intended structural behavior, the test setup must satisfy several key requirements:

1. It must allow for the removal of a column, or an equivalent element, while the applied load is maintained;
2. It must adequately represent the structural response of a building or a representative part thereof;
3. It must enable the column removal to occur in a near instantaneous manner.

Regarding the first requirement, the test setup must include a central column that can be subjected to load while remaining sufficiently short to allow for a meaningful drop height. This is achieved by introducing a short middle column combined with a load distribution element that transfers the applied load uniformly to the column.

For the second requirement, the simplified structural system must still capture the essential behavior of the full structure, or at least provide reliable information on the forces that the surrounding structure would be required to carry following column removal. This necessitates constraining the horizontal displacements and rotations at the side connections. These constraints must be capable of generating measurable reaction forces, allowing either failure of the system to be identified or the transferred forces to be quantified and assessed against the capacity of the remaining structure.

Finally, to accurately represent the sudden loss of a column, the release mechanism must operate in a near instantaneous manner. This ensures that, upon release, no external resistance is provided by the removal system itself and that the structural response is governed solely by the remaining load bearing components.

By satisfying these requirements, the notional element removal scenario can be translated into a representative column removal test setup. This scenario is selected because column removal is considered a worst case event for robustness assessment. The specific experimental configuration used to achieve this is presented in the following section.

3.2. Column removal test

The column removal test is configured in accordance with the requirements outlined above. The setup for this test is shown in figure 3.1.

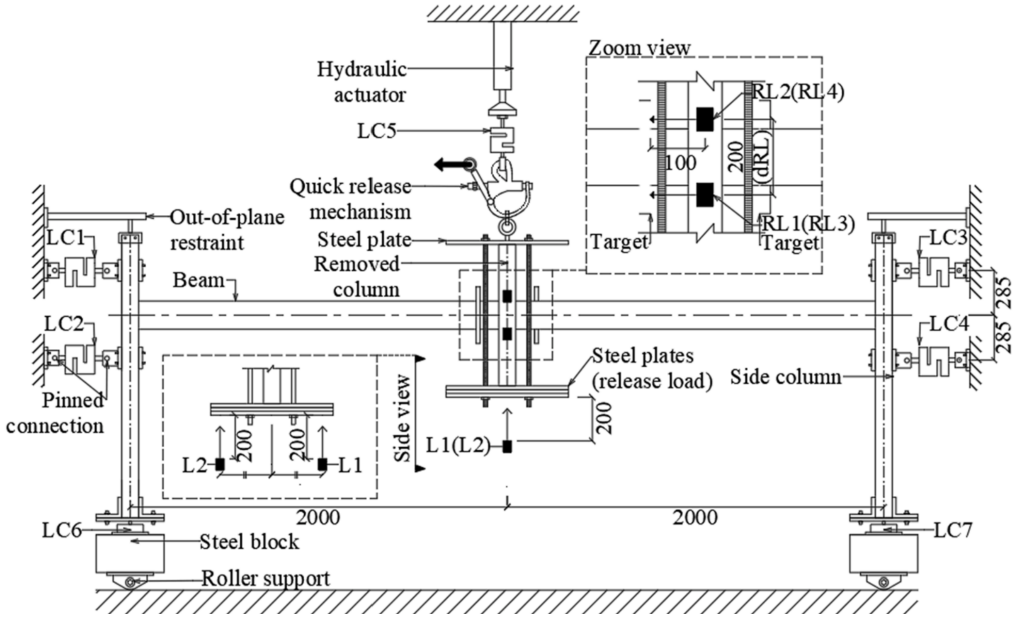

Figure 3.1: Column removal scenario setup.

Figure 3.1 illustrates the experimental configuration used for the column removal test. The setup consists of a portal frame extracted from a building structure and scaled down to one quarter of its original size. Two adjacent portal frames are included in the model, with the middle column of these neighboring frames intentionally shortened. This shortened column represents the column to be removed during the test.

Steel plates are attached to the shortened column to simulate the load acting on the structure prior to column removal. This applied load is referred to as the *release load*. The middle column is connected to two beams, which are in turn connected to the two side columns. These side columns are vertically restrained by a combination of bottom supports and applied weights to prevent uplift during the experiment.

In the horizontal direction, the side columns are restrained using load cells. These load cells simulate the interaction between the portal frame and the surrounding building structure and provide measurements of the horizontal forces. From these measurements, the moments and horizontal restraint forces required in the full scale building can be derived. In addition, out of plane movement of the portal frame is prevented at the tops of the side columns.

The middle column is supported by an actuator connected to a load cell, which is linked to the column via a quick release mechanism. This mechanism is designed to ensure that the column is released instantaneously, thereby accurately representing sudden column removal.

3.3. Chosen connection

This section describes the selected connection type investigated in this thesis. Although the experimental campaign includes multiple connection configurations, only one connection is considered here in order to remain within the defined scope and time constraints of the thesis.The selected connection configuration is shown in Figure 3.2.

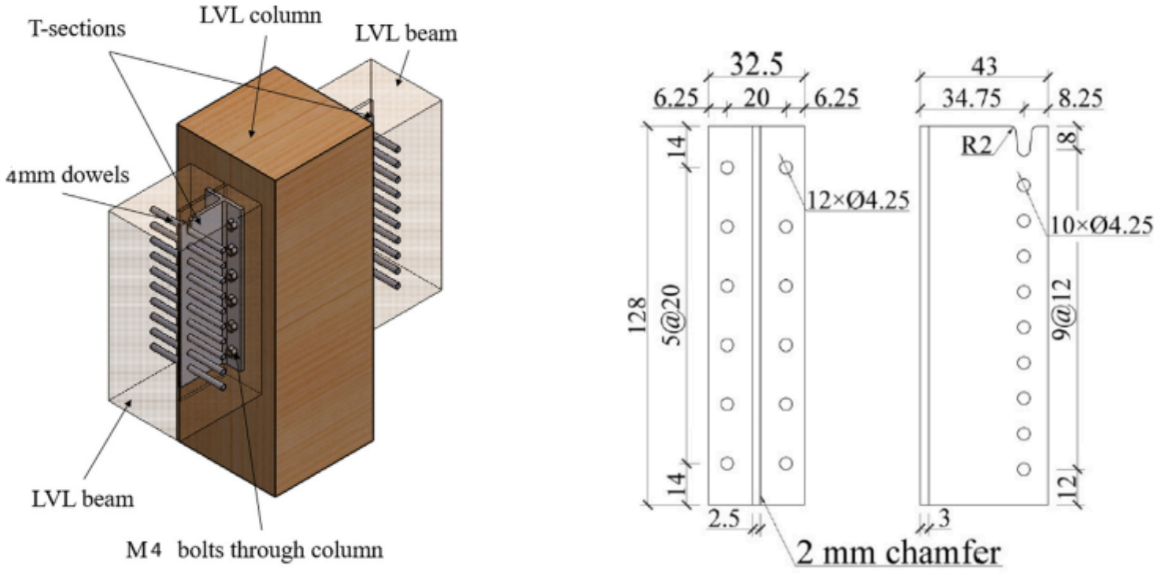

(a) Connection 3D setup Masaeli et al., 2020.

(b) Aluminum plate setup Lyu et al., 2020.

Figure 3.2: Selected connection configuration used in this thesis.

The connection used in this thesis consists of an aluminum T-stub connected to the column using M4 bolts. This aluminum T-stub is also connected to the beam using 4 mm steel dowels. This configuration represents one of the experimentally tested connection types and is suitable for detailed analytical and numerical investigation. A comprehensive description of the connection geometry, material properties, and mechanical behavior is provided in Chapter 6.

3.4. Simplifications for the models

In order to translate the experimental setup into numerical models, a number of simplifications are required. This section provides a general overview of these simplifications. First, the analytical model is introduced, explaining how the experimental configuration is reduced to a simplified and tractable mechanical representation. Subsequently, the finite element (FE) model is discussed, focusing on how the essential structural components and boundary conditions are incorporated into a numerical framework.

3.4.1. Simplification for the analytical model

For the analytical approach, the experimental frame is idealized as a simplified beam model. The full portal frame is replaced by a single beam element, with the influence of the surrounding structure and boundary conditions represented through rotational and translational springs. This allows the global structural response to be captured while maintaining a low level of model complexity.

As discussed in Section 3.1, the experimental frame is horizontally restrained by load cells in order to measure the horizontal reaction forces. These load cells also impose rotational restraint at the side connections, which must be accounted for in the analytical model. Consequently, both translational and rotational stiffness's are introduced at the beam supports to represent the combined effect of the side connections, the remaining frame, and the horizontal restraint system.

In total, the analytical model includes four rotational springs, representing the rotational stiffness of the beam column connections, and two translational springs located at the side supports. This configuration ensures that all relevant force transfer mechanisms of the experimental setup are represented in the simplified model. A schematic overview of the resulting analytical model is shown in Figure 3.3.

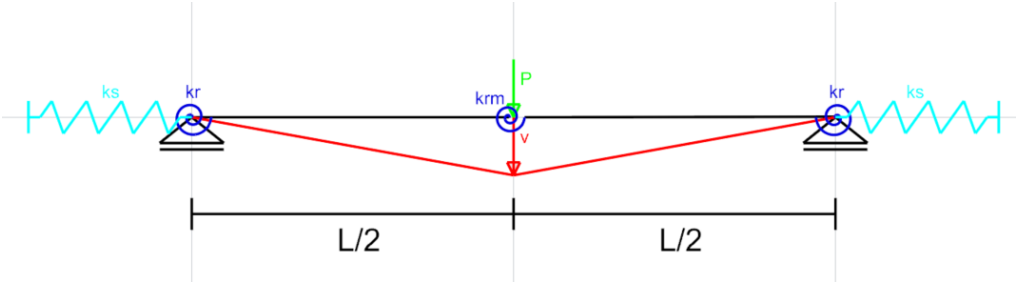

Figure 3.3: Simplified representation of the test for the analytical mode.

Figure 3.3 illustrates the adopted analytical model. The applied load P represents the force previously carried by the removed middle column and is gradually increased during the analysis to determine the maximum load carrying capacity of the system. The vertical displacement at mid-span is denoted by v.

The rotational stiffness at the middle connection, denoted by k_{rm}, is modeled as a single equivalent spring. This spring represents the combined contribution of the two central beam column connections and therefore has twice the stiffness of an individual side connection. This simplification allows the behavior of the middle joint to be captured efficiently without introducing additional degrees of freedom.

At the side connections, both rotational and translational springs are included. These springs represent the stiffness and capacity of the beam column connections, the remaining frame structure, and the load cells used in the experimental setup. The rotational and translational capacities of these springs are assumed to correspond to the maximum capacities observed in the experimental tests.

Finally, the beam supports are modeled as rollers, allowing horizontal movement. Horizontal stability is provided exclusively by the axial springs, denoted by k_s, which represent the restraint imposed by the surrounding structure and the load cells. This modeling assumption reflects the experimental boundary conditions and ensures consistency between the analytical model and the physical test setup.

3.4.2. Simplification for the FE model

For the FE model, fewer simplifications are required compared to the analytical model; however, several aspects of the experimental setup still need to be translated into a numerical representation. The resulting simplified FE model is shown in Figure 3.4.

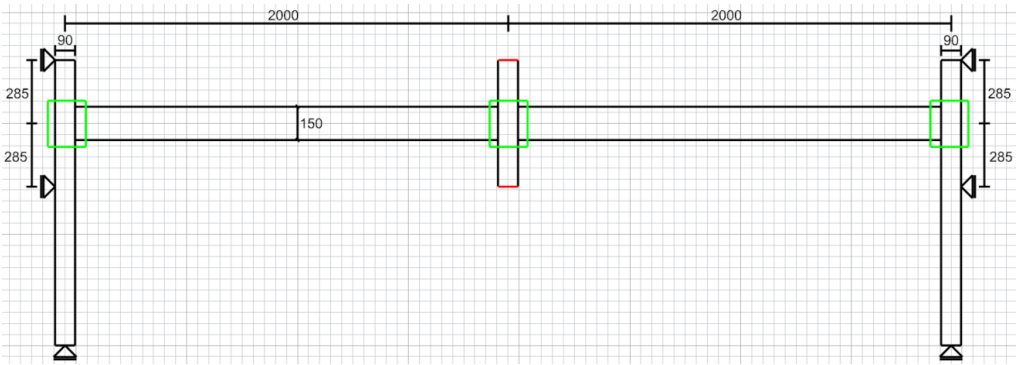

Figure 3.4: Simplified representation of the FE model.

As illustrated in Figure 3.4, the load cells at the side columns are replaced by boundary supports in the FE model. The specific implementation of these supports and the corresponding boundary conditions are described in Section 4.2. The figure also highlights the key geometric dimensions adopted in the model. The total length of the system is 4 m, consisting of two spans of 2 m each. The columns have cross-sectional dimensions of 90×90 mm, while the beam cross section measures 150×63 mm.

The location of the applied load, representing the force previously carried by the removed middle column, is indicated by red lines. The positions of the beam column connections are marked by green boxes. With this configuration, the FE model is capable of capturing the vertical displacement response, applying the prescribed loading, and extracting reaction forces at the supports. In addition, bending moments at the connections can be obtained by multiplying the relevant support reactions by their respective lever arms. A more detailed description of the FE model and its implementation is provided in Chapter 8.

4
Design methods

This chapter introduces two design methodologies aimed at analyzing structural robustness under a notional element removal scenario. The selected approaches are: (i) an analytical push down method and (ii) a finite element method (FEM)-based approach involving both push-down and drop-down simulations of the actual structure. The fundamental principles of these methods are outlined in this chapter, while detailed implementation are shown in chapter 8.

4.1. Analytical push down method

In this section, the analytical push down method is presented in detail, supported by an illustrative example. In chapter 8 additional refinements to this method will de introduced to ensure accurate representation of the validation case.

The section begins with the explanation on the static push down analysis, followed by an explanation of how the dynamic response is derived from the static push down curve. Prior to this, the fundamental assumptions underlying the model are outlined:

- The system is modeled as a single degree of freedom system (SDOF);
- No material failure mechanisms are considered for the beams or columns;
- No failure mechanisms are considered for the connections;
- The connection behavior is represented by a bi-linear model, as illustrated in Figure 4.1;
- Plasticity is assumed to occur exclusively in the central connection.

Figure 4.1 illustrates two idealized moment rotation relationships for the beam column connection: one configuration without an initial gap and one with an initial gap between the beam and the column. In the configuration without a gap, contact between the beam and column occurs immediately upon rotation, resulting in a higher initial rotational stiffness. In contrast, the presence of a gap delays this contact, which leads to a reduced initial rotational stiffness of the connection. This effect is reflected in the moment rotation response and is further illustrated in Figure 4.2.

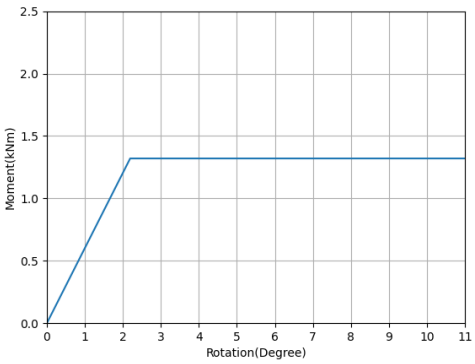

(a) Moment rotation relationship without a gap.

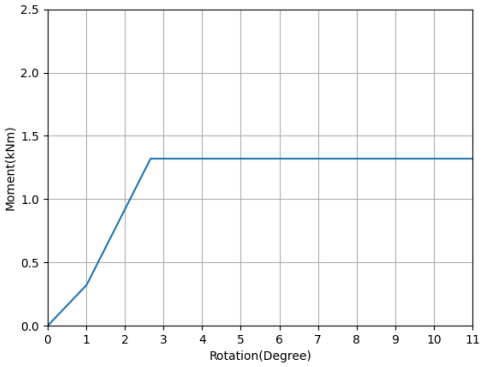

(b) Moment rotation relationship with a gap.

Figure 4.1: Idealized moment rotation behavior of connections with and without an initial gap between the beam and column.

The physical interpretation of the gap closure mechanism is shown in Figure 4.2. In the undeformed configuration, shown on the left, the beam does not make contact with the column due to the presence of the initial gap. As deformation increases, the beam rotates until contact with the column is established,

at which point the gap is considered closed. Beyond this point, the rotational stiffness of the connection increases due to direct contact between the beam and column. For a model without an initial gap, this contact condition is present from the start of loading, and the beam and column remain in contact throughout the entire deformation process.

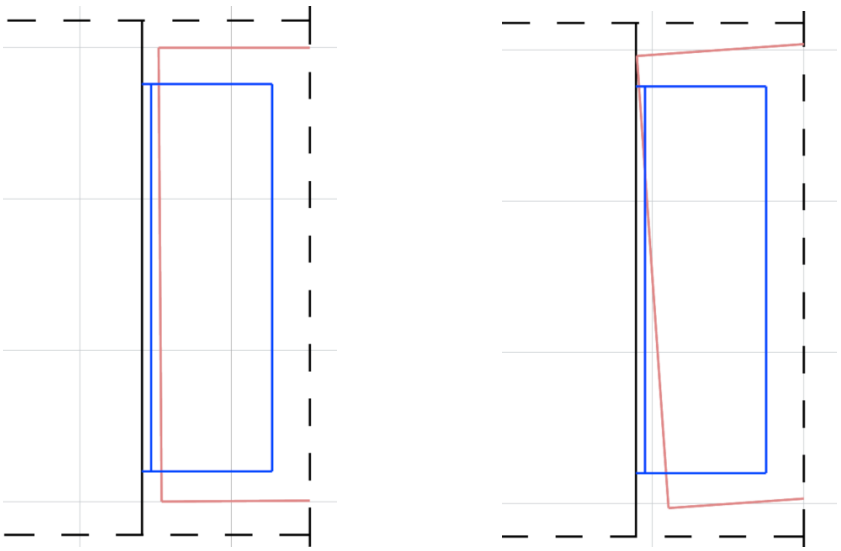

(a) Undeformed connection with an initial gap.

(b) Deformed connection after gap closure.

Figure 4.2: Illustration of gap closure in the beam column connection.

4.1.1. Analytical Push down Analysis

As shown in subsection 3.4.1 it shown how this model is simplified to a beam system this beam system can be analyzed with the analytical model shown in this chapter. to show how this analysis actually works it is here started with a model without rotational springs to make everything more clear and the math used more concise to show. the model that is used is shown in figure 4.3:

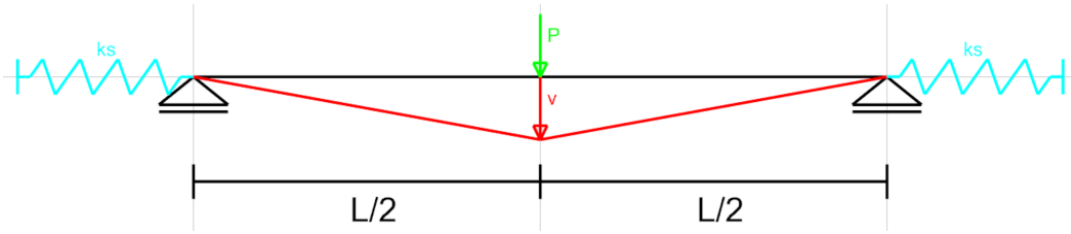

Figure 4.3: Example beam setup.

The analysis of this structure is divided into stages: elastic, plastic bending or compressive arching, transient, and catenary as shown in figure 4.4.

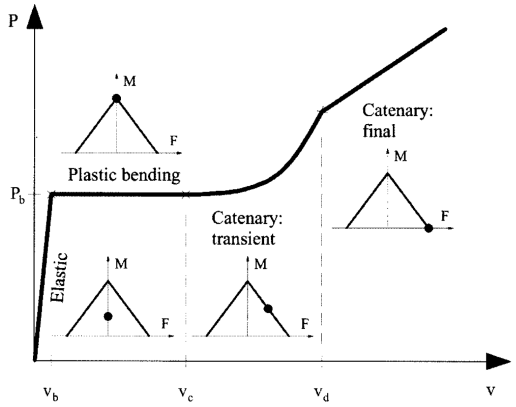

(a) Push down curve with plastic bending (B. A. Izzuddin, 2005).

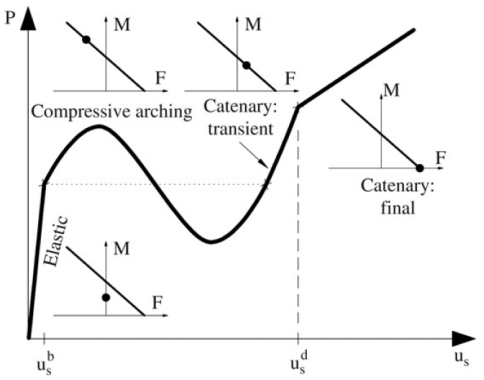

(b) Push down curve with compressive arching (B. Izzuddin et al., 2008).

Figure 4.4: Push down analysis divided into stages.

Figure 4.4 illustrates how the push down analysis is divided into distinct stages, each corresponding to specific displacement points. These displacement points are denoted by v or u in the figure; throughout this thesis, the notation v will be used.

The analysis starts with the **elastic stage**, in which the central connection remains below its plastic bending capacity and the structural response is governed by elastic deformation. Once the yield point of the middle connection is reached, the connection begins to yield and the response transitions into either **plastic bending** or **compressive arching**. The underlying mechanism of compressive arching is described in Section 2.4. In this simplified model, compressive arching is assumed to occur when the gap between the beam and column is closed; otherwise, plastic bending governs the behavior.

Following this, the structure enters the **catenary transient stage**, which begins when the displacement exceeds r_p. In this stage, the moment decreases while the axial force increases, as shown in Figure 4.4, where the moment to axial force line declines with a slope of r_p. This continues until the moment reaches zero and the axial force equals the plastic force limit F_p of the connection.

At this point, the **final catenary stage** begins. In this stage, the axial force remains constant at F_p, the moment at mid span remains zero, and the applied load P can increase due to additional deflection v. This stage has no defined limit; most structures fail before reaching it.

Elastic stage

This section formulates the first stage of the response the elastic stage and determines the transition point to the plastic bending stage. The following assumptions are adopted:

- Deflections and corresponding rotations are sufficiently small to justify the use of small angle approximations;
- The influence of bending on axial stretching is neglected;

Under these assumptions, the elastic behavior is described using Euler-Bernoulli beam theory. The governing differential equation, assuming constant elastic modulus E and second moment of inertia I along the beam length, is expressed as:

$$EI\frac{d^4v}{dx^4} = q \tag{4.1}$$

where:

- x is the coordinate along the beam;
- E is the elastic modulus of the material of the beam;
- I is the second moment of inertia of the beam;

- v is the deflection;
- q is the distributed load.

For the present case, $q = 0$, leading to the following expressions upon successive integration:
Shear force:

$$V(x) = -EI\frac{d^3v}{dx^3} = C_1 \tag{4.2}$$

Bending moment:

$$M(x) = -EI\frac{d^2v}{dx^2} = C_1x + C_2 \tag{4.3}$$

Curvature:

$$\kappa(x) = -\frac{d^2v}{dx^2} = \frac{C_1x + C_2}{EI} \tag{4.4}$$

Rotation:

$$\theta(x) = -\frac{dv}{dx} = \frac{C_1x^2}{2EI} + \frac{C_2x}{EI} + C_3 \tag{4.5}$$

Deflection:

$$v(x) = -\frac{C_1x^3}{6EI} - \frac{C_2x^2}{2EI} - C_3x + C_4 \tag{4.6}$$

The integration constants are determined using the boundary conditions. For the example case, the beam is divided into two segments due to the central point load, as illustrated in Figure 4.5. The left segment is denoted as Beam 1 and the right segment as Beam 2.

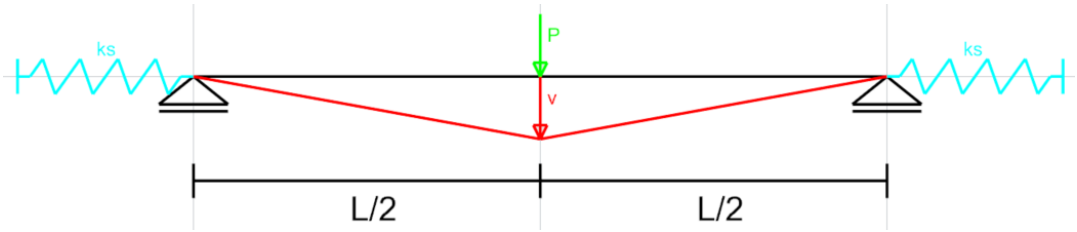

Figure 4.5: SDOF example with point force.

The boundary conditions are as follows:

- $v_1(x = 0) = 0$ (No vertical displacement at the left support)
- $M_1(x = 0) = 0$ (No bending moment at the left support)
- $v_1\left(x = \frac{L}{2}\right) = v_2\left(x = \frac{L}{2}\right)$ (Continuity of displacement at mid span)
- $M_1\left(x = \frac{L}{2}\right) = M_2\left(x = \frac{L}{2}\right)$ (Continuity of moment at mid span)
- $V_1\left(x = \frac{L}{2}\right) = V_2\left(x = \frac{L}{2}\right) + P$ (Shear force jump equals applied load)
- $\theta_1\left(x = \frac{L}{2}\right) = \theta_2\left(x = \frac{L}{2}\right)$ (Continuity of rotation at mid span)
- $v_2(x = L) = 0$ (No vertical displacement at the right support)
- $M_2(x = L) = 0$ (No bending moment at the right support)

Solving these conditions yields the mid span deflection, which can be expressed as a force–deflection relationship:

$$P = \frac{48EIv}{L^3} \tag{4.7}$$

With the initial portion of the force–deflection curve established, it is necessary to define the transition point at which the response shifts from elastic behavior to plastic bending or compressive arching. This transition occurs when the plastic moment capacity, M_p, is reached at mid span. Substituting this condition into Equation 4.3 yields:

$$M_p = M_1\left(x = \frac{L}{2}\right) = \frac{P_bL}{4} \tag{4.8}$$

Solving for P_b and substituting into Equation 4.7 provides the deflection at the onset of plasticity:

$$v_b = \frac{L^2 M_p}{12EI} \tag{4.9}$$

At this point, the analysis proceeds to the next stage of the response.

Plastic bending stage, compressive arching stage or catenary transient stage

Once the deflection v_b is reached, the system transitions into either the plastic bending stage or the compressive arching stage, depending on the presence of a gap between the beam and the column. Initially, plastic bending occurs until the beam makes contact with the column, at which point compressive arching may begin. If the deflection exceeds r_p, the system enters the catenary transient stage. Therefore, the presence or absence of a gap significantly influences the structural behavior during both the compressive arching and plastic bending stages, as well as the transient stage.

The plastic bending stage occurs between v_b and $\min(r_p, v_{\text{gap}})$, where v_{gap} is the deflection required to close the gap. During this stage, the applied force remains constant while the displacement increases. This stage leads into either compressive arching or the catenary transient stage.

For both the compressive arching and catenary transient stages, a unified force–deflection relationship can be formulated. This is possible because the axial force becomes negative, allowing a single expression to describe the behavior. The derivation of these formulas is presented in the following sections. It should be noted that the formulation for compressive arching is highly simplified, relying solely on the stiffness of the axial springs at the supports. It does not account for the beam height or other connection properties that influence this behavior. This simplification is adopted because more accurate compressive arching models are time consuming to implement and are not yet developed for timber connections or setups.

This compressive arching stage can always be omitted in favor of a plastic bending stage if there is uncertainty about its occurrence. In this thesis, it is included to illustrate that even with such a simplification, the behavior might still be represented. Although more advanced models for compressive arching exist, they are not simple enough to be used in this type of analysis (B. Izzuddin et al., 2008).

At this stage, it is assumed that the beam starts to experience axial stretching, which can be approximated as:

$$\Delta = 2u = 2\frac{v^2}{L} \tag{4.10}$$

Here, Δ denotes the total axial shortening of the beam, while u represents the axial shortening of one half of the beam. This relationship is obtained using a second order geometric approximation of the deflected shape, as illustrated in Figure 4.6, which depicts one half of the system separated at the mid span.

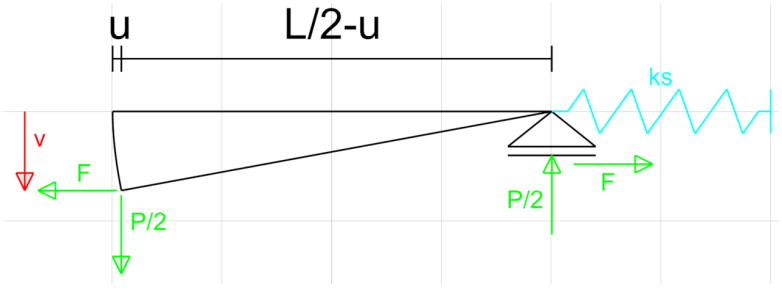

Figure 4.6: Second order approximation.

From figure 4.6, the following equation can be established:

$$\left(\frac{L}{2} - u\right)^2 + u^2 = \left(\frac{L}{4}\right)^2 \tag{4.11}$$

Assuming u^2 is negligible, the expression simplifies to:

$$u = \frac{v^2}{L} \tag{4.12}$$

The total axial deformation can be decomposed into elastic and plastic components:

$$\Delta = \Delta_e + \Delta_p \quad \Rightarrow \quad \Delta_e = \Delta - \Delta_p = 2\frac{v^2}{L} - \Delta_p \tag{4.13}$$

The corresponding axial force can be expressed as, knowing that the axial force must be zero in elastic stage:

$$F = K_e \left(2\frac{v^2}{L} - 2\frac{v_c^2}{L} - \Delta_p \right) \tag{4.14}$$

In this the $v_c = max(v_{gap}, v_b)$ so without a gap it will always be v_b if $v_c < r_p$ then this stage will be compressive arching until r_p otherwise it will a catenary transient stage if $v_c > r_p$ then $v_c = r_p$ so this will then be transient stage. because the plastic axial deformation is zero when F is zero and the rest of the formula will also be zero the Δ_p can be replaced by the increment in plastic axial deformation $\delta\Delta_p$. which gives:

$$F = K_e \left(2\frac{v^2}{L} - 2\frac{v_c^2}{L} - \delta\Delta_p \right) \tag{4.15}$$

For the example shown in Figure 4.5, the elastic stiffness K_e is given by:

$$K_e = \frac{1}{\frac{1}{K_s} + \frac{L}{EA} + \frac{1}{K_s}} \tag{4.16}$$

where K_s is the stiffness of the axial springs at the supports, and $\frac{L}{EA}$ represents the axial stiffness of the beam.

The increment in plastic deformation is related to the slope of the plastic interaction diagram (Figure 4.4) and is calculated as:

$$F_p \delta\Delta_p = M_p \delta\theta_p \quad \Rightarrow \quad \delta\Delta_p = \frac{M_p}{F_p}\delta\theta_p = r_p \delta\theta_p \tag{4.17}$$

Next, the increments of axial deformation and plastic rotation are determined. Since the elastic contribution to rotation is negligible beyond yielding, the increment in total rotation equals the increment in plastic rotation. Using the second order approximation for one half of the beam:

$$\cos(\theta_L) = \frac{\frac{L}{2} - u}{\frac{L}{2}} \quad \Rightarrow \quad 1 - \frac{\theta_L^2}{2} = \frac{1}{2} - \frac{2v^2}{L^2} \quad \Rightarrow \quad \theta_L = \frac{2v}{L} \tag{4.18}$$

Thus, the total rotation and its increment are:

$$\theta = 2\theta_L = \frac{4v}{L} \quad \Rightarrow \quad \delta\theta_p = \frac{4\delta v}{L} \tag{4.19}$$

for the increment in axial deformation it just is derivation of the axial deformation shown here:

$$\delta\Delta = 4\frac{v\delta v}{L} \tag{4.20}$$

Substituting these expressions into the axial force equation yields:

$$F = K_e \frac{2(v - v_c)(v + v_c - 2r_p)}{L} \tag{4.21}$$

The corresponding force–deflection relationship is derived by applying the equilibrium condition illustrated in Figure 4.6:

$$M = \frac{PL}{4} - Fv \tag{4.22}$$

The bending moment in this stage can also be expressed as:

$$M = M_p - r_p F \tag{4.23}$$

Substituting these relationships and Equation 4.21 yields:

$$P = \frac{4}{L}\left[M_p + K_e \frac{2(v - v_c)(v + v_c - 2r_p)(v - r_p)}{L} \right] \tag{4.24}$$

Final catenary stage

The onset of the final catenary stage occurs when the axial force reaches the plastic axial capacity F_p. Substituting $v = v_d$ and $F = F_p$ into Equation 4.21 gives:

$$v_d = r_p + \sqrt{(r_p - v_b)^2 + \frac{F_p L}{2K_e}} \tag{4.25}$$

Beyond this point, the plastic hinge at mid span no longer resists any moment ($M_p = 0$). Substituting this condition into Equation 4.22 results in a linear relationship:

$$P = 4\frac{F_p v}{L} \tag{4.26}$$

With these formulations, the complete force–deflection curve for the catenary stage is established. This curve forms the basis for subsequent dynamic response analysis, as discussed in the next section.

4.1.2. Dynamic response

The dynamic response analysis requires the previously derived push down curve as input. At this stage, it is important to clarify the objectives of the analysis, which may include:

- Determining the displacement corresponding to a given applied force;
- Calculating the dynamic amplification factor for a specified force or deflection;
- Constructing the complete amplification factor–deflection curve;
- Generating the full force–deflection curve under dynamic conditions.

In this study, the primary focus is on developing the dynamic force–deflection curve, as it provides the most comprehensive insight and facilitates comparison with existing research. The underlying principle adopted here is summarized by B. Izzuddin et al., 2008: *Sudden column loss is similar in effect to the sudden application of gravity load on the affected sub structure, particularly when significant deformations are sustained as a result.* This implies that the column removal scenario can be approximated by a sudden application of gravity loading exceeding the static resistance of the structure. Conceptually, the process can be described as follows: when gravity loading is applied, the static resistance is initially overcome, resulting in an energy imbalance where the external work exceeds the internal energy absorption. This excess energy manifests as kinetic energy, leading to an increase in structural velocities and deflections. As the deflection grows, the structural resistance eventually surpasses the applied load, causing the kinetic energy to dissipate and velocities to decrease. The maximum dynamic displacement occurs when the kinetic energy returns to zero. This energy balance concept is illustrated in Figure 4.7.

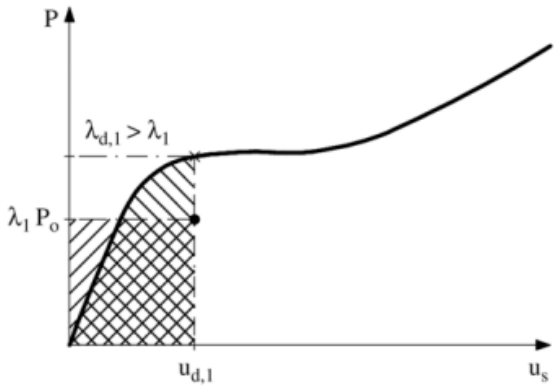

Figure 4.7: Dynamic response (B. Izzuddin et al., 2008).

In Figure 4.7, the push down response is represented by the curve. For a given displacement, the internal work corresponds to the area under this curve. this should be equal to the square from the dynamic force and the same displacement. Using this principle, either the amplification factor or the

dynamic force corresponding to a specific displacement can be determined. The energy balance can be formulated as:

$$W_n = \alpha\lambda_n P_0 u_{d,n}; \quad U_n = \int_0^{u_{d,n}} \alpha P \, du_s; \quad W_n = U_n \;\Rightarrow\; P_n = \frac{1}{u_{d,n}} \int_0^{u_{d,n}} P \, dU_s \tag{4.27}$$

By applying this method iteratively for multiple points and connecting the results, the complete dynamic force–deflection curve of the structure can be constructed.

4.2. Finite element static push down method

For this approach, a finite element (FE) model is developed using specialized software capable of performing time history analyses. In this thesis, LS-DYNA is employed for this purpose. The choice of LS-DYNA is motivated by its explicit time integration scheme, which allows the structural response to be simulated over a prescribed time interval. This capability is essential for the drop down analysis, in which the sudden loss of a structural element is represented by the dynamic release of the system.

LS-DYNA also offers considerable flexibility in defining material models, enabling the development of dedicated constitutive models for timber and aluminum, including the representation of relevant failure mechanisms. The primary structural components in this study are modeled using shell elements. This choice is made to enhance numerical stability and computational efficiency, while also facilitating the implementation of material models, particularly for timber. Since the experimental setup constrains out of plane deformations, the structural response is predominantly governed by in plane forces, making shell elements a suitable and efficient modeling choice.

The individual shell components are connected using discrete connection elements. These elements are discussed in general terms in Chapter 6, while the complete implementation of the connection model within the FE framework is described in detail in Section 8.1.

To utilize shell elements in LS-DYNA, each element requires the following input parameters:

- Part ID;
- Section card;
- Material card;

The Part ID serves as a unique identifier to distinguish components with different material properties, orientations, or sectional characteristics. The corresponding section card defines the shell thickness and specifies the number of integration points through the thickness of the shell elements. These integration points determine the number of locations at which stresses can be evaluated across the shell thickness. Since bending behavior is expected in this analysis, a minimum of two integration points is required. The optimal number of integration points depends on factors such as element thickness and material type; in practice, a higher number is often adopted to improve accuracy under combined bending and other loading conditions.

In addition, the section card defines the shell element formulation employed in the analysis. LS-DYNA provides several shell formulations, each based on different theoretical assumptions. A detailed discussion of these formulations is beyond the scope of this thesis. For the present study, shell formulation ELFORM 16 is selected, as it is well suited for this type of analysis and offers a favorable balance between numerical stability, computational efficiency, and accuracy. Further information regarding shell element formulations and the selection of integration points is available in the LS-DYNA user manual. Additionally, the section card includes the shear correction factor, which scales the transverse shear stress. This adjustment is necessary because LS-DYNA's shell formulations are based on first order shear deformation theory, which results in constant transverse shear strains and violates the zero traction condition on the shell's top and bottom surfaces. The shear correction factor compensates for this limitation and is set to $5/6$, as recommended by the LS-DYNA manual.

The individual elements are subsequently connected using the appropriate connection elements to ensure that the interactions exhibit the correct mechanical behavior. A detailed explanation of these

connection elements is provided in Chapter 6.

Once all elements are properly connected, the loading conditions can be applied. Since gravitational effects must also be considered, the gravity load is computed and distributed across the nodes of the corresponding elements. The gravitational load for an element is determined using:

$$F = \rho V \tag{4.28}$$

where F represents the total gravitational force acting on the element, ρ is the material density, and V is the element volume. This total load is then evenly distributed among the element's nodes, as illustrated in Figure 4.8 for a four node shell element.

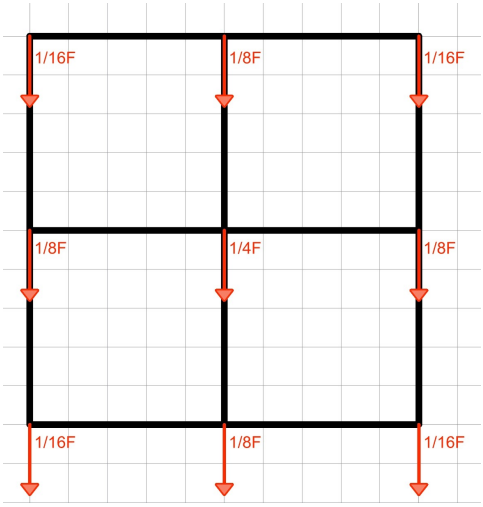

Figure 4.8: Gravity loading example.

As shown in the figure, the gravitational force is not distributed uniformly across all nodes. This occurs because corner nodes are associated with a smaller effective volume compared to other nodes. However, when all nodal forces are summed, the total equals the full gravitational load of the element. To avoid sudden dynamic effects, the gravity load is gradually ramped up, as illustrated in Figure 4.9.

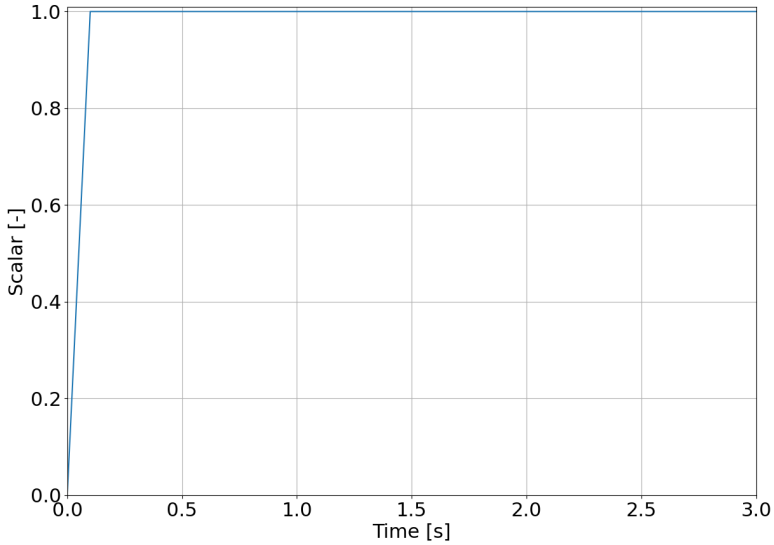

Figure 4.9: Gravity loading graph.

The ramping process increases the gravity factor from zero to one because the gravitational acceler-

ation is defined separately as $9.81[m/s^2]$. This gradual application prevents impulse forces that could lead to numerical instabilities.

Once the gravity loading is applied, the external forcing can be introduced. Since the objective is to capture the full nonlinear response, a displacement controlled loading approach is used. In this method, the prescribed displacement is incrementally applied over time. To minimize impulse effects at the start of loading, the displacement is defined through a velocity curve, as shown in Figure 4.10.

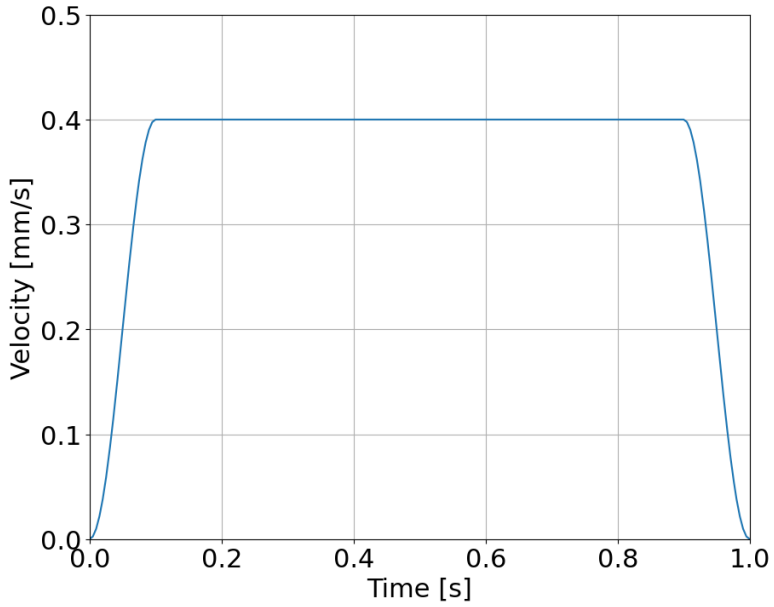

Figure 4.10: Velocity curve example.

The velocity curve shown in Figure 4.10 is defined by four key parameters: the start time, end time, rise time, and maximum velocity v_{max}. Typically, the start time, end time, and rise time are user defined inputs, while the software automatically generates the corresponding velocity curve. The total displacement is also specified as an input, which determines the max velocity the curve rises to. And the area under this curve will be equal to this set displacement.

In some simulations, nodal loading is also required due to test setup. this is done in the same way as the gravitation loading.

The force required to achieve the prescribed velocity at each time step can be extracted from the simulation output. In certain cases, reaction forces at supports are also recorded, providing a more stable representation of the total applied force. However, for the moment–rotation test this is impossible so only the forcing for the velocity can be acquired.

Displacement histories are recorded at selected nodes to track the structural response. These data are post processed using Python, which offers flexibility for generating plots, calculating stiffness values, and applying the energy based dynamic response method described in Section 4.1.2. This enables the derivation of dynamic force–displacement curves from the FE generated push down results.

4.3. Finite element drop down method

For the drop down method, a model similar to the push down approach can be utilized, with the primary difference being that the section previously subjected to displacement in the push down model is initially fully supported. This section is again subjected to gravitational loading, identical to the previous case. Additionally, a release load is introduced, as explained in section 3.1 This load is distributed among the top or bottom nodes of the section, depending on the actual location of the applied force. The total

release force is divided equally among these nodes, and, as with the gravity load, it is gradually ramped up to avoid sudden dynamic effects.

Once all loads have been applied and the system has reached a stable state—defined as a condition where several additional time steps are allowed for force redistribution—the actual drop can be initiated. At this point, the previously supported section is released, allowing it to fall under the influence of the applied loads.

This release is simulated by reducing the stiffness of the removed section to a value close to zero (as an exact zero is numerically impossible) over a defined time interval. The duration of this stiffness reduction remains a topic of debate in the literature, primarily because the nature of the triggering event can significantly influence the appropriate time frame.

Consequently, most studies adopt a removal time for instantaneously removal equal to either one tenth of the natural period of the structure or approximately 10 ms (Kiakojouri & Sheidaii, 2018). This removal time will be set in chapter 8.

After the simulation has been completed, the reaction forces and deflections can be extracted. Additionally, the available data allows for the generation of moment–rotation graphs for the connections, as well as axial force–deflection curves. These visualizations provide further insight into the structural response under the applied loading conditions.

Both FE models incorporate frequency based damping to limit excessive dynamic response during the analyses. Since the FE software operates in a fully dynamic framework, damping must be applied in both models to control large response peaks. This damping primarily serves to mitigate impulse forces and other sudden loading events that could otherwise lead to numerical instability or unrealistic structural response. In addition, damping helps to dissipate transient vibrations, preventing prolonged oscillations following impulsive loading.

For the shell elements, frequency based damping is combined with stiffness proportional damping to further suppress high frequency response components. The damping ratio is set to 5%, in accordance with recommendations provided in the LS-DYNA user manual. Frequency based damping is applied only outside the frequency range of 1 to 30 Hz, ensuring that the dominant structural response within this range remains largely unaffected. Further details on the implemented damping formulations and parameter selection can be found in the LS-DYNA documentation.

5
Structural materials

This chapter provides an overview of the structural materials utilized in this thesis. It begins with a brief introduction, followed by a detailed discussion of timber, including the specific type employed and its differences compared to clear solid timber. Subsequently, these material characteristics are translated into material models suitable for the FE methods. The methodology for implementing these models is also described.

5.1. Timber

This section introduces timber as a construction material and discusses the reasons for its widespread use in structural applications. Subsequently, laminated veneer lumber (LVL), the specific timber product employed in this thesis, is presented, highlighting its distinctive properties compared to clear solid timber. These characteristics are then translated into a material model suitable for finite element (FE) analysis. Finally, the accuracy of the developed model is evaluated by comparing its predictions with experimental test results, demonstrating that the model provides an adequate representation of the material behavior.

5.1.1. Introduction to timber

Timber is one of the oldest construction materials, yet it is increasingly regarded as a cutting-edge solution in modern engineering. This renewed interest is driven by several key factors (Arriaga et al., 2023):

- Timber is a renewable and sustainable material when sourced responsibly;
- Timber exhibits an excellent strength-to-weight ratio;
- Timber can also be produced more effectively.

To illustrate its sustainability, consider the following scenario: ”In the Limnologen building in Växjö, Sweden: a structure with seven timber floors on a concrete base each 125 m^2 apartment requires approximately 28 m^3 of wood. Assuming a spruce forest yields about 4 m^3/ha/year under current European silvicultural practices, each apartment corresponds to roughly 7 ha of forest. Over a 50 year service life and a 50 year forest rotation period, the area required to sustain this dwelling is only 0.14 ha. If the entire European population (750 million people, averaging three inhabitants per apartment) lived in similar housing, about 35×10^6 ha of forest would be needed—approximately 20% of Europe’s forest area” (Arriaga et al., 2023).

Timber also offers a superior strength to weight ratio compared to steel and concrete. For example, a laminated veneer lumber (LVL) C40 beam achieves a strength to weight ratio of 29.2 under ultimate limit state (ULS) conditions, whereas a steel beam achieves 26.7. For columns and panels, this advantage becomes even more pronounced, reinforcing timber’s suitability as a structural material.

However, timber also presents certain drawbacks (Voulpiotis et al., 2022):

- Time dependent deformation due to creep and relaxation under sustained loads;
- Sensitivity to moisture content variations;
- Size effects leading to strength reduction in large elements;
- Low strength perpendicular to the grain;
- Brittle failure mechanisms in most loading scenarios.

Creep and relaxation imply that a beam under constant load will experience gradual deformation over time, which, although small, must be considered in design due to the long service life of buildings (50–

100 years). Prolonged loading can also reduce stiffness, increasing the risk of failure. Design codes account for these effects through modification factors (Arriaga et al., 2023).

Moisture content (MC) is another critical factor: exceeding the limits specified by manufacturers or codes reduces both stiffness and strength. High humidity environments also increase the risk of fungal attack, which can rapidly degrade timber properties (Voulpiotis et al., 2021).

Size effects are more pronounced in timber than in many other materials, leading to significant strength reductions in large structural elements. Additionally, timber exhibits low strength when loaded perpendicular to the grain, particularly in tension, due to its brittle failure behavior. This brittleness is undesirable in structures requiring load redistribution for robustness. Careful design of connections—favoring ductility and compression based load transfer—can mitigate these issues (Voulpiotis et al., 2021).

5.1.2. Laminated vaneer lumber (LVL)

Timber naturally contains defects such as knots, which can significantly influence its mechanical performance. One of the most effective methods to minimize the impact of these defects and distribute them uniformly within a structural element is through the use of Laminated Veneer Lumber (LVL). Compared to glued laminated timber (glulam), LVL offers several advantages: it can be produced with higher material yield, a wider range of dimensions and shapes, and with reduced time and labor requirements than solid timber (Sasaki & Abdullahi, 2016).

LVL is manufactured from thin wood veneers that serve as laminas. Veneers are sheets of wood obtained by slicing or peeling logs. These veneers are bonded together using structural adhesives under heat and pressure, with all veneers oriented in the same grain direction. This process results in a highly uniform and dimensionally stable product, typically used for beams, columns, and other load bearing elements. Additionally, veneers can be treated with preservatives, fire retardants, or other chemical agents prior to drying, enhancing durability and fire resistance (Sasaki & Abdullahi, 2016).

Due to this manufacturing process, LVL generally exhibits higher stiffness, greater strength, and more consistent mechanical behavior across the entire element compared to solid timber or glulam. This makes LVL a preferred choice for structural applications where reliability and performance are critical.

LVL is commonly produced in two configurations: LVL-S and LVL-C. In LVL-S, all veneers are oriented in the same direction, providing high strength along the primary axis. In contrast, LVL-C incorporates cross-laminated layers, where some veneers are oriented perpendicular to the main grain direction to enhance dimensional stability. For the purposes of this thesis, only LVL-S is considered relevant.

5.1.3. Material modeling of timber for finite element analysis

To develop a material model that accurately represents LVL-S, a comprehensive review of experimental data is conducted. Prior to initiating the modeling process, several fundamental characteristics of LVL-S must be established. LVL-S exhibits orthotropic behavior, with distinct mechanical properties along three principal material directions:

- x: grain direction;
- y: edgewise direction (perpendicular to grain);
- z: flatwise direction (perpendicular to grain).

These direction are also shown in figure 5.1.

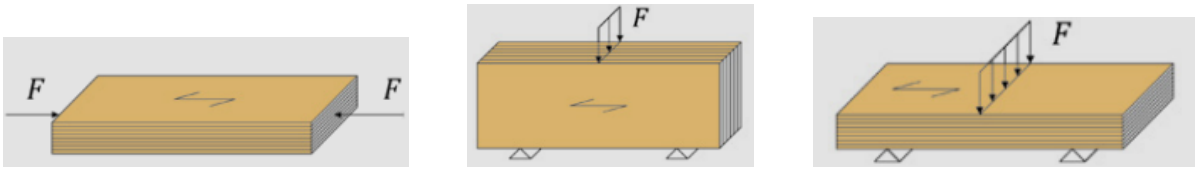

(a) Grain direction. **(b)** Edgewise direction. **(c)** Flatwise direction.

Figure 5.1: Loading direction (STEICO SE, 2026).

The elastic moduli, strength parameters, and plasticity behavior differ significantly across these directions. Therefore, the material model must be capable of capturing anisotropic plasticity. Due to the limited availability of complete datasets for LVL-S, mechanical properties are compiled from multiple sources. In cases where the density of the tested LVL-S differs from the reference material used for validation, values are scaled accordingly. The scaling is based on the known correlation between timber density and mechanical properties such as stiffness and strength.

For compression, the shape of the stress strain curves in each principal direction is analyzed and incorporated into the model. In tension, plasticity is not considered; instead, elements are removed from the simulation upon reaching the ultimate tensile strength.

The following parameters are required for the material model, along with their sources and any applied scaling:

- **Mass density:** $\rho = 595\ \mathrm{kg/m^3}$, obtained as the mean value from validation tests (Cheng et al., 2021; Lyu et al., 2020; Masaeli et al., 2020).
- **Elastic moduli:** $E_x = 15300\ \mathrm{MPa}$, $E_y = 807.5\ \mathrm{MPa}$, $E_z = 425\ \mathrm{MPa}$, derived as the mean values of the mean values of the different test in (Janowiak et al., 2001).
- **Poisson's ratios:** $\nu_{xy} = 0.44$, $\nu_{yz} = 0.34$, $\nu_{zx} = 0.37$, taken from LVL beam tests (Zhang et al., 2024). Although based on a different timber species, ν_{xy} aligns closely with Douglas fir value from (Forest product laboratory staff, 2021).
- **Shear moduli:** G_{xy}, G_{yz}, G_{zx}:
  - $G_{xy} = 989.26\ \mathrm{MPa}$: mean value of the edgewise in plane shear from (Duriot et al., 2023);
  - $G_{yz} = 50,75\ \mathrm{MPa}$: derived as the mean values of the mean values of the different test in (Janowiak et al., 2001);
  - $G_{zx} = 860.56\ \mathrm{MPa}$: mean value of the flatwise in plane shear from (Duriot et al., 2023);
- **Ultimate tensile strengths:** X_T, Y_T, Z_T
  - $X_T = 39\ \mathrm{MPa}$: characteristic value from Hyspan beam design sheet (Futurebuild), scaled by a factor of 1.3 to obtain mean value.
  - $Y_T = 4.27\ \mathrm{MPa}$, $Z_T = 2.93\ \mathrm{MPa}$: obtained from LVL larch beam tests (Shu et al., 2025), scaled by the ratio of the tested LVL larch density to ρ.
- **Ultimate compressive strengths:** X_C, Y_C, Z_C
  - $X_C = 51,15\ \mathrm{MPa}$, $Y_C = 7.85\ \mathrm{MPa}$: mean values from (Duriot et al., 2023), scaled by density.
  - $Z_C = 3.33\ \mathrm{MPa}$: characteristic value from Kerto LVL (Metsa), scaled by 1.3 to obtain mean value.
- **In plane shear strengths:** $f_{xy} = 5.98\ \mathrm{MPa}$, $f_{xz} = 4.55\ \mathrm{MPa}$
  - Both values from Hyspan beam design sheet (Futurebuild), scaled by 1.3 to obtain mean values.
- **Yield strengths in compression:** S_{xx}, S_{yy}, S_{zz}
  - $S_{xx} = 39.29\ \mathrm{MPa}$: determined from (Shu et al., 2025) as the point of deviation from linear elastic behavior, scaled by density ratio.
  - S_{yy}, S_{zz}: set equal to the design compressive strengths, consistent with observed onset of yielding (Shu et al., 2025).
- **Yield strengths in shear:** $S_{xy} = 4.6\ \mathrm{MPa}$, $S_{xz} = 3.5\ \mathrm{MPa}$ set to design values from Hyspan beam design sheet (Futurebuild).

The frequent use of density based scaling reflects the well established relationship between timber density and its mechanical properties. The scaling factor of 1.3 is applied to convert characteristic values to mean values, accounting for variability inherent in timber and the derivation of design values in structural codes. Where possible, Douglas fir is used as the reference species; otherwise, the closest

species in terms of density is selected. Some values are sourced directly from design specifications of the actual beam used (Hyspan, Futurebuild) or from similar beams provided by alternative suppliers.

The elastic response is defined using Hooke's law for orthotropic materials:

$$\boldsymbol{\sigma} = \mathbf{C}\,\boldsymbol{\varepsilon}, \tag{5.1}$$

where $\boldsymbol{\sigma}$ and ε are the stress and strain vectors in Voigt notation, and $\mathbf{C}$ is the constitutive stiffness matrix derived from the orthotropic elastic constants. The stress vector in Eq. (5.1) is expressed as:

$$\boldsymbol{\sigma} = \begin{bmatrix} \sigma_{xx} \\ \sigma_{yy} \\ \sigma_{zz} \\ \sigma_{xy} \\ \sigma_{yz} \\ \sigma_{zx} \end{bmatrix}, \tag{5.2}$$

and the corresponding strain vector is:

$$\boldsymbol{\varepsilon} = \begin{bmatrix} \varepsilon_{xx} \\ \varepsilon_{yy} \\ \varepsilon_{zz} \\ \gamma_{xy} \\ \gamma_{yz} \\ \gamma_{zx} \end{bmatrix}, \tag{5.3}$$

where γ_{ij} denotes the engineering shear strains. The relationship between stress and strain is governed by the constitutive stiffness matrix $\mathbf{C}$, which is the inverse of the compliance matrix $\mathbf{S}$. For an orthotropic material, the compliance matrix is given by:

$$\mathbf{S} = \begin{bmatrix} \frac{1}{E_x} & -\frac{\nu_{yx}}{E_y} & -\frac{\nu_{zx}}{E_z} & 0 & 0 & 0 \\ -\frac{\nu_{xy}}{E_x} & \frac{1}{E_y} & -\frac{\nu_{zy}}{E_z} & 0 & 0 & 0 \\ -\frac{\nu_{xz}}{E_x} & -\frac{\nu_{yz}}{E_y} & \frac{1}{E_z} & 0 & 0 & 0 \\ 0 & 0 & 0 & \frac{1}{G_{xy}} & 0 & 0 \\ 0 & 0 & 0 & 0 & \frac{1}{G_{yz}} & 0 \\ 0 & 0 & 0 & 0 & 0 & \frac{1}{G_{zx}} \end{bmatrix}. \tag{5.4}$$

This formulation fully defines the elastic behavior of timber in all directions, accounting for its orthotropic nature.

To accurately capture the inelastic behavior of LVL in the grain direction (x-direction), a curve is fitted to the stress strain response beyond the yield point. This fitted curve is presented in Appendix A this curve fit is base on the along grain compression curve from (Shu et al., 2025). For the perpendicular directions (y and z), the post-yield behavior is modeled using a simplified linear extension from the yield point. This assumption is made due to the high degree of uncertainty and variability observed in experimental data regarding plasticity in these directions. The variability arises from several factors:

- **Timber species**: Different wood species exhibit distinct anatomical structures and mechanical responses, which influence plasticity behavior (Ido et al., 2010).
- **Adhesive type**: The mechanical interaction between veneers is significantly affected by the type and distribution of adhesive used during manufacturing (Sudo et al., 2025).
- **Number of lamellae**: The number and arrangement of lamellae affect the homogeneity and stress distribution within the LVL, contributing to variability in mechanical response (Forest product laboratory staff, 2021).

To capture failure under multiaxial stress states, the Tsai–Hill criterion Tsai, 1965 is adopted. This criterion accounts for the orthotropic nature of timber and distinguishes between tensile and compressive

strengths in each direction. The failure condition is expressed as:

$$(G+H)\sigma_{xx}^2 + (F+H)\sigma_{yy}^2 + (F+G)\sigma_{zz}^2 - 2H\sigma_{xx}\sigma_{yy} - 2F\sigma_{yy}\sigma_{zz} - 2G\sigma_{zz}\sigma_{xx} \\ +2N\sigma_{xy}^2 + 2L\sigma_{yz}^2 + 2M\sigma_{zx}^2 < 1, \tag{5.5}$$

where the coefficients F, G, H, L, M, and N are computed as:

$$G+H = X_i, \quad F+H = Y_i, \quad F+G = Z_i, \tag{5.6}$$

$$2N = \frac{1}{S_{xy}^2}, \quad 2L = \frac{1}{S_{yz}^2}, \quad 2M = \frac{1}{S_{zx}^2}, \tag{5.7}$$

$$H = \tfrac{1}{2}\left(\frac{1}{X_i} + \frac{1}{Y_i} - \frac{1}{Z_i}\right), \; F = \tfrac{1}{2}\left(-\frac{1}{X_i} + \frac{1}{Y_i} + \frac{1}{Z_i}\right), \; G = \tfrac{1}{2}\left(\frac{1}{X_i} - \frac{1}{Y_i} + \frac{1}{Z_i}\right). \tag{5.8}$$

The directional strengths X_i, Y_i, and Z_i depend on the sign of the normal stresses, distinguishing between tension and compression:

$$X_i = \begin{cases} X_T & \text{if } \sigma_{xx} > 0, \\ X_C & \text{if } \sigma_{xx} < 0, \end{cases} \quad Y_i = \begin{cases} Y_T & \text{if } \sigma_{yy} > 0, \\ Y_C & \text{if } \sigma_{yy} < 0, \end{cases} \quad Z_i = \begin{cases} Z_T & \text{if } \sigma_{zz} > 0, \\ Z_C & \text{if } \sigma_{zz} < 0. \end{cases} \tag{5.9}$$

For shell elements, this three dimensional criterion is internally reduced to a two dimensional form by the FE software, but the underlying principle remains the same. With these definitions, the FE solver can compute stresses from strains and evaluate failure according to the Tsai–Hill criterion.

5.1.4. Validation of timber material model

Due to the large number of tests considered, it can be challenging to demonstrate that the material model performs exactly as intended or aligns perfectly with experimental data. Nevertheless, the behavior in each principal direction will be presented and evaluated to determine whether it corresponds with expected trends and to clarify the simplifications that influence this behavior.

Where available, experimental stress–strain curves will also be included. However, for most cases, these tests are primarily relevant for assessing the shape of the curve rather than the absolute values, since the available data pertains to other wood species used for LVL-S. Therefore, each mechanical behavior will be addressed individually: starting with compression in the three principal directions discussed earlier, followed by tension, and concluding with the two shear behaviors.

Compression

For the compression cases, only the longitudinal direction (along the grain) is assigned a plasticity curve after yielding. As previously mentioned, yielding in the other two compression directions is simplified. These behaviors are illustrated in the figures below.

The compression behavior in the longitudinal direction is compared to test data from LVL Larch, as reported by (Shu et al., 2025). This material was selected due to its similar density and the availability of data for most of the relevant mechanical behaviors. However, it is still a different timber species, so the comparison focuses primarily on the shape of the stress–strain curve rather than the absolute values.

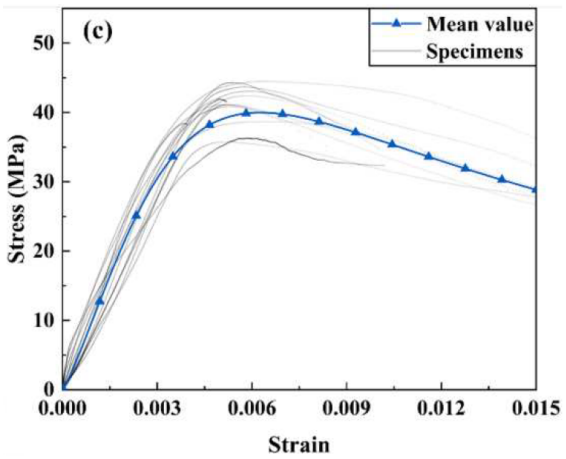

(a) Experimental curves from (Shu et al., 2025).

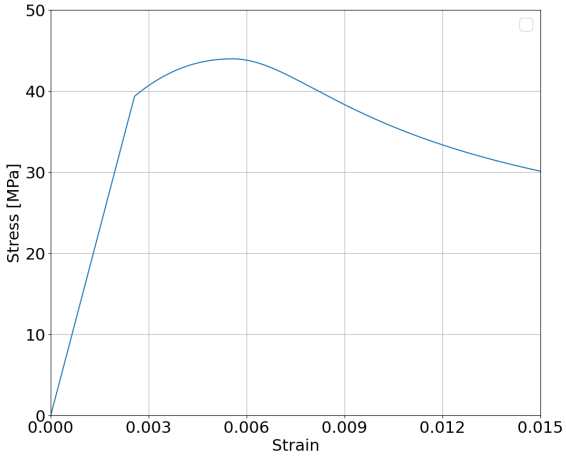

(b) LS-DYNA material model curve.

Figure 5.2: Comparison of LVL loaded in compression along the grain.

As shown in the figure, the model attempts to replicate the general shape of the experimental curve. However, the yield point in the simulation appears slightly delayed, and the transition from yielding to plasticity is smoother in the actual test data. This discrepancy is mostly due to how plasticity curve has been setup as shown in appendix A

For compression perpendicular to the grain—both flatwise and edgewise—the corresponding curves are presented below. These include both the material model predictions and the experimental curves from the LVL Larch tests.

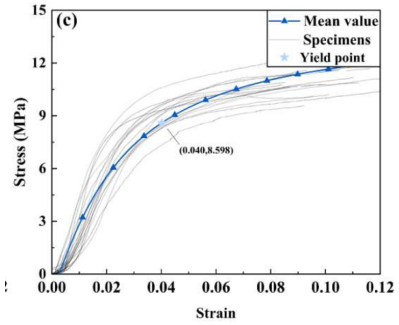

(a) Experimental curves from (Shu et al., 2025).

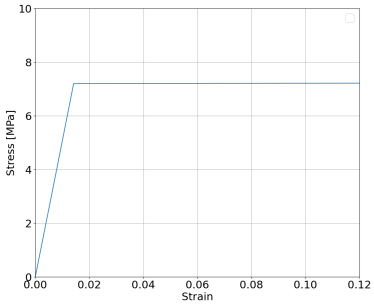

(b) LS-DYNA material model curve edgewise.

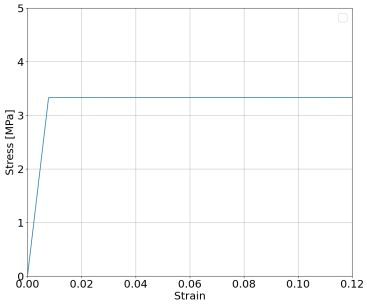

(c) LS-DYNA material model curve flatwise.

Figure 5.3: Comparison of LVL loaded in compression perpendicular to the grain.

From these curves, it can be observed that the elastic region extends further than in the experimental test, while the plastic response is represented in a highly simplified manner. This behavior is a direct consequence of the modeling assumptions discussed earlier. As a result, the initial stiffness of the numerical curve is slightly higher than that observed experimentally up to the yield point. Beyond yielding, the model exhibits reduced strength compared to the experimental response. Consequently, the adopted material model provides a conservative representation of the structural behavior, except for a limited region immediately preceding the onset of yielding. After this point, the numerical response becomes significantly more conservative than the actual behavior observed in the tests.

Tension

For tension, no experimental curves were identified that are sufficiently clear to allow a meaningful comparison with the adopted material model. This limitation is one of the reasons why tensile plasticity is not considered in the present study. Moreover, the majority of available experimental results for LVL-S do not indicate significant plastic behavior in tension, supporting this modeling assumption. Consequently, only the elastic tensile response in all three material directions is considered and presented.

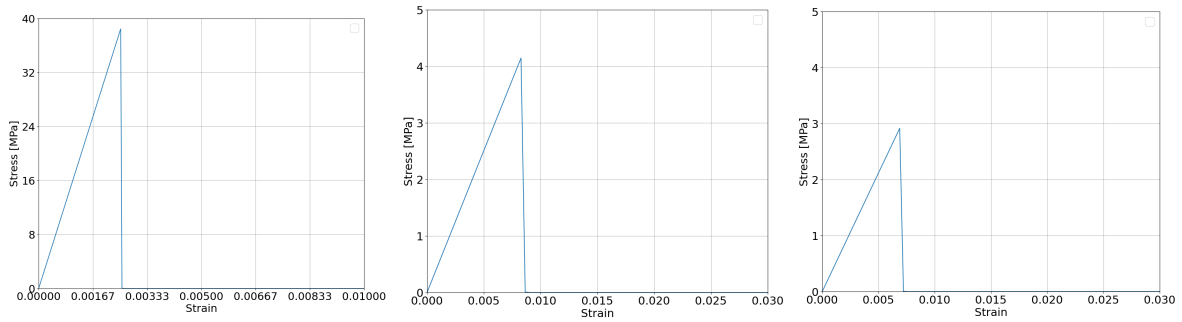

(a) Curve along the grain. **(b)** Curve perpendicular to the grain edgewise. **(c)** Curve perpendicular to the grain flatwise.

Figure 5.4: Tension behavior of LVL material model.

From these graphs, it can be observed that the tensile response follows a purely elastic behavior up to the corresponding failure stress. Once this stress level is reached, the material loses its load carrying capacity. In the numerical model, this failure is represented by a severe reduction in stiffness rather than the physical deletion of the shell elements. As a result, the affected shell elements effectively contribute no further resistance to the structural response.

Shear

For shear, no experimental stress strain curves were available that could reliably characterize the material behavior. Consequently, the shear response is also idealized using a linear relationship without plastic deformation. Although this represents a simplification of the actual material behavior, a more accurate description cannot be achieved in the absence of experimental shear data for the specific LVL-S material or for a closely related species. The resulting shear stress strain curves are therefore presented for both the flatwise and edgewise loading directions, which are both aligned with the grain direction and act in plane.

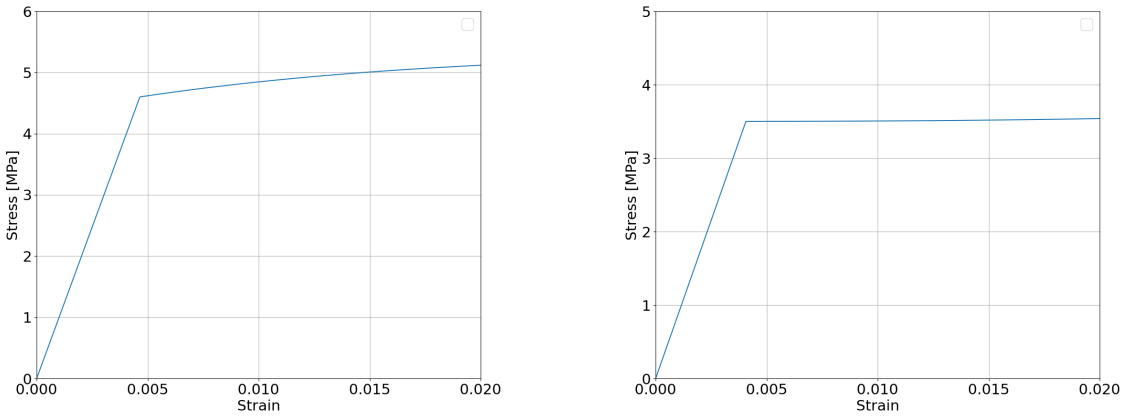

(a) LS-DYNA material model curve edgewise. **(b)** LS-DYNA material model curve flatwise.

Figure 5.5: Shear LVL-S material model.

As shown, the stress strain curves are simplified representations of the material behavior. However, the edgewise response exhibits a degree of hardening, which arises from the plastic behavior observed in compression and cannot be avoided in the present formulation. This effect remains acceptable, as the response stays below the ultimate strength of the material.

5.2. Metals

The beam column connections considered in this thesis incorporate aluminum plates and steel fasteners (bolts and dowels). Accurate modeling of these metallic components is essential for both analytical model and the FE model. This section introduces the mechanical behavior of aluminum and steel, followed by the development of material models for finite element (FE) simulations.

5.2.1. Introduction to aluminum

Aluminum is a lightweight, ductile metal characterized by isotropic elastic behavior and distinct plastic responses in tension and compression. Under elastic loading, aluminum exhibits uniform stiffness in all directions; however, once yielding occurs, its plastic behavior diverges:

- In **compression**, strain hardening typically follows a nearly linear trend, and no realistic failure strain is observed within practical limits.
- In **tension**, strain hardening diminishes progressively and may transition into softening before fracture, defining a clear ultimate strain.

These differences necessitate separate constitutive curves for tension and compression in FE modeling. Furthermore, aluminum's plasticity is sensitive to strain rate: higher loading rates generally increase ductility and delay fracture. Experimental evidence from Tucker et al., 2010 demonstrates that strain rate effects significantly influence both tensile and compressive responses. For instance, rapid loading can enhance ductility compared to quasi static conditions.

In structural applications, controlling strain rate is challenging, particularly under progressive collapse scenarios. Therefore, this thesis adopts the lowest strain rate reported in Tucker et al., 2010 ($0.001\,\mathrm{s}^{-1}$), which corresponds to conservative material properties with reduced strength and ductility. This assumption ensures that the FE model reflects a lower bound estimate of aluminum performance, consistent with safety oriented design principles.

5.2.2. Material model for FE analysis

The aluminum material model implemented in LS-DYNA must accurately capture its elastic and plastic behavior under both tension and compression. While experimental data from (Masaeli et al., 2020), (Lyu et al., 2020), and (Cheng et al., 2021) provide useful benchmarks, these tests exhibit significant variability in strain rates, as summarized below:

- 7.5×10^{-4} per min (1.25×10^{-5} s^{-1}) and 8.7×10^{-4} per min (1.45×10^{-5} s^{-1});
- 9.4×10^{-4} per min (1.57×10^{-5} s^{-1});
- 9.2×10^{-4} per min (1.50×10^{-5} s^{-1}).

Moreover, these studies do not clarify whether the reported stress values correspond to true stress or engineering stress. To ensure consistency and reliability, the material curves adopted in this thesis are derived from (Tucker et al., 2010), which provides comprehensive tension and compression data for aluminum under controlled strain rates. Among the strain rates tested in that study, the rate of 0.001 s^{-1} is selected because it closely approximates the quasi static conditions of the validation tests and represents a conservative lower bound estimate of ductility.

The LS-DYNA material model `MAT_PLASTICITY_COMPRESSION_TENSION` is employed because it allows separate definitions of plasticity for tension and compression. The following input parameters are required:

- Material density (for timestep calculation and gravity loading);
- Elastic modulus (single value, as aluminum is isotropic);
- Poisson's ratio;
- Plasticity curves in true stress–plastic strain format for both tension and compression;
- Yield stress values for tension and compression.

To simulate fracture under tension while preventing unrealistic failure in compression, an erosion card is coupled to the material model. The parameters are defined as:

- `MXPRES` = $500\,\mathrm{MPa}$ (maximum pressure in compression);
- `MNPRES` = $-100\,\mathrm{MPa}$ (minimum pressure in tension);
- `NCS` = 2 (number of criteria to satisfy before element deletion);
- `MXEPS` = 0.17 (maximum plastic strain).

These values ensure that:

- Compression failure requires an unrealistically high pressure, preventing premature deletion of elements under compressive loading;
- Tension failure is governed primarily by plastic strain, consistent with observed fracture mechanisms.

Figure 5.6 compares the experimental curves from (Tucker et al., 2010) with the LS-DYNA implementation for a strain rate of $0.001\ \mathrm{s}^{-1}$. The tension curve in the FE model exhibits slightly elevated ultimate strength to avoid premature failure, while the compression curve approximates the experimental trend despite the limitation of defining a single yield point for both loading modes.

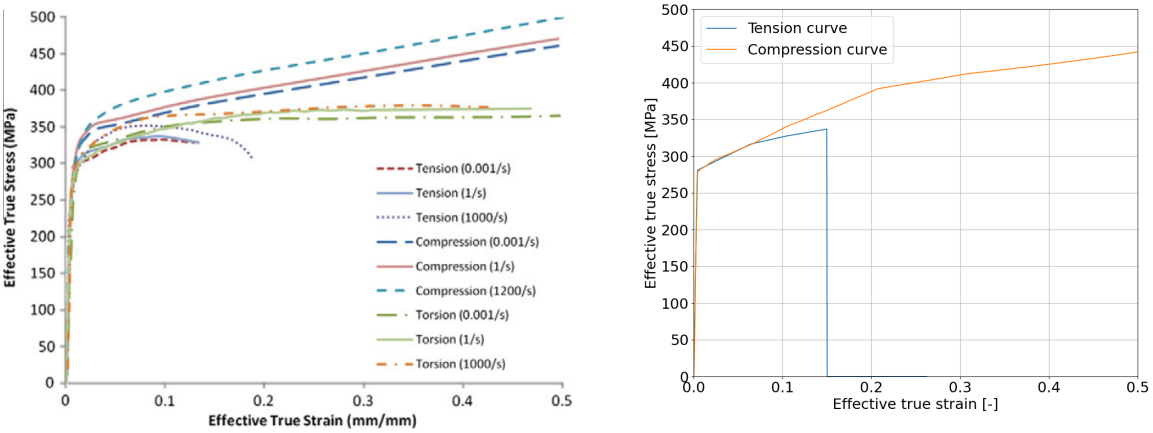

(a) Experimental curves from (Tucker et al., 2010).

(b) LS-DYNA material model curves.

Figure 5.6: Comparison of aluminum behavior under tension and compression at $0.001\ \mathrm{s}^{-1}$ strain rate.

5.2.3. Bolts and dowels of steel

Steel bolts and dowels are critical components in the beam to column connections considered in this thesis. These fasteners are typically manufactured from high carbon steel, which provides:

- High stiffness and strength;
- Elevated yield stress compared to structural steel;
- Limited ductility, as the connection's overall deformation capacity is primarily governed by other components (e.g., plates, timber embedment).

In practice, bolts rarely fail in isolation because the connection exhibits multiple interacting elements. Failure generally occurs in the aluminum plate or timber before the bolts reach their ultimate capacity.

For the analytical model, bolt properties are incorporated through their elastic stiffness and ultimate capacity. These values are obtained from Eurocode provisions (*EN 1993-1-8*) and experimental data reported in Chapter 7. The required parameters include:

- Bolt length and grip dimensions;

- Tensile stress area;
- Elastic modulus and ultimate tensile strength.

In the dynamic FE model, bolts and dowels are represented using discrete beam elements. Their nonlinear behavior is defined through force–deformation curves for:

1. **Axial tension:** Modeled using a bi-linear curve based on Eurocode tensile capacity and stiffness.
2. **Shear through timber:** Modeled using curves derived from Johansen's yield theory and validated by (J. Cao et al., 2021).

The maximum shear resistance of a dowel is calculated:

$$F_{v,Rk} = \min \begin{cases} f_{h,k}\, t_{h1}\, d & \text{(Mode 1)} \\ f_{h,k}\, t_{h1}\, d \left[\sqrt{2 + \dfrac{4M_{y,Rk}}{f_{h,k} d t_{h1}^2}} - 1 \right] & \text{(Mode 2)} \\ 2.3\sqrt{M_{y,k}\, f_{h,k}\, d} & \text{(Mode 3)} \end{cases} \tag{5.10}$$

where:

- $f_{h,k}$ = characteristic embedment strength of timber;
- t_{h1} = timber thickness;
- d = dowel diameter;
- $M_{y,Rk}$ = characteristic yield moment of the dowel.

The stiffness of the shear curve is defined using the exponential relationship proposed by (J. Cao et al., 2021):

$$F = F_{v,Rk} \left[1 - \exp\left(-\frac{\rho^{1.5} d/23}{F_{v,Rk}}\, \Delta \right) \right] \tag{5.11}$$

where:

- $F_{v,Rk}$ = maximum shear force;
- ρ = timber density;
- d = dowel diameter;
- Δ = slip displacement.

These formulations enable the generation of realistic force–displacement curves for bolts and dowels in the FE model. The resulting curves for the validation case are presented in Chapter 8.

6
Connections

This chapter establishes the modeling and verification framework for the beam to column connections used throughout this thesis. The objective of this chapter is split into two main goals:

- Define a component based representation of the connection which can be used for the analytical model;
- Show general connection elements for the FE model.

The chapter begins with general background on timber connections and their governing requirements, followed by the derivation of rotational and translational properties for the analytical model, and concludes with implementation details for the dynamic FE models.

6.1. General background on timber connections

Connections govern the global resilience of timber frames subjected to notional element removal because alternative load paths rely on large rotations, axial force transfer, and, where applicable, catenary or arching mechanisms. Consistent with *EN 1995:2024*, connection design and modeling shall:

- verify resistance against the internal actions obtained from the global analysis;
- ensure that assumed load deformation laws are consistent with the connection detailing actually provided;
- avoid brittle failure modes and splitting of timber; and
- account for the combined effect of different fastener types and load directions where applicable.

Dowel type connections (bolts, screws, dowels) combined with metal plates are prevalent in mass timber frames and may achieve ductility via yielding of steel fasteners rather than the timber substrate, which is favorable for robustness. Examples of undesirable brittle failures (e.g., row shear, block tearing, splitting) and the associated spacing and edge distance requirements are given in *EN 1995:2024*.

In the validation phase of this thesis, the connection under consideration consists of a T-stub aluminum flange with an integrated backing plate, joining an LVL beam to an LVL column through steel bolts at the T-stub and smooth dowels at the beam–flange interface. This chapter demonstrates the procedure for calculating the mechanical properties of the connections in the analytical model.

6.2. Modeling connections for the analytical method

This section describes the modeling approach for connections within the analytical method, illustrated using the T-section connection from the validations tests (Lyu et al., 2020). The focus is placed on the middle connection, since the side connection behaves almost identically. The only distinction is that the side connection contributes a single component of rotational stiffness and half of the yield moment. This reduction in yield moment is relevant only in the calculation of column compression, where a slight difference arises compared to the middle connection. The actual calculation of this connection is detailed in appendix B.

- The connection yields when the weakest component reaches its yield moment;
- The connection cannot resist additional moment beyond the yield moment;
- The connection is simplified as a spring model to represent rotational and translational stiffness.

The simplified moment rotation graph for the model with and without gap are shown in figure 6.1

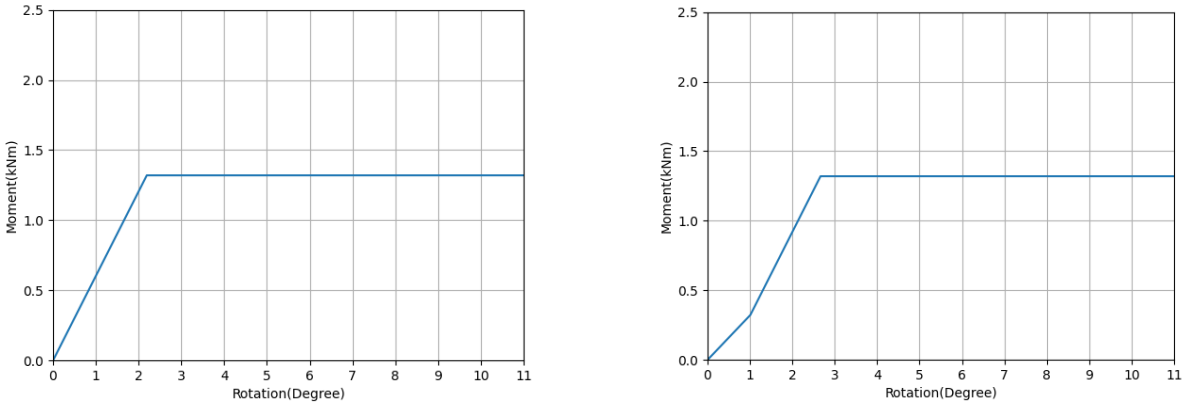

(a) Moment rotation graph without gap.

(b) Moment rotation graph with gap.

Figure 6.1: Moment rotation simplified graphs.

In the diagrams it can be observed that the moment increases up to a certain point, which in this thesis is referred to as the plastic moment. Beyond this point, yielding of the connection would normally begin. However, in the present modeling approach this behavior is simplified and represented as a straight line.
For the analytical method, the following properties are required from the connections:

- Rotational capacity;
- Rotational stiffness;
- Translational capacity;
- Translational stiffness.

These properties are calculated using the component method described in Yang et al., 2016 and *NEN-EN 1993-1-8*, 2024. In this approach, each component of the connection is represented as a spring, either in tension or compression, depending on its position and load bearing capability. Figure 6.2 presents the T-section connection in its quarter model configuration, as applied in the push down test described in Chapter 8. To provide an overview of the connection layout, a top view of the complete connection is shown in Figure 6.2.

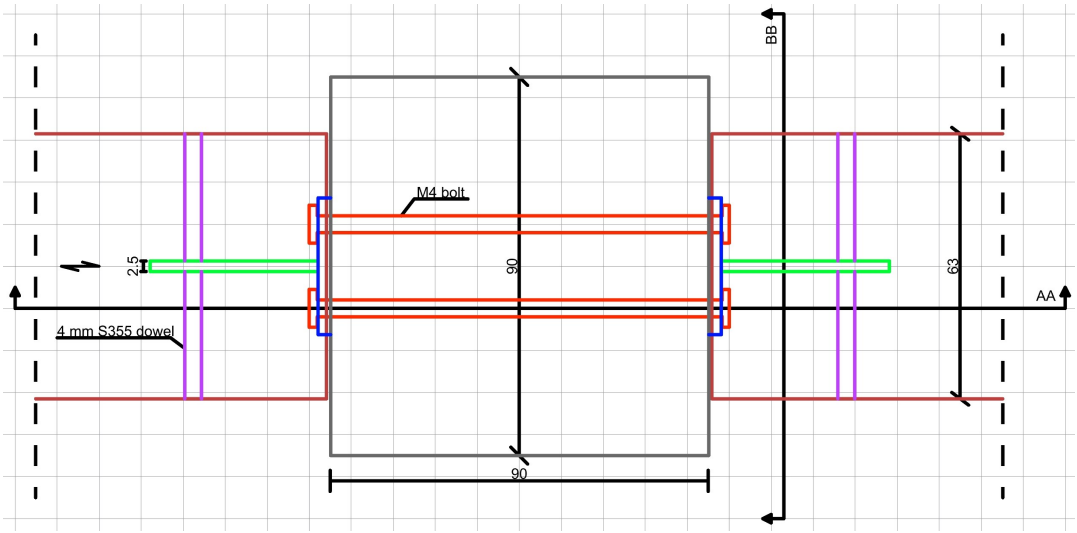

Figure 6.2: Top view of the T-section connection.

As illustrated in Figure 6.2, the interaction between the individual components of the connection can be

clearly identified. The LVL beams are shown in brown. The dowels, depicted in purple, pass through both the timber elements and the aluminum flange. The aluminum flange itself is shown in green and is connected to an end plate, indicated in blue. This end plate is bolted to a corresponding plate using bolts shown in red. The assembled connection transfers forces to the column, depicted in gray, through direct contact. The cross-sections denoted as AA and BB in the top view are presented in the following figures.

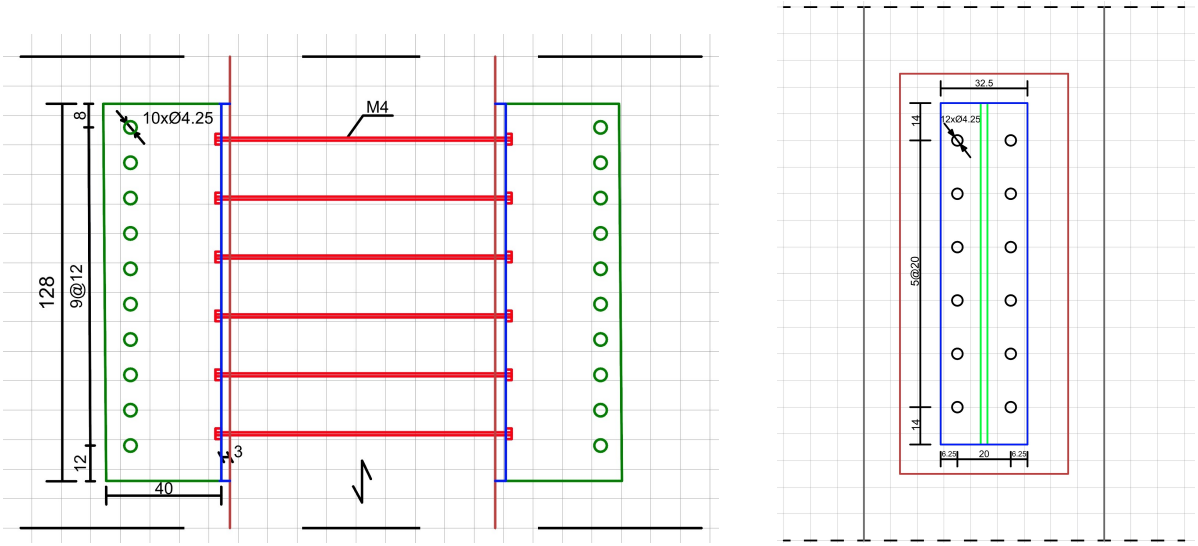

(a) Section AA of the T-section connection.

(b) Section BB of the T-section connection.

Figure 6.3: T-section connection layout.

In Figure 6.3 the AA and BB sections are shown from the figure 6.2. In these sections the relevant dimension are also shown. also the grain direction is shown for the column as the grain direction for the beam is shown in figure 6.2. also all the bolt hole dimensions are shown. so from these figure already some main behaviors can be seen the plates are connected mainly to each other with the bolts which will carry all the tension load in the connection and the compression between the plates will be mainly carried by the column. from this layout the calculations can be made to model this connection for the analytical method.

6.2.1. Rotational capacity

The rotational capacity of a connection is typically determined by identifying the weakest element within each bolt row. However, this approach becomes problematic when the column fails in shear or compression, as isolating the contribution of a single bolt row requires numerous additional assumptions. Therefore, in this study, the maximum plastic moment of each component is calculated individually, and the smallest value is adopted as the governing capacity.
The components that may govern the plastic moment are:

- Punching resistance of the bolt head or nut;
- Tensile resistance of the bolt;
- Tensile resistance of the aluminum plate (modeled as a T-stub);
- Shear strength of the dowel;
- Compression strength of the column;
- Shear strength of the column.

Most components are assumed to fail in tension (e.g., bolts and aluminum plate). For components that cannot develop tensile forces, their compression or shear strength is considered critical. The beam does not experience direct tension, as its tensile resistance is governed by the dowel strength, which already accounts for timber strength. Similarly, the column cannot be tensioned; however, the plate

can exert compressive forces on the column, making its compression or shear strength relevant.

For this connection, assumptions must be made regarding its rotational behavior, specifically whether rotation is permitted on both sides or only on one side. This distinction leads to differences between the connections modeled at the supports and the connection located at the mid span in the analytical model. In most cases, the ultimate strength and rotational stiffness of the side connections are multiplied by a factor of two to represent the resistance of the middle connection. Exceptions to this approach are made for the column compressive strength and stiffness, as well as for the column shear capacity, which are not scaled in the same manner.

Bolt resistance

The simplified model for evaluating the plastic moment contribution of the bolt rows is illustrated in Figure 6.4. The connection is idealized at the critical section by:

- A resultant compression block acting on the column side (or bearing face);
- A set of tensile resultants carried by the yielded bolt rows located below the rotation center (RC).

The RC is assumed to lie at the mid depth between the centroid of the compression block and the centroid of the tensile forces.

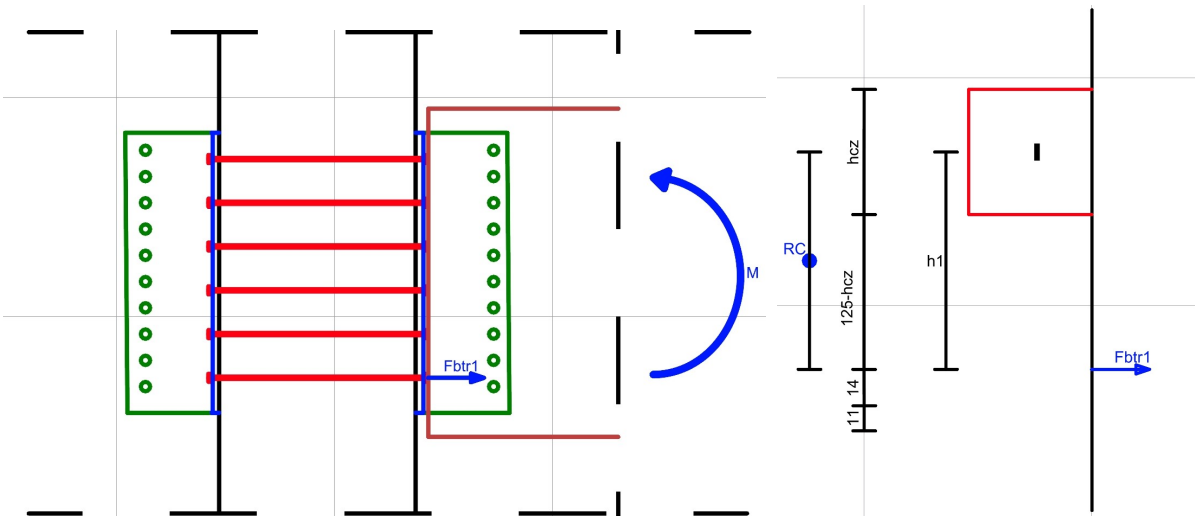

(a) Idealized force system at the connection. **(b)** Compression block and tensile resultants.

Figure 6.4: Simplified representation of bolt contribution to plastic moment capacity.

The following assumptions are adopted to establish the stress distribution:

1. Below the RC, n_y bolt rows are assumed to yield in tension. Each bolt row i develops a tensile force T_i, limited by the governing tensile failure mode in accordance with *NEN-EN 1993-1-8* (2024).
2. The RC is located at the mid depth of the compression block. Lever arms z_i are measured from the RC to the line of action of T_i (positive on the tension side).

For bolt row i, the tensile force T_i is taken as the minimum of:

$$T_i = \min(F_{bt},\, F_{pb}) \tag{6.1}$$

where:

$$F_{bt} = A_s f_{ub} \tag{6.2}$$

$$F_{pb} = \frac{0.6\pi d_m t_p f_{up}}{\gamma_m} \tag{6.3}$$

The parameters are defined as:

- A_s = tensile stress area of the bolt;
- f_{ub} = ultimate tensile strength of the bolt material;
- d_m = diameter of the bolt head or nut (whichever is smaller);
- t_p = thickness of the plate;
- f_{up} = ultimate strength of the plate material;
- γ_m = partial safety factor for material resistance.

For a complete bolt row, the resistance is doubled since two bolts act in parallel.

From the stress distribution in Figure 6.4, the height of the compression zone h_{cz} is determined by enforcing axial force equilibrium:

$$\sum_{i=1}^{n_y} F_{tb,i} = \sigma_p d_{cz} h_{cz} \tag{6.4}$$

where:

- σ_p = design compressive stress of the weakest material in compression (typically the column, perpendicular to grain);
- d_{cz} = depth of the compression block;
- h_{cz} = height of the compression zone.

Once h_{cz} is known, the lever arms h_i between the centroid of the compression block and each bolt row can be computed. The plastic moment contribution of the bolt group is then:

$$M_{pb} = \sum_{i=1}^{n_y} h_i F_{tb,i} \tag{6.5}$$

where:

- h_i = vertical distance from the centroid of the compression block to the i-th bolt row;
- $F_{tb,i}$ = governing tensile force in the i-th bolt row.

Tensile resistance of the T-stub

The tensile resistance of the aluminum plate, idealized as a T-stub, is evaluated following the component method of *NEN-EN 1993-1-8* (2024). Although the original provisions target steel connections, the same force distribution and failure mechanisms are assumed applicable to aluminum; only the material parameters (e.g., E_{al}, $f_{u,\mathrm{p}}$) differ and post-yield behavior is different. Since post-yield behavior is simplified in this study, this assumption is conservative and adequate for capacity assessment. The T-stub can fail according to the mechanisms shown in Figure 6.5:

- **Mode 1 (with prying):** combined bending of the end plate and tension in the flange with prying action. Prying forces arise when the plate is relatively flexible compared to the bolts (thin plate or high strength/stiff bolts).
- **Mode 2 (without prying):** similar to Mode 1 but with negligible prying due to a relatively stocky plate or flexible bolts.
- **Mode 3 (punching):** local punching under the bolt head/nut or net section failure; this is covered by the bolt resistance checks and is not duplicated here.

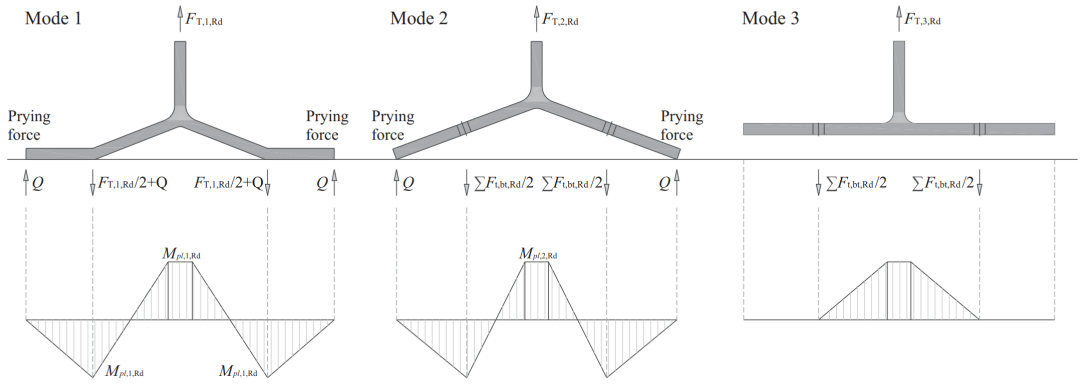

Figure 6.5: T-stub failure modes (Yang et al., 2016).

Given the geometry of the present connection (two bolts per row and a relatively thin aluminum plate), **Mode 1 with prying forces** is expected to govern.

For a bolt row at lever arm h_i (measured from the compression center to the bolt row), the tensile force carried by the row, including prying forces, is taken as:

$$F_{\mathrm{stub,row}} \;=\; \frac{4\,M_{\mathrm{pl}} \;+\; 2\,M_{\mathrm{bp}}}{m}, \tag{6.6}$$

where M_{pl} and M_{bp} are the plastic moments of the end plate and backing plate, respectively. In the example connection the backing plate and end plate are identical so one plastic moment can be used. The plate plastic moments per bolt row are evaluated as:

$$M_{\mathrm{pl}} \;=\; M_{\mathrm{bp}} \;=\; \frac{1}{4}\,l_{\mathrm{eff}}\,t_p\,f_{u,\mathrm{p}}, \tag{6.7}$$

with

$$l_{\mathrm{eff}} \;=\; 4\,m \;+\; 1.25\,e, \tag{6.8}$$

where t_p is the plate thickness, $f_{u,\mathrm{p}}$ is the ultimate strength of the plate material, m is the distance from the flange to center of the bolt, and e is the distance from the center of the bolt to the plate edge (see Figure 6.6).

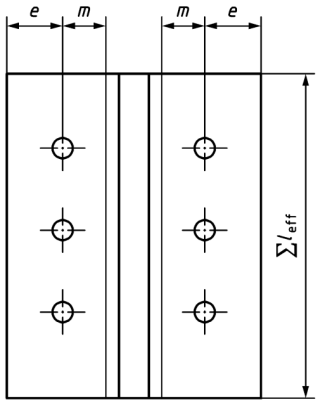

Figure 6.6: Geometrical parameters m and e entering the effective length l_{eff}.

Let n_y denote the number of tension rows below the rotation centre (RC). The plastic moment contribution of the T-stub component follows from the tensile forces $F_{\mathrm{stub,row},i}$ and their lever arms h_i to the

centroid of the compression block (cf. Section 6.2.1):

$$M_{\text{pl,T-stub}} = \sum_{i=1}^{n_y} h_i \, F_{\text{stub,row},i}. \tag{6.9}$$

The distances h_i are obtained with equation 6.4 and Figure 6.4.

Shear resistance of dowels

The contribution of dowels to the plastic moment capacity is governed by their shear resistance, as they connect the flange of the aluminum T-stub to the timber beam. The force distribution on the dowels under moment loading is illustrated in Figure 6.7. For clarity, only the force acting on the outermost dowel is shown; forces on the remaining dowels located below the rotation center (RC) are proportionally smaller. The RC is assumed to lie midway between the most compressed region and the outer dowel.

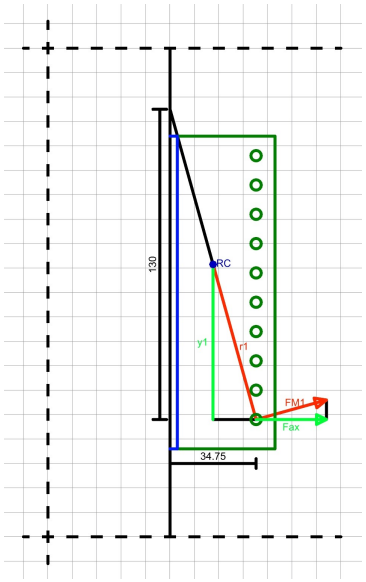

Figure 6.7: Force distribution on dowels under moment loading.

As shown in Figure 6.7, six dowels are located below the RC and are subjected to tension, while compression is assumed to be resisted by direct bearing of the beam against the column. For a conservative estimate, it is assumed that only the outermost dowel reaches its full yield capacity, while the remaining dowels contribute proportionally according to their lever arm.
This proportionality is expressed as:

$$F_{M,i} = \frac{F_{M,1} r_i}{r_1} \tag{6.10}$$

with

- $F_{M,i}$ = force in the i-th dowel;
- r_i = distance from the RC to the i-th dowel;
- $F_{M,1}$ = force in the outermost dowel.

The value of $F_{M,1}$ is determined from the dowel's shear resistance, $F_{ax,d}$, which is calculated according to *NEN-EN 1995-1-1*, 2024. The characteristic shear resistance $F_{D,k}$ is obtained as the minimum value

among the failure modes (a)–(f) defined in Eurocode EN 1995-1-1, illustrated in Figure 6.8:

$$F_{D,k} = \min \begin{cases} f_{h,1,k} t_{h1} d & \text{mode (a)} \\ f_{h,2,k} t_{h2} d & \text{mode (b)} \\ \frac{f_{h,1,k} t_{h1} d}{(1+\beta)} \left[\sqrt{\beta + 2\beta^2 \left(1 + \frac{t_{h2}}{t_{h1}} + \left(\frac{t_{h2}}{t_{h1}}\right)^2\right) + \beta^3 \left(\frac{t_{h2}}{t_{h1}}\right)^2} - \beta \left(1 + \frac{t_{n2}}{t_{h1}}\right) \right] & \text{mode (c)} \\ 1.05 \frac{f_{h,1,k} t_{h1} d}{2+\beta} \left[\sqrt{2\beta(1+\beta) + \frac{4\beta(2+\beta) M_{y,k}}{f_{h,1,k} d t_{h1}^2}} - \beta \right] & \text{mode (d)} \\ 1.05 \frac{f_{h,1,k} t_{h2} d}{1+2\beta} \left[\sqrt{2\beta^2(1+\beta) + \frac{4\beta(1+2\beta) M_{y,k}}{f_{h,1,k} d t_{h2}^2}} - \beta \right] & \text{mode (e)} \\ 1.15 \sqrt{\frac{2\beta}{1+\beta}} \sqrt{2 M_{y,k} f_{h,1,k} d} & \text{mode (f)} \end{cases} \tag{6.11}$$

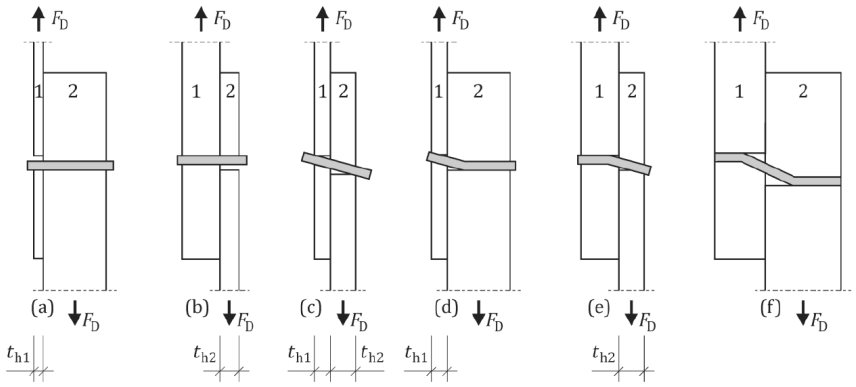

Figure 6.8: Failure modes for dowel shear (*NEN-EN 1995-1-1*, 2024).

The parameters in Equation (6.11) are:

- $f_{h,i,k}$ = embedment strength of member i;
- $t_{h,i}$ = embedment depth;
- d = dowel diameter;
- $\beta = f_{h,2,k}/f_{h,1,k}$;
- $M_{y,k}$ = characteristic yield moment of the dowel.

The embedment strength for timber is calculated as:

$$f_{h,k} = \frac{0.082(1 - 0.01d)p_k}{k_{mat}} \tag{6.12}$$

where k_{mat} accounts for the influence of grain direction and is given by for lvl:

$$k_{\text{mat}} = (k_{90} \sin^2(\alpha) + \cos^2(\alpha)) * (\sin^2(\beta) + k_4 \cos^2(\beta)) \tag{6.13}$$

where:

- $k_{90} = 1.15 + 0.15d$;
- α = the angle between the direction of the force acting on the shear plane and the grain direction;
- β = the angle between fastener axis and surface of the wide face;
- $k_4 = \frac{d}{d-2}$

The embedment depth is taken as the smaller of the member thickness or the dowel penetration length. The dowel yield moment is calculated as:

$$M_{y,k} = 0.3 f_{u,k} d_1^{2.6} \tag{6.14}$$

where:

- $f_{u,k}$ = ultimate tensile strength of the dowel material;
- d_1 = unthreaded dowel diameter.

Since the dowels in this connection are smooth (non-profiled), no rope effect is considered; thus, $F_{ax} = F_{D,k}$.
Finally, the plastic moment contribution of the dowels is computed as: Since the dowels in this connection are smooth (non-profiled), no rope effect is considered; thus, $F_{ax} = F_{D,k}$.
Finally, the plastic moment contribution of the dowels is computed as:

$$M_{pl,d} = 2 \sum_{i=1}^{n} r_i F_{M,i} \tag{6.15}$$

where n is the number of dowels below the RC (six in this case). The factor of 2 accounts for equilibrium, as the compression side balances the tension side.

Column compressive strength

For the example connection, there are two relevant modes by which the column can fail in compression. These differ depending on whether a one sided connection is assumed or a double sided connection is considered. Within the analytical method this distinction is important, since the middle connections are modeled as double sided, whereas the side connections are modeled as one sided. For the one sided connection, the manner in which the timber is compressed is illustrated in Figure 6.9 for the outer right column.

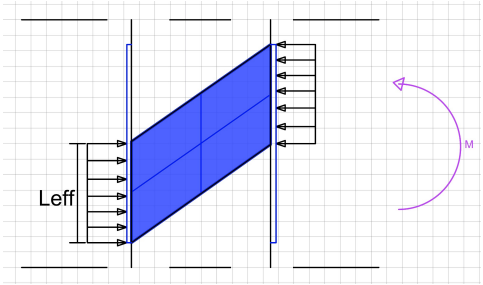

Figure 6.9: Transverse compression in the column.

As shown in Figure 6.9, the moment illustrated in the diagram is transferred to the plates, which in turn exert compressive pressure on the timber. The corresponding compressive force is then calculated as:

$$F_{cc} = f_{c,r}\, b_c\, l_{\text{eff}} \tag{6.16}$$

where:

- $f_{c,r}$ = compressive strength in the radial direction;
- b_c = width of the end plate;
- l_{eff} = effective length over which the stress acts.

For simplicity, l_{eff} is taken as half the length of the backing plate or end plate, depending on the force being evaluated. Assuming the rotation center lies at mid height of the plate, the plastic moment contribution is:

$$M_{pl,cc} = F_{t,cc} l_{\text{eff}} \tag{6.17}$$

For the two sided connection the compression behavior this is just the compression of the whole column in between the plates as shown in figure 6.10

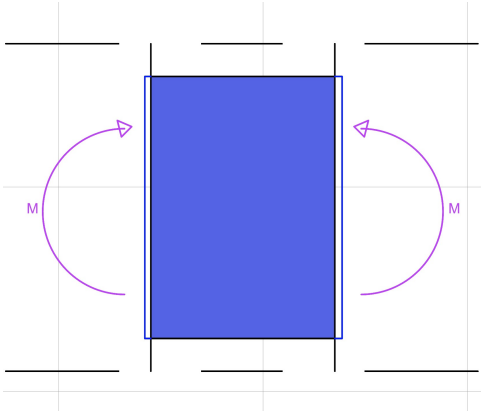

Figure 6.10: Compression in the middle column.

with this because the l_{eff} is set to half the plate height this will still give the moment for one side of this connection only now for the whole resistance this just needs to be doubled.

Column shear capacity

A secondary failure mechanism for the column under moment loading is shear induced by the bearing pressure of the plates. This shear action develops along a critical plane within the column and contributes to the overall moment resistance. The idealized shear flow and its lever arm are illustrated in Fig. 6.11.

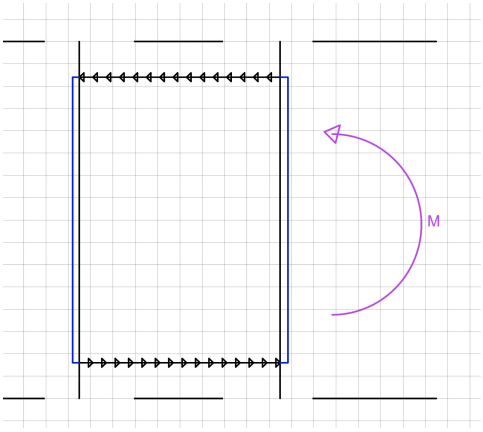

Figure 6.11: Shear forces in the column resulting from plate bearing under applied moment.

The shear force acting on the critical plane is computed as:

$$F_{\mathrm{cs}} = f_{v,LT}\, b_c\, d_c, \tag{6.18}$$

where:

- $f_{v,LR}$ = shear strength of the column in the longitudinal–radial plane;
- b_c = column width;
- d_c = column depth.

The corresponding plastic moment contribution associated with this shear force is:

$$M_{\mathrm{pl,cs}} = F_{\mathrm{cs}} h_{\mathrm{pl}}, \tag{6.19}$$

where h_{pl} denotes the effective lever arm, typically taken in the case of the example as the height of the plate.

6.2.2. Rotational stiffness

For the analytical method, the rotational stiffness of the connections must be determined for both the central and side connections. In this approach, the connections are idealized as spring systems, enabling their representation within a simplified global model.

To achieve this, the connection is decomposed into individual components, similar to the procedure used for calculating the plastic moment. On the tension side, each bolt row located below the rotation center (RC) is modeled as a separate spring, while on the compression side, a single spring represents the compression zone. This methodology follows the component based approach described in *NEN-EN 1993-1-8*, 2024 and Yang et al., 2016. The resulting simplifications are illustrated in Figure 6.12.

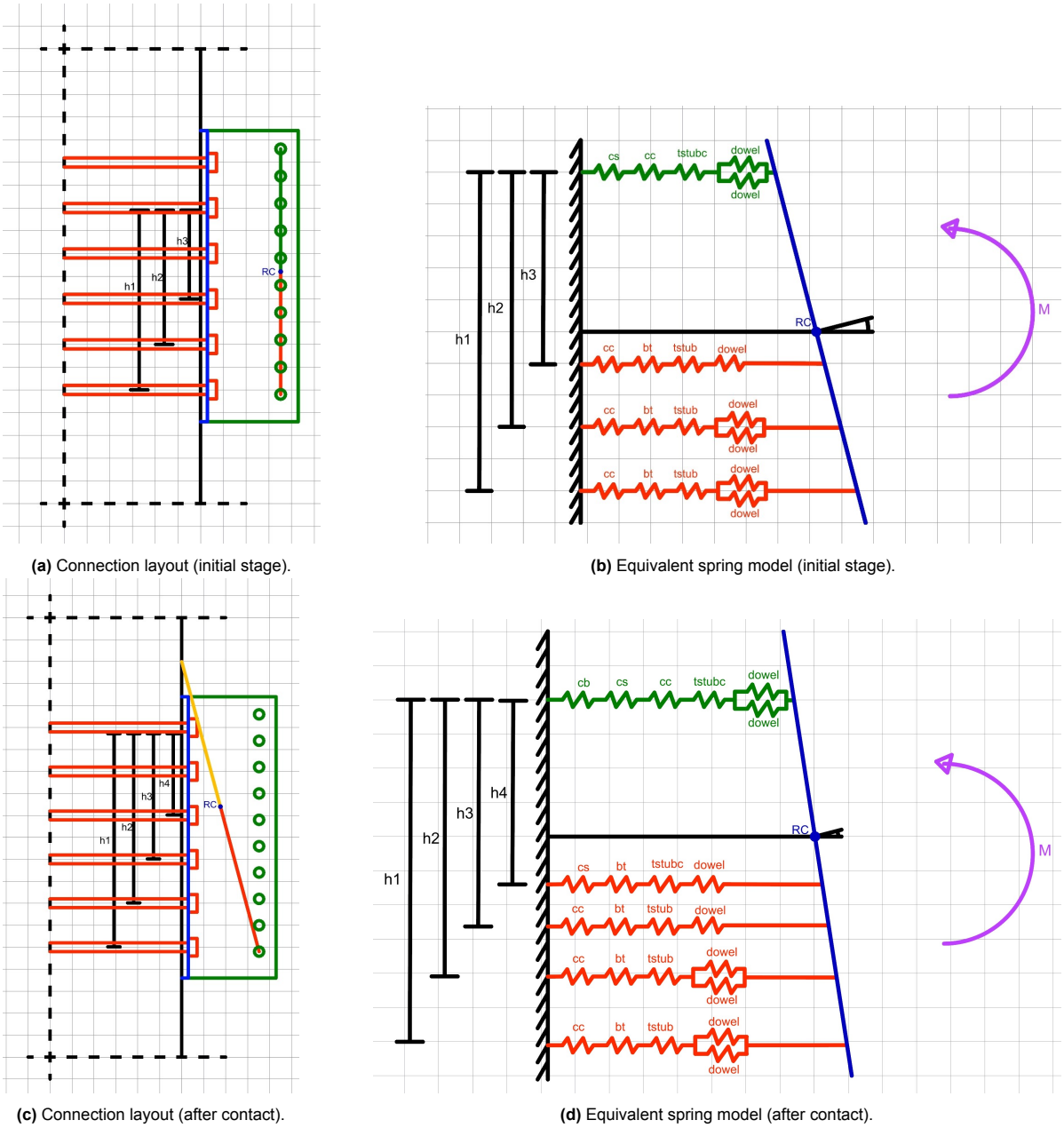

(a) Connection layout (initial stage).

(b) Equivalent spring model (initial stage).

(c) Connection layout (after contact).

(d) Equivalent spring model (after contact).

Figure 6.12: Simplification of the connection into an equivalent spring system.

Figures 6.12(a) and (b) illustrate the first configuration, where the beam has not yet come into contact with the column. In this stage, the RC is located near the dowels, as the load transfer occurs primarily through these elements. Figures 6.12(c) and (d) show the second configuration, which occurs after the beam contacts the column. In this case, the RC shifts upward and toward the column, resulting in an additional compression spring and a diagonal spring connecting the compression and tension sides. The increased lever arms of the outer components lead to a higher overall stiffness.

The equivalent spring system reflects the actual load path through the connection. For example, the compression spring shown in Figure 6.12(b) represents a series of components: two dowels in parallel (shear), the T-stub in compression, and the column, which contributes through transverse compression and shear resistance. These components are modeled as springs in series or parallel, depending on their physical arrangement, to capture the combined stiffness accurately.

For the tension side, the approach is analogous to that used for the compression side, except that the tensile stiffness of the components is considered. The compression spring representing the column remains included because, as illustrated in Figure 6.9, the applied moment causes the backing plate to press into the column. This interaction generates a horizontal reaction force, which is modeled as a tensile force in the simplified spring system.
The following component stiffness's must be calculated for both sides of the connection:

- Compression stiffness of the column (k_{cc});
- Shear stiffness of the column (k_{cs});
- Compression stiffness of the T-stub (k_{tstubc});
- Shear stiffness of the dowel (k_{dowel});
- Tension stiffness of the bolt (k_{bt});
- Tension stiffness of the T-stub (k_{tstub});
- Compression stiffness of the beam (k_{cb}).

These individual stiffness's are then combined into two equivalent springs—one for the tension side and one for the compression side—representing the entire connection. This simplification enables the calculation of the initial rotational stiffness of the connection. The concept is illustrated in Figure 6.13.

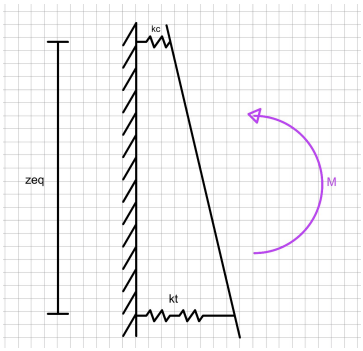

Figure 6.13: Equivalent two spring model for rotational stiffness.

In this model, all the springs are made into a equivalent tension and compression spring, the equivalent lever arm between them must be determined. This distance, z_{eq}, is calculated as:

$$z_{eq} = \frac{\sum k_i h_i^2}{\sum k_i h_i} \tag{6.20}$$

where:

- k_i = stiffness of the i-th spring row;
- h_i = vertical distance from the reference compression spring to the i-th spring row.

The initial rotational stiffness of the connection is then expressed as:

$$S_{\text{ini}} = \frac{z_{\text{eq}}^2}{\frac{1}{k_t} + \frac{1}{k_c}} \tag{6.21}$$

Where k_t and k_c denote the equivalent stiffness's of the tension and compression springs, respectively. These equivalent stiffness's are obtained by combining the component stiffness's in series and parallel according to their physical arrangement, as expressed below:

$$k_c = \frac{1}{\frac{1}{k_{cs}} + \frac{1}{k_{cc}} + \frac{1}{k_{\text{tstubc}}} + \frac{1}{2 \cdot k_{\text{dowel}}}} \tag{6.22}$$

This formulation assumes that all components on the compression side act in series, except for the dowels, which act in parallel with each other but remain in series with the other components.

For the tension side, the calculation is more complex because the springs are located at different distances from the compression spring. The equivalent stiffness for the tension side is computed as:

$$k_t = \frac{\sum k_{t,i} \cdot h_i}{z_{\text{eq}}} \tag{6.23}$$

where h_i is the vertical distance from the compression spring to the i-th tension spring row, and $k_{t,i}$ is the stiffness of that row. For example, the stiffness of the bottom row in the first configuration is:

$$k_{t,1} = \frac{1}{\frac{1}{k_{cc}} + \frac{1}{k_{bt}} + \frac{1}{k_{\text{tstub}}} + \frac{1}{2 \cdot k_{\text{dowel}}}} \tag{6.24}$$

The component stiffness's required for these calculations are:

- k_{bc} = compression stiffness of the beam;
- k_{cs} = shear stiffness of the column (see Figure 6.11);
- k_{cc} = compression stiffness of the column (see Figure 6.9);
- k_{tstubc} = compression stiffness of the T-stub;
- k_{dowel} = shear stiffness of a dowel;
- k_{tstub} = tension stiffness of the T-stub;
- k_{bt} = tension stiffness of the bolt.

The calculation of these stiffness's is detailed below.

Beam compression stiffness

The beam experiences compression once the gap between the beam and column has closed. This stiffness is calculated according to Tomasi et al., 2008:

$$k_{bc} = \frac{E_{w,0} \sqrt{b_b l_{\text{eff,cb}}}}{\beta} \tag{6.25}$$

where:

- $E_{w,0}$ = modulus of elasticity of the beam along the grain;
- b_b = beam width;
- $l_{\text{eff,cb}}$ = effective height of the beam in contact with the column;
- β = 4 from Tomasi et al., 2008.

For $l_{\text{eff,cb}}$, a simplification is adopted: half the compression zone height is assumed, as the actual contact area may vary due to deformation.

Column shear stiffness

The shear stiffness of the column is calculated following Yang et al., 2016:

$$k_{cs} = \frac{G_c b_c h_c}{z_{\text{eq}}} \tag{6.26}$$

where:

- G_c = shear modulus of the column;
- b_c = column width;
- h_c = column depth;
- z_{eq} = equivalent lever arm (see Equation 6.20).

Column compression stiffness

The compression stiffness of the column is given by:

$$k_{cc} = \frac{E_{c,r} b_c l_{\text{eff,cc}}}{h_c} \tag{6.27}$$

where:

- $E_{c,r}$ = modulus of elasticity in radial direction;
- $l_{\text{eff,cc}}$ = effective height so the middle of compression zone to RC.

T-Stub compression stiffness

The compression stiffness of the T-stub flange is calculated as:

$$k_{\text{tstubc}} = \frac{0.7 d_{fl} t_{fl} E_{fl}}{h_{c,fl}} \tag{6.28}$$

where:

- d_{fl} = flange length;
- t_{fl} = flange thickness;
- $h_{c,fl}$ = effective compression height so the middle of compression zone to RC;
- E_{fl} = Elastic modulus of the flange.

Dowel shear stiffness

The dowel shear stiffness is calculated according to *NEN-EN 1995-1-1*, 2024:

$$k_{\text{dowel}} = \frac{p_{\text{mean}}^{1.5} d_{\text{dowel}}}{23} \tag{6.29}$$

where:

- p_{mean} = mean timber density;
- d_{dowel} = dowel diameter.

T-Stub tension stiffness

For a single bolt row under prying action, the tension stiffness of the T-stub is:

$$k_{\text{tstub}} = \frac{0.85 E_{\text{al}} l_{\text{eff}} t_{f,e}^3}{m^3} \tag{6.30}$$

where:

- E_{al} = elastic modulus of aluminum;
- l_{eff} = effective length of the bolt row;
- $t_{f,e}$ = end plate thickness;
- m = geometric parameter (see Figure 6.6).

Bolt tension stiffness

The last stiffness that needs to be calculated is the bolt tension stiffness

$$k_{bt} = \frac{E_b\, A_{bt}}{l_{bt}} \tag{6.31}$$

where:

- E_b = elastic modulus of the bolt material;
- A_{bt} = tensile stress area of the bolt;
- l_{bt} = grip length of the bolt.

After determining the stiffness of all individual components (e.g., bolts, dowels, T-stub elements, and compression zones), the following steps are performed:

1. Combine component stiffness's in series and parallel to obtain equivalent stiffness for the tension and compression sides of the connection;
2. Compute the equivalent lever arm z_{eq} using the stiffness weighted distance method (Equation (6.20));
3. Calculate the initial rotational stiffness of the connection using the two spring model (Equation (6.21)).

The resulting moment–rotation relationship is constructed in two stages:

- **Stage 1:** Initial configuration prior to beam–column contact, governed by the first stiffness layout;
- **Stage 2:** Post contact configuration, where additional compression springs become active, increasing the overall stiffness.

This staged approach enables the simplified component model to capture the nonlinear stiffness evolution observed in experimental tests while maintaining computational efficiency for global structural analysis.

6.2.3. Horizontal translation capacity

The translational capacity of the connection, illustrated in Figure 6.3, is governed by the weakest component resisting axial displacement. To determine this capacity, the following individual resistances must be evaluated:

- Bolt tensile resistance (F_{bt});
- Dowel shear resistance (F_{dv});
- T-stub tensile resistance (F_{tstub});
- Column compression resistance (F_{cc}).

Each resistance is calculated in accordance with the relevant provisions of EN 1993-1-8 and EN 1995-1-1, considering the governing failure modes for steel and timber components. The overall translational capacity of the connection is then defined as:

$$F_{trans} = \min\left(F_{bt}, F_{dv}, F_{tstub}, F_{cc}\right) \tag{6.32}$$

This approach ensures that the global connection model reflects the most critical failure mechanism under axial loading. The calculated translational capacity is subsequently integrated into the simplified spring model used for the analytical mode;, enabling accurate representation of the connection's load–displacement behavior.

Bolt tensile strength

The tensile resistance of a bolt is governed by two potential failure mechanisms: (i) bearing failure of the bolt head or washer on the aluminum plate, and (ii) tensile failure of the bolt shaft. Both resistances are calculated in accordance with EN 1993-1-8 *NEN-EN 1993-1-8*, 2024.
The bearing resistance is given by:

$$F_{bb} = \frac{0.6\,\pi\, d_m\, f_{up}\, t_p}{\gamma_m} \tag{6.33}$$

where:

- d_m = diameter of the bolt head or equivalent washer;
- f_{up} = ultimate tensile strength of the plate material;
- t_p = thickness of the plate;
- γ_m = partial safety factor (taken as 1.25).

The tensile resistance of the bolt shaft is expressed as:

$$F_{ts} = \frac{0.9\, f_{ub}\, A_s}{\gamma_m} \tag{6.34}$$

where:

- f_{ub} = ultimate tensile strength of the bolt material;
- A_s = tensile stress area of the bolt.

The governing tensile resistance of a single bolt is determined as:

$$F_{bt} = \min(F_{bb}, F_{ts}) \tag{6.35}$$

For the complete connection, the total tensile capacity is obtained by multiplying F_{bt} by the number of bolts in the connection. This value is subsequently compared with the resistances of other components (dowels, T-stub, and column) to identify the critical mechanism governing the translational capacity of the connection.

Dowel shear strength

The dowel resistance under tensile loading of the connection is governed by shear failure, as dowels primarily transfer forces through shear rather than axial tension. The characteristic shear resistance of a dowel is calculated according to EN 1995-1-1 as:

$$F_{vd} = F_{D,k} + F_{rpd} \tag{6.36}$$

where:

- $F_{D,k}$ = characteristic dowel shear resistance;
- F_{rpd} = rope effect contribution.

Since dowels have no head and therefore cannot develop a rope effect, the term F_{rpd} is neglected in this calculation. Consequently, the dowel shear resistance simplifies to:

$$F_{vd} \approx F_{D,k} \tag{6.37}$$

The value of $F_{D,k}$ is determined using the Johansen yield theory as specified in EN 1995-1-1, considering the governing failure mode for the timber–steel interface (see Equation 6.11). The total dowel shear capacity of the connection is then obtained by multiplying the resistance of a single dowel by the number of dowels present:

$$F_{dv,\text{total}} = n_d \cdot F_{vd} \tag{6.38}$$

where n_d is the number of dowels in the connection. This total resistance is subsequently compared with the capacities of other components (bolts, T-stub, and column) to identify the critical mechanism governing the translational capacity of the connection.

T stub tensile strength

The tensile capacity of the T-stub connection must account for two potential governing mechanisms: (i) failure of the flange alone and (ii) failure of the entire T-stub assembly under tension. The design procedure therefore involves evaluating both capacities and adopting the smaller value as the governing resistance.
The tensile resistance of the flange cross-section is calculated as:

$$F_{\text{tstub,fl}} = A_{\text{fl}}\, f_{u,\text{fl}}, \tag{6.39}$$

where:

- A_{fl} = net cross-sectional area of the flange;
- $f_{u,\mathrm{fl}}$ = ultimate tensile strength of the flange material.

The second check considers the entire T-stub assembly, including prying effects and bolt interaction. This capacity is evaluated using the component method described in *EN 1993-1-8*, applying the governing failure mode (typically Mode 1 with prying action) for each bolt row:

$$F_{\mathrm{stub,row}} = \frac{4M_{\mathrm{pl}} + 2M_{\mathrm{bp}}}{m}, \tag{6.40}$$

where M_{pl} and M_{bp} are the plastic moments of the end plate and backing plate, respectively, and m is the lever arm between bolt rows. The total tensile capacity of the T-stub is obtained by summing the contributions of all bolt rows:

$$F_{\mathrm{tstub,total}} = \sum_{i=1}^{n_{\mathrm{row}}} F_{\mathrm{stub,row},i}. \tag{6.41}$$

Column compression strength

When the backing plate bears against the timber column, the compressive resistance of the column in the radial direction becomes critical. This capacity is evaluated by considering the effective contact area of the end plate and the ultimate compressive strength of the column perpendicular to the grain. The governing expression is:

$$F_{\mathrm{cc,u}} = A_{\mathrm{end,pl}}\, f_{u,c,\perp}, \tag{6.42}$$

where:

- $A_{\mathrm{end,pl}}$ = effective contact area of the end plate bearing on the column;
- $f_{u,c,\perp}$ = ultimate compressive strength of the column perpendicular to the grain (radial direction for LVL).

For the example connection considered in this thesis, $f_{u,c,\perp}$ corresponds to the radial direction of the laminated veneer lumber (LVL) column.

6.2.4. Horizontal translational stiffness

The final property required for the analytical connection model is the translational stiffness, which governs the axial response of the beam under tension. This stiffness is derived by considering all components activated along the axial load path and assembling them into an equivalent spring system. The configuration adopted for the example connection is illustrated in Fig. 6.14.

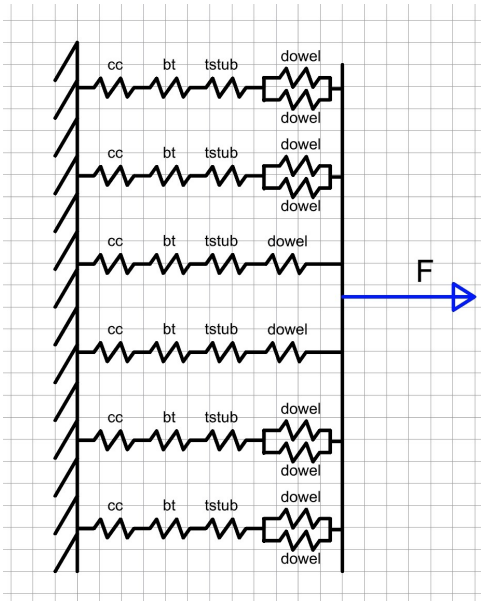

Figure 6.14: Idealized spring model for translational stiffness of the T-stub connection.

In this model, each bolt row is represented by an individual spring comprising the relevant components acting in series. This approach simplifies the calculation because the geometry of the T-stub and the distribution of dowels are closely related to the bolt rows. Although the actual connection includes more dowels than bolts, the dowels are proportionally assigned to bolt rows for simplicity. For instance, the middle rows may be assigned one dowel each, while the outer rows receive two. This approximation has negligible influence on the overall stiffness.
The following component stiffness's are required:

- Column compression stiffness per bolt row (k_{cc});
- Bolt tension stiffness (k_{bt});
- T-stub tension stiffness per bolt row (k_{tstub});
- Dowel shear stiffness (k_{dowel}).

These stiffness's are calculated using the expressions introduced in previous subsections:

k_{cc} from Eq. (6.27), using effective height per row;
k_{bt} from Eq. (B.29);
k_{tstub} from Eq. (6.30), with row specific geometry;
k_{dowel} from Eq. (6.29).

Each bolt row is modeled as a series assembly of its components, with dowels acting in parallel. The equivalent stiffness for a single row is:

$$k_{\mathrm{row},i} = \left(\frac{1}{k_{cc}} + \frac{1}{k_{\mathrm{tstub}}} + \frac{1}{k_{bt}} + \frac{1}{2k_{\mathrm{dowel}}} \right)^{-1}, \tag{6.43}$$

where the factor of two accounts for the two dowels acting in parallel.
The total translational stiffness of the connection is obtained by summing the equivalent stiffness of all bolt rows:

$$k_{\mathrm{trans}} = \sum_{i=1}^{n_{\mathrm{row}}} k_{\mathrm{row},i}. \tag{6.44}$$

This stiffness is then implemented in the analytical model to represent the axial response of the connection under tension. The staged activation of components (e.g., gap closure between beam and column) should be reflected by adjusting k_{cc} and k_{tstub} when bearing initiates.

6.3. Modeling connections for the dynamic method

This section describes the implementation of beam to column connections in the dynamic finite element (FE) model using LS-DYNA. The objective is to accurately reproduce the mechanical behavior of the connection under sudden column removal scenarios, including large rotations, axial force transfer, and potential catenary action. The modeling strategy comprises three main components:

1. Discrete beam elements representing dowels and bolts;
2. Contact elements ensuring realistic bearing and frictional interaction between components;
3. Nodal rigid bodies (NRBs) for connectivity between non conforming meshes.

6.3.1. Discrete beam elements

Discrete beams are two node elements with three translational degrees of freedom per node. They are employed to simulate the axial and shear behavior of dowels, bolts, and screws. Each element is oriented along the physical axis of the fastener, with local directions defined as:

- One axis for axial tension/compression;
- Two axes for shear in orthogonal directions.

The following input parameters are required for each discrete beam in LS-DYNA:

- Axial tension strength and maximum tensile strain;

- Axial compression strength and maximum compressive strain;
- Shear strength in two directions (to account for timber grain orientation);
- Element density;
- Fastener diameter.

These properties are derived from Eurocode provisions (*EN 1993-1-8*, *EN 1995-1-1*) and experimental data presented in Chapter 7. The force–deformation behavior is defined by three curves:

1. Axial tension/compression curve;
2. Shear curve in the longitudinal–tangential (LT) plane;
3. Shear curve in the radial–longitudinal (RL) plane.

Compression capacity is often assigned a high arbitrary value because compressive forces are primarily transmitted through contact surfaces rather than through the fastener itself. These curves can be seen in theory in chapter 6 and for the example connection in chapter 8.

6.3.2. Contact elements

Contact elements ensure proper interaction between steel plates, aluminum flanges, and timber components. Two types of contact are employed:

1. **Surface to surface contact:** Used for bearing and friction between plates and timber faces. This method requires aligned shell normals; therefore, dummy shell layers are introduced where necessary. These dummy shells are tied to the structural components using nodal rigid bodies.
2. **Node to node friction links:** Used for localized contact where sliding is minimal and mesh alignment is challenging. These links act along a predefined local axis, typically the negative z-direction, to transmit compression forces.

Figure 6.15 illustrates the contact configuration for an end plate bearing against a timber column.

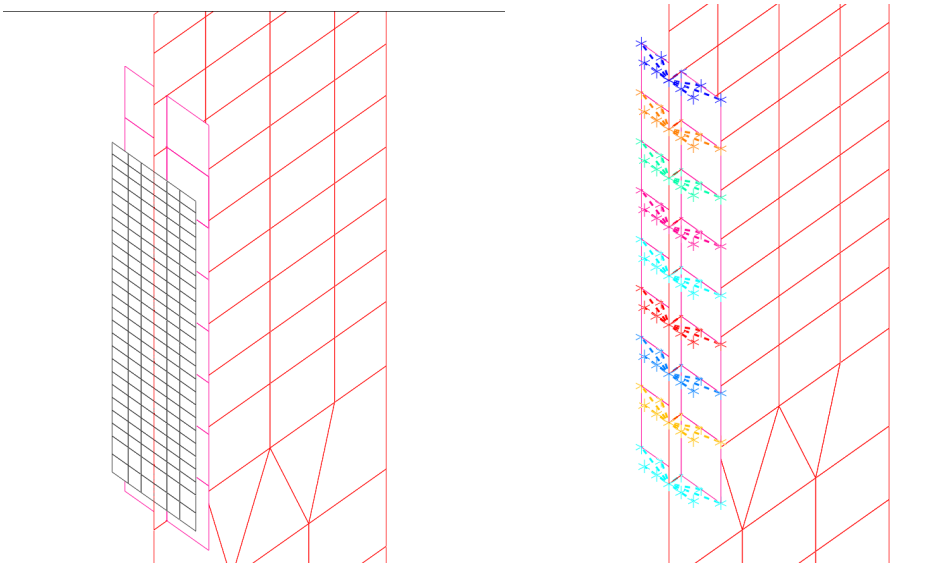

(a) End plate and contact surface. **(b)** Contact surface tied to column via NRB.

Figure 6.15: Contact modeling approach for plate–column interaction.

Penalty stiffness for surface contact is selected based on the softer of the two interacting components to avoid instability. Friction coefficients are assigned according to material pairing. Activation of contact occurs when the outer surfaces, including shell thickness, intersect (see Fig. 6.16).

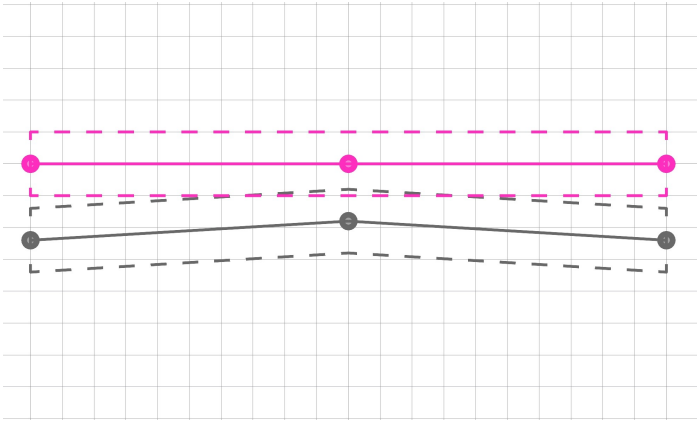

Figure 6.16: Penetration criterion for contact activation.

Node to node friction beams are defined with a high stiffness (typically $k = 1 \times 10^8\,\mathrm{N/m^2}$) to ensure negligible deformation under compression. A deletion criterion based on free displacement (e.g., $u_{\text{max}} = 0.1\,\mathrm{m}$) is applied to remove inactive elements and improve computational efficiency. Figure 6.17 shows an example configuration.

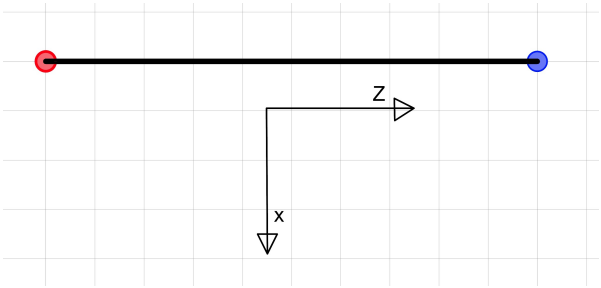

Figure 6.17: Node to node friction beam configuration.

6.3.3. Nodal rigid bodies

Nodal rigid bodies (NRBs) are multi point constraints that kinematically tie a set of slave nodes to a master node so that all tied nodes undergo identical rigid body motion. NRBs are particularly useful when coupling non conforming meshes, distributing contact reactions over a patch of elements, and preserving the physical line of action for discrete fasteners. When defined with negligible mass and without additional elastic links, NRBs do not add artificial stiffness to the underlying structure; they simply transmit displacements and forces between connected nodes.
In this work, NRBs are employed in three principal ways:

1. To connect a discrete beam (e.g., friction link or connector) to a shell when meshes do not meet at a common node;
2. To tie thin, dummy contact layers to the load carrying shells so that contact reactions are transferred to the physical components (cf. Fig. 6.15 (b)).

Figure 6.18 illustrates two typical NRB configurations. In Fig. 6.18 (a), a node to node *friction* beam is used to transmit compression along its local negative z-axis between an end plate (grey) and a timber beam. Because the shell meshes are not aligned, the supported end of the friction beam is tied to the timber shell patch via an NRB. This prevents the discrete beam from being initially inclined (which would introduce unintended transverse components) and ensures that compression is transmitted strictly along its local axis.

In Fig. 6.18 (b), a dowel is represented by a discrete beam connecting the aluminum flange (yellow) to the timber beam (blue). The dowel's "far" end is connected to a representative patch of timber nodes

using an NRB to (i) distribute the shear across the local timber area, (ii) preserve the intended lever arm and line of action, and (iii) avoid unrealistic stress concentrations that would arise if the discrete beam were tied to a single node.

As discussed in Section 6.3.2, thin dummy shells are sometimes introduced to facilitate robust surface to surface contact (aligned normals and controllable penalty stiffness). These dummy layers are tied to the underlying structural shells using NRBs (see Fig. 6.15 (b)) so that contact forces and penetrations are transferred to the physical components without adding spurious flexibility.

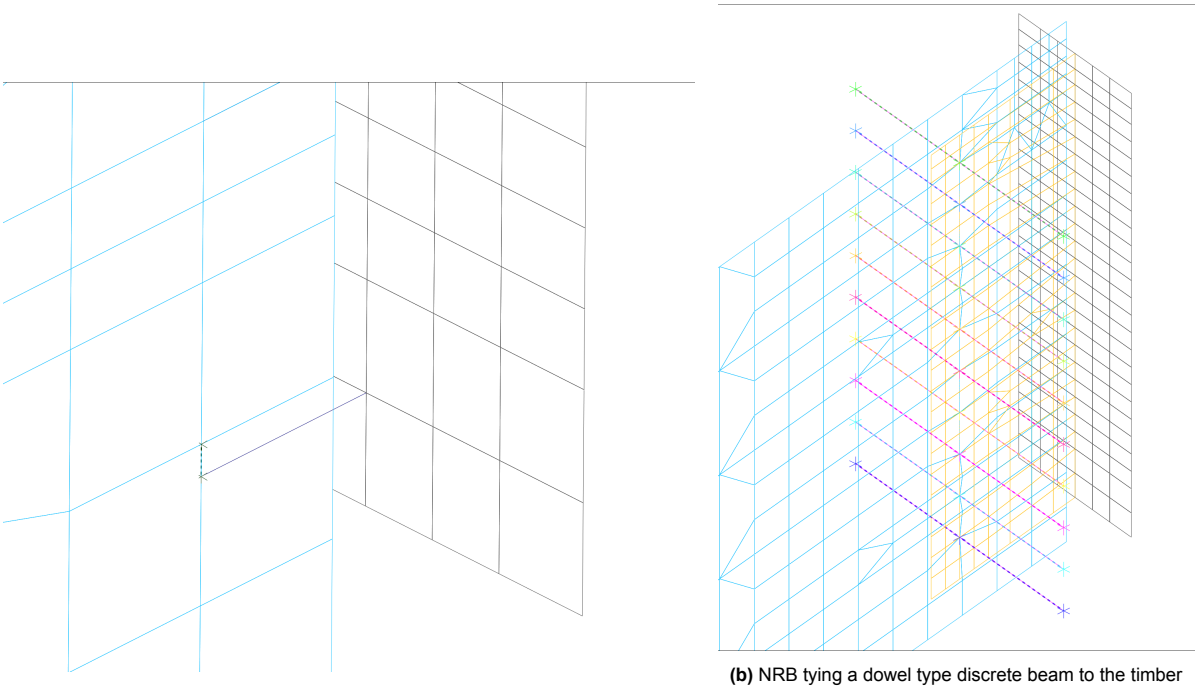

(a) NRB tying a friction (compression only) discrete beam to a shell patch.

(b) NRB tying a dowel type discrete beam to the timber shell patch.

Figure 6.18: Examples of nodal rigid body (NRB) applications for non conforming meshes.

To avoid over restraint, the following good practices are adopted:

- Place the NRB master node on the stiffer component (e.g., steel/aluminum plate) to enhance stability and condition the constraint equations.
- Limit each NRB to a compact, physically meaningful patch of slave nodes that represents the impacted area of the fastener or contact interface.
- Ensure that NRB clusters do not overlap on the same shell nodes, which could over constrain the mesh and introduce artificial stiffness.

NRBs enforce rigid kinematics within the tied patch; they should therefore not be used where significant in plane deformation within that patch is physically expected (e.g., local plate bending to distribute bearing) unless the affected flexibility is modeled elsewhere (e.g., via the discrete fastener or the contact law). Care is also required to avoid closed loops of rigid links that can lead to singular constraint systems.

Part II: Tests and models

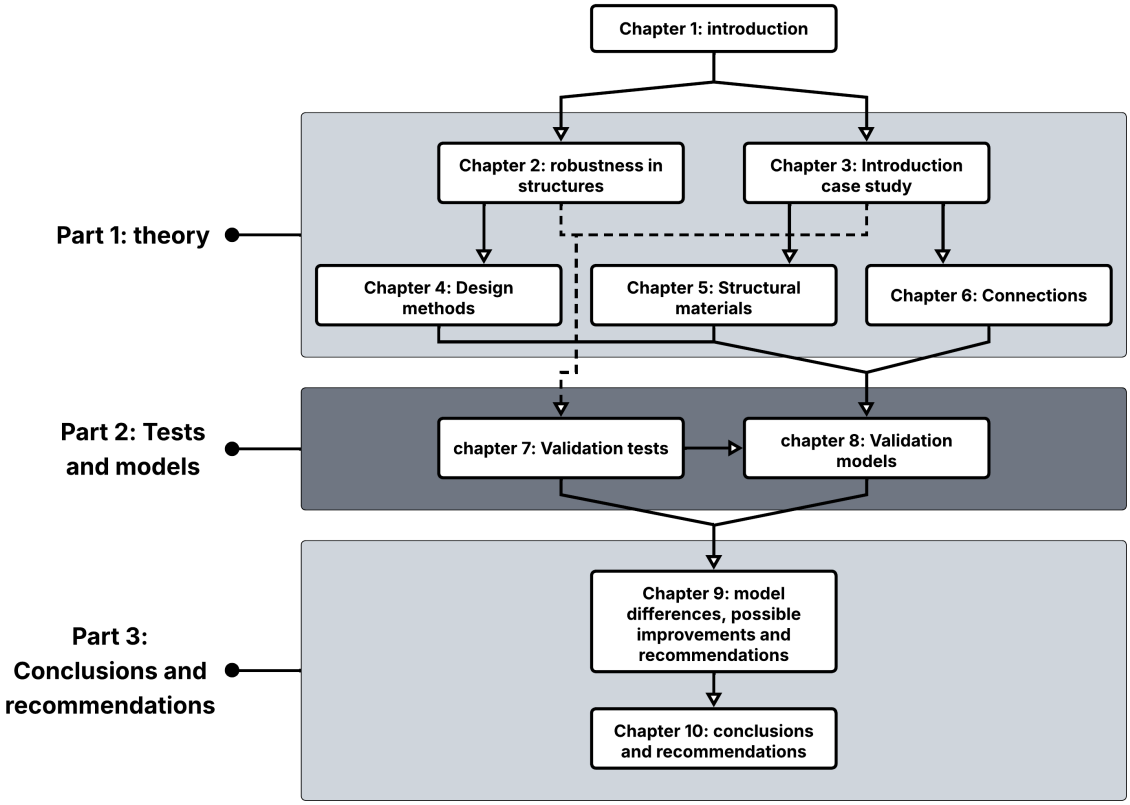

7
Validation Tests

This chapter presents the experimental programs used to validate the numerical models developed in this thesis. Each test is described with respect to its setup, loading protocol, and measured response quantities. The experimental results provide the benchmark data required to calibrate and verify the pseudo static and dynamic modeling approaches discussed in Chapter 4. The chapter concludes with a summary of the key observations and conclusions derived from the test data.

7.1. Overview of the tests

Three experimental studies form the basis of the validation process:

1. **Connection moment tests** (Masaeli et al., 2020): These tests investigate the moment and shear capacity of beam to column connections at both full scale and quarter scale. The scaling analysis is critical because the quarter scale configuration is employed in subsequent portal frame tests.
2. **Quasi static push down tests** (Lyu et al., 2020): These tests assess the global response of a timber portal frame under a notional column removal scenario using displacement controlled loading.
3. **Dynamic column removal tests** (Cheng et al., 2021): These tests simulate sudden column loss by releasing the middle column under various pre applied loads, enabling evaluation of dynamic amplification and residual load paths.

The first study provides detailed connection level data, including moment–rotation curves and failure modes, which are essential for component based modeling. The second and third studies capture system level behavior under progressive collapse scenarios, offering insight into load redistribution mechanisms such as catenary action and arching.

The quarter scale connection tested in Masaeli et al., 2020 is geometrically similar to the full scale prototype, although differences in material properties arise due to manufacturing constraints. These discrepancies are addressed through the normalization procedure described in the connection study presented in J. Cao et al., 2021. The normalized results demonstrate that the scaled connection provides a representative and reliable basis for modeling the behavior of the portal frame. The combined objectives of these tests are:

- To quantify the rotational and translational capacities of the T-stub connection under monotonic loading;
- To establish the global load–displacement response of a portal frame under quasi static and dynamic column removal scenarios;
- To identify governing failure mechanisms and deformation patterns for calibration of numerical models.

The following sections describe each test in detail, including instrumentation, loading protocol, and key observations.

7.2. Connection moment test

This test evaluates the moment capacity of the beam to column connection, providing insight into its ductility and governing failure mechanisms under large rotations. The experimental setup for the quarter scale ($\frac{1}{4}$) connection is shown in Fig. 7.1.

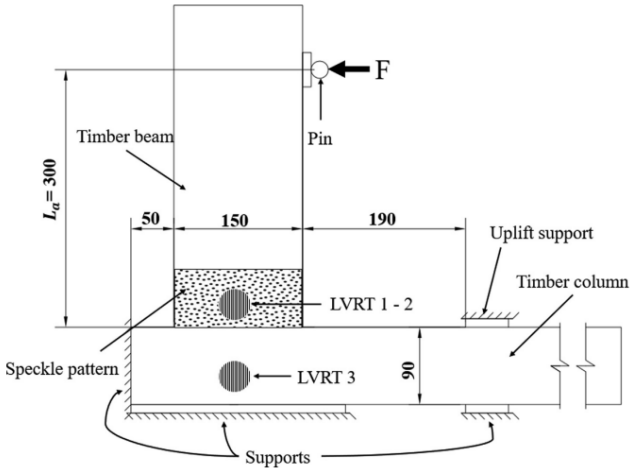

Figure 7.1: Quarter scale connection moment test setup (Masaeli et al., 2020).

The horizontal load F is applied at a lever arm of $L_a = 300\,\mathrm{mm}$ from the connection using a $50\,\mathrm{kN}$ hydraulic jack operating at a displacement rate of $2\,\mathrm{mm/min}$. Rotation of the connection is measured using Linear Variable Displacement Transducers (LVDTs) positioned as shown in Fig. 7.1. The connection rotation ϕ_c is computed as:

$$\phi_c = r_1 - r_3, \tag{7.1}$$

where r_1 and r_3 denote the readings of the respective LVDTs. The applied moment is calculated as:

$$M = F \cdot L_a, \tag{7.2}$$

with $L_a = 300\,\mathrm{mm}$ as indicated in Fig. 7.1. The full scale configuration employs the same loading principle but with dimensions scaled by a factor $\alpha = 4$. To compare results across scales, the measured moments from the full scale tests are normalized by dividing by $\alpha^3 = 64$, accounting for the combined effect of force scaling (α^2) and lever arm scaling (α). Figure 7.2 presents the moment–rotation curves for five tests: three quarter scale and two full scale specimens (normalized for comparison).

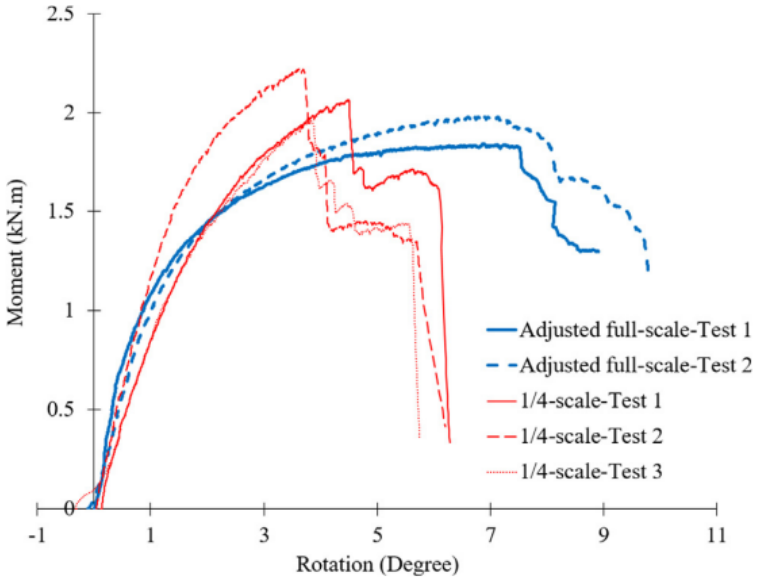

Figure 7.2: Moment–rotation response of T-stub connection (Masaeli et al., 2020).

Key observations include:

- Full scale connections exhibit greater ductility compared to quarter scale specimens.
- Both scales display similar behavioral trends: an initial elastic phase followed by gradual yielding and eventual failure.

Table in Figure 7.3 summarizes the observed and normalized capacities, as well as elastic stiffness values for both scales.

Connection	Test	¼-scale specimens			Adjusted full-scale specimens		
		Observed capacity kN·m	Normalised capacity kN·m	Elastic stiffness kN·m/Deg	Observed capacity kN·m	Normalised capacity kN·m	Elastic stiffness kN·m/Deg
T-section	Test1	2.08	1.63	0.85	1.86	2.10	1.57
	Test2	2.25	1.77	1.22	2.01	2.27	1.14
	Test3	1.99	1.56	0.86	–	–	–
	Average	2.11	1.65	0.98	1.93	2.19	1.36

Figure 7.3: Summary of moment test results for T-stub connection (Masaeli et al., 2020).

The normalized capacity of the full scale connection exceeds that of the quarter scale specimen, indicating that material property differences and fabrication effects influence scaling. Elastic stiffness is also higher for the full scale configuration.

Figure 7.4 illustrates the observed failure mechanisms for both scales. In all cases, failure occurred in the aluminum flange of the T stub, typically at large rotations near the end of the test.



(a) Quarter scale specimen. **(b)** Full scale specimen.

Figure 7.4: Failure modes of T-stub connections (Masaeli et al., 2020).

7.3. Push down test

The quasi static push down test evaluates the maximum load carrying capacity of the portal frame under a notional column removal scenario. This test provides critical data for validating the pseudo static modeling approach and assessing the ability of the frame to develop alternative load paths.

The experimental configuration, shown in Fig. 7.5, corresponds to a quarter scale ($\frac{1}{4}$) portal frame, consistent with the connection tests described in Section 7.2. The full scale setup, reported in Lyu et al., 2020, follows the same principles but with scaled dimensions and loading.

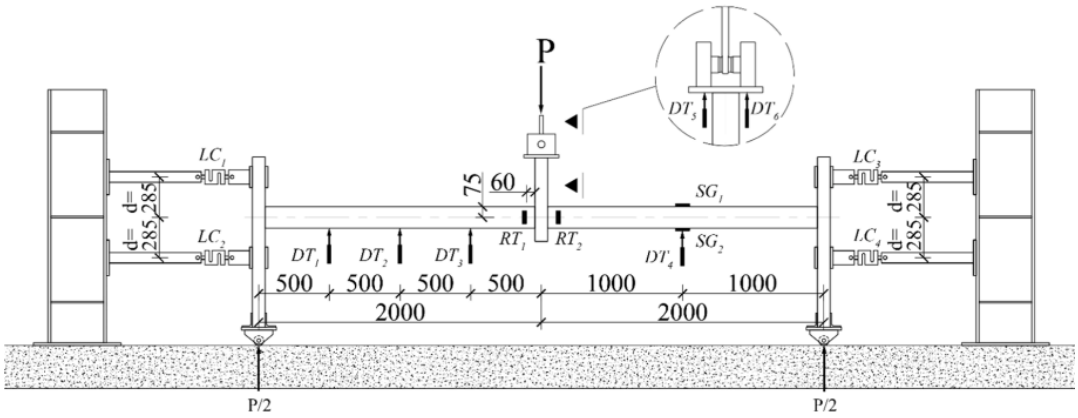

Figure 7.5: Quasi static push down test setup (Lyu et al., 2020).

The frame is supported on rollers at the column bases to allow horizontal movement while restricting rotation through load cells (LC), which also record horizontal reactions. The middle column is shortened and loaded vertically using a hydraulic jack operating at a displacement rate of $10\,\mathrm{mm/min}$. Six vertical LVDTs measure the displacement of the middle column and adjacent beams; the average of DT5 and DT6 is taken as the column deflection. Two rotation transducers monitor the connection rotations for moment–rotation analysis.

Figure 7.6 shows the force–deflection curve obtained from the test. The curve exhibits an initial elastic phase, followed by a plateau indicating significant yielding, and finally a sharp drop corresponding to ultimate failure.

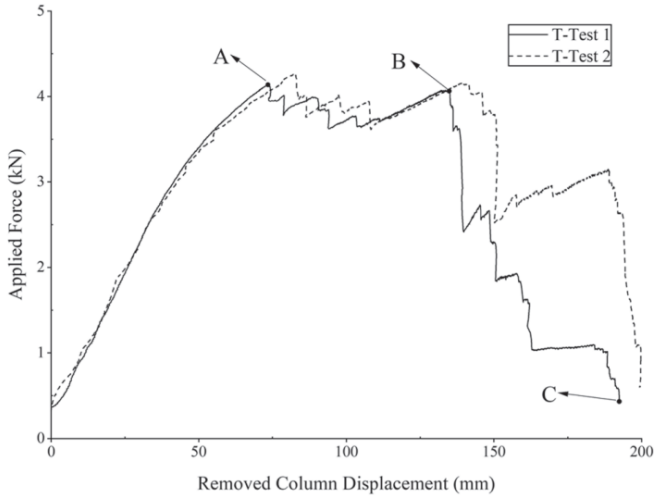

Figure 7.6: Push down response of the portal frame with T-stub connections.

The letters A, B, and C in Fig. 7.6 correspond to key stages of the test, illustrated in Fig. 7.8. Point A marks the onset of extensive yielding, while Point B indicates progressive damage in the timber and plates. Point C represents ultimate failure, characterized by fracture of the aluminum flange.

Figure 7.7 presents the moment–rotation and axial force–deflection relationships for the critical connection. The maximum recorded moment is approximately $1.95\,\mathrm{kNm}$, which is lower than the capacity observed in isolated connection tests. This reduction is attributed to the simultaneous development of axial tension, which accelerates flange failure before full moment capacity is reached. The axial force curve reveals partial catenary action; however, full development is prevented by premature flange fracture.

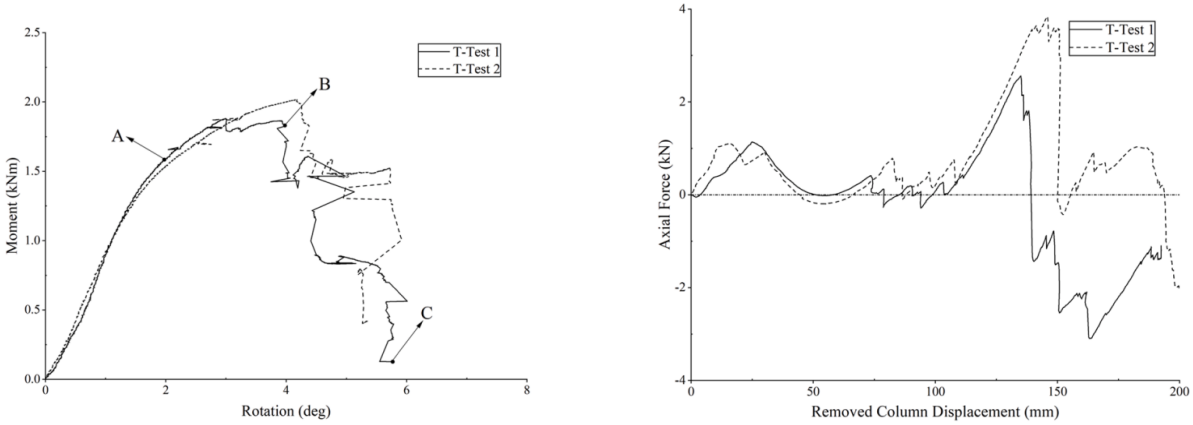

(a) Moment–rotation curve.

(b) Axial force–deflection curve.

Figure 7.7: Connection response during push down test (Lyu et al., 2020).

Figure 7.8 shows the physical condition of the connection at stages A, B, and C. The final stage confirms that failure is governed by fracture of the aluminum flange, consistent with the component based predictions in Chapter 6.

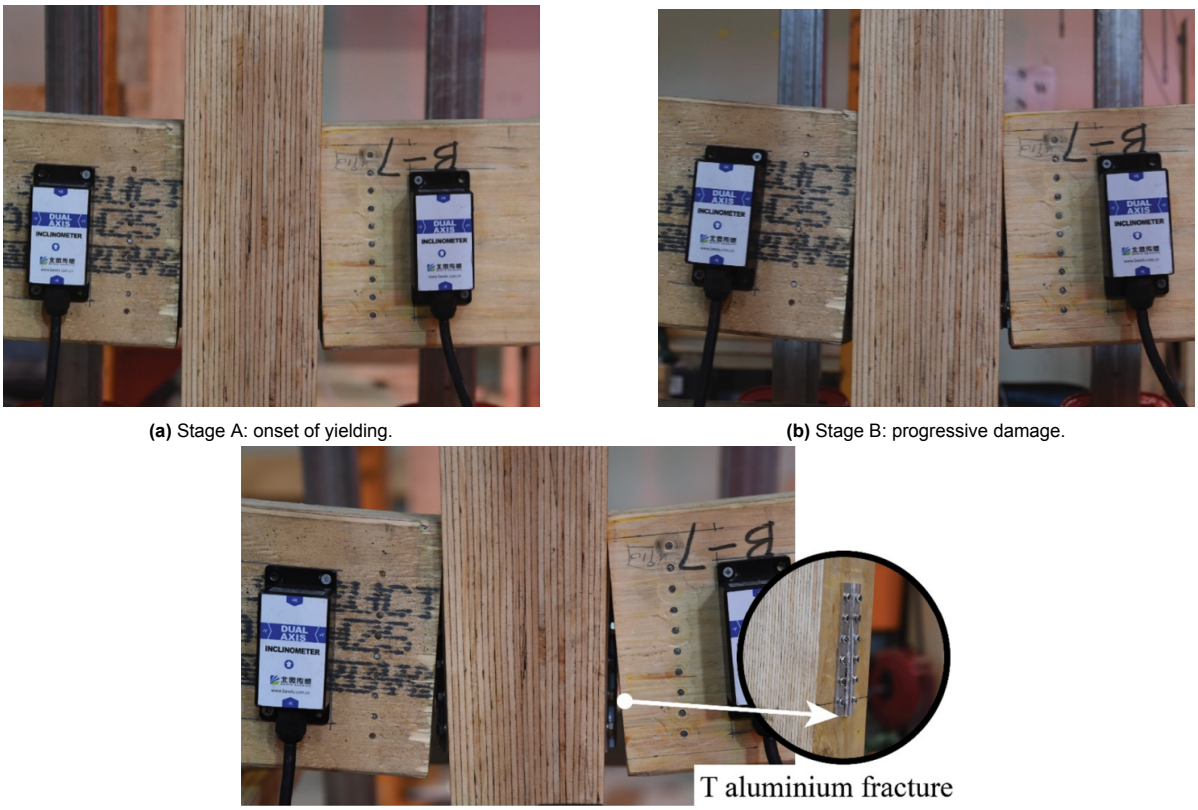

(a) Stage A: onset of yielding.

(b) Stage B: progressive damage.

(c) Stage C: ultimate failure.

Figure 7.8: Failure progression during push down test (Lyu et al., 2020).

Table in Figure 7.9 summarizes the maximum applied load, corresponding deflection, and comparison with design loads from various codes. The results indicate that the actual static capacity of the frame is approximately six times lower than the design load prescribed by DoD guidelines (including a dynamic amplification factor of 2). This highlights the necessity of alternative load paths for robustness.

Connector		P_{max} (kN)	UDP_{max} (kPa)	$UDP_{max}/UDP_{design_DoD}$	$UDP_{max}/UDP_{design_IStructE}$	$UDP_{max}/UDP_{design_AS/NZS}$
T-section	T-Test 1	4.14	1.38	0.15	0.35	0.38
	T-Test 2	4.26	1.42	0.16	0.36	0.39

Figure 7.9: Summary of push down test results (Lyu et al., 2020).

7.4. Sudden column removal test

The sudden column removal test investigates the dynamic response of the portal frame under an instantaneous loss of a critical vertical support. This scenario represents a progressive collapse trigger and is essential for validating the dynamic modeling approach.

The experimental configuration, illustrated in Fig. 7.10, is similar to the quasi static push down test described in Section 7.3, with roller supports at the column bases and rotation restraint provided by load cells. The key difference is the introduction of a release mechanism for the middle column, which is initially supported by a hydraulic actuator and loaded with steel plates to simulate gravity effects.

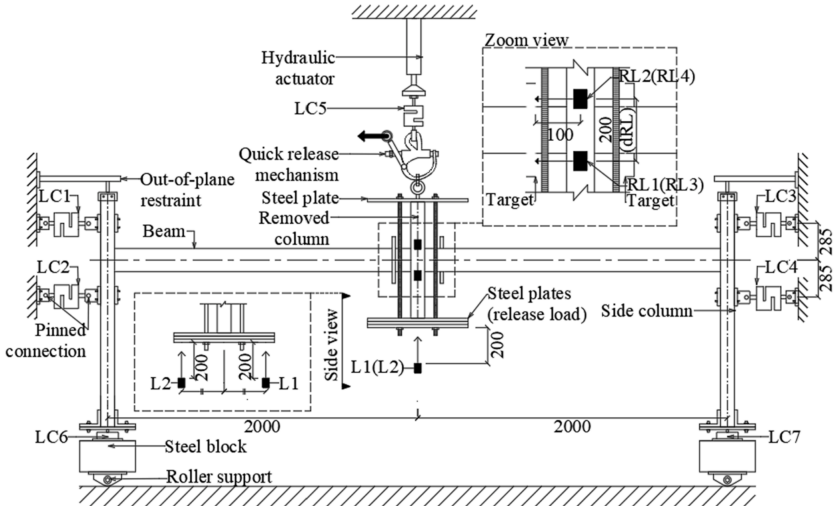

Figure 7.10: Sudden column removal test setup (Cheng et al., 2021).

Two laser displacement transducers (L1 and L2) monitor the vertical motion of the released column, while four additional sensors (LR1–LR4) measure beam rotations. The average beam rotation is computed as:

$$R = \tan^{-1}\left(\frac{L_{RL1} - L_{RL2} + L_{RL3} - L_{RL4}}{2d_{RL}}\right), \tag{7.3}$$

where L_{RLi} are laser readings and d_{RL} is the reference spacing between sensors. The column is subjected to multiple release loads, expressed as percentages of the static capacity:

- 11.5% = $0.47\,\mathrm{kN}$
- 12.7% = $0.52\,\mathrm{kN}$
- 13.4% = $0.55\,\mathrm{kN}$
- 24.6% = $1.01\,\mathrm{kN}$
- 48.5% = $1.99\,\mathrm{kN}$
- 61.2% = $2.51\,\mathrm{kN}$
- 73.2% = $3.00\,\mathrm{kN}$

Figure 7.11 shows the displacement–time histories for all release loads. Each curve exhibits a sharp increase immediately after release (at $t \approx 0.5$ s), followed by oscillations and eventual stabilization. Collapse occurred for the highest release load.

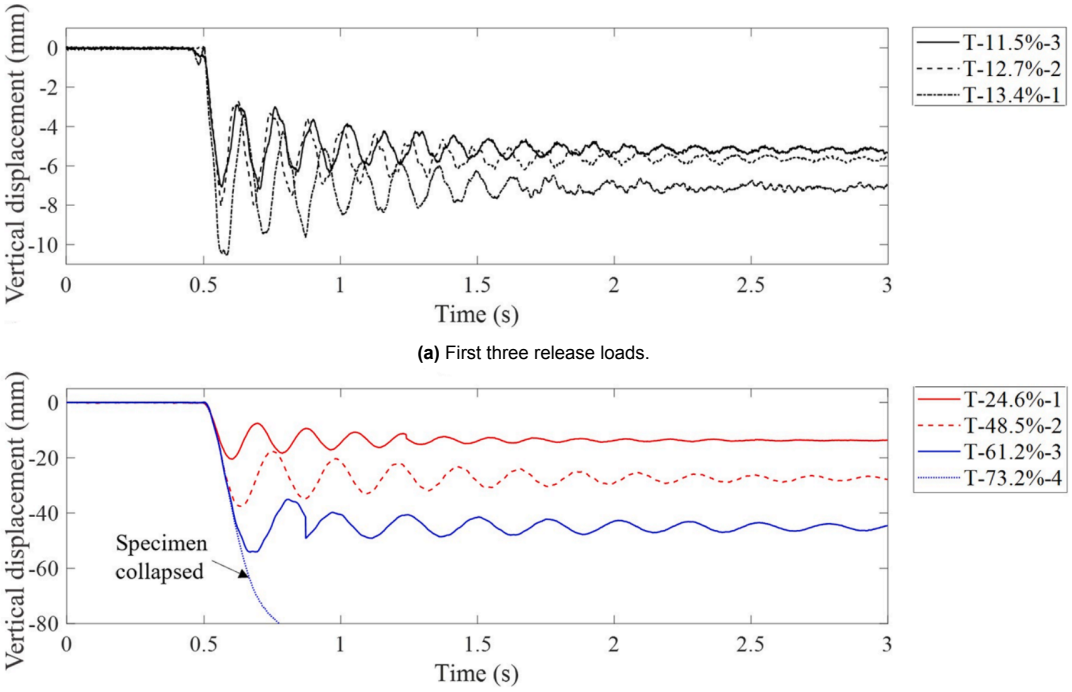

(a) First three release loads.

(b) Last four release loads.

Figure 7.11: Displacement–time response for sudden column removal (Cheng et al., 2021).

Figure 7.12 presents the corresponding reaction force–time histories. For most cases, the peak force occurs shortly after release, followed by damping toward a steady state. Data for the 61.2% case is unavailable due to power error.

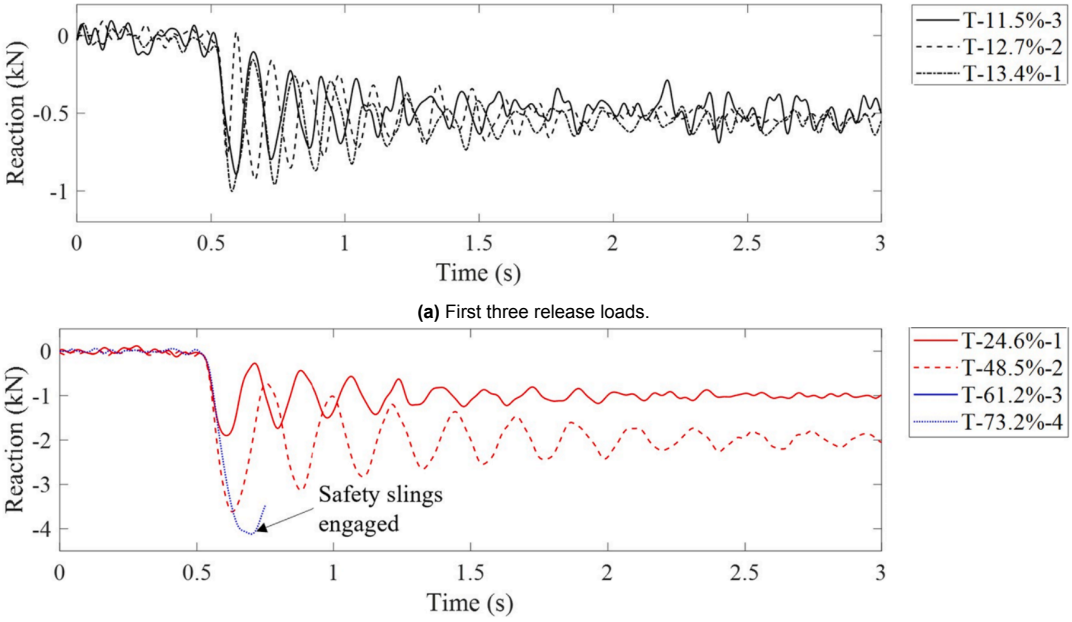

(a) First three release loads.

(b) Last four release loads.

Figure 7.12: Reaction force–time histories for sudden column removal (Cheng et al., 2021).

The study by Cheng et al. (2021) presents force displacement curves for dynamic column removal tests, together with the corresponding pseudo static predictions obtained using the energy based approach described in Section 4.1.2. In addition, the study provides discrete data points corresponding to each

release load applied during the drop down tests, as shown in Figure 7.13, alongside the pseudo static response curves.

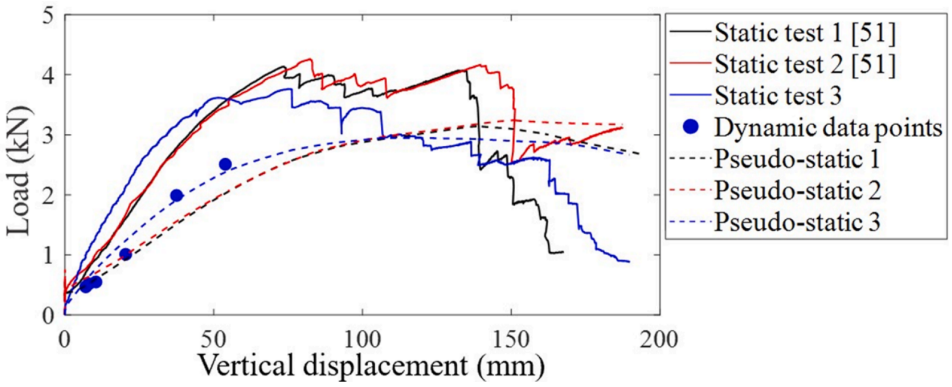

Figure 7.13: Comparison of force displacement curves for dynamic and pseudo static analyses.

As illustrated in Figure 7.13, the pseudo static energy based response curves derived from the push down tests correspond to the same portal frame configuration used in the drop down tests and are shown as Static Tests 1, 2, and 3. The predicted dynamic response follows the experimental results closely, while remaining slightly conservative. This is evidenced by the close agreement between the discrete dynamic data points from the drop down tests and the pseudo static curves. Furthermore, the response curves do not exceed a force level of approximately 3 kN, which is consistent with the experimentally observed release load at which failure of the frame occurred.

Figure 7.14 shows the static curves for the moment rotation and the axial force curves this also shows the highest release load without failure dynamic curves for moment rotation and axial force. with the black curves being the static curves from the push down paper, the gray curve the static curve of the drop down paper and the red line the dynamic curve of the drop down paper.

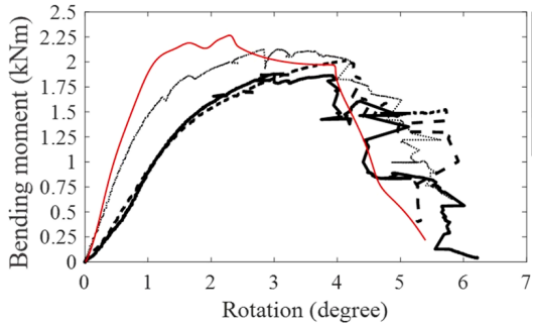

(a) Moment rotation curve.

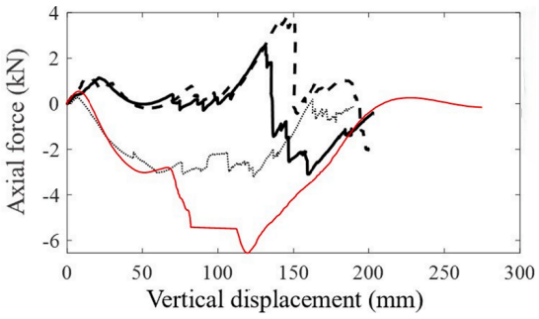

(b) Axial force deflection curve.

Figure 7.14: Bending and axial force curves for static and dynamic tests (Cheng et al., 2021).

Figure 7.14 shows that the dynamic response differs from the static response, but it also highlights that the static responses reported in the two experimental studies already diverge substantially. For example, the grey moment rotation curve exhibits a significantly higher initial stiffness than the other two static curves, while reaching failure at approximately the same rotation level. This suggests that the underlying connection capacity is not fundamentally altered, but that the pre-yield stiffness is strongly influenced by differences in the test configuration or initial conditions.

A similar inconsistency is evident in the axial force response. Clear compressive arching is observed in the grey curve (static) and in the red curve (dynamic), whereas the two black static curves show little to no compressive arching. The referenced study attributes these discrepancies to differences in

the gap between the beam and the column, but does not quantify whether this gap is larger or smaller for the respective tests. As discussed in Chapter 8, a reduced gap is expected to increase stiffness due to earlier contact and activation of compressive mechanisms. This interpretation should be explicitly noted, and further investigation is recommended to confirm whether the observed differences in stiffness and compressive arching can indeed be fully attributed to variations in the beam column gap.

Table 7.15 summarizes the key metrics for each release load. Notably, displacement amplification under dynamic conditions can reach nearly three times the static value, while force amplification remains below two, consistent with Eurocode assumptions for dynamic amplification factor for the force.

Test	Release time t_r (ms)	Natural period T (ms)	Maximum dynamic vertical displacement (mm)	Damping ratio ξ	Maximum dynamic vertical reaction (kN)	Displacement- based DIF_Δ	Force-based DIF_p
T-11.5%-3	3	141	7.0	2.7%	0.89	2.93	1.74
T-12.7%-2	2	118	8.0	3.6%	0.78	2.62	1.72
T-13.4%-1	8	151	10.4	5.0%	1.00	3.06	1.98
T-24.6%-1	16	188	20.4	5.0%	1.90	2.11	1.79
T-48.5%-2	–	235	37.5	4.6%	3.62	1.61	1.45
T-61.2%-3	3	269	53.9	5.0%	–	1.77	1.42
T-73.2%-4	25	Collapsed					
				Average:	2.35	1.68	

Figure 7.15: Summary of sudden column removal test results (Cheng et al., 2021).

7.5. Conclusions from test data

Based on the experimental results presented in this study, several key conclusions can be drawn that are relevant for both the development and evaluation of the numerical models. The most important observations derived from the test data are summarized below:

- The connection exhibits a maximum bending moment capacity of approximately 2.25 kNm and typically fails at a rotation of about $4.5°$.
- At full scale, the connection demonstrates a comparable strength to the scaled down specimen but exhibits significantly greater ductility.
- The push down test initially shows predominantly elastic behavior up to a load of approximately 3 kN. Beyond this point, yielding begins, with a pronounced increase in plastic deformation after point A. Point B appears to indicate the onset of failure, while point C corresponds to the ultimate failure of the aluminum flange.
- The axial force responses exhibit substantial variation in the predicted compressive arching behavior, but they consistently indicate the development of catenary action;
- The ultimate release load leading to failure corresponds to 73.2% of the applied load, which is approximately 3 kN.
- The pseudo static response obtained from the static test curves closely matches the discrete data points measured during the drop down tests.
- The moment rotation response from the drop down tests indicates that both the static and dynamic configurations exhibit higher stiffness than the push down tests, with the dynamic tests showing the highest stiffness.
- The test configuration used for the drop down experiments exhibits compressive arching in the axial force response for both the static and dynamic loading cases.

8
Validation models

This chapter presents the developed models and compares their results with the experimental outcomes introduced in Chapter 7. In this chapter, the results are summarized concisely, while the detailed conclusions and explanations for the observed differences between the models and the tests are provided in Chapter 9.

The chapter begins with a discussion of the general modeling requirements, outlining the common assumptions and input parameters applied across most models. Following this, the connection test models are introduced and their results are examined. Subsequently, the push down models are presented with their outcomes. Finally, the drop down scenario is modeled, and the corresponding results are discussed.

8.1. General modeling requirements

The finite element (FE) and analytical models developed for each validation test share most of their input parameters. These general inputs are required to ensure consistency across the different modeling approaches. For the analytical model, the following inputs are necessary:

- Connection model as described in Section 6.2;
- Beam cross-section dimensions;
- Bending elastic modulus of timber, taken from the validation test (Lyu et al., 2020).

All of these values are also provided as input in the Python code for this method, which is included in the appendix C.

For the FE model, the connections are modeled as described in the following section. In addition, a slight modification is required for the column material model to ensure that the axes are oriented correctly. In LS-DYNA, the shell formulation always interprets the second material axis (not the x-direction) as the y-direction. Consequently, the y- and z-directions must be interchanged: every z is replaced by y, and every y is replaced by z. This transformation produces a new constitutive matrix, and the corresponding strength parameters are updated accordingly. Also for the FE model the other material models shown in chapter 5 are used.

Connections in FE model

This section provides a comprehensive description of the beam to column connection modeled in the finite element (FE) framework. The middle connection of the push down test is selected as a representative case because it incorporates all critical components. The connection consists of the following sub assemblies:

- Flange to beam connection with dowels;
- Beam to end plate connection through friction elements;
- Beam to column connection through friction surfaces;
- End plate to end plate connection with bolts;
- End plate to column connection with bolts;
- End plate to column connection through friction surfaces.

The dowel connection between the aluminum flange and the timber beam is illustrated in Figure 8.1. The timber beam is shown in light blue, the aluminum flange in yellow, and the dowels in purple and

the NRB's are shown in red. In figure 8.1 the flange has been moved out of the beam but in the actual models the NRB's are straight so the flange would be inside the beam as in the actual test.

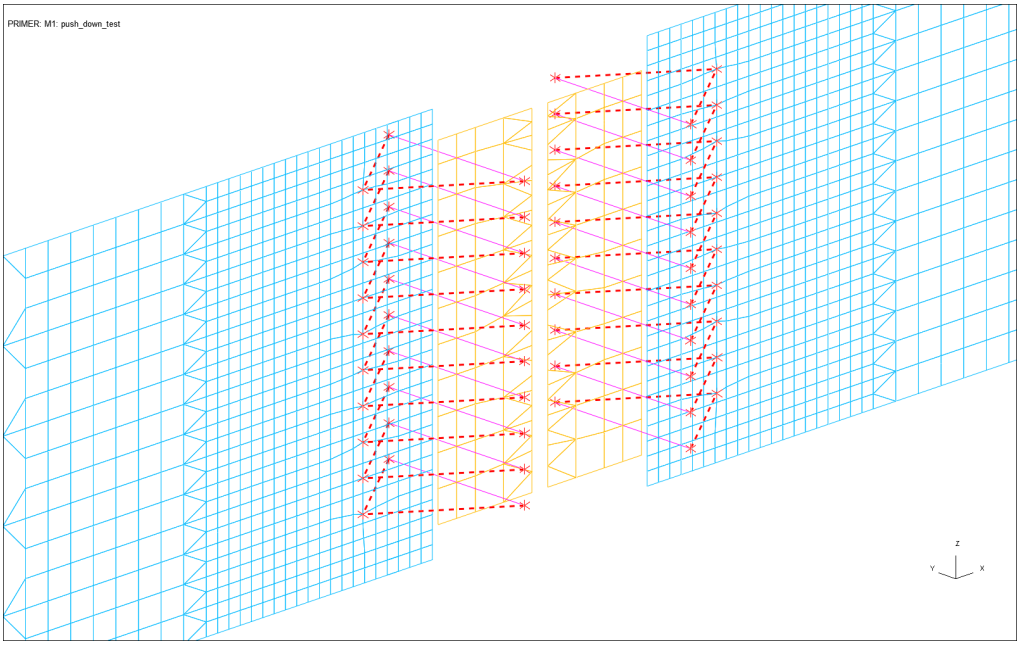

Figure 8.1: Flange to beam connection with dowels in LS-DYNA.

Dowels are modeled as discrete beam elements with master nodes tied to the flange and slave nodes connected to the beam via NRBs. This approach minimizes unrealistic.
Each dowel requires three force–displacement curves corresponding to the local axes:

- **X-direction:** Along the grain of the timber, calculated using Equation (5.11) and parameters from Eurocode and validation studies.
- **Y-direction:** Assigned a high stiffness ($1 \times 10^9\,\mathrm{N/m}$) to prevent excessive out of plane displacement.
- **Z-direction:** Similar to the X-direction but perpendicular to the grain, resulting in lower stiffness and ultimate strength.

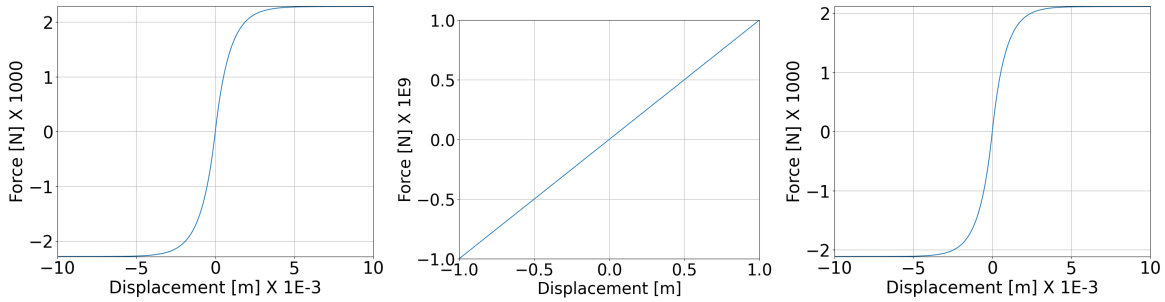

(a) X-direction curve. **(b)** Y-direction curve. **(c)** Z-direction curve.

Figure 8.2: Force–displacement curves for dowels.

The beam to end plate interface is modeled using friction elements, as shown in Figure 8.3. The beam is depicted in blue, the end plates in gray, and the friction elements in red. And four NRB's in green that tranlate the not conforming meshes in the top and bottom points.

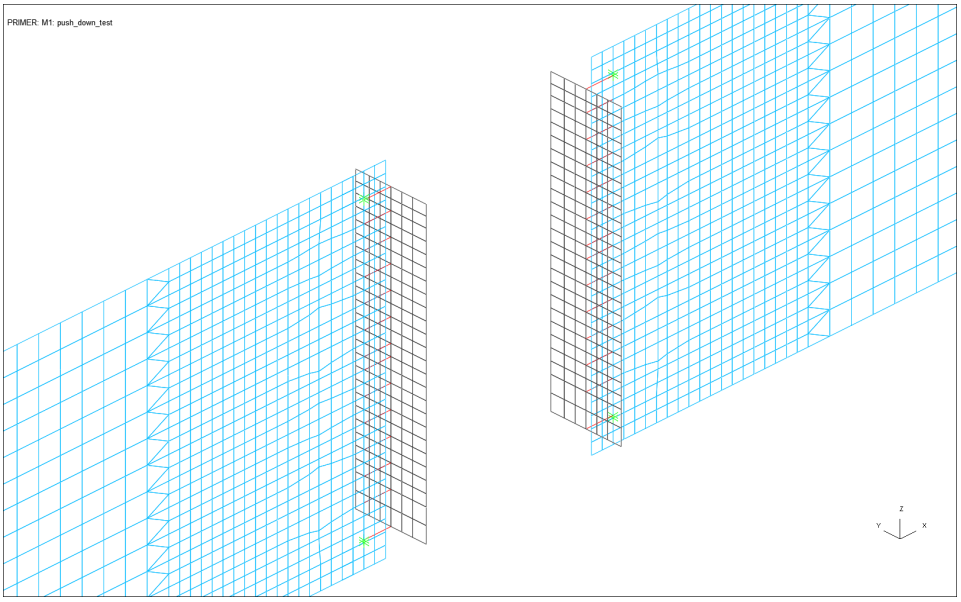

Figure 8.3: Beam to end plate connection using friction elements.

Friction elements operate in local coordinate systems. For the left element, the local negative z-axis aligns with the global negative x-direction; for the right element, it aligns with the global positive z-direction. Penalty stiffness is set to $1 \times 10^9\,\mathrm{N/m}$, slightly lower than surrounding components to avoid excessive point forces.

Figure 8.4 illustrates the contact connection between the beam and column on the left side of the column this contact is shown without its NRB's with the dark blue shells being the dummy shells belonging to the column and the dark gray shells being the dummy shells belonging to the beam.

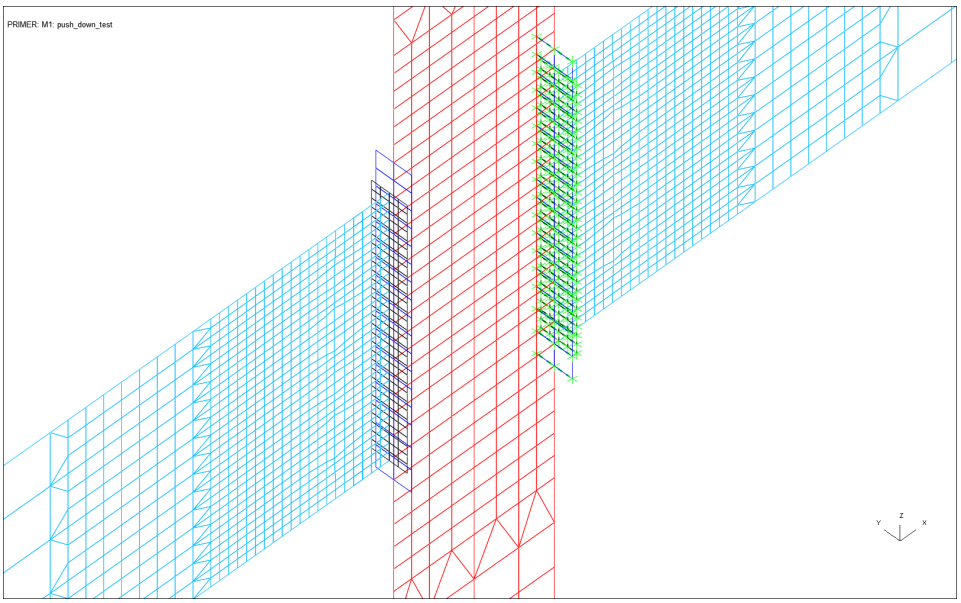

Figure 8.4: Beam to column connection with friction surfaces.

The column side surface acts as the master contact surface, while the beam side surface is the slave. this contact also simulates sliding with friction.

Bolts connecting the end plates are modeled as discrete beam elements, divided into two segments to

avoid excessive element length. These segments are in dark blue for the left side and green for right side the nodes that they are connected on are their master nodes and the nodes on the end plate are their slave nodes this can al be seen in Figure 8.5.

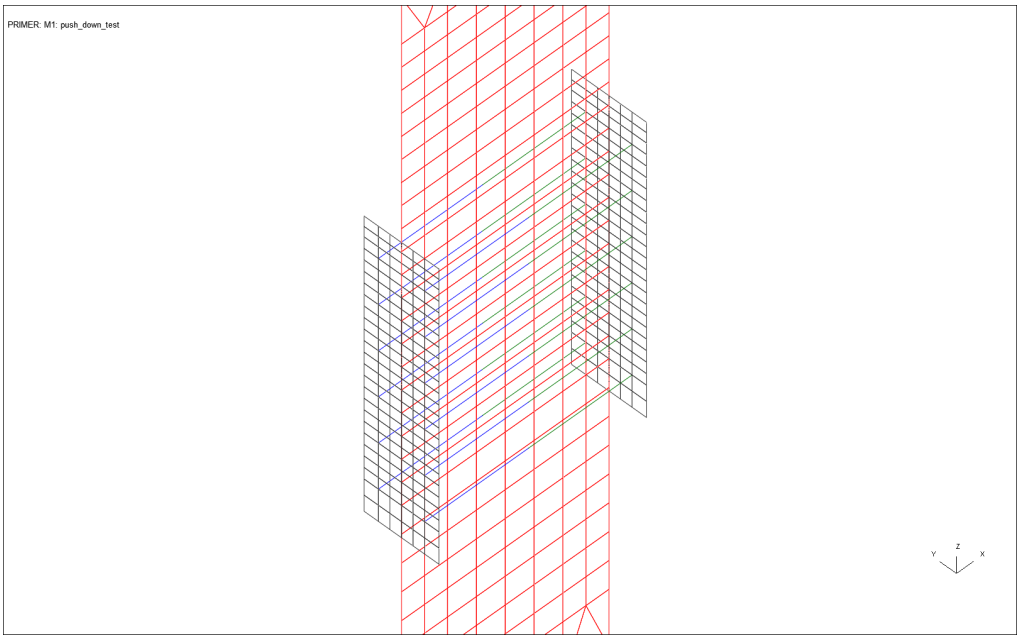

Figure 8.5: End plate to end plate connection with bolts.

The nonlinear behavior of bolts is defined through three directional curves:

- **X-direction:** Axial tension–compression curve based on Eurocode stiffness and capacity. The curve shown below for this behavior is for the right bolt because it slave nodes moves in postive x direction the beam becomes in tension and vise versa. so for the other bolt pointing the other way this curve will inverted;
- **Y-direction:** Arbitrary stiffness of $1 \times 10^9\,\mathrm{N/m}$ to prevent excessive out of plane displacement.
- **Z-direction:** Assigned $1 \times 10^5\,\mathrm{N/m}$ to avoid unrealistic displacement in this direction but low enough to not add much more strength.

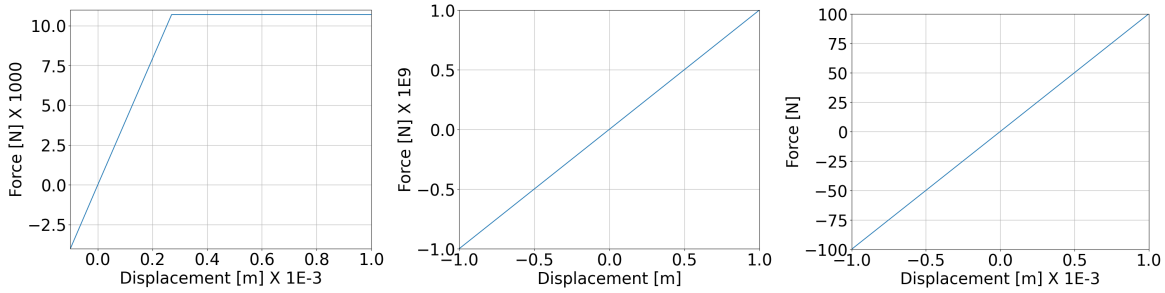

(a) X-direction curve. **(b)** Y-direction curve. **(c)** Z-direction curve.

Figure 8.6: Force–displacement curves for bolts.

Figure 8.6 shows the implemented curves. Subfigure (a) represents the axial tension–compression behavior, characterized by high compression stiffness and tensile capacity derived from Eurocode calculations. The ultimate tensile force corresponds to the bearing failure of the aluminum plate. Secondary directions are modeled with arbitrary stiffness values to ensure stability without introducing unrealistic flexibility.

Because these bolts do not directly connect to the column, they do not transmit shear forces. Shear transfer is achieved through a separate element, shown in Figure 8.7.

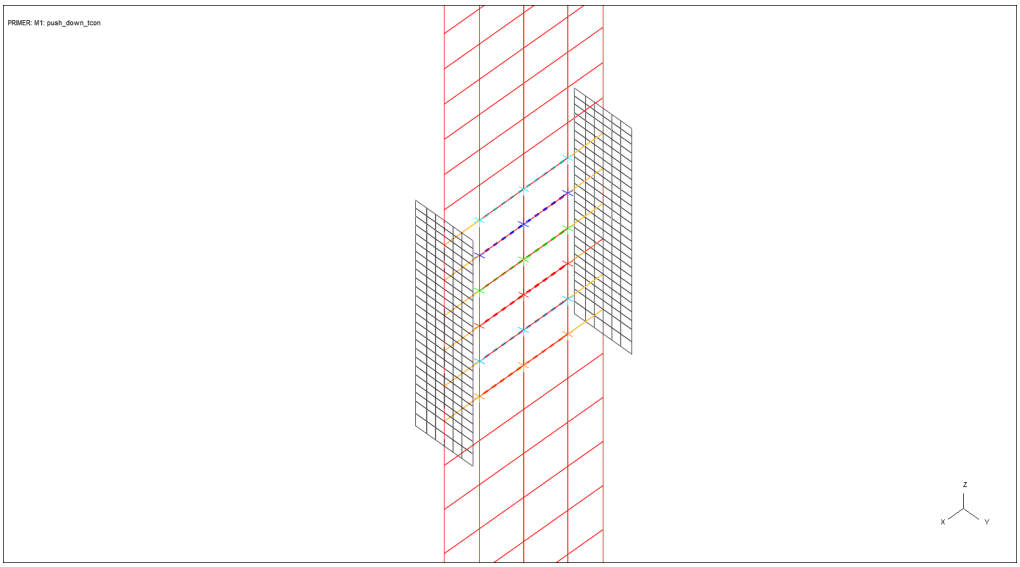

Figure 8.7: End plate to column connection with bolts.

This connection primarily facilitates force transfer in the global z-direction, representing shear behavior. The corresponding force–displacement curves for the shear bolt element are presented in Figure 8.8.

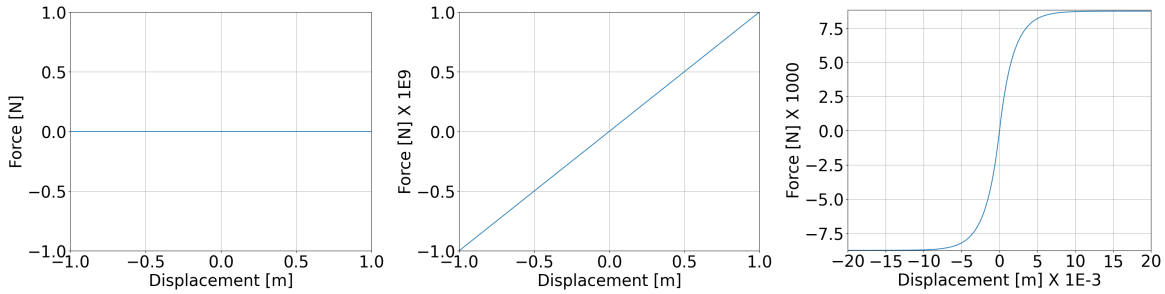

(a) X-direction curve. **(b)** Y-direction curve. **(c)** Z-direction curve.

Figure 8.8: Force–displacement curves for shear bolts.

As shown in Figure 8.8, the shear response is defined using the same formulation applied to dowels (see Equation (5.11)), but scaled to reflect the higher capacity of steel bolts. The stiffness is governed by bolt diameter and timber embedment strength, calculated in accordance with Eurocode EN 1995-1-1. For the y-direction, the same arbitrary stiffness ($1 \times 10^9\,\mathrm{N/m}$) is applied to prevent instability. In the x-direction, no force is assigned to avoid introducing unintended axial tension in the timber, as axial forces are already accounted for by the primary bolt elements.

The last component of the connection is similar to the frictional interface shown in Figure 8.4, but here the end plate is connected to a single dummy element rather than two, as its orientation already aligns with the required contact configuration.

This concludes the detailed description of the LS-DYNA connection model. With these components defined, the FE model is fully prepared for replicating the experimental tests described in Chapter 7.

8.2. Moment connection test models

This chapter presents the validation models for the moment connection tests. First, the analytical method is introduced using a bilinear moment rotation curve, which is then compared to the actual experimental curve. Subsequently, the LS-DYNA FE model setup is described, followed by the results.

8.2.1. Analytical method connection model

In the analytical method, the connection is modeled using a bilinear moment–rotation relationship. The connection stiffness and plastic moment are calculated based on the layout described in Chapter 6. Due to the test setup (see Chapter 7), the beam is fully connected to the column without a gap. Therefore, only the second layout is considered here.

- Rotational stiffness: $k_{r,2} = 0.60\ \mathrm{kNm/deg}$
- Plastic moment capacity: $M_{\mathrm{pl}} = 1.34\ \mathrm{kNm}$

These parameters are derived in Appendix B and together define the bilinear moment rotation relationship shown in Figure 8.9, alongside the actual test curve.

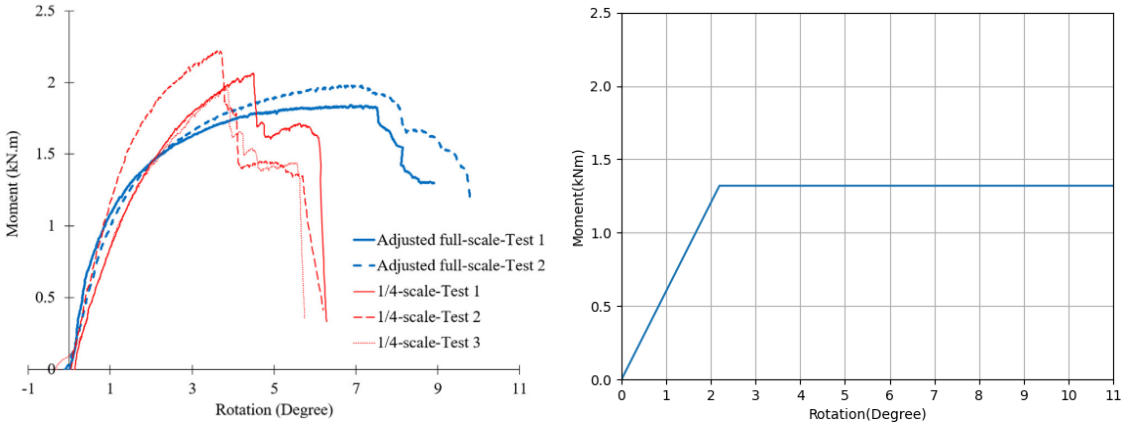

(a) Experimental moment–rotation curve Masaeli et al., 2020.

(b) Pseudo static bilinear moment–rotation curve.

Figure 8.9: Comparison of moment–rotation curves.

The analytical model exhibits lower stiffness and strength compared to the actual connection. The experimental connection has an average elastic stiffness of $0.98\ \mathrm{kNm/deg}$, while the model assumes $0.60\ \mathrm{kNm/deg}$, indicating a significant difference.

8.2.2. FE connection model

The FE model for the moment–rotation test is developed in LS-DYNA to replicate the experimental setup as accurately as possible. The objective is to validate the connection behavior under rotational loading and compare it with experimental results.

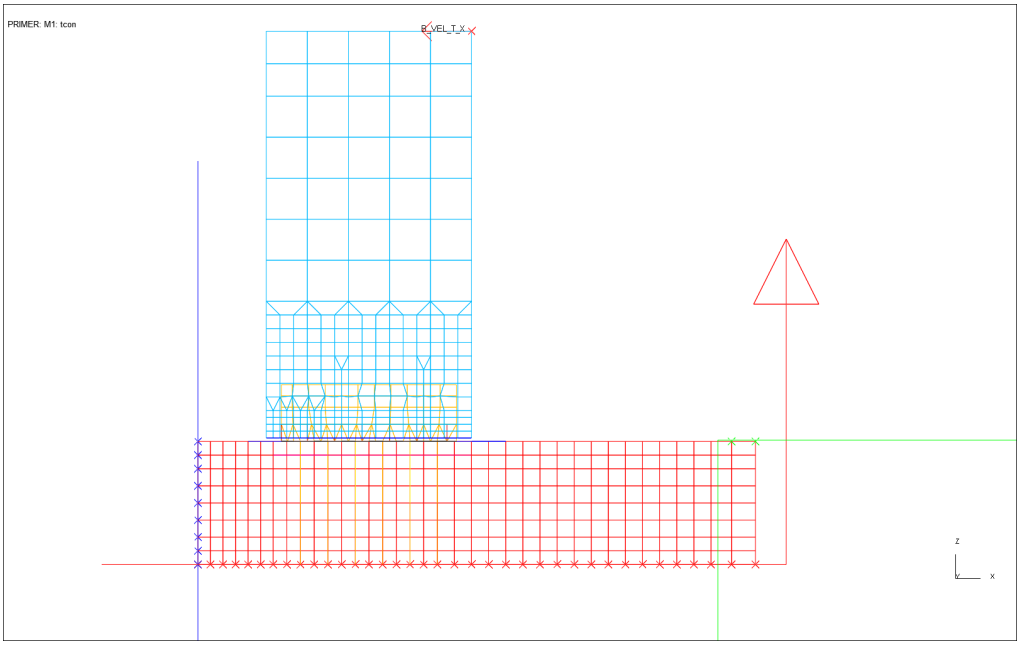

Figure 8.10: Moment–rotation test setup in LS-DYNA.

Figure 8.10 shows the LS-DYNA model configuration. Rigid walls are implemented to constrain node movement. The red wall at the base prevents downward displacement of the column's bottom nodes while allowing upward movement. Additional supports include a green rigid wall to prevent uplift and a blue wall for horizontal constraint. The displacement is applied at the top right corner of the beam, as indicated by the red arrow with the red cross being the node this displacement is on.

The displacement is applied with a smooth curve as shown in section 4.2. The inputs for this curve are:

- Start time = 0.3 s;
- Rise time = 0.5 s;
- End time = 3.5 s;
- Distance = 38 mm.

The finite element (FE) model computed a maximum velocity of approximately 14.1 mm/s for the prescribed velocity curve. As outlined in Section 4.2, the applied velocity forcing can be extracted. Additionally, the displacement of the node subjected to this velocity is recorded, enabling the calculation of both force and displacement histories. These data are subsequently transformed into a moment rotation curve, as illustrated in Figure 8.11.

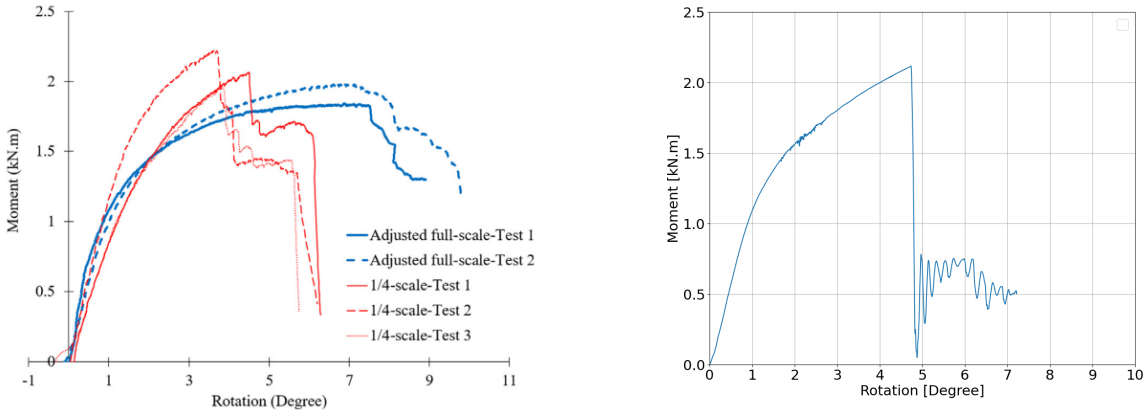

(a) Experimental moment–rotation curve Masaeli et al., 2020.

(b) Fe model moment–rotation curve.

Figure 8.11: Comparison of moment–rotation curves.

Figure 8.11 compares the moment rotation response of the FE model with the experimental results. The model demonstrates a comparable stiffness and reaches a similar peak moment. The average elastic stiffness observed in the experiments is 0.98 kNm/deg, whereas the FE model achieves 1.41 kNm/deg, which is slightly higher than the stiffness reported in the second test by (Masaeli et al., 2020) (1.22 kNm/deg). In terms of capacity, the experiments indicate an average peak moment of 2.11 kNm, with a maximum of 2.25 kNm, while the FE model reaches 2.12 kNm. This represents a very good estimate of the maximum strength, lying close to the average experimental value.

One notable difference is that the FE model exhibits a single step failure, whereas the tests show a two step failure process, culminating in rupture of the aluminum plate. Despite this difference in failure mechanism, the FE model correctly predicts the governing failure mode: fracture of the aluminum T-stub, as illustrated in Figure 8.12.

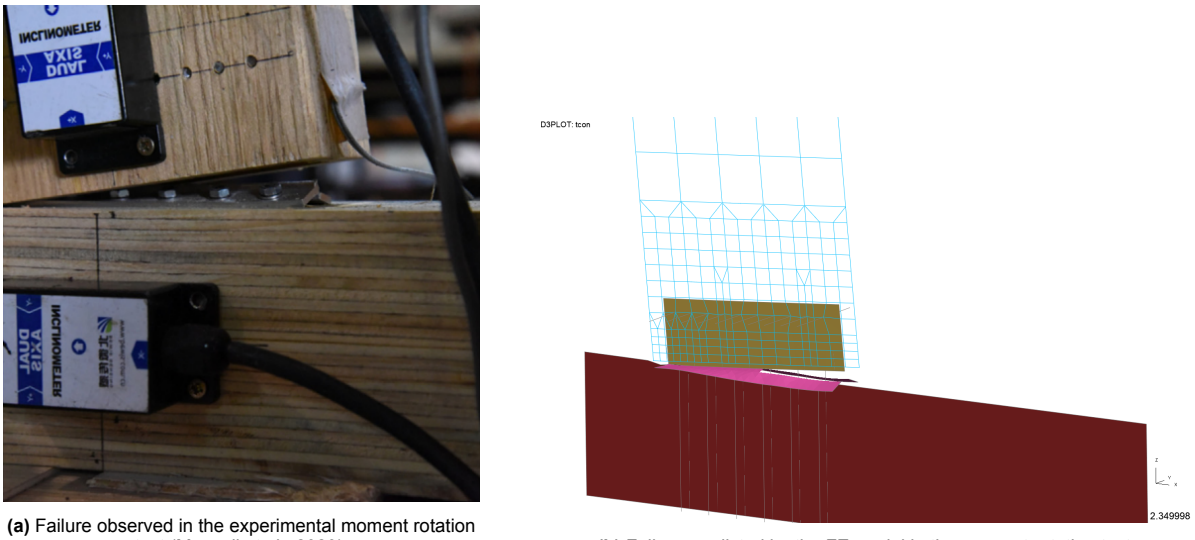

(a) Failure observed in the experimental moment rotation test (Masaeli et al., 2020).

(b) Failure predicted by the FE model in the moment rotation test.

Figure 8.12: Comparison of failure modes in the moment rotation test.

As illustrated in Figure 8.12, the LS-DYNA simulation also exhibits failure in the aluminum T-stub, consistent with the experimental observations. In both cases, comparable bending behavior is observed, confirming that the FE model captures the governing failure mechanism observed in the tests.

8.3. Push down test models

This chapter replicates the push down test described in Chapter 7 using both the analytical method and the finite element (FE) method. The section begins with a description of the model setups, followed by presentation of the corresponding results.

8.3.1. Analytical push down model

The analytical method described in Chapter 4 is refined here to better represent the experimental setup. The following enhancements are introduced:

- Implementation of two distinct rotational stiffness values in the moment rotation behavior;
- Introduction of a gap between the beam and column;
- Addition of rotational springs to simulate the connections at the supports and the central connection.

Separate models are developed with and without the gap in order to evaluate whether this modification improves the accuracy of the analytical predictions. For the closing of the gap, the deflection required to rotate the structure sufficiently to close a 1 mm gap is calculated.

In all of these models, the axial force is considered during the different stages of behavior. This force is non zero in the compressive arching and catenary stages, and in the final catenary stage it remains constant at F_p. For the bending moment, values are computed for each stage until the final catenary stage, where the moment should reduce to zero.

The modifications to the method described in Section 4.1 are explained here. First, for the introduction of the gap: before the gap is closed, a rotational stiffness k_{r1} is used for the springs, which is the only change in the elastic stage. In the compressive arching stage, Equation 4.21 is modified such that v_c is replaced by the deflection required to close the gap. If this deflection is smaller than the value for r_p, the catenary transient stage begins. Once the gap is closed, the deflection values for all stage transitions must be recalculated using the higher rotational stiffness of the springs. This ensures continuity in the response curve without artificial jumps. The adjustment is achieved by introducing a force difference between the stiffness values and the corresponding displacement difference. These differences are then incorporated into the equations by adding them to the displacement and subtracting them from the forces. The implementation of these refinements is also shown in the code used to generate the graphs, as presented in the appendix C

The addition of rotational springs are implemented by modifying the boundary conditions defined in Section 4.1.1. The updated boundary conditions are expressed as:

$$M_1(x=0) = k_{r,i}\,\theta_1(x=0) \tag{8.1}$$

$$M_2(x=L) = -k_{r,i}\,\theta_2(x=L) \tag{8.2}$$

$$M_1\left(x=\tfrac{L}{2}\right) + 2k_{r,i}\,\theta_1\left(x=\tfrac{L}{2}\right) = M_2\left(x=\tfrac{L}{2}\right) \tag{8.3}$$

The factor of two in the central connection accounts for the doubled rotation due to symmetry, allowing a single stiffness value to be applied consistently across all connections. These modifications enable recalculation of the elastic moment, which is then used to determine the transition to the plastic and catenary stages.

The rotational stiffness values used in the model, derived from Chapter 6, are:

- $k_{r1} = 0.32\ \mathrm{kNm/deg}$
- $k_{r2} = 0.60\ \mathrm{kNm/deg}$

These values are fully worked out in the appendix. Using these parameters, the push down curves are generated and compared to the experimental results.

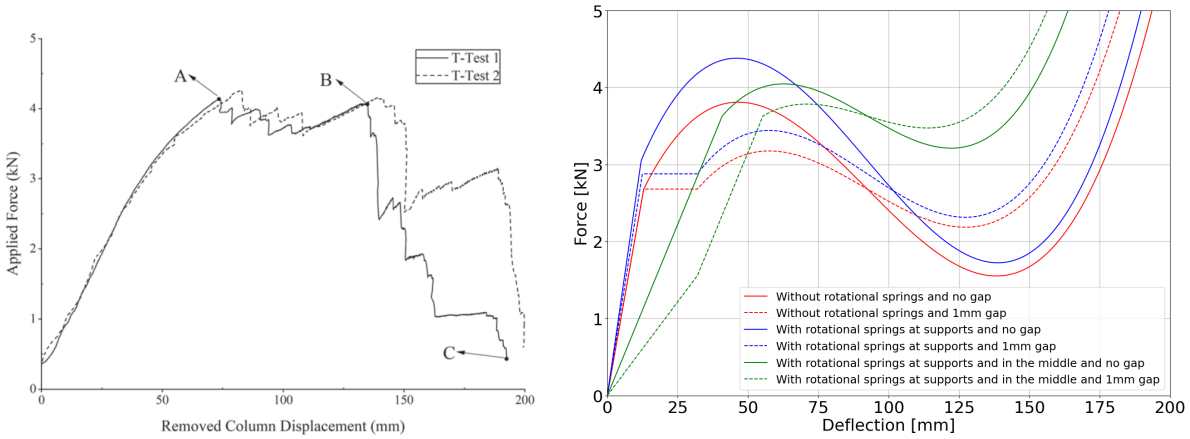

(a) Experimental push down curve (Lyu et al., 2020).

(b) Analytical push down curve.

Figure 8.13: Comparison of push down curves.

The elastic stiffness values for the different model configurations are summarized below. These values are obtained by calculating the slope of the force–displacement response between 0 and 40 mm of displacement.

- Experimental model: $0.068\ \mathrm{kN/mm}$ (Lyu et al., 2020);
- Without rotational springs and no gap: $0.207\ \mathrm{kN/mm}$;
- Without rotational springs and 1 mm gap: $0.207\ \mathrm{kN/mm}$;
- With rotational springs at supports and no gap: $0.255\ \mathrm{kN/mm}$;
- With rotational springs at supports and 1 mm gap: $0.231\ \mathrm{kN/mm}$;
- With rotational springs at all connections and no gap: $0.089\ \mathrm{kN/mm}$;
- With rotational springs at all connections and 1 mm gap: $0.066\ \mathrm{kN/mm}$.

As shown in Figure 8.13, introducing rotational springs at the central connection significantly reduces stiffness, resulting in behavior that more closely resembles the experimental test. However, the analytical model still underestimates the experimental response, even when compressive arching is included. Beyond approximately 125 mm of displacement, the analytical model diverges from the test results because no failure mechanism is incorporated. Instead, the model continues to gain strength. For the configuration with rotational springs at every connection, the load does not exceed 4 kN before 140 mm of displacement, and the initial point of the curve starts at zero, whereas the experimental curve does not.

It can be observed that the rotational springs assigned to each connection provide a reasonable approximation of the experimental behavior. The calculated stiffness values are close to those measured in the tests with a gap present. However, the comparison shows that the modeled stiffness is still insufficient to fully reproduce the experimental curve. This indicates that the connections require greater initial strength, rather than reduced stiffness, in order to capture the observed response more accurately.

Maximum force values are not directly compared, since the pseudo static response does not simulate failure but instead emphasizes yielding behavior. However, both axial force and moment can be calculated. Although simplified, these values provide useful insight into potential shortcomings of the model and highlight which components may be overloaded. The axial force is calculated for the compressive arching and catenary transient stages using Equation 4.15. The resulting graph is presented here for each model, alongside the experimental test results, to facilitate comparison.

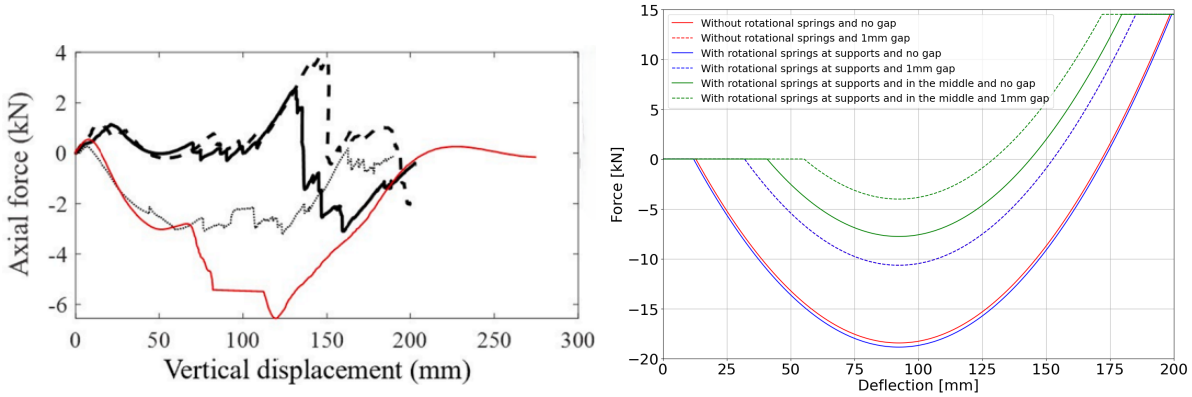

(a) Experimental axial force curve (Cheng et al., 2021). **(b)** Analytical axial force curve.

Figure 8.14: Comparison of axial force curves.

Figure 8.14 (a) contains four curves, of which three are relevant for the present discussion: the two black curves and the grey curve. The red curve corresponds to the dynamic case and is therefore not considered here. The remaining three curves represent quasi static axial force responses: the black curves originate from the push down test study, while the grey curve is taken from the drop down study, in which the specimen was also tested under quasi static loading prior to the dynamic release.

As discussed in Section 7.4, the available experimental datasets exhibit notable differences and therefore imply different expectations regarding the development of compressive arching. Nevertheless, even the quasi static test that does display compressive arching (gray curve) remains below the numerical predictions, including those of the best performing model.

For the numerical results, it is observed that models incorporating rotational springs at all connections provide a noticeably improved prediction once the axial force begins to increase again, which occurs at approximately $125\,\mathrm{mm}$ deflection. In this range, the rate of axial force increase is comparable between the experiments and these models, with significant divergence occurring primarily after failure initiates in the tests.

It can also be observed that compressive arching is absent, or at least minimal, in the experimental test, since the axial force never drops below zero. The next step in the analysis is the moment rotation graph, which can be calculated for each stage of behavior and is set to zero in the final catenary stage.

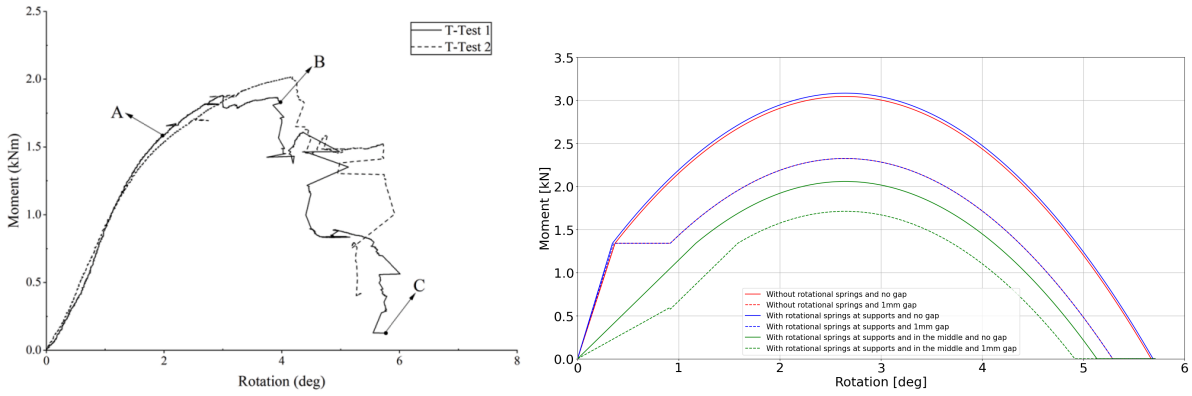

(a) Experimental moment rotation curve (Lyu et al., 2020). **(b)** Analytical moment rotation curve.

Figure 8.15: Comparison of moment rotation curves.

As shown in Figure 8.15, only the configurations with rotational springs exhibit realistic stiffness values, avoiding excessive rigidity and remaining below the actual maximum moment capacity of the connec-

tion, which is approximately 2.11 kNm. Nevertheless, the elastic stiffness predicted for these rotational setups is still lower than observed experimentally. This highlights that the analytical methods capture certain aspects of the early stage behavior but fail to reproduce the later stages of the test. The absence of a failure mechanism in the model means that, instead of brittle fracture as seen in the experiment, the response is simplified by reducing the moment through a plastic interaction diagram. As a result, the analytical model does not fully replicate the abrupt failure observed in the physical test.

8.3.2. Push down FE model

For this model, the entire portal frame was constructed in LS-DYNA and subjected to a displacement controlled push down analysis up to a deflection of 2000 mm. The setup is illustrated in Figure 8.16.

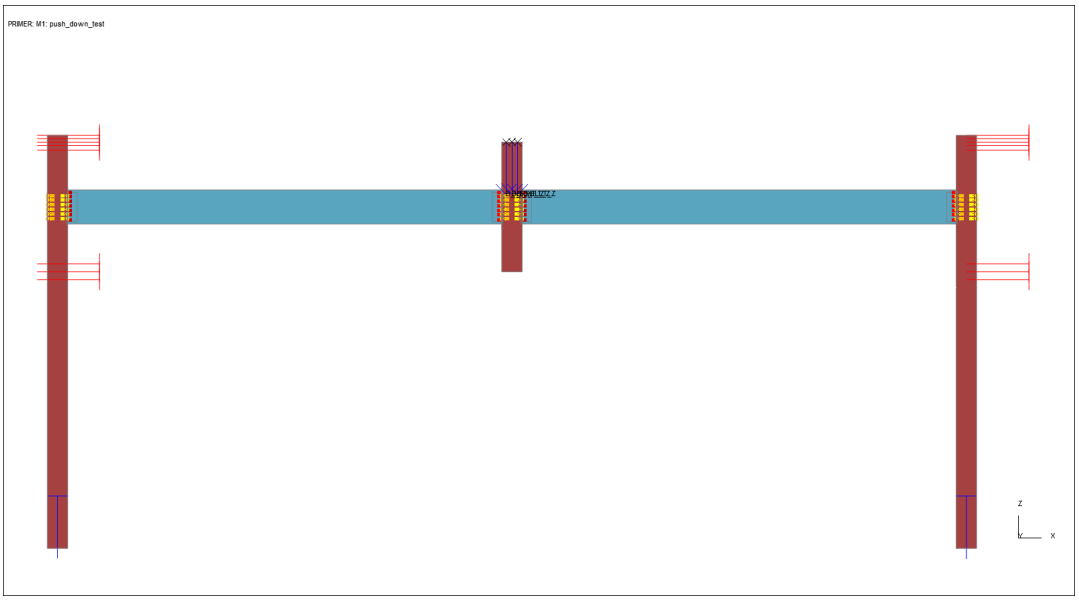

Figure 8.16: Push down test setup in LS-DYNA.

As shown in Figure 8.16, the model incorporates the connection details described previously. The applied boundary conditions are indicated in the figure: red markers represent constraints in the global x-direction, while blue markers denote constraints in the z-direction. Each beam includes a single z-constraint to allow rotation about this axis, whereas multiple x-constraints are applied to better replicate the experimental setup, which uses surface supports.

Reaction forces from these constraints are recorded to construct the force–deflection curve, the axial force–deflection curve, and the moment–rotation curve. For the moment calculation, the forces at the top and bottom x-constraints are extracted and multiplied by the lever arm of $285\,\mathrm{mm}$. The rotation is computed from the vertical displacement of the middle node of the central column using:

$$\theta = \arctan\left(\frac{v_{mid}}{2000}\right),$$

where v_{mid} is the measured displacement and 2000 mm is the beam length. These outputs form the basis for the subsequent comparison of numerical and experimental results, starting with the force–deflection curve.

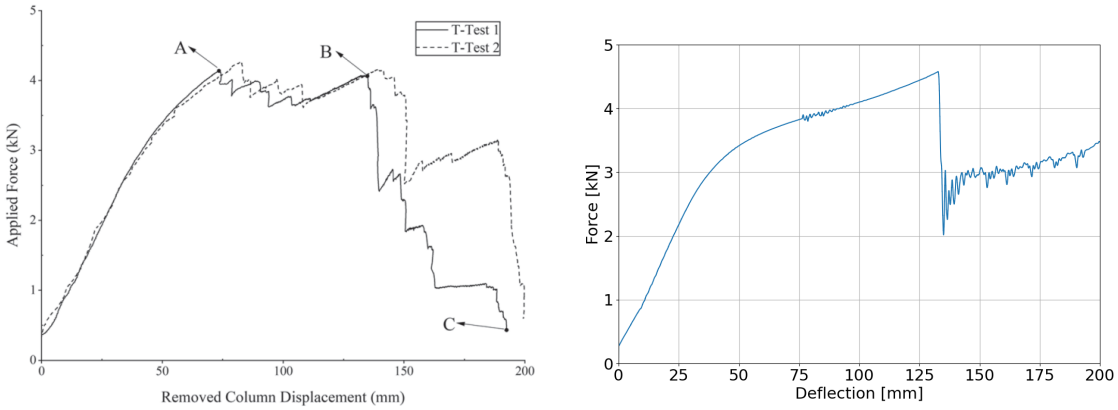

(a) Experimental push down curve (Lyu et al., 2020).

(b) Push down curve from LS-DYNA model.

Figure 8.17: Comparison of validation test and FE model.

As shown in Figure 8.17, the elastic behavior of the FE model aligns closely with the experimental results. However, at point A in the test curve, the model begins to deviate significantly. This corresponds to the onset of plasticity in the column and in the aluminum flanges and plate connections. In the model, plasticity develops more gradually, leading to a faster loss of stiffness. After this stage, the curve rises toward point B. While the experimental curve exhibits distinct drops in strength, the model response remains smoother, resulting in slightly higher values. Since the precise source of the drop in the experimental curve is uncertain, this behavior is difficult to replicate numerically. At point B, the system stiffness decreases sharply, likely due to significant plasticity in the aluminum. In the FE model, this reduction in stiffness is treated as failure, which explains the pronounced strength drop near point B. Beyond this stage, the model response increases again, resembling the second test reported in the validation study, though it does not fully drop within the displacement range considered. If extended further, the model curve would likely continue to decrease.

The elastic stiffness is captured very well: $0.068\ \mathrm{kN/mm}$ in the experiment compared to $0.070\ \mathrm{kN/mm}$ in the model. In terms of maximum force, the model performs less accurately. Test 2 reports a peak of $4.26\ \mathrm{kN}$, whereas the model reaches $4.58\ \mathrm{kN}$. This increase occurs deep in the plastic range, making it less relevant for the intended purpose of the test

Overall, the force–deflection response shows reasonably good agreement between the model and the experimental results. To further assess the model performance, additional comparisons are presented, starting with the axial force response. This response is obtained from the horizontal load cells and represents the horizontal force developed in the system. The axial force response for the push down test is presented below.

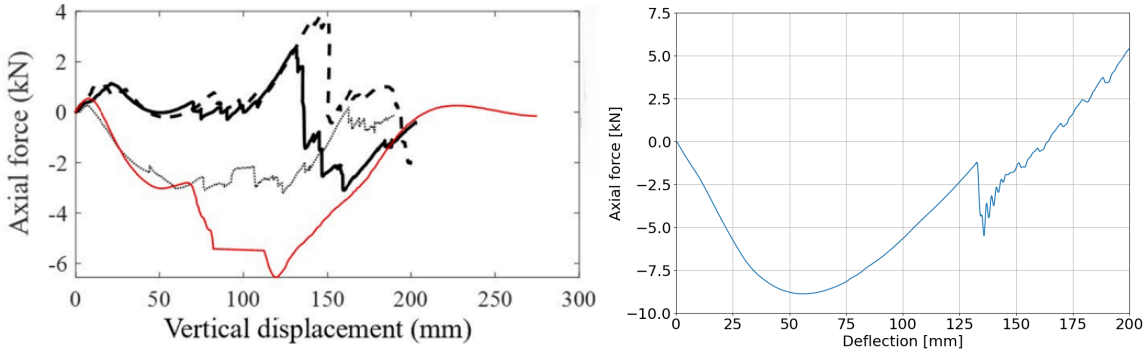

(a) Experimental axial force curve (Cheng et al., 2021).

(b) Axial force curve from the LS-DYNA model.

Figure 8.18: Comparison of axial force from the push down test.

Figure 8.18 (a) contains four curves, of which three are relevant for the present discussion: the two black curves and the grey curve. The remaining three curves represent quasi static axial force responses: the black curves originate from the push down test study, while the grey curve is taken from the drop down study, in which the specimen was also tested under quasi static loading prior to the dynamic release.

It can be observed that the model again substantially overpredicts the development of compressive arching. Relative to the individual quasi static test results, the agreement is closest to the grey curve; however, the predicted compression remains overly pronounced, particularly in the initial phase of loading. In addition, the post arching increase in axial force is steeper in the model than in the experiments. This is most clearly seen by comparison with the black curves, which exhibit this trend earlier and therefore provide a clearer basis for evaluation. Between approximately $100\,\mathrm{mm}$ and $125\,\mathrm{mm}$ deflection, the tests show an axial force increase of about $2\,\mathrm{kN}$, whereas the model increases by roughly $3\,\mathrm{kN}$. This suggests that the model response is overly stiff, both in the compressive arching regime and in the subsequent catenary action development.

The next comparison between the numerical model and the experimental results focuses on the moment rotation response. Specifically, the moment rotation behavior of one of the side connections in the push down test is examined and presented below.

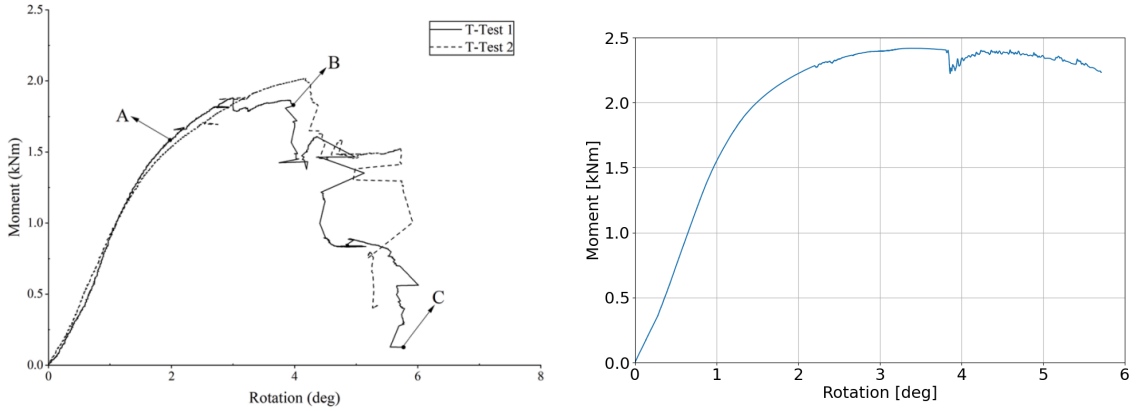

(a) Experimental moment rotation curve (Cheng et al., 2021).

(b) Moment rotation curve from the LS-DYNA model.

Figure 8.19: Comparison of moment rotation curves from the push down test.

As shown in Figure 8.19, the moment predicted by the FE model is both higher and stiffer than that observed in the experimental test. It also exceeds the stiffness reported in the moment test presented in Section 8.2. This discrepancy can be attributed to the assumption of infinitely stiff boundary conditions. In the model, the moment is calculated as the horizontal reaction force at the boundary multiplied by the distance to the mid span of the beam, consistent with the methodology used in (Cheng et al., 2021; Lyu et al., 2020).

As a result, failure in the model occurs at a lower rotation but later in terms of overall behavior, since the increased stiffness drives higher forces deeper into the plastic range. Following failure, the connection moment in the model decreases slightly before stabilizing around the same level as prior to failure. In contrast, the experimental test shows a sharp drop in moment, falling almost to zero before reaching $6°$ of rotation. This highlights the inability of the model to capture the brittle failure mechanism observed in the physical test.

8.4. Sudden column loss models

This section presents the modeling approaches used to simulate sudden column loss scenarios. Two methods are employed: the pseudo static energy approach and a dynamic FE model. The objective is to evaluate the structural response under instantaneous column removal and to compare the responses

to the drop down test from chapter 7.

8.4.1. Pseudo static energy model

In this section, push down curve developed earlier is used with the pseudo static energy approach described in Chapter 4 to evaluate the sudden column loss scenario.

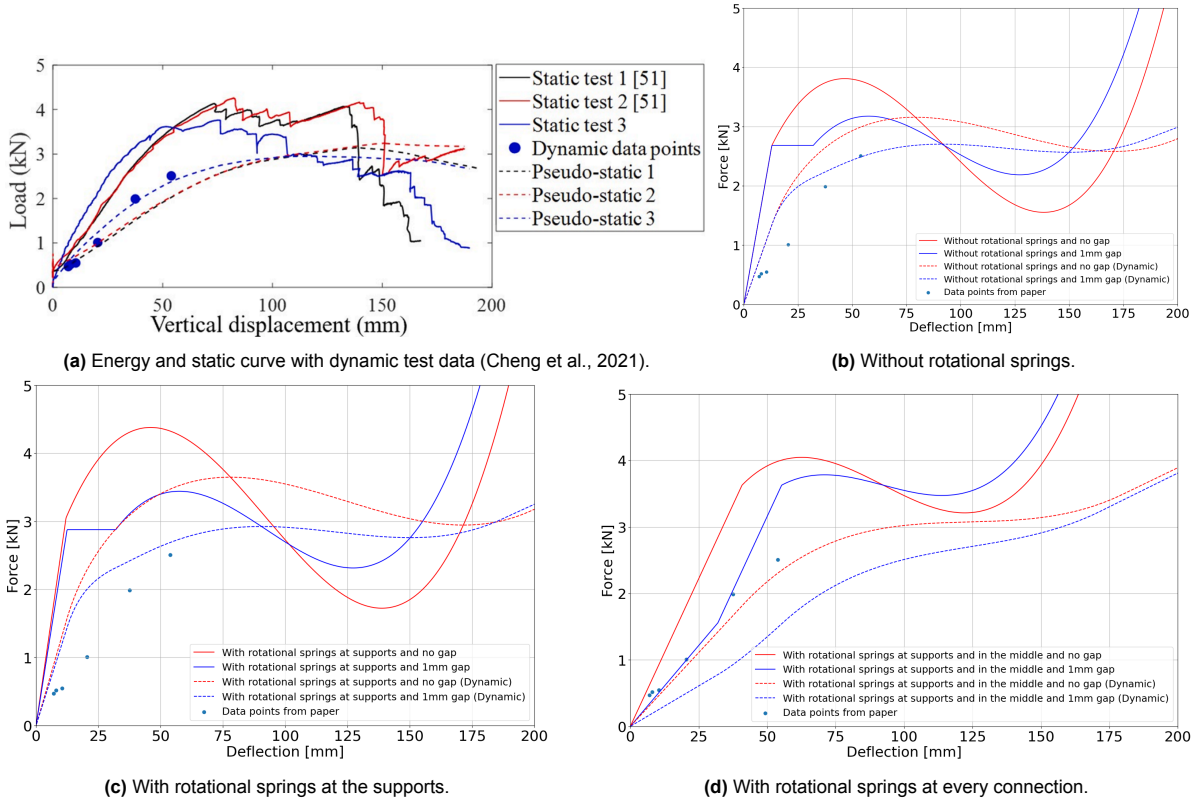

(a) Energy and static curve with dynamic test data (Cheng et al., 2021).

(b) Without rotational springs.

(c) With rotational springs at the supports.

(d) With rotational springs at every connection.

Figure 8.20: Comparison of energy method predictions and dynamic test results for sudden column loss.

As shown in Figure 8.20, all models except those with rotational springs at every connection overestimate the stiffness of the structure under dynamic loading. This behavior, particularly at the start of the curve, is consistent with observations from the push down test. Interestingly, even the stiffest configuration with rotational springs at every connection is not sufficiently stiff in the dynamic case, despite being overly stiff in the push down test.

When comparing the dynamic test curves with their pseudo static approximations, the models with rotational springs at every connection provide the closest match. However, they begin to deviate around $150\,\text{mm}$ of displacement. This divergence occurs because the analytical models do not incorporate explicit failure or damage mechanisms. Consequently, the model without a gap remains conservative but still provides a reasonably accurate representation of the structural behavior prior to failure.

The dynamic amplification factors (DAF) are shown in Figure 8.21, together with the experimental values reported in (Cheng et al., 2021) for the force response.

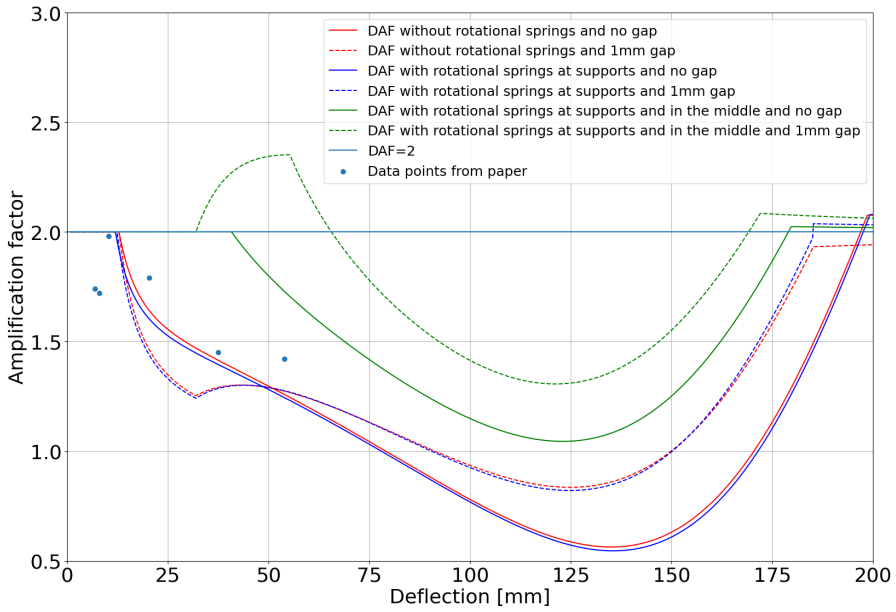

Figure 8.21: Comparison of dynamic amplification factors (DAF).

As illustrated in Figure 8.21, the models incorporating rotational springs are generally conservative, producing higher DAF values. Notably, only the configuration with a gap and rotational springs at every connection exceeds a DAF of 2 prior to the final catenary stage. Most models fall below this threshold as they enter the plastic range. Some configurations, particularly those without rotational springs at the central connection, yield values close to the experimental data but still fail to follow the overall trend of the measured points.

This comparison indicates that the adopted modeling approach is not well suited for evaluating the problem, as it consistently produces unrealistically high Dynamic Amplification Factor (DAF) values during the initial stages of loading. Such behavior does not accurately represent the dynamic response observed in the experimental results. The unrealistic nature of the predictions is further emphasized by the fact that four of the models yield DAF values below unity. This would imply that, for certain displacement levels, the dynamic response is smaller than the corresponding static response, which is physically questionable.

This behavior suggests that the models without rotational springs at the middle connection tend to overestimate the dynamic response. The underlying cause appears to be the pronounced compressive arching behavior predicted by these models, followed by a significant drop in the static load displacement curve. Both the magnitude of the compressive arching and the subsequent reduction in static resistance seem unrealistic when compared to experimental observations. As a result, the derived DAF values are strongly influenced by modeling artifacts rather than by a realistic representation of the structural response.

8.4.2. FE sudden column loss model

In this section, the sudden column loss scenario is modeled using the FE approach. The analysis is divided into two parts: first, the drop down model, and second, the pseudo static approach. The latter employs the push down curve from Section 8.3.2 to construct an energy curve, which is then used to approximate the dynamic response of the structure.

Drop down model

The drop down model is based on the same configuration described in Section 8.3.2, with only minor modifications introduced to simulate the release of load and the subsequent dropping of the column. The adapted setup is shown in Figure 8.22.

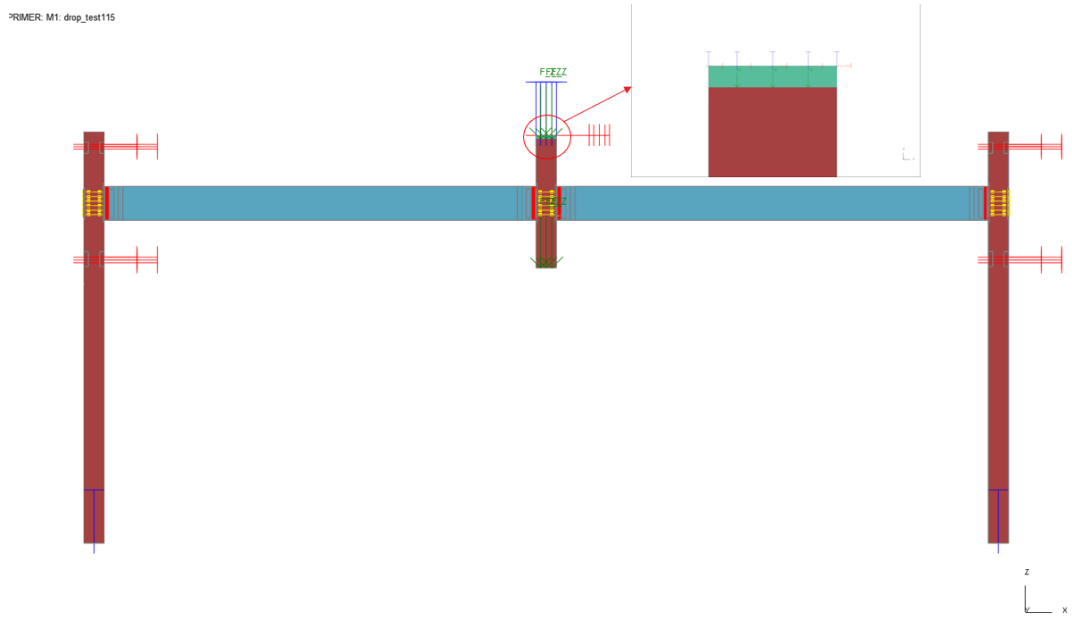

Figure 8.22: Drop down model test setup.

As illustrated in Figure 8.22, the drop down test setup in LS-DYNA is based on the same boundary conditions as the push down model. In this configuration, the middle column is subjected to nodal force loading applied to the top and bottom three central nodes, resulting in a total of six nodes being loaded. This approach distributes the load more evenly across the column while maintaining consistency over its entire cross-section.

Additionally, four extra shell elements are added to the top of the column and assigned to a separate part. This part is subsequently removed to simulate the dropping of the column. The added shells are constrained such that their top nodes cannot move in any direction. They are modeled as elastic shells with stiffness properties approximately equal to the timber stiffness in the grain direction, ensuring realistic representation of the structural response during the drop down simulation.

For the drop down simulation, a staged construction card is employed to remove parts from the analysis. This removal is achieved by gradually reducing their stiffness to a very low value over a specified duration, referred to as the ramp time. The ramp time is set to $10\,\text{ms}$, representing an instantaneous case, as it corresponds to approximately one tenth of the natural period obtained from the drop test (Cheng et al., 2021). As discussed in Section 4.3, this duration is assumed to be sufficiently short to approximate an instantaneous column removal. Thus, within $10\,\text{ms}$, the stiffness of the four shell elements at the top of the column is reduced to nearly zero, leaving only a negligible residual stiffness.

For the release loads, the values reported in the validation test are applied and divided by six, corresponding to the number of nodes on which the forces are distributed. The loading sequence begins with ramping up both nodal and gravity loads until $0.1\,\text{s}$. The structure then remains static until $0.49\,\text{s}$, after which the stiffness of the designated shell elements is reduced. At $0.5\,\text{s}$, the column drop is fully initiated. The displacement responses for the first three release loads are compared between the experimental test and the FE model, as shown in Figure 8.23.

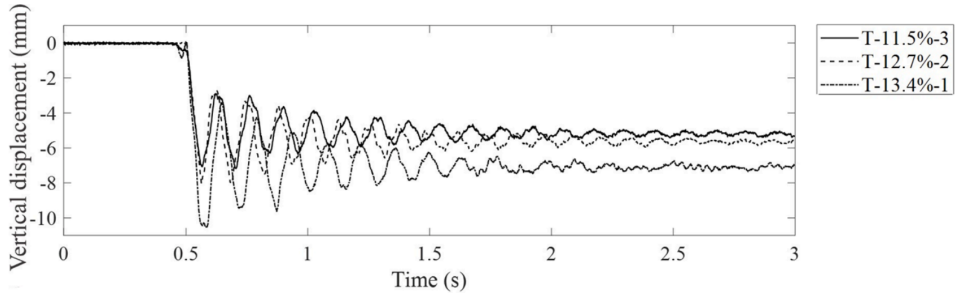

(a) Displacement over time curve from test (Cheng et al., 2021).

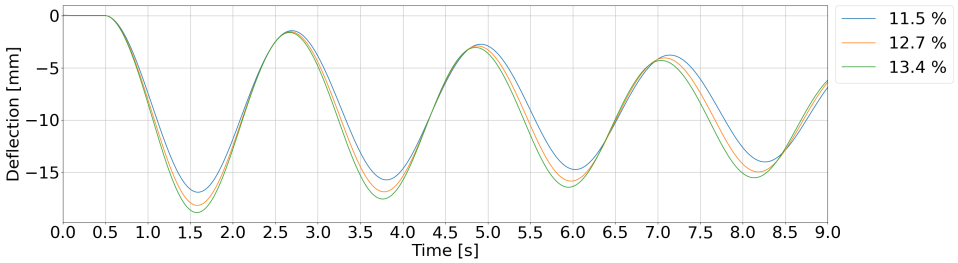

(b) Displacement over time curve from model.

Figure 8.23: Comparison of displacement over time for first three release loads.

As shown in Figure 8.23, noticeable differences exist between the numerical and experimental responses. As anticipated, the damping behavior of the system is not accurately reproduced by the model. However, damping is not the primary focus of this study, as the maximum displacement is the key parameter of interest. This is not only because damping behavior is difficult to predict reliably, but also because the structural response beyond the maximum displacement becomes highly uncertain. The maximum displacement corresponds to the most critical state in terms of rotation and deformation. Consequently, if a given release load in the model leads to this displacement, it provides a suitable basis for assessing the rotational and bending capacity of the structure.

The maximum displacement predicted by the model is considerably larger than that observed in the test. Furthermore, the model exhibits slower falling behavior: failure begins at approximately $0.5\,\mathrm{s}$, and the displacement of $7\,\mathrm{mm}$ is reached just before the $1\,\mathrm{s}$ mark. In contrast, the experimental test achieves the same displacement much earlier, at around $0.6\,\mathrm{s}$.

For the next four release load cases, including the 73.2% release load, both the test and the FE model exhibit failure. The corresponding displacement time curves are shown in Figure 8.24.

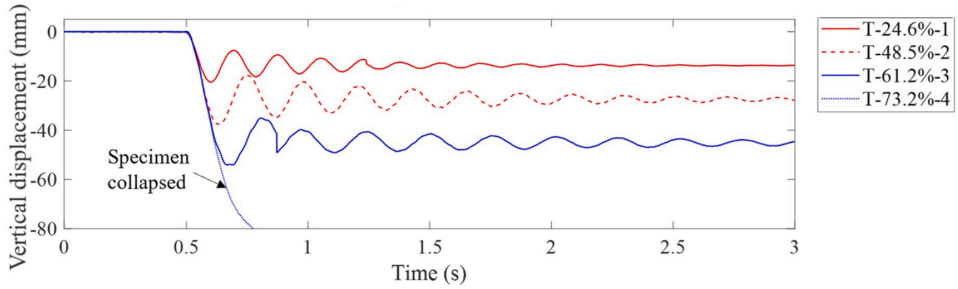

(a) Displacement over time curve from test (Cheng et al., 2021).

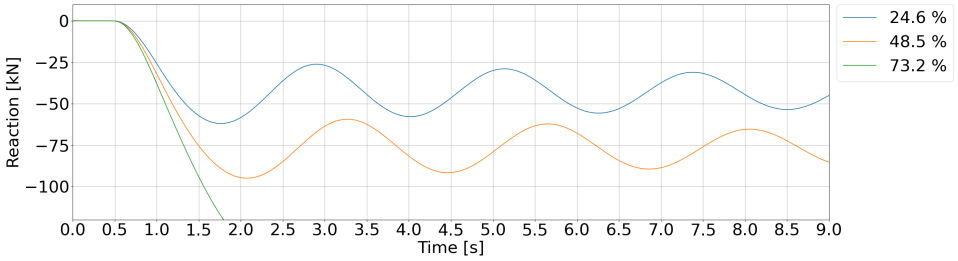

(b) Displacement over time curve from model.

Figure 8.24: Comparison of displacement over time for higher release loads, including 73.2% release load.

As shown in Figure 8.24, the same discrepancies observed earlier are present here: the FE model predicts significantly larger displacements, the damping behavior is not accurately represented, and the structure falls more slowly compared to the experimental test. To clarify these differences, Table 8.1 summarizes the maximum displacement values for each release load, comparing the test and model results. The differences are expressed both in absolute terms and as percentages relative to the test displacement.

Release load	Max displacement (test)	Max displacement (model)	Difference
11.5% (470 N)	7 mm	16.9 mm	9.9 mm (141%)
12.7% (520 N)	8 mm	18.1 mm	10.1 mm (126%)
13.4% (550 N)	10.4 mm	18.9 mm	8.5 mm (82%)
24.6% (1010 N)	20.4 mm	29.9 mm	9.5 mm (47%)
48.5% (1990 N)	37.5 mm	61.9 mm	24.4 mm (65%)
61.2% (2510 N)	53.9 mm	94.9 mm	41.0 mm (76%)

Table 8.1: Comparison of maximum displacement between tests and FE models for different release loads.

From Table 8.1, it can be observed that for the first four release load cases the differences in maximum displacement between the test and the FE model are relatively consistent. Although the model displacements remain too high overall, the incremental increase between successive low release load scenarios is reasonably close to the experimental trend. However, as the release loads approach the actual collapse load, the model displacements become significantly larger, and the discrepancy with the test results increases. In percentage terms, only the 24.6% release load shows a reasonably close agreement.

The reaction forces are now examined for the first three release loads, followed by the remaining four. The 61.2% release load is excluded, as the experimental test suffered a power fault during this specimen, leaving no available results. The comparison between the experimental and FE model reaction force responses for the first three release loads is shown in Figure 8.25.

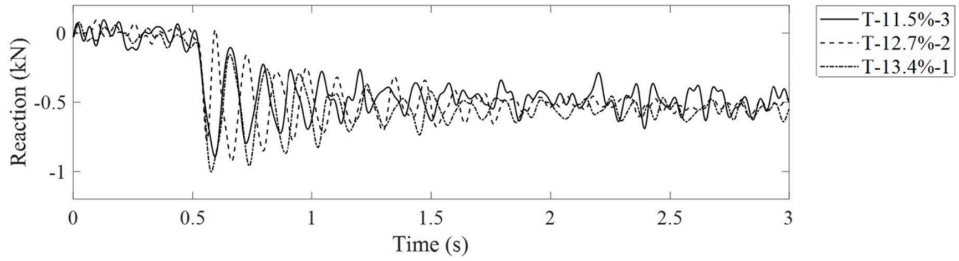

(a) Reaction force over time curve from test (Cheng et al., 2021).

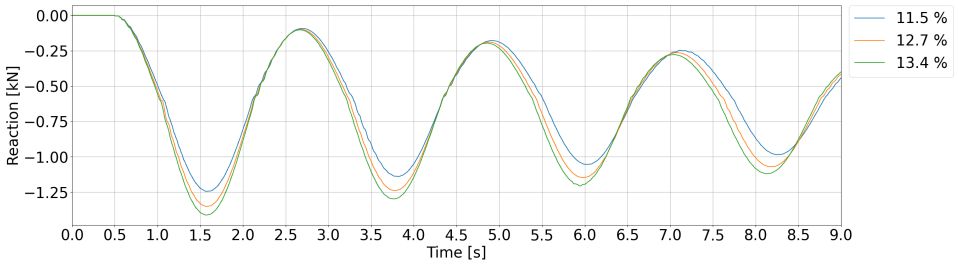

(b) Reaction force over time curve from model.

Figure 8.25: Comparison of reaction force over time for three different release loads.

As shown in Figure 8.25, the rate at which the reaction force reaches its maximum is slower in the FE model compared to the experimental test. However, the model results are much closer to the experimental forces than they were to the corresponding displacements, indicating a better agreement in terms of load prediction.

The next three release load cases are presented in Figure 8.26, excluding the 61.2% case due to the absence of experimental data caused by a power fault during testing.

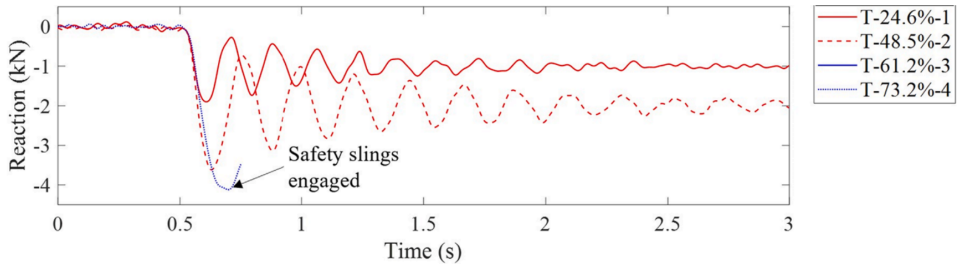

(a) Reaction force over time curve from test (Cheng et al., 2021).

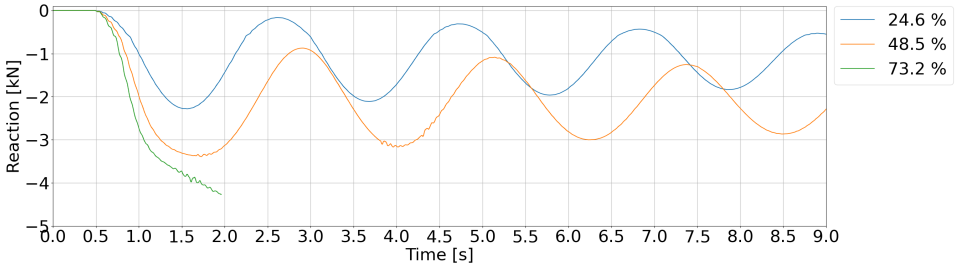

(b) Reaction force over time curve from model.

Figure 8.26: Comparison of reaction force over time for three different release loads (excluding 61.2% case).

As shown in Figure 8.26, the FE model again exhibits slower dropping behavior and lower damping compared to the experimental test. In terms of force prediction, the model underestimates the reaction force for the 48.5% release load, while it overestimates the reaction force for the 24.6% release load. To provide a clearer comparison, Table 8.2 summarizes the maximum reaction forces obtained from both

the tests and the FE model, along with the absolute and relative differences.

Release load	Max reaction force (test)	Max reaction force (model)	Difference
11.5% (470 N)	0.89 kN	1.24 kN	0.35 kN (39%)
12.7% (520 N)	0.78 kN	1.35 kN	0.57 kN (73%)
13.4% (550 N)	1.00 kN	1.41 kN	0.40 kN (40%)
24.6% (1010 N)	1.90 kN	2.30 kN	0.40 kN (21%)
48.5% (1990 N)	3.62 kN	3.53 kN	0.09 kN (2%)

Table 8.2: Comparison of maximum reaction forces between tests and FE models for different release loads.

From Table 8.2, it can already be observed that the reaction force values are much closer to the experimental results than the displacement values, although they remain noticeably different except for the 48.5% release load. Furthermore, as the applied force increases, the model predictions tend to converge toward the test values, showing improved agreement at higher load levels.

For the collapsed release load case of 73.2%, additional comparisons are made by examining the bending moment rotation relationship and the axial force deflection response. These comparisons are presented as far as possible for both the experimental test and the FE model, as shown in Figure 8.27.

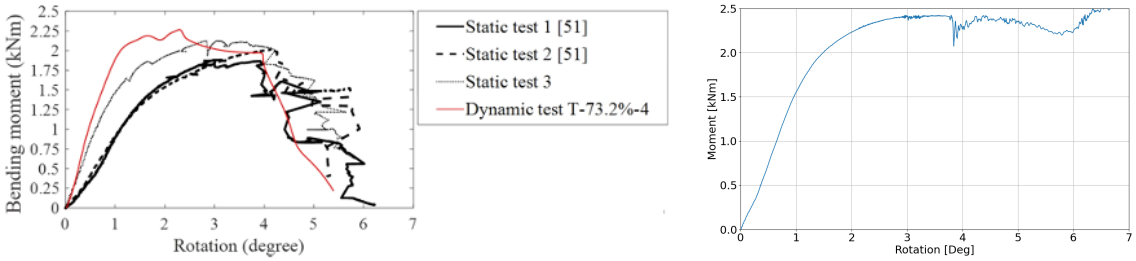

(a) Experimental moment rotation curve (Cheng et al., 2021).

(b) Model moment rotation curve.

Figure 8.27: Comparison of moment rotation curves for the 73.2% release load.

From Figure 8.27, it can be observed that the dynamic test curve is initially stiffer than the FE model curve. The model also reaches a higher peak moment than the experimental curve. However, after failure—indicated by the dip at approximately 4° in the model curve—the subsequent behavior diverges significantly from the test, failing to replicate the sharp reduction observed experimentally.

Next, the axial force response is examined for the case where the column is dropped. The comparison between the experimental test and the FE model is shown in Figure 8.28.

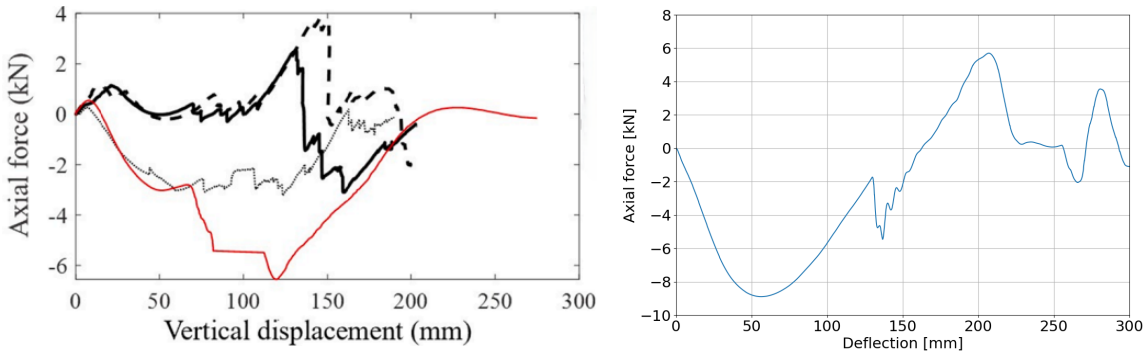

(a) Experimental axial force curve (Cheng et al., 2021).

(b) Model axial force curve.

Figure 8.28: Comparison of axial force curves for the 73.2% release load.

In Figure 8.18(a), only the red curve is relevant, as it represents the dynamic axial force response for the 73.2% release load. This loading level corresponds to the collapse case, which is evident from the response dropping to zero at the end when the safety system engages. The experimental curve shows the development of compressive arching, but its magnitude remains lower than predicted by the model. In addition, the evolution of compression differs: the test reaches its peak compressive force at approximately $60\,\mathrm{mm}$ deflection, whereas the model reaches its maximum compression at around $120\,\mathrm{mm}$.

An additional aspect of interest in these tests is the dynamic amplification of both force and displacement. For the force, a displacement is selected and the static force is divided by the dynamic force at that displacement; this factor is denoted as DIF_p. For the displacement, a force is selected and the static displacement is divided by the dynamic displacement at that force; this factor is denoted as DIF_Δ. The results of these calculations for both the tests and the FE model are presented in Table 8.3.

Release load	DIF_p (test)	DIF_p (model)	DIF_Δ (test)	DIF_Δ (model)
11.5% (470 N)	1.74	3.23	2.93	5.85
12.7% (520 N)	1.72	3.07	2.62	4.40
13.4% (550 N)	1.98	3.11	3.06	4.30
24.6% (1010 N)	1.79	2.52	2.11	2.80
48.5% (1990 N)	1.45	1.84	1.61	2.70
61.2% (2510 N)	1.42	1.58	1.77	3.20

Table 8.3: Dynamic amplification factors for force (DIF_p) and displacement (DIF_Δ) from tests and FE models.

From Table 8.3, it can again be observed that the displacement based amplification factors (DIF_Δ) are significantly larger than the experimental values. This overestimation also translates into the force amplification factors (DIF_p), particularly for the first few release load cases, which are considerably higher than the test results. However, the agreement improves as the applied load increases, with the force amplification factors showing closer correspondence to the experimental values at higher load levels.

Pseudo static push down model

As demonstrated previously, a push down analysis has been performed on the FE model. As described in Section 4.1.2, an alternative approach to obtaining the dynamic displacement for a given force is the energy method. This method can also be applied to the FE model to generate a curve that can be compared with the dynamic data points and the pseudo static curves obtained from the validation test (Cheng et al., 2021).

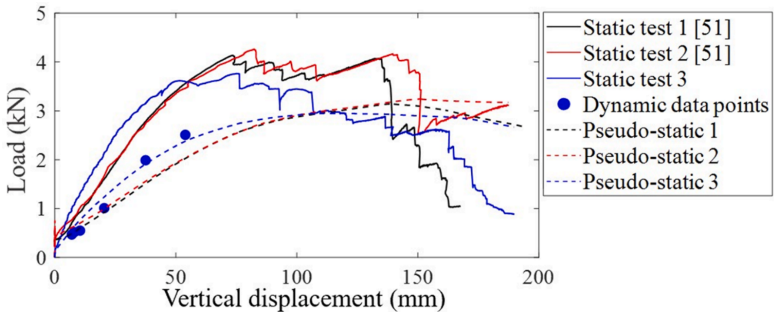

(a) Experimental force displacement curves (Cheng et al., 2021).

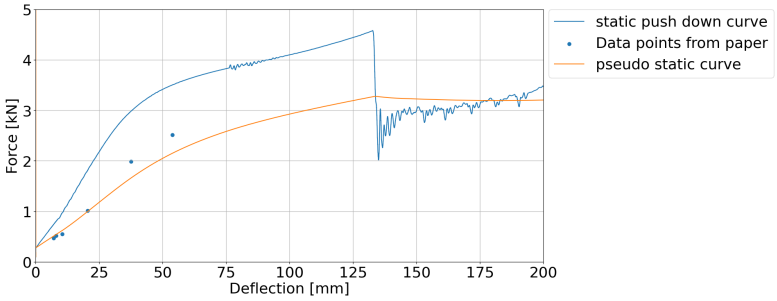

(b) FE push down model pseudo static curve.

Figure 8.29: Comparison of pseudo static curves and dynamic data points.

Figure 8.29 illustrates how the FE model curves align with the experimental data points and their relation to the pseudo static curves derived from the push down analysis. The comparison demonstrates that this approach provides a relatively good prediction of the dynamic force and displacement, as the data points lie close to the pseudo static curve.

This approach can again be translated into amplification factors. The curve shown in Figure 8.30 is obtained by dividing the static curve by the pseudo static curve, thereby providing, for each displacement, the amplification factor between the dynamic and static force. The experimental data points are taken from (Cheng et al., 2021).

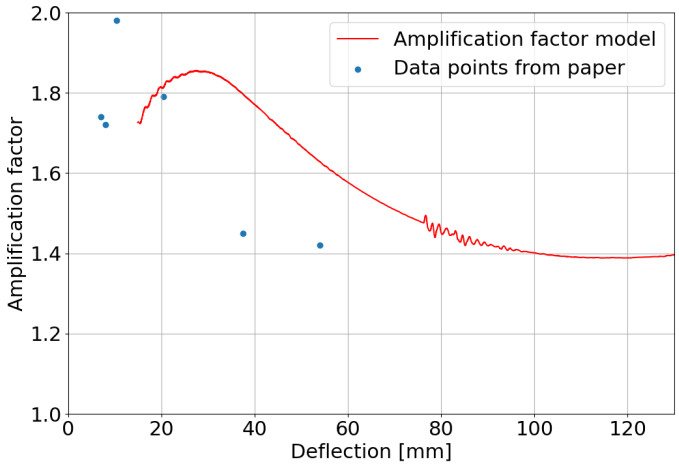

Figure 8.30: Comparison of force amplification factors using the pseudo static approach and experimental data.

From Figure 8.30, it can be observed that the pseudo static curve does not closely match the actual amplification factors. The method tends to overestimate, particularly at higher displacements. This suggests that the approach provides better predictions when the structure is more heavily loaded, but is less reliable at lower load levels.

Part III: Conclusions and recommendations

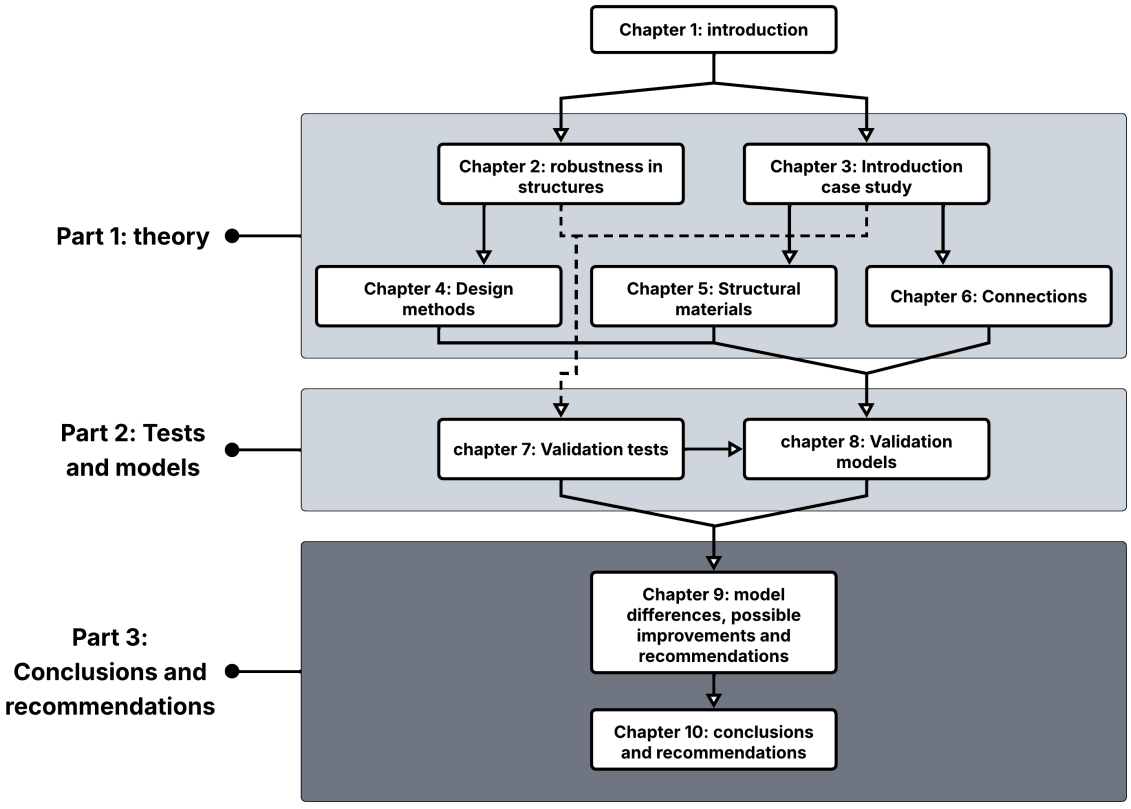

9 Model differences, possible improvements and recommendations

This chapter aims to explain the differences observed between the analytical, FE models and the experimental tests. First, these differences will be briefly summarized, as they have already been presented in detail in Chapter 8. The discussion will then focus on potential sources of these discrepancies, considering both modeling assumptions and experimental limitations.

Subsequently, possible improvements to the modeling methods are proposed, with the goal of providing solutions to reduce or eliminate the identified differences. Finally, general recommendations are made regarding the most effective ways to apply the FE model for structural analysis. This discussion is carried out systematically for each model and each corresponding test.

Finally, the comparison between the numerical models and the experimental results is discussed by assigning scores based on a set of relevant evaluation criteria. These criteria are first introduced and defined, including the sub-criteria from which they are composed. Subsequently, the scoring results are presented and discussed through a detailed assessment of each model's performance. The chapter concludes by demonstrating an improved analytical model, illustrating how incorporating insights from the FE model can lead to significant gains in accuracy without requiring substantial additional input.

9.1. Analytical method

In this section, the analytical method is examined in detail. The discussion begins with the moment calculation and its differences compared to the moment rotation test. Following this, the push down response and the pseudo static response are addressed together, as these two are closely related and best considered in a single section.

For each of these tests, the differences already presented in Chapter 8 are revisited and analyzed. Potential solutions to these discrepancies are then introduced, along with broader suggestions for improving the analytical models. Finally, a set of modeling recommendations is provided, highlighting strategies to keep the models straightforward to implement while also noting important considerations and limitations to be aware of when applying them.

9.1.1. Moment model

The comparison between the experimental test and the numerical model reveals several key discrepancies:

- The model exhibits lower stiffness than observed in the test;
- The model reaches a significantly lower maximum moment compared to the test;
- The model does not exhibit failure.

Quantitatively, the stiffness of the model is approximately 39% lower than that measured in the test. This represents a substantial deviation. As shown in the appendix, the dowels contribute very little stiffness, which strongly reduces the overall stiffness of the connection in the calculation. This suggests two possible explanations: either the dowels in reality provide greater stiffness than assumed, or the current modeling approach does not adequately represent the connection behavior.

Another potential source of discrepancy lies in the placement of the compressive spring. If the spring is positioned too low within the connection, most of the compressive force, particularly once the beam and column come into contact may be transferred directly through the beam–column interface rather

than through the spring. In such a case, the compressive spring should be positioned higher, and the rotation center adjusted accordingly. Both modifications would increase the calculated stiffness and bring the model closer to the experimental results.

A possible way to improve the model would be to test a larger number of connections, thereby demonstrating that such models can be applied under different setups or assumptions. Another approach could be to replace the current connection calculation with a moment–rotation curve derived using, for example, a finite element (FE) model this is shown at the end of this chapter. This would provide a more accurate representation of the connection behavior. Although such a model would be more complex to set up, it would significantly increase accuracy.

The next notable difference concerns the lower maximum moment in the model. This reduction is partly due to the fact that the model captures the yield moment rather than the maximum moment. However, the yield moment itself also appears lower than that observed in the structure. As shown in the appendix, this yield moment arises because the dowels govern the lowest moment capacity. This suggests that the calculated yield moment is underestimated and requires adjustment. One way to increase this value is to assume that more dowels at the top and bottom are fully yielding, two or even three instead of one which would raise the yield moment.

This discrepancy is further highlighted by the experimental results, where the dowels do not appear to be the critical failure component and do not yield as much as assumed in the calculation. Instead, failure seems to occur in the plate–flange connection. The calculation also indicates that the yield moment of the bolt bearing is approximately 1.63 kNm, which aligns more closely with the observed yield moment in the test, as the experimental curve begins to deviate significantly from its initial stiffness at this point. Therefore, it is recommended to carefully review the calculations to ensure that the correct component governs the yield moment. Additionally, when performing yield calculations for the dowels, it is advisable to increase the assumed number of dowels in yielding to better reflect the actual behavior.

The final difference is that the model does not fail. This is, of course, because no failure mechanism has been implemented in the model. A remedy would be to introduce such a mechanism by calculating the maximum rotation required for an element to fail. This is more straightforward when the cause of failure is known. For example, if dowels govern failure, the allowable horizontal displacement of a dowel must be assumed, which can be obtained from tests such as J. Cao et al., 2021. However, it is important to consider the specific failure mechanism, as bolts can fail in three different ways, some of which require axial restraint (e.g., a bolt nut), which dowels do not possess. For the plates, maximum strain values can be assumed for the aluminum plate and flange, as discussed in Chapter 5. For the bolts, a maximum tension test should be included to ensure proper representation of failure.

9.1.2. Push down model and pseudo static model

In this section, the main differences between the analytical model and the experimental results are first summarized. These differences are then examined in detail, with possible improvements and recommendations introduced. Finally, some general modeling suggestions are provided.

- The model starts at zero rather than at a higher point;
- The maximum force prior to failure is too low;
- The stiffness of the most accurate model is underestimated;
- The magnitude of the compressive arching force appears to be overestimated;
- No failure mechanism is included after a certain point.

In the experimental tests, the curves do not begin at zero. This is primarily due to the self weight of the structure, which is supported until the pressing begins. This introduces a reaction force in the supports. To remedy this, the self weight force can be subtracted from the applied load P, ensuring that the curve starts at a higher point. Additional adjustments in the moment calculation are required to maintain zero displacement at the start.

The lower maximum force observed in the model, particularly at the first peak (denoted as point a

in the test graph), can be attributed to the low starting point and the underestimated yield moment discussed earlier. Correcting these assumptions would raise the model response and reduce this discrepancy.

The stiffness of the model is also underestimated. This issue is consistent with the lower stiffness observed in the connection test model. Conversely, other stiffness values appear too high. The use of rotational springs at each connection seems to be a reasonable assumption, and introducing a small gap can help reduce stiffness to more realistic levels.

The predicted axial force is considerably higher than the experimental results, even compared to the test that exhibits compressive arching. Several factors may contribute to this discrepancy; however, the most plausible explanations are related to the modeling assumptions. First, the representation of compressive arching solely through connection spring behavior may be overly simplified and therefore unable to reproduce the physical mechanism realistically. Second, the translational spring stiffness may be overestimated. This is consistent with the observed response, in which the model shows excessively pronounced compressive arching in the early loading phase and a stiffer development of catenary action at larger deflections.

9.1.3. Conclusion and recommendations

As demonstrated in this chapter, there is considerable freedom in the development of these analytical models. This flexibility also highlights that much remains to be explored in order to improve their accuracy. The discussion above has shown several aspects that can be modified, yet it is likely that certain behaviors have been overlooked, since no single test can capture all possible structural responses. Consequently, modeling based on one test alone will never fully represent the complete range of behaviors. It is therefore strongly recommended that further research be conducted on these types of models, using different setups and test configurations.

One good practice identified in this research is the avoidance of introducing a gap between the column and the beam. Such a gap reduces the initial stiffness excessively and leads to unrealistic results. Eliminating this assumption improves the early stiffness and provides a more representative response.

Finally, the most critical aspect is the modeling of the connection. This thesis has shown that connection models play a decisive role in the overall structural response. More detailed investigation into the behavior of these connections is essential for developing more accurate models. Since the connection significantly influences the eventual performance of the system, future research should prioritize refining connection modeling approaches to ensure reliable and realistic predictions.

9.2. Finite element model

In this section, all observed differences, possible improvements, and recommendations for the finite element (FE) model are discussed. The analysis begins with the connection test and its corresponding model. Following this, the push down test model is examined. Finally, the drop down test and its model are presented, together with the pseudo static response derived from the push down model.

9.2.1. Connection model

As discussed in Section 8.2.2, two main differences are observed between the finite element (FE) model and the experimental test:

- Difference in stiffness;
- Difference in failure and failure propagation.

The stiffness of the FE model is 1.41 kNm/deg, whereas the highest measured test stiffness was 1.22 kNm/deg, with an average of 0.98 kNm/deg. This indicates a considerable difference, particularly in the initial stiffness. However, as shown in the graph in Section 8.2.2, the model and the test results converge at approximately 1° of rotation. The discrepancy in stiffness can be attributed to several factors:

- The experimental setup incorporated oversized holes for both bolts and dowels;

- The stiffness of the bolts is overestimated in the model;
- The stiffness of the dowels is overestimated in the model;
- The stiffness of the timber beam and column is overestimated in the model;
- The stiffness of the aluminum components is overestimated in the model.

The high stiffness of the bolts and dowels arises mainly from uncertainty regarding their behavior in timber. The dowels used are very small, with a diameter of only 4 mm, and there is limited test data available to determine their stiffness. Furthermore, there is little research on dowels and bolts tested in shear through laminated veneer lumber (LVL) timber, meaning their stiffness remains uncertain.

For the timber elements, uncertainty stems from the way the timber model was constructed. It relies heavily on fitting and rewriting values from various tests, which introduces variability. This is largely due to the scarcity of relevant LVL studies that provide more than just bending stiffness data for beams or columns.

Uncertainty in the aluminum model is most relevant at later stages. Validation tests (Cheng et al., 2021; Lyu et al., 2020; Masaeli et al., 2020) show that the plate and flange possess different stiffness values, which could also influence the overall stiffness of the model.

To further increase accuracy and usability of these models, the following actions are recommended:

- Conduct more studies on bolts and dowels through timber to better understand their stiffness;
- Investigate full scale setups, as more data is available for larger connectors;
- Perform additional LVL material tests in all relevant directions under tension and compression;
- Develop a more refined timber model specifically for LVL;
- Improve aluminum models by accounting for differences in stiffness between plate and flange.

The second major difference concerns failure behavior. The FE model fails abruptly in a single step, whereas the experimental test shows a two step failure process. Possible reasons for this discrepancy include:

- The plate and flange are modeled with identical behavior, despite having different mechanical properties;
- The aluminum tension curve does not soften at the end, whereas experimental data shows softening;
- The welded connection between the aluminum plate and flange is not accounted for in the model;
- No area thinning is included when strain levels are high.

The mechanical behaviors discussed earlier are again relevant here. For example, the aluminum tension curve could contribute to the difference: if the curve were to drop, stress would be released, producing a small initial failure step. In reality, failure occurs at the welded part of the T-section, which should be considered for greater accuracy. Additionally, the current model does not account for thinning at high strain levels. Such thinning could redistribute stresses, weaken the cross-section, and produce an initial drop before the final failure.

Although these differences are notable, the failure behavior of the FE model is still acceptable for the relevant case. After failure, the structural response becomes less significant, as the force decreases substantially and the behavior deteriorates. Therefore, while the modeled failure may not perfectly replicate the experimental two step process, it remains conservative and sufficiently accurate for representing the most critical aspects of the structure.

9.2.2. Push down model

This model performs very well in capturing the elastic portion of the structural response. However, deviations become increasingly apparent once plasticity sets in. Specifically, the model curve shows a gradual reduction in stiffness, whereas the experimental test graph exhibits stiffness loss in distinct

steps. All previously discussed connection related differences remain valid here, including uncertainties in material properties, dowel behavior, and bolt stiffness.

The gradual stiffness decrease may arise from several factors. One key difference appears to be that the top of the connection calculation loses stiffness more gradually before experiencing a sharp drop. Additionally, the way contacts are modeled could introduce extra stiffness. Since these contacts must be defined as very stiff, the inclusion of dummy elements may add stiffness to the system, potentially causing parts of the timber to yield earlier. This behavior increases model complexity and uncertainty, making it difficult to fully explain certain discrepancies. Nonetheless, it is clear that yielding in the columns and beams occurs too early in the model. The overestimation of maximum force may also be linked to this gradual stiffness loss, which diverts stress away from flange failure. As a result, more force is required to reach failure, and the connection itself appears overly strong.

Other plots reveal significantly more compressive arching in the model compared to the experimental test. This difference may stem from variations in gap size between the model and the test, although the actual gap dimensions are not documented, making this difficult to confirm. Stronger contact definitions could also introduce additional force transfer through the beam–column interface. Furthermore, the boundary conditions in the model are assumed to be infinitely stiff, whereas in the test the horizontal load cells are not perfectly rigid. This discrepancy can amplify forces in the model and may explain the stiffer response and higher maximum force observed in the moment–rotation curve.

To improve accuracy and reliability of these models, the following research directions are recommended:

- Apply all recommendations previously outlined for connection models;
- Investigate the influence of gap size on both model behavior and experimental results;
- Modify horizontal boundary conditions to represent less stiff supports;
- Validate that the contact definitions used in these models can accurately reproduce real contact behavior.

9.2.3. Column loss scenario models

For these models, the actual dynamic drop down model is first examined to identify the differences compared to the experimental results, followed by recommendations for improvement. Subsequently, the pseudo static approach is discussed to evaluate whether it provides a better measure than the drop down model. As the pseudo static approach is closely linked to the push down model, improvements made to the push down model are also applicable here. Finally, the suitability of the pseudo static approach for achieving the desired outcomes is assessed.

Drop down model

As shown previously, the drop down model exhibits several differences compared to the experimental results. These differences are summarized below:

- Falling time not equal to the experiment;
- Excessive displacement under all load levels;
- Larger displacement differences at lower loads compared to higher loads;
- Excessive reaction force under all release loads;
- Larger reaction force differences at lower loads compared to higher loads;
- Moment rotation curve is not stiff enough but is to high;
- Axial force indicates excessive compressive arching;
- DAF deviate significantly for both displacement and force;

The discrepancy in falling time compared to the experiment can arise from several factors. Since this behavior is primarily related to damping and time history algorithms, it lies outside the main scope of this thesis. Falling time is not a primary outcome of interest, but it may influence results. The following possible causes are identified, though they require further investigation:

- Frequency damping reduces the initial high acceleration at the onset of falling;
- Stiffness damping overly damps the structure, preventing sufficient velocity buildup and spreading the response over time;
- Excessive stiffness in contacts or penalty based connections dissipates kinetic energy, prolonging the velocity phase;
- Over constrained nodes alter velocity profiles by making components too stiff, e.g., stiffening the column and delaying acceleration;
- No rate affects for the material models this can influence the falling rate but also this influences the connection behavior in the dynamic test;
- Too slow removal rate of the element reduces initial acceleration;
- Numerical instabilities such as hourglassing may also influence the response.

The excessive displacement observed under all load levels can be attributed to several factors. First, the longer falling time in the simulation results in larger displacements, as the structure continues to fall for a longer duration. Second, the gap between the beam and the column may be too large, allowing excessive free fall. Additional reasons include insufficient connection stiffness in the dynamic case, as indicated by the comparison between the model and the experimental moment–rotation curve. This issue is less pronounced under higher loads, suggesting that stiffness at low loads and at the start of the simulation is underestimated relative to the test. This discrepancy may arise because certain materials exhibit higher modulus of elasticity under dynamic loading, which is not accounted for in the current model. Furthermore, rate effects of bolts and timber are neglected, even though these components are sensitive to strain rate behavior.

The excessive reaction force under all release loads may result from overly stiff boundary conditions, particularly the horizontal supports of the column. It may also stem from stiff contact elements, which exaggerate compressive arching in the axial force response. Additionally, the low initial stiffness of the connection and other elements at the start of the simulation contributes to this issue. Interestingly, this discrepancy diminishes as the model approaches failure. The final release load that does not result in collapse produces reaction forces that are nearly identical to those observed experimentally. This indicates that, once the system enters a regime of significant yielding, the energy balance is captured more accurately by the model and the influence of earlier stiffness related discrepancies is reduced. Alternatively, the initially overestimated stiffness may be offset by the yielding behavior at later stages, resulting in an improved overall energy balance. In either case, the results suggest that increased yielding leads to a more accurate prediction of both force and displacement responses.

The moment–rotation curve of the 73.2% release load model is insufficiently stiff in the elastic range. While the experimental test is significantly stiffer than its static counterpart, the model shows stiffness comparable to the static case. This difference can again be explained by the absence of rate effects in the material models.

The primary reason why the connection appears insufficiently stiff in the dynamic test, while being overly stiff in the static test, is the absence of strain rate effects in the material models used in the FE analysis. As a result, the numerical model does not capture the increase in stiffness that occurs in reality when transitioning from static to dynamic loading conditions. In practice, the materials exhibit strain rate sensitivity and generally respond with higher stiffness when subjected to faster loading rates.

The excessive compressive arching observed in the axial force response likely results from overly stiff column supports and an underestimated gap size. Experimental results show that axial force initially appears in tension before transitioning to compression, indicating that the gap is not immediately closed and remains significant. The model, however, assumes a smaller gap, leading to exaggerated compressive arching.

Finally, the calculated DAF values for both force and displacement deviate substantially from the experimental results. Even for the release load that produces the closest agreement (48.5%), the values

remain far off. This discrepancy arises primarily because both force and displacement predictions are inaccurate, compounding the error in DAF estimation.

Pseudo static model

It is recognized that the differences in this model are primarily caused by the push down model, which serves as its input. Consequently, most of the discrepancies can be traced back to that source. Nevertheless, the actual results show that when evaluating a certain force at a given deflection in the dynamic behavior, the model captures this relationship reasonably well. The response is slightly conservative at higher load levels, but this is not problematic. Overall, the model follows the pseudo static response from the experimental test quite closely.

Deviations begin to appear once failure occurs, but these are not particularly significant. By the time the structure reaches the displacement associated with this part of the curve, it has already failed under the applied load, meaning the later differences have limited practical relevance.

Regarding amplification points, the initial amplification factors are not well captured. This is mainly because both the pseudo static approach and push down model start at the same point, resulting in values close to one at the beginning. After some deflection, the amplification factors improve, though they remain somewhat higher than the experimental values. Despite this, the indication provided by the model is better than in the other tests, showing improved consistency in capturing the amplification behavior.

9.3. Model comparison

In this section, the analytical model, the finite element (FE) model, and the experimental tests are compared using a set of predefined criteria. The purpose of this comparison is to evaluate the relative performance of the different approaches, to identify their strengths and limitations, and to determine in which aspects one approach outperforms another. This assessment forms the basis for selecting and developing a more optimized modeling approach, which is presented at the end of this section. The models are evaluated using the following criteria:

- Model accuracy;
- Model setup complexity;
- Model simulation time;
- Model flexibility;
- Model costs.

Since these criteria are relatively broad, they are further explained and subdivided below.

Model accuracy

Model accuracy describes how well a model is able to reproduce the behavior observed in the experimental tests. To capture the different aspects of structural response, accuracy is divided into the following sub-criteria:

- Connection behavior: the ability of the model to represent the mechanical behavior of the connections, including stiffness, strength, and failure mechanisms;
- Push down behavior: the accuracy with which the model predicts the structural response under gradually applied vertical loading;
- Drop down behavior: the ability of the model to capture the dynamic response and load redistribution following sudden element removal or failure.

A model that closely follows the experimental response in these aspects receives a higher accuracy score.

Model setup complexity

Model setup complexity reflects the amount of time, effort, and expertise required to construct and prepare a model for analysis. This criterion is subdivided into:

- Required input: the quantity of input data needed to define the model;
- Complexity of input: the difficulty and time required to determine or calculate the necessary input parameters;
- Use complexity: the level of expertise needed to operate the modeling software and implement the model correctly or to setup the test.

Models that require less input, simpler parameter determination, and lower user expertise score higher on this criterion.

Model simulation time

Model simulation time refers to the computational time required to perform the analysis. or the time it takes to the test this will include all tests. Models with shorter simulation times are considered more efficient and therefore receive higher scores.

Model flexibility

Model flexibility describes how easily a model can be adapted to represent alternative structural configurations. This includes:

- Modifications to the overall structural system;
- Changes in connection type.

Models that allow such changes with minimal additional effort score higher in flexibility.

Model costs

Model costs account for the financial aspects associated with each approach. This includes software licensing and maintenance costs for numerical models, as well as material, equipment, and execution costs for experimental testing. Lower overall costs result in a higher score.

All criteria and their corresponding sub-criteria are summarized in Table 9.1. Each item is rated on a scale from 1 to 10, where 1 represents the poorest performance and 10 represents the best possible performance. For example, a score of 10 for model accuracy indicates that the model is able to reproduce the experimental behavior with a high level of precision across all evaluated aspects.

		Models		
Criteria	**Sub-criteria**	**Analytical**	**FE model**	**Tests**
Accuracy	Connection	3	8	10
	Push down	6	7	10
	Drop down	6	7	10
Setup complexity	Needed input	9	4	6
	Complexity of needed input	7	6	4
	Use complexity	8	6	1
Simulation time		9	1	4
Model flexibility	System change	8	6	1
	Connection change	7	6	1
Costs		9	7	1
Total		72	58	48

Table 9.1: Comparison of analytical models, FE models, and tests

The rationale behind the scoring presented in this table is explained by briefly discussing why each model receives a different score for every sub-criterion. The scores are assigned on a relative basis, allowing a direct comparison between the different modeling approaches. Consequently, the values do not represent absolute performance levels; instead, they indicate how each model performs in relation

to the others. As a result, if all models perform poorly for a given sub-criterion, they will not necessarily receive very low scores, but will instead be ranked on a comparative scale.

Starting with the criterion of model accuracy, the experimental tests score a value of 10 for all sub-criteria. This is because the experimental results represent the actual structural behavior and therefore form the reference against which the models are evaluated. For the accuracy of the connection modeling, the FE model scores significantly higher than the analytical model. This difference is mainly caused by the high level of simplification applied to the connection behavior in the analytical model. Despite this simplification, the analytical model still scores relatively well for the push down response. This is due to the fact that both numerical models exhibit certain limitations that lead to comparable deviations from the experimental results. The FE model scores slightly higher for this sub-criterion because it captures the failure mechanism at the correct location and predicts an initial stiffness that is close to the experimental stiffness. However, it loses some points due to the high levels of yielding observed and the difficulty in directly explaining these effects, which limits insight into the underlying structural behavior.

For the drop down response, the analytical model scores lower mainly because all models exceed the maximum release load, making it difficult to accurately identify this value. While the FE model is able to capture the maximum force during the drop down event, it shows limited predictive accuracy in the post peak response. However, the pseudo static approach applied to the push down response in the FE model provides a better estimate of the maximum force, which results in a slightly higher overall score for the FE model compared to the analytical model.

The next criterion is model setup complexity, which is divided into three sub-criteria. The first sub-criterion, required input, considers both the amount of input data needed and how easily this data can be obtained. For the analytical model, the required input is relatively straightforward, as it mainly consists of parameters that are either known, can be looked up, or can be calculated using established methods. For the FE model, this becomes more challenging due to the need for orthotropic material properties of timber, such as elastic moduli in different directions, which are often not well documented for many timber species. Although material properties for steel connectors are generally better known, their interaction with timber introduces additional uncertainty. In this research, this issue was further complicated by the small scale of the connectors, for which suitable experimental reference data was limited.

For the experimental tests, the required input is relatively simple, as the primary input consists of the physical materials themselves. However, to ensure that the materials behave as expected, additional material testing is required, which reduces the overall simplicity of the input. As a result, the experimental approach scores higher than the FE model but lower than the analytical model for this sub-criterion.

The model simulation time refers solely to the time required to perform the analysis or test and does not include the time needed to determine or calculate input parameters. The analytical model performs very well in this regard, as simulations take only a few seconds and could potentially be further optimized. In contrast, the FE model requires significantly longer simulation times. The connection model has a simulation time of approximately half an hour, while the push down and drop down analyses require several hours. These simulation times are considerably longer than those of the experimental tests. The connection tests take approximately 12 to 17 minutes, the push down tests take around 20 minutes, and the drop down tests take only a few seconds. Even when multiple tests are conducted to account for variability, the total testing time remains shorter than the FE simulations. It should be noted, however, that the simulation time of FE models can be substantially reduced through optimization and increased user experience. With sufficient expertise, FE simulations may eventually become faster than experimental testing, although this requires a highly experienced engineer.

Model flexibility is evaluated based on the effort required to implement a full system change or a connection change. For full system changes, such as modifying beam lengths, cross-sections, or adding structural components, the analytical model performs well because the system can be simplified into an equivalent frame model. However, incorporating additional elements such as floor systems requires ex-

tra assumptions and modeling effort, which prevents a higher score. For the FE model, system changes generally require more time, but adding components such as floors does not introduce fundamentally new modeling challenges, as long as the required material input is available. Changes in geometry, such as member length or cross-section modifications, are more time consuming, which results in a slightly lower score than the analytical model.

For experimental testing, full system changes are the most demanding. Modifications typically require new beams or columns, complete reassembly of the setup, and may be limited by available laboratory space. As a result, the experimental approach scores the lowest for system flexibility.

For connection changes, the analytical model allows relatively straightforward adjustments by recalculating the connection properties, as described in Section 6.2. Although these calculations can be time consuming, the connection behavior can be modified by adjusting input parameters. In the FE model, connection changes are relatively easy when the engineer is familiar with the connector types and materials involved. Small modifications can often be implemented quickly without extensive recalculation. However, introducing new materials or connection types requires careful verification, which can significantly increase modeling time. Consequently, the required effort depends strongly on the engineer's experience and the nature of the changes. For experimental testing, connection changes are particularly challenging, as the entire system often needs to be disassembled and reassembled. Even small changes can require substantial time and resources, resulting in the lowest score for this sub-criterion.

The final criterion considered is model cost, which includes both setup and execution costs. For the analytical model, costs are minimal, as the analyses can be performed using general purpose programming environments or even manual calculations, requiring only a computer. The FE model involves higher costs due to the need for specialized software, which can range from relatively affordable to very expensive depending on the package used. Experimental testing is by far the most costly approach, as it requires physical materials, laboratory facilities, and specialized equipment. Furthermore, the materials used in the tests are typically damaged or destroyed during testing, making them unsuitable for reuse. As a result, experimental testing receives the lowest score for the cost criterion.

9.4. Improved model

With all these comparisons it can be clearly seen how the models can improved the easiest improvement here would be done with these things this is done for analytical model because this scores the best and can be mostly easily be changed and improved:

- Use the connection model of the FE model in the analytical model;
- Use a failure mechanism in the analytical model.

this means that the outcome of the FE model connection test can be used as input for the analytical model. this also means that this model gives a certain rotation on where it fails which can be used as input for the analytical model as failure mechanism this the will be checked and when the middle connection goes over this rotation the simulation is stopped.

to use the actual FE model's connection result as input for the analytical model this first needs to be simplified this is done here by making two straight lines with the first going from zero to the point where yielding seems to start and the second line from this point to the max moment point this is shown below what this will look like.

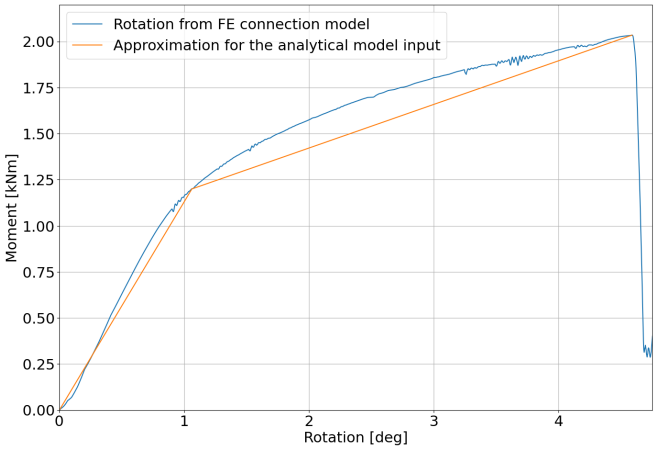

Figure 9.1: Moment approximation for the improved model.

so with the lines from figure 9.1 the stiffness can be calculated by reading out these points and calculating the slope of the line between the two point which is then the stiffness. so this is done for both lines and it assumed this changes at the point where yielding starts. in figure 9.1 it can be seen that the first lines goed from zero to 1.2 kNm at 1.06 deg and the from this to the max point which is at 2.12 kNm at 4.59 deg. this will result in the rotational stiffness's of 1.13 kNm/deg and 0.24 kNm/deg. with knowing where the max point is which also seems to be from figure 9.1 before failure this wil also be the failure point so the max rotation of the middle connection is set to 4.59 deg.

With all this the whole analytical model can be run with the pseudo static approach to get to the dynamic response. this,the push down response and the data points from the paper Cheng et al., 2021 are shown in figure 9.2

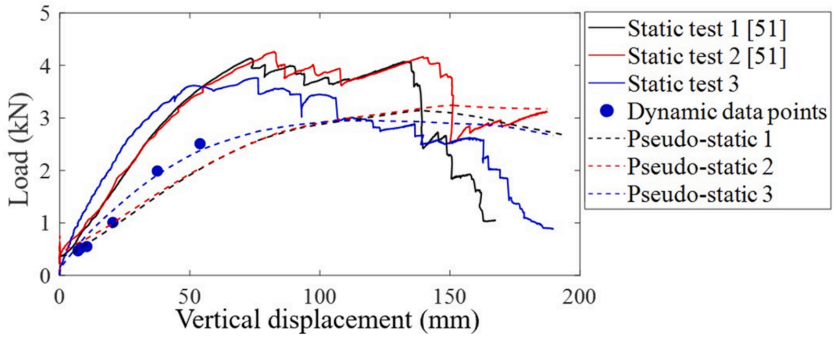

(a) Experimental force displacement curves (Cheng et al., 2021).

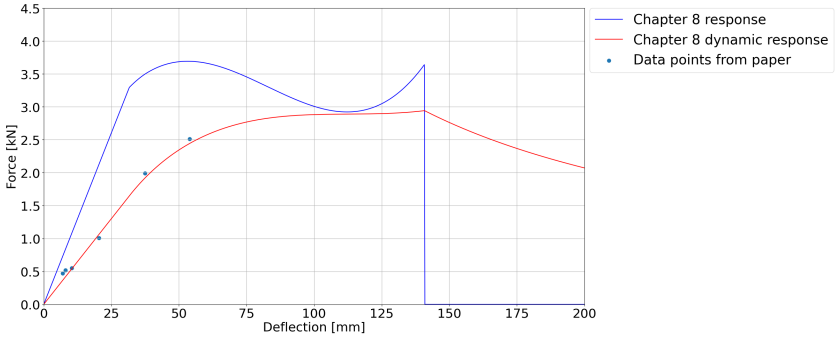

(b) Improved analytical response.

Figure 9.2: Comparison of improved model and tests.

in figure 9.2 it can be seen how the improved model stack up against the dynamic repsonse from the pseudo static approach lines in the first figure and the data points from the drop down test plotted in both figures for reference. it caqn be seen that now the dynamic response from pseudo static approach stays below the 3kN mark which is good so that this keeps below the actual failure force. it can also be seen that this follows the data point very wel. so this model improves on accurcy and on predicting failure force for the price of making a good connection model in an FE model. this means that the needed input is a bit more and the complexity of this input is higher. so overall this model would perform beter and would be a good idea to acctually use if there is confidence in the FE models connection model.

10
Conclusions and recommendations

This chapter summarizes the key findings and offers recommendations for both practical application and further research. This chapter starts with a discussion of the findings with respect to the primary objective of the thesis. evaluating the reliability of analytical and finite element (FE) models in simulating column removal scenarios in timber structures. Subsequently, general conclusions are drawn, followed by recommendations for future work.

10.1. Primary objective conclusion

The primary objective of this thesis was to evaluate whether analytical and FE models can reliably simulate column removal scenarios, thereby validating their application in robustness design. This objective has been addressed for both modeling approaches individually:

The analytical model, based on non linear springs and pseudo static energy approach, demonstrates potential as an early stage design tool. Although there are discrepancies compared to experimental results, the model provides conservative outcomes when connection springs are properly defined and gaps are set to zero. Its relative simplicity makes it suitable for preliminary design, offering engineers a practical means to assess whether a structure can withstand column loss. While the model is usable and flexible, its accuracy is somewhat limited. Nevertheless, it can be expanded in later design stages to incorporate floor effects or additional beams, as suggested by (B. Izzuddin et al., 2008).

For the FE models, two approaches were examined: the drop down model and the push down pseudo static approach.

- The drop down model showed poor accuracy at low release loads and is therefore unsuitable for simulating dynamic displacements. It is only reliable when high release loads are applied and the output is restricted to reaction forces.
- The push down pseudo static FE approach proved to be more accurate and conservative, making it a robust design approach. However, its usability is limited by the complexity of connection modeling and the computational effort required. While it is less flexible than the analytical model, FE models can be extended to represent entire structural systems, thereby capturing building level resistance more effectively.

So to conclude and give an answer to the primary objective of this thesis: The analytical model is best suited for early design stages due to its usability and flexibility, while the FE push down model provides higher accuracy for advanced design stages, but with greater modeling effort.

10.2. Overarching conclusions and recommendations

Beyond the findings that address the primary objective, the research has yielded several overarching insights that inform broader conclusions and recommendations:

- A simplified timber material model be adequate for FE analysis, as dynamic forces rarely approach timber failure thresholds. Introducing basic plasticity could reduce complexity without compromising accuracy.
- Compressive arching should generally be excluded from the analytical model, as observed in test setups. However, this may vary depending on connection details.
- The current yield moment calculation in the analytical method appears inaccurate, particularly regarding dowel behavior. Assuming a greater number of dowels in yielding improves reliability.

- Compression springs in the connection model should be stiffer when contact governs rotational behavior.
- The FE connection model captures behavior effectively and could serve as input for refining the analytical method.
- Designing directly with applied forces and corresponding dynamic displacements is preferable to relying on Dynamic Amplification Factors (DAF), which were shown to be poorly estimated by both methods.

These findings provide deeper insight into how the models operate, highlight their strengths, and offer practical recommendations to simplify future modeling efforts.

10.3. Recommendations for further research

Despite the progress achieved, several uncertainties remain. The following topics are therefore recommended for further investigation:

- Verification that single column removal in a portal frame represents a worst case scenario.
- Development of simplified analytical models that incorporate compressive arching more accurately.
- Investigation of drop times in the FE drop down model to assess whether instantaneous removal is necessary.
- Comprehensive characterization of LVL-S beams and columns, including mechanical properties in multiple directions, to facilitate model development.
- Creation of simplified timber models capable of representing plasticity in multiple directions.
- Improved aluminum models that capture rate effects and ductility more accurately.
- Further study of the behavior bolts and dowels in timber, in particularly with metal plates, to enhance the simulation of bolt plasticity.
- Expansion of the analytical connection model to include a wider range of timber connections, incorporating enhanced non linear behavior.
- Validation of shell element FE models to ensure accurate representation of timber connections..
- Extension of both analytical and FE methods to include floor systems in column removal scenarios.
- Investigation of falling behavior in the drop down model, as highlighted in Chapter 9.
- Detailed study of compressive arching mechanisms and the influence of connection gaps.
- Validation of the pseudo static approach in both analytical and FE models against experimental data to confirm its suitability as a design method;
- The application of robustness enhancement measures within these methods appears feasible, as both approaches can, in principle, represent most common robustness improvements. However, their performance in such modified configurations remains uncertain. Further work is therefore required to assess whether the models can simulate strengthened or otherwise improved systems accurately, and whether the predicted benefits of these robustness measures are reliable.

These recommendations aim to address existing gaps in knowledge and enhance the understanding of timber robustness in structural design.

References

Arriaga, F., Wang, X., Íñiguez-González, G., Llana, D. F., Esteban, M., & Niemz, P. (2023, June). Mechanical Properties of Wood: A Review. https://doi.org/10.3390/f14061202

Arup. (2011). *Review of international research on structural robustness and disproportionate collapse*.

Cao, A. S., Palma, P., & Frangi, A. (2025). Dynamic amplification factors in instantaneously loaded structures. *Engineering Structures*, *345*, 121464. https://doi.org/https://doi.org/10.1016/j.engstruct.2025.121464

Cao, J., Xiong, H., & Liu, Y. (2021). Experimental study and analytical model of bolted connections under monotonic loading. *Construction and Building Materials*, *270*, 121380. https://doi.org/https://doi.org/10.1016/j.conbuildmat.2020.121380

Cheng, X., Gilbert, B. P., Guan, H., Underhill, I. D., & Karampour, H. (2021). Experimental dynamic collapse response of post-and-beam mass timber frames under a sudden column removal scenario. *Engineering Structures*, *233*, 111918. https://doi.org/https://doi.org/10.1016/j.engstruct.2021.111918

Duriot, R., Frayssinhes, R., Rescalvo, F. J., Collet, R., Denaud, L., Girardon, S., & Pot, G. (2023). Bending, shearing, and compression properties of fast growing french douglas fir lvl. https://api.semanticscholar.org/CorpusID:263257945

Ellingwood, B. R., Smilowitz, R., Associates, W., Dusenberry, D. O., Gumpertz, S., Dat, H., Lew, D. H. S., Carino, N. J., Gutierrez, C. M., & Jeffrey, W. A. (2007). *Best Practices for Reducing the Potential for Progressive Collapse in Buildings* (tech. rep.).

Forest product laboratory staff. (2021). Wood handbook.

Huber, J. A., Ekevad, M., Girhammar, U. A., & Berg, S. (2018, March). Structural robustness and timber buildings–a review. https://doi.org/10.1080/17480272.2018.1446052

Ido, H., Nagao, H., Kato, H., Miyatake, A., & Hiramatsu, Y. (2010). Strength properties of laminated veneer lumber in compression perpendicular to its grain. *Journal of Wood Science*, *56*(5), 422–428. https://doi.org/10.1007/s10086-010-1116-3

Izzuddin, B., Vlassis, A., Elghazouli, A., & Nethercot, D. (2008). Progressive collapse of multi-storey buildings due to sudden column loss — part i: Simplified assessment framework. *Engineering Structures*, *30*(5), 1308–1318. https://doi.org/https://doi.org/10.1016/j.engstruct.2007.07.011

Izzuddin, B. A. (2005). A simplified model for axially restrained beams subject to extreme loading. *International journal of steel structures*, *5*(5), 421–429.

J, A., M, A., B, B., F, B., R, C., J, D., B, I., P, M., T, M., A, O., F, P., J, S., ML, S., T, T., R, C., T, T., & ML, S. (2024). Guidance on the design for structural robustness. (KJ-NA-32-018-EN-N (online),KJ-NA-32-018-EN-C (print)). https://doi.org/10.2760/525706(online),10.2760/4945167(print)

Janowiak, J. J., Hindman, D. P., & Manbeck, H. B. (2001). Orthotropic behavior of lumber composite materials. *Wood and Fiber Science*, *33*(4), 580–594.

Kiakojouri, F., & Sheidaii, M. (2018). Effects of finite element modeling and analysis techniques on response of steel moment-resisting frame in dynamic column removal scenarios. *Asian Journal of Civil Engineering*, *19*, 295–307. https://doi.org/10.1007/s42107-018-0027-2

Liu, Y., Guo, H., Sun, C., & Chang, W.-S. (2016). Assessing Cross Laminated Timber (CLT) as an Alternative Material for Mid-Rise Residential Buildings in Cold Regions in China—A Life-Cycle Assessment Approach. *Sustainability*, *8*(10). https://doi.org/10.3390/su8101047

Lu, X., Lin, K., Li, C., & Li, Y. (2018). New analytical calculation models for compressive arch action in reinforced concrete structures. *Engineering Structures*, *168*, 721–735. https://doi.org/https://doi.org/10.1016/j.engstruct.2018.04.097

Lyu, C. H., Gilbert, B. P., Guan, H., Underhill, I. D., Gunalan, S., Karampour, H., & Masaeli, M. (2020). Experimental collapse response of post-and-beam mass timber frames under a quasi-static column removal scenario. *Engineering Structures*, *213*, 110562. https://doi.org/https://doi.org/10.1016/j.engstruct.2020.110562

Masaeli, M., Gilbert, B. P., Karampour, H., Underhill, I. D., Lyu, C. H., & Gunalan, S. (2020). Scaling effect on the moment and shear responses of three types of beam-to-column connectors used

in mass timber buildings. *Engineering Structures*, *208*, 110329. https://doi.org/https://doi.org/10.1016/j.engstruct.2020.110329

Mpidi Bita, H. (2019). *Disproportionate collapse prevention analyses for mid-rise cross-laminated timber platform-type buildings* [Doctoral dissertation]. https://open.library.ubc.ca/collections/24/items/1.0379207

Mpidi Bita, H., Huber, J. A., Voulpiotis, K., & Tannert, T. (2019, November). Survey of contemporary practices for disproportionate collapse prevention. https://doi.org/10.1016/j.engstruct.2019.109578

NEN-EN 1990 (tech. rep.). (2021). CEN.

NEN-EN 1991-1-7 (tech. rep.). (2021). CEN.

NEN-EN 1993-1-8 (tech. rep.). (2024). CEN.

NEN-EN 1995-1-1 (tech. rep.). (2024). CEN.

Palma, P., & Fink, G. (2022). *COST ACTION CA 20139 Holistic design of taller timber buildings (HELEN) STATE OF THE ART REPORT* (tech. rep.).

Sasaki, H., & Abdullahi, A. A. (2016). *Lumber: Laminated veneer* (tech. rep.).

Shu, Z., Guan, Z., Srivaro, S., Luo, J., Peng, Z., Gao, Y., Zhang, X., & Song, T. (2025). Properties of laminated veneer lumber made of italian poplar, eucalyptus, larch, masson pine, and spruce. *Architectural Engineering and Design Management*, *0*(0), 1–24. https://doi.org/10.1080/17452007.2025.2558807

Starossek, U. (2018). *Progressive Collapse of Structures (2nd Edition)*. ICE Publishing. https://app.knovel.com/hotlink/toc/id:kpPCSE001T/progressive-collapse/progressive-collapse

STEICO SE. (2026). *Steico lvl / laminated veneer lumber – design guide* [Technical detailing and mechanical properties of STEICO LVL products]. STEICO SE. Feldkirchen, Germany.

Sudo, R., Miyamoto, K., & Ido, H. (2025). Quantitative assessment of adhesive effects on partial and full compressive strength of LVL in the edge-wise direction. *Journal of Wood Science*, *71*(1), 19. https://doi.org/10.1186/s10086-025-02195-z

Tomasi, R., Riccardo, Z., Maurizio, P., & Andreolli, M. (2008). Ductile End Connections for Glulam Beams. *Structural Engineering International*, *18*(3), 290–296. https://doi.org/10.2749/101686608785096595

Tsai, S. W. (1965). *Strength characteristics of composite materials*. NASA Washington, DC.

Tucker, M., Horstemeyer, M., Whittington, W., Solanki, K., & Gullett, P. (2010). The effect of varying strain rates and stress states on the plasticity, damage, and fracture of aluminum alloys. *Mechanics of Materials*, *42*(10), 895–907. https://doi.org/https://doi.org/10.1016/j.mechmat.2010.07.003

Voulpiotis, K., Köhler, J., Jockwer, R., & Frangi, A. (2021). A holistic framework for designing for structural robustness in tall timber buildings. *Engineering Structures*, *227*. https://doi.org/10.1016/j.engstruct.2020.111432

Voulpiotis, K., Schär, S., & Frangi, A. (2022). Quantifying robustness in tall timber buildings: A case study. *Engineering Structures*, *265*. https://doi.org/10.1016/j.engstruct.2022.114427

Yang, H., Liu, W., & Ren, X. (2016). A component method for moment-resistant glulam beam–column connections with glued-in steel rods. *Engineering Structures*, *115*, 42–54. https://doi.org/https://doi.org/10.1016/j.engstruct.2016.02.024

Zhang, D., Wang, Z., Bilal, H., Shen, Z., & Zhou, Y. (2024). Study on elastic constants of laminated veneer lumber by dynamic test. *Materials and Structures*, *57*(4), 98. https://doi.org/10.1617/s11527-024-02364-4

Part IV

Appendix

A

Softening curve material model

In this appendix, the setup of the softening curve for the LS-DYNA model is described. The model assumes a function that can be controlled with five variables:

- **SIGY** = General yield strength;
- **CR1** = Fitted parameter;
- **CR2** = Fitted parameter;
- **QR1** = Fitted parameter;
- **QR2** = Fitted parameter.

The function used to generate the curve is given by:

$$\sigma = \sigma_Y + QR1\left(1 - e^{-CR1\epsilon_p}\right) + QR2\left(1 - e^{-CR2\epsilon_p}\right) \tag{A.1}$$

with:

- σ = output stress;
- ϵ_p = plastic strain.

To fit a curve that follows the desired softening branch, the curve is first reconstructed in Python code. Afterwards, the fitting function is applied. For this fit, some values are predefined:

- **maxfev** = maximum iterations for the fit, set to 100000;
- **bounds** = parameter bounds: QR values between 1 and 2000, CR values between -1×10^8 and -1×10^5, and between 1×10^5 and 1×10^8 respectively.

The Python implementation is shown below:

```python
import matplotlib.pyplot as plt
import numpy as np
import scipy as sc

# Elastic stiffness
E_c1 = 15300e6

# Making stres strain curve
ep_c1 = np.linspace(0,0.0164,2001)
st_c1_1 = np.linspace(0,39.29e6,305)
st_c1_2 = np.linspace(39.4e6,44.9e6,363)
st_c1_3 = np.linspace(45e6,31.4e6,1333)
st_c1 = np.hstack([st_c1_1, st_c1_2, st_c1_3])

# Calculating effective stress and plastic strain
el_st_c1 = st_c1/E_c1
st_pl_c1 = st_c1[305::]
ep_pl_c1 = ep_c1 - el_st_c1
ep_pl_c1 = ep_pl_c1[305:]

# Relavant function to curve fit for LS-DYNA
def plastic_curve_c1(ep,C1,C2,Q1,Q2):
    st = 39.3e6 + Q1*(1-np.exp(-C1*ep)) + Q2*(1-np.exp(-C2*ep))
    return st
```

Figure A.1: Python code for fitting the softening branch of the material model (1).

```
# Curve fitting with data from above and initial start value
C1,C2,Q1,Q2 = sc.optimize.curve_fit(plastic_curve_c1, xdata=ep_pl_c1, ydata=st_pl_c1,
                                    p0=[10,1000,-1e8,1e7], maxfev=100000, bounds=([1,1,-1e8,1e5],[2000,2000,-1e5,1e8]))[0]
C1 = np.round(C1,2)
C2 = np.round(C2,2)
Q1 = np.round(Q1,2)
Q2 = np.round(Q2,2)
print(f'LVL along grain parameters; C1={C1},C2={C2},Q1={Q1},Q2={Q2}')

# Plotting curves to show the fit
fit_curve_c1 = plastic_curve_c1(ep_pl_c1,C1,C2,Q1,Q2)
plt.plot(ep_c1, st_c1, label='stress strain curve')
plt.plot(ep_pl_c1,st_pl_c1, label='effective stress plastic strain curve')
plt.plot(ep_pl_c1, fit_curve_c1, label='fitted curve')
plt.grid()
plt.legend()
plt.xticks(np.linspace(0,0.015,7))
plt.yticks(np.linspace(0,50e6,6),labels=[0,10,20,30,40, 50])
plt.ylim(0,50e6)
plt.xlim(0,0.015)
plt.show()
plt.close()
```

Figure A.2: Python code for fitting the softening branch of the material model (2).

In the code, the elastic modulus is first set to the value corresponding to the relevant behavior. The strain is then defined as an array over which the desired stress response is known and should be modeled. The experimental curve is replicated with simplified straight segments. Next, the effective stress and plastic strain are calculated, since only the plastic portion of the curve requires fitting. This is achieved by setting the strain to zero at the end of the elastic phase and assigning the yield stress at that point.

The fitting function is then defined, and the fitting procedure is executed. The resulting parameter values are rounded to two decimal places, as LS-DYNA does not accept excessive precision. Finally, the fitted curve is compared with the original test curve, as shown below:

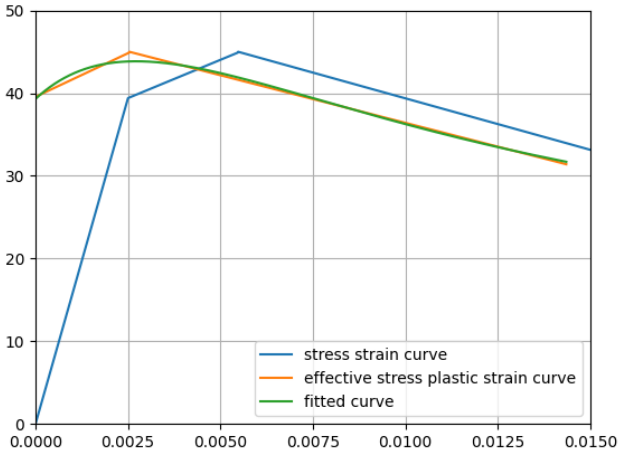

Figure A.3: Curve fit graph comparing fitted and original curves.

B

Analytical connection calculation

In this appendix, the connection calculations for the analytical model are presented in detail. The procedure follows four steps: first the rotational capacity, then the rotational stiffness, followed by the translational capacity, and finally the translational stiffness. All formulas used here are introduced in Chapter 6, but are repeated for completeness. The input values for these formulas are also provided, together with their sources.6 but will be shown again here. the inputs for all these formulas will also be shown and where they are from.

B.1. Rotational capacity

As explained in Chapter 6, the maximum rotational capacity is taken as the plastic moment. The components that may govern the plastic moment are:

- Punching resistance of the bolt head or nut;
- Tensile resistance of the bolt;
- Tensile resistance of the aluminum plate (modeled as a T-stub);
- Shear strength of the dowel;
- Compression strength of the column;
- Shear strength of the column.

Bolt resistance

For bolt row i, the tensile force T_i is defined as:

$$T_i = \min(F_{bt},\, F_{pb})\,, \tag{B.1}$$

where:

$$F_{bt} = A_s f_{ub}, \tag{B.2}$$

$$F_{pb} = \frac{0.6\pi d_m t_p f_{up}}{\gamma_m}. \tag{B.3}$$

Since only the lowest bolt row needs to be calculated, the following values are used:

- $A_s = 8.78\,\text{mm}^2$ (from technical design sheet for metric bolts);
- $f_{ub} = 1214\,\text{MPa}$ (average from validation test);
- $d_m = 7.66\,\text{mm}$ (from technical design sheet for metric bolts);
- $t_p = 3\,\text{mm}$ (from validation test);
- $f_{up} = 370\,\text{MPa}$ (average from validation test);
- $\gamma_m = 1.25$ (from *NEN-EN 1990*, 2021).

This yields:

- $F_{bt} = 10.7\,\text{kN}$;
- $F_{pb} = 12.8\,\text{kN}$.

Since the shaft resistance is lower, it is adopted as the design value. Multiplying by two for the bolt row force, the plastic moment contribution is calculated as:

$$M_{pb} = \sum_{i=1}^{n_y} h_i F_{tb,i}, \tag{B.4}$$

with h_1 given by:

$$h_1 = h_b - 25 - \frac{h_{cz}}{2}, \tag{B.5}$$

where the constant 25 represents the distance from the bolt row to the bottom of the beam. The compression zone height h_{cz} is obtained from:

$$\sum_{i=1}^{n_y} F_{tb,i} = \sigma_p d_{cz} h_{cz}. \tag{B.6}$$

The parameters are:

- $\sigma_p = 3.5$ MPa (from timber material model in radial direction);
- $d_{cz} = 63$ mm (beam width from validation tests).

This gives $h_1 = 76.7$ mm, resulting in a plastic moment from the bolts of $M_{pb} = 1.63$ kNm.

Tensile resistance of the t-stub

From Chapter 6 it is established that only a single failure mode requires evaluation. The tensile force corresponding to this mode is determined as:

$$F_{\text{stub,row}} \;=\; \frac{4\,M_{\text{pl}} \;+\; 2\,M_{\text{bp}}}{m}, \tag{B.7}$$

where the plastic and bearing moments are defined identically as:

$$M_{\text{pl}} \;=\; M_{\text{bp}} \;=\; \tfrac{1}{4}\,l_{\text{eff}}\,t_p\,f_{u,\text{p}}, \tag{B.8}$$

with the effective length given by:

$$l_{\text{eff}} \;=\; 4\,m \;+\; 1.25\,e. \tag{B.9}$$

The parameters required for this calculation are obtained from the validation tests:

- $m = 8.75$ mm;
- $t_p = 3$ mm;
- $f_{u,p} = 370$ MPa (average);
- $e = 6.25$ mm.

Substituting these values yields the tensile resistance of the lowest bolt row:

$$F_{\text{stub},1} = 32.6\,\text{kN}.$$

Using the same procedure for the lever arm h_1 as previously defined, the plastic moment capacity of the T-stub can be expressed as:

$$M_{\text{pl,T-stub}} \;=\; \sum_{i=1}^{n_y} h_i\,F_{\text{stub,row},i}. \tag{B.10}$$

For the lowest bolt row this results in:

$$M_{\text{pl,T-stub}} = 1.67\,\text{kNm}.$$

Shear resistance of dowels

For the shear resistance of the dowels, the force per bolt in rotation can be calculated as:

$$F_{M,i} = \frac{F_{M,1} r_i}{r_1} \tag{B.11}$$

with

- $F_{M,i}$ = force in the i-th dowel;

- r_i = distance from the rotational center (RC) to the i-th dowel;
- $F_{M,1}$ = force in the outermost dowel.

For the outermost dowel, the shear force can be calculated from *NEN-EN 1995-1-1*, 2024 using:

$$F_{D,k} = \min \begin{cases} f_{h,1,k}\, t_{h1}\, d & \text{mode (a)} \\ f_{h,2,k}\, t_{h2}\, d & \text{mode (b)} \\ \frac{f_{h,1,k} t_{h1} d}{(1+\beta)} \left[\sqrt{\beta + 2\beta^2 \left(1 + \frac{t_{h2}}{t_{h1}} + \left(\frac{t_{h2}}{t_{h1}}\right)^2\right) + \beta^3 \left(\frac{t_{h2}}{t_{h1}}\right)^2} - \beta \left(1 + \frac{t_{h2}}{t_{h1}}\right) \right] & \text{mode (c)} \\ 1.05 \frac{f_{h,1,k} t_{h1} d}{2+\beta} \left[\sqrt{2\beta(1+\beta) + \frac{4\beta(2+\beta) M_{y,k}}{f_{h,1,k} d t_{h1}^2}} - \beta \right] & \text{mode (d)} \\ 1.05 \frac{f_{h,1,k} t_{h2} d}{1+2\beta} \left[\sqrt{2\beta^2(1+\beta) + \frac{4\beta(1+2\beta) M_{y,k}}{f_{h,1,k} d t_{h2}^2}} - \beta \right] & \text{mode (e)} \\ 1.15 \sqrt{\frac{2\beta}{1+\beta}} \sqrt{2 M_{y,k} f_{h,1,k} d} & \text{mode (f)} \end{cases} \tag{B.12}$$

Since our connection has two shear planes and a central metal plate, only modes (a), (b), (d), and (f) are relevant. The following input parameters are used:

- $f_{h,1,k} = \frac{(0.082(1-0.01d))p_k}{k_{mat}}$;
- $\beta = \frac{f_{h,2,k}}{f_{h,1,k}}$;
- $M_{y,k} = 0.3 f_{u,k} d^{2.6}$;
- $k_{mat} = (k_{90} \sin(\phi_\alpha)^2 + \cos(\phi_\alpha)^2)(\sin(\phi_\beta)^2 + k_4 \cos(\phi_\beta)^2)$;
- $k_{90} = 1.15 + 0.015d$.

Substituting the test values:

- $t_{h1} = 63\,\text{mm}$;
- $d = 4\,\text{mm}$;
- $f_{h,2,k} = 600\,\text{MPa}$;
- $t_{h2} = 2.5\,\text{mm}$;
- $p_k = 595\,\text{kg/m}^3$;
- $f_{u,k} = 573\,\text{MPa}$;
- $\phi_\alpha = 0°$;
- $\phi_\beta = 90°$;
- $k_4 = 2$.

This yields shear resistances:

- mode (a): $9.8\,\text{kN}$;
- mode (b): $6.0\,\text{kN}$;
- mode (d): $4.6\,\text{kN}$;
- mode (f): $4.4\,\text{kN}$.

Accounting for the two shear planes, mode (f) governs with $F_{m1} = 4.4\,\text{kN}$. For the bottom six dowels (top six are symmetric, so the moment is doubled):

- $r_1 = 65\,\text{mm}$, $F_{m1} = 4.4\,\text{kN}$;
- $r_2 = 53\,\text{mm}$, $F_{m2} = 3.6\,\text{kN}$;
- $r_3 = 41\,\text{mm}$, $F_{m3} = 2.8\,\text{kN}$;

- $r_4 = 29\,\text{mm}$, $F_{m4} = 2.0\,\text{kN}$;
- $r_5 = 17\,\text{mm}$, $F_{m5} = 1.2\,\text{kN}$;
- $r_6 = 5\,\text{mm}$, $F_{m6} = 0.3\,\text{kN}$.

The plastic moment capacity of the dowel group is then:

$$M_{pl,d} = 2\sum_{i=1}^{n} r_i \cdot F_{M,i} \tag{B.13}$$

which results in:

$$M_{pl,d} = 1.34\,\text{kNm}.$$

Column compressive strength

From Chapter 6 it is shown that both moment–rotation setups are essentially the same in calculation. For the middle connection the result is simply doubled compared to the side connections. Therefore, the following calculation focuses on a single side connection.The compressive force is first determined as:

$$F_{cc} = f_{c,r}\, b_c\, l_{\text{eff}} \tag{B.14}$$

with parameters:

- $f_{c,r} = 17.65\,\text{MPa}$, maximum compressive strength against the grain from the material model (see Chapter 5). This value is intentionally set higher than the actual strength reported in that chapter, since the stress–strain curve exhibits significant increase at higher strains. It therefore represents a design strength rather than an ultimate strength value;
- $b_c = 32.5\,\text{mm}$, width of the end plate bearing against the column (validation tests);
- $h = 64\,\text{mm}$, half of the end plate height (validation tests).

Substitution yields:

$$F_{cc} = 36.7\,\text{kN}.$$

The corresponding plastic moment capacity is then obtained from:

$$M_{pl,cc} = F_{t,cc}\, l_{\text{eff}} \tag{B.15}$$

with $l_{\text{eff}} = 64\,\text{mm}$ as defined in Chapter 6. This results in:

$$M_{pl,cc} = 2.35\,\text{kNm}.$$

Column shear capacity

For this capacity, the shear force is first calculated as:

$$F_{\text{cs}} = f_{v,LT}\, b_c\, d_c, \tag{B.16}$$

with the following parameters:

- $f_{v,LT} = 2.5\,\text{MPa}$, shear strength from the material model (see Chapter 5),
- $b_c = d_c = 90\,\text{mm}$, width and depth of the column (validation tests).

Substitution yields:

$$F_{\text{cs}} = 20.25\,\text{kN}.$$

The corresponding plastic moment due to this shear force is then calculated as:

$$M_{\text{pl,cs}} = F_{\text{cs}}\, h_{\text{pl}}, \tag{B.17}$$

with $h_{\text{pl}} = 128\,\text{mm}$, resulting in:

$$M_{\text{pl,cs}} = 2.6\,\text{kNm}.$$

Considering all calculated capacities, it is evident that the moment due to the dowels is the lowest. Therefore, the dowel capacity governs and is adopted as the plastic moment. This gives a plastic moment of:

- $M_{\mathrm{pl}} = 1.34$ kNm for the side connections,
- $M_{\mathrm{pl}} = 2.68$ kNm for the middle connection.

B.2. Rotational stiffness

For this analysis, two layouts are considered: one before the gap is closed and one after. The setups, simplifications, and equations from Chapter 6 are applied. The initial stiffness of the whole connection can be expressed as:

$$S_{\mathsf{ini}} = \frac{z_{\mathsf{eq}}^2}{\frac{1}{k_t} + \frac{1}{k_c}} \tag{B.18}$$

with the equivalent lever arm defined as:

$$z_{\mathsf{eq}} = \frac{\sum k_i h_i^2}{\sum k_i h_i}, \tag{B.19}$$

and the combined column stiffness:

$$k_c = \frac{1}{\frac{1}{k_{cs}} + \frac{1}{k_{cc}} + \frac{1}{k_{\mathsf{tstubc}}} + \frac{1}{2 \cdot k_{\mathsf{dowel}}}}, \tag{B.20}$$

while the tensile stiffness for the first spring is:

$$k_{t,1} = \frac{1}{\frac{1}{k_{cc}} + \frac{1}{k_{bt}} + \frac{1}{k_{\mathsf{tstub}}} + \frac{1}{2 \cdot k_{\mathsf{dowel}}}}, \tag{B.21}$$

and the overall tensile stiffness is given by:

$$k_t = \frac{\sum k_{t,i} \cdot h_i}{z_{\mathsf{eq}}}. \tag{B.22}$$

All stiffness components are calculated individually and then assembled into the relevant springs for each layout.

Beam compression stiffness

The beam compression spring stiffness is determined as:

$$k_{bc} = \frac{E_{w,0} \sqrt{b_b \, l_{\mathsf{eff,cb}}}}{\beta}, \tag{B.23}$$

with parameters:

- $E_{w,0} = 15300$ MPa, modulus of elasticity parallel to grain (Chapter 5);
- $b_b = 63$ mm, beam width (validation tests);
- $l_{\mathsf{eff,cb}} = 28.5$ mm, half of the assumed compression zone height;
- $\beta = 4$, from Tomasi et al., 2008.

Substitution yields the following rotational stiffness values for the beam compression spring:

- Layout 1: $k_{bc,1} = 0.162$ kNm/rad;
- Layout 2: $k_{bc,2} = 0.177$ kNm/rad.

Column shear stiffness

The next spring to be calculated is the column shear stiffness spring, given by:

$$k_{cs} = \frac{G_c \, b_c \, h_c}{z_{\mathsf{eq}}} \tag{B.24}$$

with parameters:

- $G_c = 860.56$ MPa, shear modulus of the column (see Chapter 5);
- $b_c = 90$ mm, column width (validation tests);
- $h_c = 90$ mm, column depth (validation tests);
- z_{eq}, equivalent lever arm (see Equation 6.20).

This stiffness is evaluated once the lever arm is determined, and results for both layouts are:

- Layout 1: $k_{cs,1} = 0.112$ kNm/rad;
- Layout 2: $k_{cs,2} = 0.082$ kNm/rad.

Column compression stiffness

The compression stiffness of the column is calculated as:

$$k_{cc} = \frac{E_{c,r}\, b_c\, l_{\text{eff,cc}}}{h_c} \tag{B.25}$$

with parameters:

- $E_{c,r} = 807.5$ MPa, modulus of elasticity in radial direction of the column (see Chapter 5;
- $l_{\text{eff,cc}} = 68$ mm, effective length from connection setup (validation tests).

The resulting stiffness values for both layouts are:

- Layout 1: $k_{cc,1} = 4.65$ kNm/rad;
- Layout 2: $k_{cc,2} = 4.94$ kNm/rad.

T-Stub compression stiffness

The compression stiffness of the T-stub flange is given by:

$$k_{\text{tstubc}} = \frac{0.7\, d_{fl}\, t_{fl}\, E_{fl}}{h_{c,fl}} \tag{B.26}$$

with parameters:

- $d_{fl} = 128$ mm, flange depth (validation tests);
- $t_{fl} = 2.5$ mm, flange thickness (validation tests);
- $h_{c,fl} = 64$ mm, compression height (validation tests);
- $E_{fl} = 72000$ MPa, average elastic modulus of the flange (validation tests).

The calculated stiffness values for each layout are:

- Layout 1: $k_{\text{tstubc},1} = 0.252$ kNm/rad;
- Layout 2: $k_{\text{tstubc},2} = 0.267$ kNm/rad.

Dowel shear stiffness

The dowel shear stiffness is calculated according to *NEN-EN 1995-1-1*, 2024 as:

$$k_{\text{dowel}} = \frac{p_{\text{mean}}^{1.5}\, d_{\text{dowel}}}{23} \tag{B.27}$$

with parameters:

- $p_{\text{mean}} = 595$ kg/m^3, average density from validation tests;
- $d_{\text{dowel}} = 4$ mm, dowel diameter from connection setup (validation tests).

Substitution yields the following stiffness values for the dowel spring:

- Layout 1: $k_{\text{dowel},1} = 0.005$ kNm/rad;
- Layout 2: $k_{\text{dowel},2} = 0.005$ kNm/rad.

T-stub tension stiffness

For a single bolt row under prying action, the tension stiffness of the T-stub is given by:

$$k_{\text{tstub}} = \frac{0.85\, E_{\text{al}}\, l_{\text{eff}}\, t_{f,e}^3}{m^3} \tag{B.28}$$

with parameters:

- $E_{\text{al}} = 70000$ MPa, average elastic modulus of aluminum (validation tests);
- $l_{\text{eff}} = 4m + 1.25e$, effective length from *NEN-EN 1993-1-8*, 2024;
- $t_{f,e} = 3$ mm, flange thickness (validation tests);
- $m = 8.75$ mm, bolt spacing (validation tests);
- $e = 6.25$ mm, edge distance (validation tests).

The resulting stiffness values for the T-stub spring are:

- Layout 1: $k_{\text{tstub},1} = 0.033$ kNm/rad;
- Layout 2: $k_{\text{tstub},2} = 0.067$ kNm/rad.

Bolt tension stiffness

The last stiffness that needs to be calculated is the bolt tension stiffness

$$k_{bt} = \frac{E_b\, A_{bt}}{l_{bt}} \tag{B.29}$$

where:

- $E_b = 205000[mPa]$ average elastic modulus of the bolts (validation tests);
- $A_{bt} = 8.78[mm^2]$ tensile stress area of the bolt (validation tests);
- $l_{bt} = 45[mm]$ grip length of the bolt from *NEN-EN 1993-1-8*, 2024.

this will give the stiffness of the two layouts as:

- Layout 1: $k_{\text{tstub},1} = 0.040$ kNm/rad;
- Layout 2: $k_{\text{tstub},2} = 0.040$ kNm/rad.

Rotational springs stiffness

with this the initial rotational springs stiffness can be calculated by calculating the stiffness which can be made with taking the setup from chapter 6 into account these are shown here for layout 1

- $k_c = \frac{1}{\frac{1}{k_{cs}}+\frac{1}{k_{cc}}+\frac{1}{k_{\text{tstubc}}}+\frac{1}{2\cdot k_{\text{dowel}}}} = 0.009[kNm/rad]$;
- $k_{t,1} = \frac{1}{\frac{1}{k_{cc}}+\frac{1}{k_{bt}}+\frac{1}{k_{\text{tstub}}}+\frac{1}{2\cdot k_{\text{dowel}}}} = 0.006[kNm/rad]$;
- $k_{t,2} = \frac{1}{\frac{1}{k_{cc}}+\frac{1}{k_{bt}}+\frac{1}{k_{\text{tstub}}}+\frac{1}{2\cdot k_{\text{dowel}}}} = 0.006[kNm/rad]$;
- $k_{t,3} = \frac{1}{\frac{1}{k_{cc}}+\frac{1}{k_{bt}}+\frac{1}{k_{\text{tstub}}}+\frac{1}{2\cdot k_{\text{dowel}}}} = 0.004[kNm/rad]$;
- $h_1 = 75[mm]$ connection setup (validation tests);
- $h_2 = 55[mm]$ connection setup (validation tests);
- $h_3 = 35[mm]$ connection setup (validation tests);
- $z_{\text{eq}} = \frac{\sum k_i h_i^2}{\sum k_i h_i} = 62[mm]$;
- $k_t = \frac{\sum k_{t,i}\cdot h_i}{z_{\text{eq}}} = 0.016[kNm/rad]$;
- $S_{\text{ini}} = \frac{z_{\text{eq}}^2}{\frac{1}{k_t}+\frac{1}{k_c}} = 22[kNm/rad]$.

and for layout 2:

- $k_c = \frac{1}{\frac{1}{k_{cb}}+\frac{1}{k_{cs}}+\frac{1}{k_{cc}}+\frac{1}{k_{\text{tstubc}}}+\frac{1}{2\cdot k_{\text{dowel}}}} = 0.009[kNm/rad]$;
- $k_{t,1} = \frac{1}{\frac{1}{k_{cc}}+\frac{1}{k_{bt}}+\frac{1}{k_{\text{tstub}}}+\frac{1}{2\cdot k_{\text{dowel}}}} = 0.0072[kNm/rad]$;
- $k_{t,2} = \frac{1}{\frac{1}{k_{cc}}+\frac{1}{k_{bt}}+\frac{1}{k_{\text{tstub}}}+\frac{1}{2\cdot k_{\text{dowel}}}} = 0.0072[kNm/rad]$;
- $k_{t,3} = \frac{1}{\frac{1}{k_{cc}}+\frac{1}{k_{bt}}+\frac{1}{k_{\text{tstub}}}+\frac{1}{2\cdot k_{\text{dowel}}}} = 0.0042[kNm/rad]$;
- $k_{t,4} = \frac{1}{\frac{1}{k_{cc}}+\frac{1}{k_{bt}}+\frac{1}{k_{\text{tstub}}}+\frac{1}{2\cdot k_{\text{dowel}}}} = 0.0042[kNm/rad]$;
- $h_1 = 104.25[mm]$ connection setup (validation tests);
- $h_2 = 84.25[mm]$ connection setup (validation tests);
- $h_3 = 64.25[mm]$ connection setup (validation tests);
- $h_4 = 44.25[mm]$ connection setup (validation tests);
- $z_{\text{eq}} = \frac{\sum k_i h_i^2}{\sum k_i h_i} = 85[mm]$;
- $k_t = \frac{\sum k_{t,i}\cdot h_i}{z_{\text{eq}}} = 0.021[kNm/rad]$;
- $S_{\text{ini}} = \frac{z_{\text{eq}}^2}{\frac{1}{k_t}+\frac{1}{k_c}} = 44.4[kNm/rad]$.

B.3. Translational capacity

For translational capacity, the governing value is determined by the weakest element. This can be expressed as:

$$F_{\text{trans}} = \min\left(F_{bt}, F_{dv}, F_{tstub}, F_{cc}\right) \tag{B.30}$$

using the equations defined in Chapter 6:

- $F_{bt} = n_b \, \min(F_{bb}, F_{ts})$;
- $F_{bb} = \frac{0.6\,\pi\, d_m\, f_{up}\, t_p}{\gamma_m}$;
- $F_{ts} = \frac{0.9\, f_{ub}\, A_s}{\gamma_m}$;
- $F_{dv} = n_d\, F_{D,k}$;
- $F_{stub} = \min(F_{\text{tstub,total}}, F_{\text{tstub,fl}})$;
- $F_{\text{tstub,total}} = \sum_{i=1}^{n_{\text{row}}} F_{\text{stub,row},i}$;
- $F_{\text{tstub,fl}} = A_{\text{fl}}\, f_{u,\text{fl}}$;
- $F_{\text{stub,row}} = \frac{4M_{\text{pl}}+2M_{\text{bp}}}{m}$;
- $F_{\text{cc,u}} = A_{\text{end,pl}}\, f_{u,c,\perp}$.

The parameters used in these calculations are:

- $n_b = 12$, number of bolts (validation tests);
- $d_m = 7.66$ mm, bolt diameter (technical sheet);
- $f_{up} = 370$ MPa, average ultimate strength of plate material (validation tests);
- $t_p = 3$ mm, end plate thickness (validation tests);
- $\gamma_m = 1.25$, partial safety factor *NEN-EN 1990*, 2021;
- $f_{ub} = 1214$ MPa, average ultimate strength of bolt material (validation tests);
- $A_s = 8.78$ mm^2, bolt cross-sectional area (technical sheet);
- $n_d = 10$, number of dowels (validation tests);
- $F_{D,k} = 4.4$ kN, dowel shear resistance (previous calculation);
- $A_{fl} = 320$ mm^2, flange area (validation tests);
- $f_{u,fl} = 370$ MPa, average ultimate strength of flange material (validation tests);

- $M_{\mathrm{pl}} = M_{\mathrm{bp}} = 47521$ Nmm, plastic and bearing moments (rotational capacity calculation);
- $A_{end,pl} = 8320\,\mathrm{mm}^2$, end plate area (validation tests);
- $f_{u,c,\perp} = 3.5$ MPa, compressive strength perpendicular to grain (Chapter 5).

Substituting these values yields the following results:

- $F_{bt} = 92$ kN;
- $F_{bb} = 12$ kN;
- $F_{ts} = 7.6$ kN;
- $F_{dv} = 44$ kN;
- $F_{stub} = 118$ kN;
- $F_{\mathrm{tstub,total}} = 195$ kN;
- $F_{\mathrm{tstub,fl}} = 118$ kN;
- $F_{\mathrm{stub,row}} = 32$ kN;
- $F_{\mathrm{cc,u}} = 29.12$ kN.

so the translation capacity is equal to the weakest element which is: $F_{\mathrm{cc,u}} = 29.12$ kN

B.4. Translational stiffness

The translational stiffness can be derived from the compression springs used in the rotational stiffness model. For each bolt row, the equivalent spring stiffness is calculated as:

$$k_{\mathrm{row},i} = \left(\frac{1}{k_{cc}} + \frac{1}{k_{\mathrm{tstub}}} + \frac{1}{k_{bt}} + \frac{1}{2k_{\mathrm{dowel}}} \right)^{-1}, \tag{B.31}$$

and the total translational stiffness of the connection is obtained by summing over all rows:

$$k_{\mathrm{trans}} = \sum_{i=1}^{n_{\mathrm{row}}} k_{\mathrm{row},i}. \tag{B.32}$$

Using the previously determined spring values, the stiffness for each row is:

- $k_{\mathrm{row},1} = 7.2$ kN/mm;
- $k_{\mathrm{row},2} = 7.2$ kN/mm;
- $k_{\mathrm{row},3} = 2.7$ kN/mm;
- $k_{\mathrm{row},4} = 2.7$ kN/mm;
- $k_{\mathrm{row},5} = 7.2$ kN/mm;
- $k_{\mathrm{row},6} = 7.2$ kN/mm.

Summing these contributions gives the overall translational stiffness of the connection:

$$k_{\mathrm{trans}} = 34\,\mathrm{kN/mm}.$$

C

Code for the analytical method

In this chapter the full code used for the analytical method is presented. The implementation is organized into separate Python files, each corresponding to a specific model setup. Because every model differs slightly in its boundary conditions, a dedicated file was created for each case. This approach keeps the coding streamlined, facilitates debugging in the early stages, and allows complexity to be added gradually. The first part concerns the beam setup without rotational springs:

```
# Importing libraries
import sympy as sym

# Setting variable
q = 0
x, EI, L, w, Mp, v, P, w, F, rp, ke, fp, vc, F1, M_tr = sym.symbols('x EI L w Mp v P w F rp ke fp vc F1 M_tr')
C11, C12, C13, C14 = sym.symbols('C11, C12, C13, C14')
C21, C22, C23, C24 = sym.symbols('C21, C22, C23, C24')
# Integration
V_1 = -sym.integrate(q,x) + C11
V_2 = -sym.integrate(q,x) + C21
M_1 = sym.integrate(V_1,x) + C12
M_2 = sym.integrate(V_2,x) + C22
kappa_1 = M_1/EI
kappa_2 = M_2/EI
phi_1 = sym.integrate(kappa_1,x) + C13
phi_2 = sym.integrate(kappa_2,x) + C23
w_1 = -sym.integrate(phi_1,x) + C14
w_2 = -sym.integrate(phi_2,x) + C24
# Setting boundary conditions
eq1 = sym.Eq(w_1.subs(x,0),0)
eq2 = sym.Eq(M_1.subs(x,0),0)
eq3 = sym.Eq(w_1.subs(x,(1/2)*L),w_2.subs(x,(1/2)*L))
eq4 = sym.Eq(M_1.subs(x,(1/2)*L),M_2.subs(x, (1/2)*L))
eq5 = sym.Eq(V_1.subs(x,(1/2)*L),P+V_2.subs(x,(1/2)*L))
eq6 = sym.Eq(phi_1.subs(x,(1/2)*L),phi_2.subs(x,(1/2)*L))
eq7 = sym.Eq(M_2.subs(x,L),0)
eq8 = sym.Eq(w_2.subs(x,L),0)
# Solving boundary conditions
C_sol = sym.solve([eq1, eq2, eq3, eq4, eq5, eq6, eq7, eq8], [C11, C12, C13, C14, C21, C22, C23, C24])
w = w_1.subs(C_sol)
M = M_1.subs(C_sol)
w = w.subs(x,(1/2)*L)
M = M.subs(x,(1/2)*L)
# Calculating needed function and values
Mpeq = sym.Eq(Mp,M)                                 # Set moment equality for vb
Pp = sym.solve(Mpeq,P)[0]                           # Solving for the force needed for vb
vb = sym.simplify(w.subs(P,Pp))                     # Solving for vb
P_el = sym.solve(sym.Eq(v,w),P)[0]                  # Force function (elastic)
eq9 = sym.Eq(M-F*v+rp*F,Mp)                         # Plastic interaction equality
eq9 = eq9.subs(F,ke*(2*(v-vc)*(v+vc-2*rp))/L)       # Subbing in F
Fax = (ke*2*(v - vc)*(v +vc-2*rp))/L                # Axial force function (transient)
P_tr = sym.solve(eq9, P)[0]                         # Force function (transient)
eq10 = sym.Eq(M-fp*v,0)                             # Moment equality (catenary)
P_fr = sym.solve(eq10,P)[0]                         # Force function (catenary)
eq11 = sym.Eq(M_tr+F*rp,Mp)                         # Moment equality (transient)
eq11 = eq11.subs(F,ke*(2*(v-vc)*(v+vc-2*rp))/L)     # Subbing in F
M_tr = sym.solve(eq11,M_tr)[0]                      # Moment function (transient)
```

Figure C.1: Beam setup without rotational springs

As shown in Figure C.1, the code begins by defining the variables required for later integration. Since sympy python library is used, all inputs can be parameterized. The integration is then performed on the governing differential equation, as introduced in Chapter 4. After integration, the boundary conditions are applied, enabling the system to be solved. The solution is subsequently evaluated at the mid-span of the beam, which is the region of interest in this thesis. From this, all relevant equations for the analytical method—outlined in Chapter 4—are generated. These functions are later called within the main run file, which is presented at the end of this appendix.

The second file introduces rotational springs at the beam ends. In this setup, additional functions are required to capture the change in stiffness once the gap closes. When the gap is present, the rotational springs exhibit reduced stiffness; however, as the gap closes, the stiffness increases. To correctly represent this transition, the equations are modified with correction terms to ensure continuity of the response curve. This prevents the graph from showing an unrealistic jump at the point where the gap disappears.

```
# Importing libraries
import sympy as sym

# Setting variable
q = 0
x, EI, L, kr, w, Mp, v, P, w, F, rp, ke, fp, kr_in, v_g, vc, M_tr = sym.symbols('x EI L kr w Mp v P w F rp ke fp kr_in v_g vc M_tr')
C11, C12, C13, C14 = sym.symbols('C11, C12, C13, C14')
C21, C22, C23, C24 = sym.symbols('C21, C22, C23, C24')
# Integration
V_1 = -sym.integrate(q,x) + C11
V_2 = -sym.integrate(q,x) + C21
M_1 = sym.integrate(V_1,x) + C12
M_2 = sym.integrate(V_2,x) + C22
kappa_1 = M_1/EI
kappa_2 = M_2/EI
phi_1 = sym.integrate(kappa_1,x) + C13
phi_2 = sym.integrate(kappa_2,x) + C23
w_1 = -sym.integrate(phi_1,x) + C14
w_2 = -sym.integrate(phi_2,x) + C24
# Setting boundary conditions
eq1 = sym.Eq(w_1.subs(x,0),0)
eq2 = sym.Eq(M_1.subs(x,0),phi_1.subs(x,0)*kr)
eq3 = sym.Eq(w_1.subs(x,(1/2)*L),w_2.subs(x,(1/2)*L))
eq4 = sym.Eq(M_1.subs(x,(1/2)*L),M_2.subs(x, (1/2)*L))
eq5 = sym.Eq(V_1.subs(x,(1/2)*L),P+V_2.subs(x,(1/2)*L))
eq6 = sym.Eq(phi_1.subs(x,(1/2)*L),phi_2.subs(x,(1/2)*L))
eq7 = sym.Eq(M_2.subs(x,L),-phi_2.subs(x,L)*kr)
eq8 = sym.Eq(w_2.subs(x,L),0)
# Solving boundary conditions
C_sol = sym.solve([eq1, eq2, eq3, eq4, eq5, eq6, eq7, eq8],
                  [C11, C12, C13, C14, C21, C22, C23, C24])
w = w_1.subs(C_sol)
M = M_1.subs(C_sol)
w = w.subs(x,(1/2)*L)
M1 = M.subs(x,(1/2)*L)
# Calculating needed function and values
P_el = sym.solve(sym.Eq(v,w),P)[0]                              # Force function (elastic)
Mpeq = sym.Eq(Mp,M1)                                            # Set moment equality for vb
Pp = sym.solve(Mpeq,P)[0]                                       # Solving for the force needed for vb
vb = sym.simplify(w.subs(P,Pp))                                 # Solving for vb
eq9 = sym.Eq(M1-F*v+rp*F,Mp)                                    # Plastic interaction equality
eq9 = eq9.subs(F,ke*(2*(v-vc)*(v+vc-2*rp))/L)                   # Subbing in F
P_tr = sym.solve(eq9, P)[0]                                     # Force function (transient)
Fax = (ke*2*(v - vc)*(v +vc-2*rp))/L                            # Axial force function (transient)
P_tr_diff = P_tr.subs(v,v_g) - P_tr.subs({v:v_g, kr:kr_in})     # Difference function (transient)
P_tr_2 = P_tr - P_tr_diff                                       # Corrected function (transient)
eq10 = sym.Eq(M1-fp*v,0)                                        # Moment equality (catenary)
P_fr = sym.solve(eq10,P)[0]                                     # Force function (catenary)
P_fr_diff = P_fr.subs(v,v_g) - P_fr.subs({v:v_g, kr:kr_in})     # Difference function (catenary)
P_fr_2 = P_fr - P_fr_diff                                       # Corrected function (caternary)
eq11 = sym.Eq(M_tr+F*rp,Mp)                                     # Moment equality (transient)
eq11 = eq11.subs(F,ke*(2*(v-vc)*(v+vc-2*rp))/L)                 # Subbing in F
M_tr = sym.solve(eq11,M_tr)[0]                                  # Moment function (transient)
```

Figure C.2: Beam setup with rotational springs at the supports

The last file is the one with the rotational springs also in the middle so only change is a boundary condition this is shown here:

```
# Importing libraries
import sympy as sym

# Setting variable
q = 0
x, EI, L, kr, krm, w, Mp, v, P, w, F, rp, ke, fp, v_g, kr_in, vc, krm_in, M_tr = sym.symbols('x EI L kr krm w Mp v P w F rp ke fp v_g kr_in vc krm_in M_tr')
C11, C12, C13, C14 = sym.symbols('C11, C12, C13, C14')
C21, C22, C23, C24 = sym.symbols('C21, C22, C23, C24')
# Integration
V_1 = -sym.integrate(q,x) + C11
V_2 = -sym.integrate(q,x) + C21
M_1 = sym.integrate(V_1,x) + C12
M_2 = sym.integrate(V_2,x) + C22
kappa_1 = M_1/EI
kappa_2 = M_2/EI
phi_1 = sym.integrate(kappa_1,x) + C13
phi_2 = sym.integrate(kappa_2,x) + C23
w_1 = -sym.integrate(phi_1,x) + C14
w_2 = -sym.integrate(phi_2,x) + C24
# Setting boundary conditions
eq1 = sym.Eq(w_1.subs(x,0),0)
eq2 = sym.Eq(M_1.subs(x,0),phi_1.subs(x,0)*kr)
eq3 = sym.Eq(w_1.subs(x,(1/2)*L),w_2.subs(x,(1/2)*L))
eq4 = sym.Eq(M_1.subs(x,(1/2)*L),M_2.subs(x, (1/2)*L))
eq5 = sym.Eq(V_1.subs(x,(1/2)*L),P+V_2.subs(x,(1/2)*L))
eq6 = sym.Eq(phi_1.subs(x,(1/2)*L)+M_1.subs(x,(1/2)*L)/krm,phi_2.subs(x,(1/2)*L))
eq7 = sym.Eq(M_2.subs(x,L),-phi_2.subs(x,L)*kr)
eq8 = sym.Eq(w_2.subs(x,L),0)
# Solving boundary conditions
C_sol = sym.solve([eq1, eq2, eq3, eq4, eq5, eq6, eq7, eq8], [C11, C12, C13, C14, C21, C22, C23, C24])
w = w_1.subs(C_sol)
M = M_1.subs(C_sol)
kappa = kappa_1.subs(C_sol)
w = w.subs(x,(1/2)*L)
kappa = kappa.subs(x,(1/2)*L)
M1 = M.subs(x,(1/2)*L)
# Calculating needed function and values
P_el = sym.solve(sym.Eq(v,w),P)[0]                                          # Force function (elastic)
P_el_diff = P_el.subs(v,v_g) - P_el.subs({v:v_g, kr:kr_in, krm:krm_in})     # Difference function (elastic)
P_el_2 = P_el - P_el_diff                                                   # Corrected function (elastic)
Mpeq = sym.Eq(Mp,M1)                                                        # Set moment equality for vb
Pp = sym.solve(Mpeq,P)[0]                                                   # Solving for the force needed for vb
vb = sym.simplify(w.subs(P,Pp))                                             # Solving for vb
Pp_2 = P_el.subs({kr:kr_in, krm:krm_in,v:v_g})                              # Corrected force for vb
vb_diff =  v_g - w.subs(P,Pp_2)                                             # Difference vb
vb2 = vb + vb_diff                                                          # Corrected vb
eq9 = sym.Eq(M1-F*v+rp*F,Mp)                                                # Plastic interaction equality
eq9 = eq9.subs(F,ke*(2*(v-vc)*(v+vc-2*rp))/L)                               # Subbing in F
P_tr = sym.solve(eq9, P)[0]                                                 # Force function (transient)
P_tr_diff = P_tr.subs(v,v_g) - P_tr.subs({v:v_g, kr:kr_in, krm:krm_in})     # Difference function (transient)
P_tr_2 = P_tr - P_tr_diff                                                   # Corrected function (transient)
eq10 = sym.Eq(M1-fp*v,0)                                                    # Moment equality (catenary)
P_fr = sym.solve(eq10,P)[0]                                                 # Force function (catenary)
P_fr_diff = P_fr.subs(v,v_g) - P_fr.subs({v:v_g, kr:kr_in, krm:krm_in})     # Difference function (catenary)
P_fr_2 = P_fr - P_fr_diff                                                   # Corrected function (caternary)
Fax = (ke*2*(v - vc)*(v +vc-2*rp))/L                                        # Axial force function (transient)
eq11 = sym.Eq(M_tr+F*rp,Mp)                                                 # Moment equality (transient)
eq11 = eq11.subs(F,ke*(2*(v-vc)*(v+vc-2*rp))/L)                             # Subbing in F
M_tr = sym.solve(eq11,M_tr)[0]                                              # Moment function (transient)
```

Figure C.3: Beam setup with rotational springs at the supports

The main run file integrates all components of the analytical method. It begins by importing the required libraries and the individual Python files described in the previous sections. Next, variables are defined to serve as inputs for the functions, followed by the specification of all parameters relevant to the connection setup.For each case—both with and without a gap, and for every rotational spring configuration—functions are created to represent the different stages of the analysis. Where necessary, a secondary function is introduced to account for gap closure within a stage, ensuring that changes in rotational spring stiffness are correctly reflected in the results. In addition, moment and axial force functions are defined for each stage to capture the structural response. Finally, the results are plotted and saved, including the data points from the validation tests, to allow direct comparison between analytical predictions and experimental observations.

```
# Importing libraries
import sympy as sym
import numpy as np
import matplotlib.pyplot as plt
import scipy as sc
import pfbeam
import pfbeam_kr
import pfbeam_kr_krm
plt.rcParams.update({'font.size': 18})

# set running variables and fixed variables
x, EI, L, kr, ks, krm, w, Mp, v, P, w, ke, rp, vb, fp, mp, kr_in, v_g, vc, krm_in, w_b = sym.symbols('x EI L kr ks krm w Mp v P w ke rp vb fp mp kr_in v_g vc krm_in w_b')
q = 0                                                                   # Distributed load
vs = np.linspace(0,0.2,1001)                                            # Deflection array [m]
gap = 0.001                                                             # Setting connection gap [m]
v_gap = 0.032                                                           # Deflection needed to close gap [m]
mp1 = 1.34*2                                                            # Plastic moment of the connection [kNm]
fp1 = 29.01                                                             # Ultimate axial strength connection [kN]
rp1 = mp1/fp1                                                           # Plastic interation term
ks1 = 34208                                                             # Axial stiffness connection [kN/m]
kr1 = 22                                                                # Rotational stiffness support springs [kNm/rad] (1)
krm1 = 22*2                                                             # Rotational stiffness middle springs [kNm/rad] (1)
kr2 = 44.4                                                              # Rotational stiffness support springs [kNm/rad] (2)
krm2 = 44.4*2                                                           # Rotational stiffness middle springs [kNm/rad] (2)
E1 = 15600000                                                           # Bending modulus of elasticity [kN/m^2]
b1 = 0.063                                                              # Width of the beam [m]
h1 = 0.150                                                              # Height of the beam [m]
A1 = b1*h1                                                              # Area of the cross section of the beam [m^2]
I1 = (1/12)*b1*h1**3                                                    # Moment of inertia of the beam [m^4]
EA1 = E1*A1                                                             # Axial stiffness of the beam [kN]
EI1 = E1*I1                                                             # Bending stiffness of the beam [kNm^2]
L1 = 4                                                                  # Length of the system [m]
ke1 = 1/((1/ks1)+(L1/EA1)+(1/ks1))                                      # Axial stiffness of the whole system [kN/m]

# setting new values for chapter 8 calculation
kr3 = 56.15                                                             # Rotational stiffness support springs [kNm/rad] (chp8)
krm3 = 56.15*2                                                          # Rotational stiffness middle springs [kNm/rad] (chp8)
mp2  = 1.63*2                                                           # Plastic moment of the connection [kNm] (chp8)
rp2 = mp2/fp1                                                           # Plastic interation term (chp8)
rot_max = 5.5*(np.pi/180)                                               # Maximum rotation until failure [rad]

# Functions and deflection for the lay out without rotational springs and with gap
ps1 = np.zeros(len(vs))                                                 # Make zero array for the Force
Fs1 = np.zeros(len(vs))                                                 # Make zero array for the axial Force
Ms1 = np.zeros(len(vs))                                                 # Make zero array for the Moment
As1_list = []                                                           # Make list for dynamic response
lam1_list = []                                                          # Make list for dynamic amplification factors
P_el1 = pfbeam.P_el.subs({L:L1,EI:EI1})                                 # Get the elastic function
M_el1 = pfbeam.M.subs({L:L1,EI:EI1,P:P_el1})                            # Get the Moment in the elastic stage
Fax1 = pfbeam.Fax.subs({ke:ke1,vc:v_gap,rp:rp1,L:L1})                   # Get axial force of the system
Pp1 = pfbeam.Pp.subs({L:L1,EI:EI1,Mp:mp1})                              # PLastic bending force
vb1 = float(pfbeam.vb.subs({L:L1,EI:EI1,Mp:mp1}))                       # Get the point where plastic bending starts
P_tr1 = pfbeam.P_tr.subs({EI:EI1,ke:ke1,rp:rp1,L:L1,Mp:mp1,vc:v_gap})   # Get the transient function
M_tr1 = pfbeam.M_tr.subs({EI:EI1,ke:ke1,rp:rp1,L:L1,Mp:mp1,vc:v_gap})   # Get the Moment in transient stage
vd1 = rp1 + np.sqrt((rp1-v_gap)**2+((fp1*L1)/(2*ke1)))                  # Get the point where final catenary stage starts
P_fr1 = pfbeam.P_fr.subs({fp:fp1,L:L1})                                 # Get the final catenary function

# Functions and deflection for the lay out without rotational springs and no gap
ps2 = np.zeros(len(vs))                                                 # Make zero array for the Force
Fs2 = np.zeros(len(vs))                                                 # Make zero array for the axial Force
Ms2 = np.zeros(len(vs))                                                 # Make zero array for the Moment
As2_list = []                                                           # Make list for dynamic response
lam2_list = []                                                          # Make list for dynamic amplification factors
Fax2 = pfbeam.Fax.subs({ke:ke1,vc:vb1,rp:rp1,L:L1})                     # Get the axial Force
P_tr2 = pfbeam.P_tr.subs({EI:EI1,ke:ke1,rp:rp1,L:L1,Mp:mp1,vc:vb1})     # Get the transient function
M_tr2 = pfbeam.M_tr.subs({EI:EI1,ke:ke1,rp:rp1,L:L1,Mp:mp1,vc:vb1})     # Get the Moment in transient stage
vd2 = rp1 + np.sqrt((rp1-vb1)**2+((fp1*L1)/(2*ke1)))                    # Get the point where final catenary stage starts
P_fr2 = pfbeam.P_fr.subs({fp:fp1,L:L1})                                 # Get the final catenary function

# Functions and deflection for the lay out with rotational springs at the supports and no gap
ps3 = np.zeros(len(vs))                                                 # Make zero array for the Force
Fs3 = np.zeros(len(vs))                                                 # Make zero array for the axial Force
Ms3 = np.zeros(len(vs))                                                 # Make zero array for the Moment
As3_list = []                                                           # Make list for dynamic response
lam3_list = []                                                          # Make list for dynamic amplification factors
P_el3 = pfbeam_kr.P_el.subs({L:L1,EI:EI1,kr:kr2})                       # Get the elastic function
M_el3 = pfbeam_kr.M1.subs({L:L1,EI:EI1,P:P_el3,kr:kr2})                 # Get the Moment in the elastic stage
vb3 = float(pfbeam_kr.vb.subs({L:L1,EI:EI1,Mp:mp1,kr:kr2}))             # Get the point where plastic bending starts
Fax3 = pfbeam_kr.Fax.subs({ke:ke1,vc:vb3,rp:rp1,L:L1})                  # Get axial force of the system
P_tr3 = pfbeam_kr.P_tr.subs({EI:EI1,ke:ke1,rp:rp1,L:L1,Mp:mp1,vc:vb3,kr:kr2})   # Get the transient function
M_tr3 = pfbeam_kr.M_tr.subs({EI:EI1,ke:ke1,rp:rp1,L:L1,Mp:mp1,vc:vb3,kr:kr2})   # Get the Moment in transient stage
```

Figure C.4: Main run file (1).

```
vd3 = rp1 + np.sqrt((rp1-vb3)**2+((fp1*L1)/(2*ke1)))                                    # Get the point where final catenary stage starts
P_fr3 = pfbeam_kr.P_fr.subs({fp:fp1,L:L1,kr:kr2,EI:EI1})                                # Get the final catenary function

# Functions and deflection for the lay out with rotational springs at the supports and with gap
ps4 = np.zeros(len(vs))                                                                 # Make zero array for the Force
Fs4 = np.zeros(len(vs))                                                                 # Make zero array for the axial Force
Ms4 = np.zeros(len(vs))                                                                 # Make zero array for the Moment
As4_list = []                                                                           # Make list for dynamic response
lam4_list = []                                                                          # Make list for dynamic amplification factors
P_el4 = pfbeam_kr.P_el.subs({L:L1,EI:EI1,kr:kr1})                                       # Get the elastic function
M_el4 = pfbeam_kr.M1.subs({L:L1,EI:EI1,P:P_el4,kr:kr1})                                 # Get the moment in the elastic stage
Fax4 = pfbeam_kr.Fax.subs({L:L1,EI:EI1,kr:kr1,vc:v_gap,ke:ke1,rp:rp1})                  # Get axial force of the system
vb4 = float(pfbeam_kr.vb.subs({L:L1,EI:EI1,Mp:mp1,kr:kr1}))                             # Get the point where plastic bending starts
P_tr4 = pfbeam_kr.P_tr_2.subs({EI:EI1,ke:ke1,rp:rp1,L:L1,Mp:mp1,
                               vc:v_gap,kr:kr2,v_g:v_gap,kr_in:kr1})                    # Get the transient function
M_tr4 = pfbeam_kr.M_tr.subs({EI:EI1,ke:ke1,rp:rp1,L:L1,Mp:mp1,vc:v_gap,kr:kr2})         # Get the moment in transient stage
Pp4 = pfbeam_kr.Pp.subs({L:L1,EI:EI1,kr:kr1,Mp:mp1})                                    # Get the plastic bending Force

# Functions and deflection for the lay out with rotational springs at the supports and no gap
ps5 = np.zeros(len(vs))                                                                 # Make zero array for the Force
Fs5 = np.zeros(len(vs))                                                                 # Make zero array for the axial Force
Ms5 = np.zeros(len(vs))                                                                 # Make zero array for the moment
As5_list = []                                                                           # Make list for dynamic response
lam5_list = []                                                                          # Make list for dynamic amplification factors
P_el5 = pfbeam_kr_krm.P_el.subs({L:L1,EI:EI1,kr:kr2,krm:krm2})                          # Get the elastic function
M_el5 = pfbeam_kr_krm.M1.subs({L:L1,EI:EI1,Mp:mp1,kr:kr2,krm:krm2,P:P_el5})             # Get the moment in the elastic stage
vb5 = float(pfbeam_kr_krm.vb.subs({L:L1,EI:EI1,Mp:mp1,kr:kr2,krm:krm2}))                # Get the point where plastic bending starts
Fax5 = pfbeam_kr_krm.Fax.subs({ke:ke1,vc:vb5,rp:rp1,L:L1,krm:krm2,kr:kr2})               # Get axial force of the system
P_tr5 = pfbeam_kr_krm.P_tr.subs({EI:EI1,ke:ke1,rp:rp1,L:L1,Mp:mp1,vc:vb5,kr:kr2,krm:krm2})  # Get the transient function
M_tr5 = pfbeam_kr.M_tr.subs({EI:EI1,ke:ke1,rp:rp1,L:L1,Mp:mp1,vc:vb5,kr:kr2,krm:krm2})  # Get the moment in transient stage
vd5 = rp1 + np.sqrt((rp1-vb5)**2+((fp1*L1)/(2*ke1)))                                    # Get the point where final catenary stage starts
P_fr5 = pfbeam_kr_krm.P_fr.subs({fp:fp1,L:L1,kr:kr2,EI:EI1,krm:krm2})                   # Get the final catenary function

# Functions and deflection for the lay out with rotational springs at the supports and with gap
ps6 = np.zeros(len(vs))                                                                 # Make zero array for the Force
Fs6 = np.zeros(len(vs))                                                                 # Make zero array for the axial Force
Ms6 = np.zeros(len(vs))                                                                 # Make zero array for the moment
As6_list = []                                                                           # Make list for dynamic response
lam6_list = []                                                                          # Make list for dynamic amplification factors
P_el6 = pfbeam_kr_krm.P_el.subs({L:L1,EI:EI1,kr:kr1,krm:krm1,v_g:v_gap})                # Get the elastic function
P_el6_2 = pfbeam_kr_krm.P_el_2.subs({L:L1,EI:EI1,kr:kr2,v_g:v_gap,
                                     kr_in:kr1,krm_in:krm1,krm:krm2})                   # Get the elastic function corrected for gap
M_el6 = pfbeam_kr_krm.M1.subs({L:L1,EI:EI1,Mp:mp1,kr:kr1,krm:krm1,P:P_el6})             # Get the moment in the elastic stage
M_el6_2 = pfbeam_kr_krm.M1.subs({L:L1,EI:EI1,Mp:mp1,kr:kr2,krm:krm2,
                                 P:P_el6_2,kr_in:kr1,krm_in:krm1,v_g:v_gap})            # Get the moment in the elastic stage corrected for gap
vb6 = float(pfbeam_kr_krm.vb2.subs({L:L1,EI:EI1,kr:kr2,krm:krm2,
                                    krm_in:krm1,kr_in:kr1,v_g:v_gap,Mp:mp1}))           # Get the point where plastic bending starts
Fax6 = pfbeam_kr_krm.Fax.subs({ke:ke1,vc:vb6,rp:rp1,L:L1,krm:krm2,kr:kr2})               # Get axial force of the system
P_tr6 = pfbeam_kr_krm.P_tr.subs({EI:EI1,ke:ke1,rp:rp1,L:L1,Mp:mp1,vc:vb6,kr:kr2,
                                 v_g:v_gap,kr_in:kr1,krm_in:krm1,krm:krm2})             # Get the transient function
M_tr6 = pfbeam_kr_krm.M_tr.subs({EI:EI1,ke:ke1,rp:rp1,L:L1,Mp:mp1,vc:vb6,kr:kr2,krm:krm2})  # Get the moment in transient stage
Pp6 = pfbeam_kr_krm.Pp.subs({L:L1,EI:EI1,kr:kr1,Mp:mp1,krm:krm1})                       # Get the plastic bending Force
vd6 = rp1 + np.sqrt((rp1-vb6)**2+((fp1*L1)/(2*ke1)))                                    # Get the point where final catenary stage starts

# Function for Chapter 8 calculation
ps7 = np.zeros(len(vs))                                                                 # Make zero array for the Force
As7_list = []                                                                           # Make list for dynamic response
P_el7 = pfbeam_kr_krm.P_el.subs({L:L1,EI:EI1,kr:kr1,krm:krm1,v_g:v_gap})                # Get the elastic function
P_el7_2 = pfbeam_kr_krm.P_el_2.subs({L:L1,EI:EI1,kr:kr3,krm:krm3,v_g:v_gap,
                                     kr_in:kr1,krm_in:krm1})                            # Get the elastic function with corrected for gap
vb7 = float(pfbeam_kr_krm.vb2.subs({L:L1,EI:EI1,kr:kr3,krm:krm3,krm_in:krm1,
                                    kr_in:kr1,v_g:v_gap,Mp:mp2}))                       # Get the point where plastic bending starts
P_tr7 = pfbeam_kr_krm.P_tr.subs({EI:EI1,ke:ke1,rp:rp2,L:L1,Mp:mp2,vc:vb7,kr:kr3,
                                 v_g:v_gap,kr_in:kr1,krm_in:krm1,krm:krm3})             # Get the transient function
P_fr7 = pfbeam_kr_krm.P_fr.subs({EI:EI1,ke:ke1,rp:rp2,L:L1,Mp:mp2,vc:vb7,kr:kr3,
                                 v_g:v_gap,kr_in:kr1,krm_in:krm1,krm:krm3})             # Get the final catenary function
Pp7 = pfbeam_kr_krm.Pp.subs({L:L1,EI:EI1,kr:kr3,Mp:mp2,krm:krm3})                       # Get the plastic bending Force
vd7 = rp1 + np.sqrt((rp1-vb7)**2+((fp1*L1)/(2*ke1)))                                    # Get the point where final catenary stage starts
kappa7 = pfbeam_kr_krm.kappa.subs({EI:EI1,ke:ke1,rp:rp2,L:L1,Mp:mp2,vc:vb7,
                                   kr:kr3,krm:krm3})                                    # Get the rotation of the cross section of the beam

# Looping through all the displacements
for n in range(len(vs)):
    if vs[n] < vb1:
        ps1[n] = P_el1.subs(v,vs[n])
        Fs1[n] = 0
        Ms1[n] = M_el1.subs(v,vs[n])
    elif vs[n] >= vb1 and vs[n] < v_gap:
        ps1[n] = Pp1
        Fs1[n] = 0
        Ms1[n] = mp1
    elif vs[n] >= v_gap and vs[n] < vd1:
        ps1[n] = P_tr1.subs(v,vs[n])
        Fs1[n] = Fax1.subs(v,vs[n])
```

Figure C.5: Main run file (2).

```
        Ms1[n] = M_tr1.subs(v,vs[n])
    else:
        ps1[n] = P_fr1.subs(v,vs[n])
        Fs1[n] = fp1

for n in range(len(vs)):
    if vs[n] < vb1:
        ps2[n] = P_el1.subs(v,vs[n])
        Fs2[n] = 0
        Ms2[n] = M_el1.subs(v,vs[n])
    elif vs[n] >= vb1 and vs[n] < vd2:
        ps2[n] = P_tr2.subs(v,vs[n])
        Fs2[n] = Fax2.subs(v,vs[n])
        Ms2[n] = M_tr2.subs(v,vs[n])
    else:
        ps2[n] = P_fr2.subs(v,vs[n])
        Fs2[n] = fp1

for n in range(len(vs)):
    if vs[n] < vb3:
        ps3[n] = P_el3.subs(v,vs[n])
        Fs3[n] = 0
        Ms3[n] = M_el3.subs(v,vs[n])
    elif vs[n] >= vb3 and vs[n] < vd3:
        ps3[n] = P_tr3.subs(v,vs[n])
        Fs3[n] = Fax3.subs(v,vs[n])
        Ms3[n] = M_tr3.subs(v,vs[n])
    else:
        ps3[n] = P_fr3.subs(v,vs[n])
        Fs3[n] = fp1

for n in range(len(vs)):
    if vs[n] < vb4:
        ps4[n] = P_el4.subs(v,vs[n])
        Fs4[n] = 0
        Ms4[n] = M_el4.subs(v,vs[n])
    elif vs[n] >= vb4 and vs[n] < v_gap:
        ps4[n] = Pp4
        Fs4[n] = 0
        Ms4[n] = mp1
    elif vs[n] >= v_gap and vs[n] < vd1:
        ps4[n] = P_tr4.subs(v,vs[n])
        Fs4[n] = Fax4.subs(v,vs[n])
        Ms4[n] = M_tr4.subs(v,vs[n])
    else:
        ps4[n] = P_fr3.subs(v,vs[n])
        Fs4[n] = fp1

for n in range(len(vs)):
    if vs[n] < vb5:
        ps5[n] = P_el5.subs(v,vs[n])
        Fs5[n] = 0
        Ms5[n] = M_el5.subs(v,vs[n])
    elif vs[n] >= vb5 and vs[n] < vd5:
        ps5[n] = P_tr5.subs(v,vs[n])
        Fs5[n] = Fax5.subs(v,vs[n])
        Ms5[n] = M_tr5.subs(v,vs[n])
    else:
        ps5[n] = P_fr5.subs(v,vs[n])
        Fs5[n] = fp1

for n in range(len(vs)):
    if vs[n] < v_gap:
        ps6[n] = P_el6.subs(v,vs[n])
        Fs6[n] = 0
        Ms6[n] = M_el6.subs(v,vs[n])
    elif vs[n] >= v_gap and vs[n] < vb6:
        ps6[n] = P_el6_2.subs(v,vs[n])
        Fs6[n] = 0
        Ms6[n] = M_el6_2.subs(v,vs[n])
    elif vs[n] >= vb6 and vs[n] < vd6:
        ps6[n] = P_tr6.subs(v,vs[n])
        Fs6[n] = Fax6.subs(v,vs[n])
        Ms6[n] = M_tr6.subs(v,vs[n])
    else:
        ps6[n] = P_fr5.subs(v,vs[n])
        Fs6[n] = fp1

for n in range(len(vs)):
    if vs[n] < v_gap:
        ps7[n] = P_el7.subs(v,vs[n])
        rot_mid = np.arcsin(vs[n]/2) + kappa7.subs(P,ps7[n])
    elif vs[n] >= v_gap and vs[n] < vb7:
        ps7[n] = P_el7_2.subs(v,vs[n])
```

Figure C.6: Main run file (3).

```
        rot_mid = np.arcsin(vs[n]/2) + kappa7.subs(P,ps7[n])
    elif vs[n] >= vb7 and vs[n] < rp2 and rot_mid < rot_max:
        ps7[n] = Pp7
        rot_mid = np.arcsin(vs[n]/2) + kappa7.subs(P,ps7[n])
    elif vs[n] >= rp2 and rot_mid < rot_max:
        ps7[n] = P_tr7.subs(v,vs[n])
        rot_mid = np.arcsin(vs[n]/2) + kappa7.subs(P,ps7[n])
    elif vs[n] >= vd7 and rot_mid < rot_max:
        ps7[n] = P_fr7.subs(v,vs[n])
        rot_mid = np.arcsin(vs[n]/2) + kappa7.subs(P,ps7[n])
    else:
        ps7[n] = 0

# Making Pseudo static repsonses and amplififcations factors
As1_list = sc.integrate.cumulative_simpson(y=ps1[0:1001],x=vs[0:1001])/vs[1:]
lam1_list = ps1[1:]/As1_list
As2_list = sc.integrate.cumulative_simpson(y=ps2[0:1001],x=vs[0:1001])/vs[1:]
lam2_list = ps2[1:]/As2_list
As3_list = sc.integrate.cumulative_simpson(y=ps3[0:1001],x=vs[0:1001])/vs[1:]
lam3_list = ps3[1:]/As3_list
As4_list = sc.integrate.cumulative_simpson(y=ps4[0:1001],x=vs[0:1001])/vs[1:]
lam4_list = ps4[1:]/As4_list
As5_list = sc.integrate.cumulative_simpson(y=ps5[0:1001],x=vs[0:1001])/vs[1:]
lam5_list = ps5[1:]/As5_list
As6_list = sc.integrate.cumulative_simpson(y=ps6[0:1001],x=vs[0:1001])/vs[1:]
lam6_list = ps6[1:]/As6_list
As7_list = sc.integrate.cumulative_simpson(y=ps7[0:1001],x=vs[0:1001])/vs[1:]
lam7_list = ps7[1:]/As7_list

# Print elastic stiffness values
print(f'Without rotational springs and no gap, the stiffness = {ps2[np.where(vs>=vb1)[0][0]]/(vb1*1000)}')
print(f'Without rotational springs and 1mm gap, the stiffness = {ps1[np.where(vs>=vb1)[0][0]]/(vb1*1000)}')
print(f'With rotational springs at supports and no gap, the stiffness = {ps3[np.where(vs>=vb3)[0][0]]/(vb3*1000)}')
print(f'With rotational springs at supports and 1mm gap, the stiffness = {ps4[np.where(vs>=vb4)[0][0]]/(vb4*1000)}')
print(f'With rotational springs at supports and in the middle and no gap, the stiffness = {ps5[np.where(vs>=vb5)[0][0]]/(vb5*1000)}')
print(f'With rotational springs at supports and in the middle and 1mm gap, the stiffness = {ps6[np.where(vs>=vb6)[0][0]]/(vb6*1000)}')
print(f'chap8 modifications, the stiffness = {ps7[np.where(vs>=vb7)[0][0]]/(vb7*1000)}')

# Plotting and saving the push down response
plt.figure(figsize=(16,11))
plt.plot(vs*1000,ps2, label='Without rotational springs and no gap', color='r', linestyle='-')
plt.plot(vs*1000,ps1, label='Without rotational springs and 1mm gap', color='r', linestyle='--')
plt.plot(vs*1000,ps3, label='With rotational springs at supports and no gap', color='b', linestyle='-')
plt.plot(vs*1000,ps4, label='With rotational springs at supports and 1mm gap', color='b', linestyle='--')
plt.plot(vs*1000,ps5, label='With rotational springs at supports and in the middle and no gap', color='g', linestyle='-')
plt.plot(vs*1000,ps6, label='With rotational springs at supports and in the middle and 1mm gap', color='g', linestyle='--')
plt.xlim(0,200)
plt.ylim(0,5)
plt.xlabel('Deflection [mm]')
plt.ylabel('Force [kN]')
plt.grid()
plt.legend()
plt.savefig('Push_down_final.png')
plt.close()

# Plotting and saving the axial force from push down response
plt.figure(figsize=(18,12))
plt.plot(vs*1000,Fs2/2, label='Without rotational springs and no gap', color='r', linestyle='-')
plt.plot(vs*1000,Fs1/2, label='Without rotational springs and 1mm gap', color='r', linestyle='--')
plt.plot(vs*1000,Fs3/2, label='With rotational springs at supports and no gap', color='b', linestyle='-')
plt.plot(vs*1000,Fs4/2, label='With rotational springs at supports and 1mm gap', color='b', linestyle='--')
plt.plot(vs*1000,Fs5/2, label='With rotational springs at supports and in the middle and no gap', color='g', linestyle='-')
plt.plot(vs*1000,Fs6/2, label='With rotational springs at supports and in the middle and 1mm gap', color='g', linestyle='--')
plt.xlim(0,200)
plt.ylim(-20,15)
plt.xlabel('Deflection [mm]')
plt.ylabel('Force [kN]')
plt.grid()
plt.legend()
plt.savefig('Push_down_final_axial.png')
plt.close()

# Plotting and saving the moment from push down response
plt.figure(figsize=(26,14))
plt.plot(np.arctan(vs/2)*(180/np.pi),Ms2/2, label='Without rotational springs and no gap', color='r', linestyle='-')
plt.plot(np.arctan(vs/2)*(180/np.pi),Ms1/2, label='Without rotational springs and 1mm gap', color='r', linestyle='--')
plt.plot(np.arctan(vs/2)*(180/np.pi),Ms3/2, label='With rotational springs at supports and no gap', color='b', linestyle='-')
plt.plot(np.arctan(vs/2)*(180/np.pi),Ms4/2, label='With rotational springs at supports and 1mm gap', color='b', linestyle='--')
plt.plot(np.arctan(vs/2)*(180/np.pi),Ms5/2, label='With rotational springs at supports and in the middle and no gap', color='g', linestyle='-')
plt.plot(np.arctan(vs/2)*(180/np.pi),Ms6/2, label='With rotational springs at supports and in the middle and 1mm gap', color='g', linestyle='--')
plt.xlim(0,6)
plt.ylim(0,3.5)
plt.xlabel('Rotation [deg]')
plt.ylabel('Moment [kN]')
```

Figure C.7: Main run file (4).

```
plt.grid()
plt.legend()
plt.savefig('Push_down_final_Moment.png')
plt.close()

# Plotting and saving the first two dynamic repsonses with data points
plt.figure(figsize=(16,11))
plt.plot(vs*1000,ps2, label='Without rotational springs and no gap', color='r', linestyle='-')
plt.plot(vs*1000,ps1, label='Without rotational springs and 1mm gap', color='b', linestyle='-')
plt.plot(vs[1:]*1000,As2_list, label='Without rotational springs and no gap (Dynamic)', color='r', linestyle='--')
plt.plot(vs[1:]*1000,As1_list, label='Without rotational springs and 1mm gap (Dynamic)', color='b', linestyle='--')
plt.scatter([7,8,10.4,20.4,37.5,53.9],[0.47,0.52,0.55,1.01,1.99,2.51], label='Data points from paper')
plt.grid()
plt.legend()
plt.xlim(0,200)
plt.ylim(0,5)
plt.xlabel('Deflection [mm]')
plt.ylabel('Force [kN]')
plt.savefig('Pseudo_static_push_analytical_1.png')
plt.close()

# Plotting and saving the second two dynamic repsonses with data points
plt.figure(figsize=(16,11))
plt.plot(vs*1000,ps3, label='With rotational springs at supports and no gap', color='r', linestyle='-')
plt.plot(vs*1000,ps4, label='With rotational springs at supports and 1mm gap', color='b', linestyle='-')
plt.plot(vs[1:]*1000,As3_list, label='With rotational springs at supports and no gap (Dynamic)', color='r', linestyle='--')
plt.plot(vs[1:]*1000,As4_list, label='With rotational springs at supports and 1mm gap (Dynamic)', color='b', linestyle='--')
plt.scatter([7,8,10.4,20.4,37.5,53.9],[0.47,0.52,0.55,1.01,1.99,2.51], label='Data points from paper')
plt.grid()
plt.legend()
plt.xlim(0,200)
plt.ylim(0,5)
plt.xlabel('Deflection [mm]')
plt.ylabel('Force [kN]')
plt.savefig('Pseudo_static_push_analytical_2.png')
plt.close()

# Plotting and saving the third two dynamic repsonses with data points
plt.figure(figsize=(18,11))
plt.plot(vs*1000,ps5, label='With rotational springs at supports and in the middle and no gap', color='r', linestyle='-')
plt.plot(vs*1000,ps6, label='With rotational springs at supports and in the middle and 1mm gap', color='b', linestyle='-')
plt.plot(vs[1:]*1000,As5_list, label='With rotational springs at supports and in the middle and no gap (Dynamic)', color='r', linestyle='--')
plt.plot(vs[1:]*1000,As6_list, label='With rotational springs at supports and in the middle and 1mm gap (Dynamic)', color='b', linestyle='--')
plt.scatter([7,8,10.4,20.4,37.5,53.9],[0.47,0.52,0.55,1.01,1.99,2.51], label='Data points from paper')
plt.grid()
plt.legend()
plt.xlim(0,200)
plt.ylim(0,5)
plt.xlabel('Deflection [mm]')
plt.ylabel('Force [kN]')
plt.savefig('Pseudo_static_push_analytical_3.png')
plt.close()

# Plotting and saving the amplifications factors with data points
plt.rcParams.update({'font.size': 14})
plt.figure(figsize=(26,14))
plt.plot(vs[4:]*1000,lam2_list[3:],label='DAF without rotational springs and no gap', color='r', linestyle='-')
plt.plot(vs[4:]*1000,lam1_list[3:],label='DAF without rotational springs and 1mm gap', color='r', linestyle='--')
plt.plot(vs[4:]*1000,lam3_list[3:],label='DAF with rotational springs at supports and no gap', color='b', linestyle='-')
plt.plot(vs[4:]*1000,lam4_list[3:],label='DAF with rotational springs at supports and 1mm gap', color='b', linestyle='--')
plt.plot(vs[4:]*1000,lam5_list[3:],label='DAF with rotational springs at supports and in the middle and no gap', color='g', linestyle='-')
plt.plot(vs[4:]*1000,lam6_list[3:],label='DAF with rotational springs at supports and in the middle and 1mm gap', color='g', linestyle='--')
plt.axhline(2,label='DAF=2')
plt.scatter([7,8,10.4,20.4,37.5,53.9],[1.74,1.72,1.98,1.79,1.45,1.42], label='Data points from paper')
plt.grid()
plt.xlabel('Deflection [mm]')
plt.ylabel('Amplification factor')
plt.legend()
plt.xlim(0,200)
plt.ylim(0.5,2.5)
plt.savefig('DAF_analytical.png')
plt.close()

# Plotting chapter 8 push down response
plt.rcParams.update({'font.size': 22})
plt.figure(figsize=(16,11))
plt.plot(vs*1000,ps7, label='Chapter 8 response', color='b')
plt.grid()
plt.legend()
plt.xlim(0,200)
plt.ylim(0,5)
plt.xlabel('Deflection [mm]')
plt.ylabel('Force [kN]')
plt.savefig('chp8_push_down.png')

# Plotting chapter 8 dynamic response
plt.rcParams.update({'font.size': 22})
plt.figure(figsize=(16,11))
plt.plot(vs*1000,ps7, label='Chapter 8 response', color='b')
plt.plot(vs[1:]*1000,As7_list, label='Chapter 8 pseudo static response', color='r')
plt.scatter([7,8,10.4,20.4,37.5,53.9],[0.47,0.52,0.55,1.01,1.99,2.51], label='Data points from paper')
plt.grid()
plt.legend()
plt.xlim(0,200)
plt.ylim(0,5)
plt.xlabel('Deflection [mm]')
plt.ylabel('Force [kN]')
plt.savefig('chp8_pseudo_static.png')
```

Figure C.8: Main run file (5).